Modeling and experimental observation of mixing and violent relaxation in an analogue gravitational system

Martino Lovisetto

UNIVERSITÉ CÔTE D'AZUR

ÉCOLE DOCTORALE
SCIENCES FONDAMENTALES ET APPLIQUÉES

MODÉLISATION ET OBSERVATION EXPÉRIMENTALE DU MIXING ET DE LA RELAXATION VIOLENTE DANS UN SYSTÈME GRAVITATIONNEL ANALOGUE

Martino LOVISETTO

Laboratoire de Mathématiques J. A. Dieudonné (LJAD)

Présentée en vue de l'optenation du grade de:
Docteur en Sciences de l'Université Côte d'Azur
Discipline: Mathématiques

THÈSE DIRIGÉE PAR: Didier CLAMOND
CO-DIRIGÉE PAR: Bruno MARCOS

SOUTENUE LE: 10 Mai 2022

DEVANT LE JURY COMPOSÉ DE:

Pierre-Henri CHAVANIS	Directeur de recherche, Université Paul Sabatier	Président du jury
Didier CLAMOND	Professeur, Université Côte d'Azur	Directeur de thése
Guillaume DUJARDIN	Chargé de recherche, Centre Inria de l'Université de Lille	Rapporteur
Oliver HAHN	Professeur, Universität Wien	Examinateur
Bruno MARCOS	Maître de conférences, Université Côte d'Azur	Co-Directeur de thése
Antonio PICOZZI	Directeur de recherche, Université Bourgogne Franche-Comté	Rapporteur
Francesca RAPETTI	Maitre de Conférences, Université Côte d'Azur	Examinatrice
Delphine WOLFERSBERGER	Professeure, CentraleSupélec Université Paris-Saclay	Examinatrice

MODELING AND EXPERIMENTAL OBSERVATION OF MIXING AND VIOLENT RELAXATION IN AN ANALOGUE GRAVITATIONAL SYSTEM

Martino LOVISETTO

Laboratoire de Mathématiques J. A. Dieudonné (LJAD)

Université Côte d'Azur

PhD Thesis

Discipline: Mathematics

SUPERVISOR: Didier CLAMOND
CO-SUPERVISOR: Bruno MARCOS

DEFENSE DATE: May 10th 2022

JURY MEMBERS:

Pierre-Henri CHAVANIS	Senior Researcher, Université Paul Sabatier	President of the Jury
Didier CLAMOND	Professor, Université Côte d'Azur	Supervisor
Guillaume DUJARDIN	Researcher, Centre Inria de l'Université de Lille	Reviewer
Oliver HAHN	Professor, Universität Wien	Examinator
Bruno MARCOS	Senior Lecturer, Université Côte d'Azur	Co-Supervisor
Antonio PICOZZI	Senior Researcher, Université Bourgogne Franche-Comté	Reviewer
Francesca RAPETTI	Senior Lecturer, Université Côte d'Azur	Examinator
Delphine WOLFERSBERGER	Professor, CentraleSupélec Université Paris-Saclay,	Examinator

RÉSUMÉ

Les équations du type Schrödinger-Newton apparaissent naturellement dans nombreux domaines de recherche. En cosmologie elles sont employées dans la modélisation de structures à grandes échelles dans l'Univers, alors qu'en astrophysique, elles sont employées comme description semi-classique pour l'évolution des particules élémentaires de matière noire. L'équation de Schrödinger-Newton est aussi utilisée en optique, pour décrire la propagation d'un rayon de lumière à travers un milieu avec une non-linéarité thermo-optique. Tous ces systèmes, bien qu'ils soient très différents les uns des autres, sont caractérisés par des interactions à longue portée. Les systèmes avec interactions à longue portée, en général relaxent vers un état quasi-stationnaire hors de l'équilibre, avec examples astrophysiques significatifs comme les galaxies et les amas globulaires. Ces états ne peuvent pas être décrits par la mécanique statistique standard, mais sont formés par un processus de nature très différente, appelé relaxation violente. Cependant, les échelles de temps astrophysiques sont si grandes qu'il n'est pas possible d'observer directement la dynamique de relaxation. Dans cette thèse, nous développons un simple modèle expérimental qui capture la dynamique des systèmes avec interactions à longue portée et permet d'observer directement le mécanisme de la relaxation violente, qui donne lieu à la formation d'un analogue optique d'une galaxie. L'expérience permet de contrôler une gamme de paramètres, y compris la force d'interaction non locale (gravitationnelle) et la force du couplage gravitationnel quantique $\hbar/m$, fournissant ainsi un banc d'essai efficace pour les modèles gravitationnels qui ne peuvent autrement être directement étudiés dans des expériences expérimentales.

Par ailleurs, une partie centrale de la thèse est dédiée à l'étude numérique de l'équation de Schrödinger-Newton. Ici, nous présentons une nouvelle méthode numérique efficace qui peut être utilisée non seulement pour résoudre l'équation de Schrödinger-Newton, mais toutes les équations du type Schrödinger, avec différents types d'interactions. La méthode numérique développée, qui exploite la liberté offerte par la condition de jauge du potentiel, est une amélioration de la technique du facteur intégrant (méthode de Lawson). Les conditions de jauge optimales sont dérivées en considérant l'équation et la résolution numérique temporelle avec un schéma intégré adaptatif d'ordre arbitraire. Nous montrons que cette optimisation augmente significativement la vitesse de calcul globale, parfois d'un facteur cinq ou plus. De plus, nous effectuons une comparaison approfondie de la nouvelle méthode développée, avec d'autres intégrateurs populaires, souvent utilisés pour résoudre numériquement ce type d'équations. Nous nous concentrons en particulier sur les algorithmes du type Split-Step et les méthodes appartenant à la famille du facteur intégrant. Les comparaisons sont faites dans une et deux dimensions spatiales, avec des conditions aux limites différentes, soit pour l'équation de Schrödinger–Newton soit pour l'équation de Schrödinger non-linéaire. Nous concluons que pour le potentiel à courte portée de l'équation de Schrödinger non-linéaire, le facteur intégrant est plus efficace que le Split-Step, tandis que pour le potentiel à longue portée de l'équation de Schrödinger–Newton, cela dépend du système considéré.

Mot clés : équation de Schrödinger–Newton ; optique non-linéaire ; gravité analogique ; méthodes spectrales ; pas de temps adaptatif ; méthodes de Lawson ; interaction à long portée ; réduction du paquet d'onde

ABSTRACT

Equations of the Schrödinger-Newton type appear naturally in different domains of research. In cosmology, they are used to model the formation of large scale structures in the universe, while, in astrophysics, they are employed as a semi-classical description for the evolution of elementary particles of dark matter. The Schrödinger-Newton equation is also used in optics, to describe the propagation of a beam of light through a medium with a thermo-optical nonlinearity. All of these systems, despite being very different from each other, are characterized by long range interactions. Long range interacting systems, relax generically to out-of-equilibrium quasi-stationary states, with significant astrophysical examples such as galaxies and globular clusters. These states cannot be described by standard statistical mechanics, but are formed through a process of very different nature, called violent relaxation. However, astrophysical time-scales are so large that it is not possible to directly observe the relaxation dynamics. In this thesis, we develop a table-top experimental model that captures the dynamics of long range interacting systems and allows to directly observe violent relaxation mechanism, leading to the formation of a table-top optical analogue of a galaxy. The experiment allows to control a range of parameters, including the nonlocal (gravitational) interaction strength and the strength of quantum gravity coupling $\hbar/m$, thus providing an effective test-bed for gravitational models that cannot otherwise be directly studied in experimental settings.

In addition, a central part of the thesis is devoted to the numerical study of the Schrödinger-Newton equation. Here, we present a new efficient numerical method which can be employed not only to solve the Schrödinger-Newton equation, but any Schrödinger-like equations, with different kind of interactions. The numerical method developed, which exploits the freedom provided by the gauge condition of the potential, is an improvement of the integrating factor technique. Optimal gauge conditions are derived considering the equation and the temporal numerical resolution with an adaptive embedded scheme of arbitrary order. We show that this optimization increases significantly the overall computational speed, sometimes by a factor five or more. Moreover, we make an extensive comparison of the new method developed, together with other popular integrators, commonly use to numerically solve this kind of equations. We focus in particular on splitting algorithms and methods belonging to the integrating factor family. Comparisons are done in one and two spatial dimensions, with different boundary conditions, both for the Schrödinger–Newton equation and the Non-Linear Schrödinger equation. We conclude that for the short range potential of the Non-Linear Schrödinger equation, integrating factor methods perform better than the Split-Step algorithm, while for the long range potential of the Schrödinger–Newton equation it depends on the particular system considered.

Keywords: Schrödinger–Newton equation; nonlinear optics; analogue gravity; spectral methods; time-stepping; Lawson methods; long range interactions; wavefunction collapse

ACKNOWLEDGEMENTS

I would like to thank my supervisors, Didier Clamond and Bruno Marcos. Working with you during these years taught me and made me appreciate the real value of scientific research.

I also would like to thank all the collaborators which made the realization of the experiment possible: Radivoje Prizia, Maria Chiara Braidotti, Daniele Faccio, Ewan Wright, Matthieu Bellec and Claire Michel.

Also, many thanks to my thesis monitoring committee, Pascal Viot and Benjamin Mauroy, for their kindness and useful discussions.

My gratitude and many thanks go to Guillaume Dujardin and Antonio Picozzi for being referees of my thesis, and also to Pierre-Henri Chavanis, Oliver Hahn, Francesca Rapetti and Delphine Wolfersberger for accepting to be a part of the jury.

Many thanks to Jean-Marc Lacroix, for all the explanations he gave me for using the computational resources of the university and the pleasant time spent together sharing our passion for music.

I also would like to thank all my friends and colleagues for their support, encouragement and for the inspiration they gave me.

Finally, I'm grateful to my family, in particular to my mother, Rosa, for her unconditional support.

CONTENTS

1 INTRODUCTION

Equations of the Schrödinger–Newton (or Schrödinger–Poisson) type, are used to describe a large variety of phenomena in different domains of science. Historically, the Newton–Schrödinger equation was introduced in 1969 by Ruffini and Bonazzola [1]. In their work, they derived the equation from the coupling between the weak field limit of general relativity and quantum mechanics, to describe a many-body system of self-gravitating bosons. The resulting state, is a gravitationally bounded Bose–Einstein condensate, which they called "Boson star" [2]. This equation has also been used to describe the phenomenon of the quantum wavefunction collapse, by Diosi [3] in 1984 and then by Penrose [4, 5] in 1996. In their works, they tried to describe the quantum state reduction mechanism, a phenomenon which takes place whenever a measurement is performed for a given quantum system, as a consequence of some self-gravitational interaction. As shown for the first time by Widrow and Kaiser [6] in 1993, the Schrödinger–Newton equation can be used also for simulating numerically collisionless matter, modeled as a continuous fluid. This is often done in astrophysics, plasma physics and cosmology. For example, it is used to model Fuzzy Dark Matter [7, 8] as well as to simulate the formation of large-scale structures in the early universe [9, 10]. The Newton–Schrödinger equation is also used in optics, to describe the evolution of a laser beam propagating through a nonlinear and nonlocal medium [11–13].

Regardless of the particular domain of application considered, in dimensionless units the equation takes the form

$$i\frac{\partial\psi}{\partial t} + \frac{1}{2}\nabla^2\psi - V\psi = 0, \tag{1.1a}$$

$$\nabla^2 V = g|\psi|^2, \tag{1.1b}$$

where ψ is a function of the spatial coordinates $\mathbf{r}$ and of the time t, ∇^2 is the Laplace operator, and V is the potential, given by the Poisson equation (1.1b), g being a coupling constant. The sign of g determines the nature of the interaction: for $g > 0$ it is attractive, while, for $g < 0$, it is repulsive. The reason why this equation is called Schrödinger–Newton, is because if $|\psi|^2$ is interpreted as a mass density, the potential V results in the classical, newtonian, potential.

The Newton–Schrödinger system can also be written in a different form. Introducing $U(\mathbf{r}-\mathbf{r}')$, the Green function of the laplacian, defined such that $\nabla U(\mathbf{r}-\mathbf{r}') = \delta(\mathbf{r}-\mathbf{r}')$, one has

$$V(\mathbf{r}, t) = g\int d\mathbf{r}'\, U(\mathbf{r}-\mathbf{r}')\,|\psi(\mathbf{r}', t)|^2, \tag{1.2}$$

and plugging (1.2) into (1.1a) yields

$$i\frac{\partial\psi}{\partial t} = -\frac{1}{2}\nabla^2\psi + g\psi\int d\mathbf{r}'\, U(\mathbf{r}-\mathbf{r}')\,|\psi(\mathbf{r}', t)|^2, \tag{1.3}$$

which, being the same as (1.1), is a nonlinear, nonlocal integro-differential equation. For this reason, even though (1.1) is a system of two coupled partial differential equations, we often refer to it as Newton–Schrödinger equation.

1.1 THE VIOLENT RELAXATION MECHANISM

The non-locality of the equation implies that the interaction associated with the potential V is long range. In general, many-body systems with long range interactions exhibit a macroscopic dynamics which gives rise to collective phenomena [14]. In these systems, starting from an arbitrary initial condition, a generic formation of out-of-equilibrium quasi stationary state rapidly takes place. The process that leads to the formation of such out-of-equilibrium quasi-stationary states is called violent relaxation [15]. The reason why these structures are called quasi-stationary states is because, at least in the astrophysical context, they evolve over a much longer timescale towards thermodynamic equilibrium [16]. A well known example of such quasi-stationary state is a galaxy, for which the time needed to reach the thermodynamic equilibrium is indeed typically larger than the age of the Universe.

The violent relaxation mechanism is also included in the dynamics of the Newton–Schrödinger equation in the form of (1.1) when it is regarded as a mean-field limit, namely as a system of N particles in the limit where $N \to \infty$. However, in this case there are two crucial aspects which must be taken into account: quantum effects and the mean-field approximation itself. Indeed, the former must be negligible compared to the contribute of the long range interacting potential, which is the term responsible for the violent relaxation. On the other hand, as long as the mean-field approximation is concerned, the system cannot relax to the thermodynamic equilibrium because of the limit $N \to \infty$, which avoids collisions to occur. This is because the relaxation to the Maxwell-Boltzmann thermodynamic equilibrium takes place in a time which scales generically with the number of elementary constituents of the system[15]. Therefore, the mean-field Newton–Schrödinger equation does not describe the thermodynamic equilibrium, however it fully incorporates the dynamics of the formation of the quasi-stationary state through the violent relaxation mechanism.

A central part of the thesis, is devoted to the realization of a table-top experiment with an optical setup modeled by the Newton–Schrödinger equation. Theoretically and numerically preparing the experiment, we report the first observations of a violent relaxation process and the subsequent formation of a quasi-stationary state.

1.2 NUMERICAL SOLUTION

The other key part of this thesis work, is related to the numerical study of the Schrödinger–Newton equation. In addition, we also focus on other Schrödinger-like equations with nonlinear potentials: the nonlinear Schrödinger and the Gross–Pitaevskii–Poisson equations.

In the case of the nonlinear Schrödinger equation, the potential term, $g|\psi|^2$, is nonlinear, but local,

$$i\,\partial_t\,\psi \;+\; \frac{1}{2}\,\nabla^2\,\psi \;-\, g\,|\psi|^2 \;=\; 0, \tag{1.4}$$

where g is a coupling constant. For $g > 0$ the interaction is repulsive, while it is attractive for $g < 0$. This equation describes various physical phenomena, such as Bose–Einstein condensates [17], laser beams in some nonlinear media [18] and water wave packets [19].

The Gross–Pitaevskii–Poisson (GPP) equation involves both the interaction term appearing in the nonlinear Schrödinger and Schrödinger–Newton systems,

$$i\,\partial_t\,\psi \;+\; \frac{1}{2}\nabla^2\,\psi \;-V_1\,\psi - V_2\,\psi = 0 \tag{1.5a}$$

$$\nabla^2 V_1 = g_1\,|\,\psi\,|^2 \tag{1.5b}$$

$$V_2 = g_2\,|\,\psi\,|^2\,. \tag{1.5c}$$

This equation appears in many fields, such as optics [20, 21], Bose-Einstein condensates [22] and cosmology, to simulate scalar field dark matter [23–25].

The above equations cannot be solved analytically (except for very special cases) and numerical methods must be employed. In this thesis, we focus on spectral methods for the spatial resolution, which are known to be particularly efficient and accurate [26]. Specifically, we rely on fast Fourier transform techniques. For the temporal resolution, two families of methods are commonly employed to solve Schrödinger-like equations: integrating factors [27] and split-step integrators [28]. The latter methods have been used to integrate both the Schrödinger–Newton and nonlinear Schrödinger equations, but the former is used essentially to solve the nonlinear Schrödinger equation, with very performing results [29, 30]. A natural question, which is one of the subjects of the thesis, is how the integrating factor performs when considering the long range interactions of the Schrödinger–Newton system instead of short range ones of the nonlinear Schrödinger. In addition, we perform an extensive numerical study of equations of the Schrödinger–Newton type, introducing a new, efficient, numerical method to integrate them.

1.3 THESIS OVERVIEW

This thesis is organized in three parts: theoretical aspects, numerical aspects and experiment. Each part is organized in different chapters, outlined below.

- Theoretical aspects.
  - In Chapter 2, we introduce and discuss in details the Newton–Schrödinger equation in its different domains of applications, focusing in particular on self-gravitating systems and optics.
  - In Chapter 3, we explain in details the main features of the dynamics of long-range interacting systems, focusing in particular on classical self-gravitating systems.
  - In Chapter 4, we list the main theoretical results achieved in the context of the preparation of the experiment.
- Numerical aspects.
  - In Chapter 5, we list and explain the different numerical algorithms we use to solve not only the Newton–Schrödinger system but also other Schrödinger-like equations with different potential terms.
  - In Chapter 6, we introduce a new method to solve Schrödinger-like equations.

  - In Chapter 7, we make an extensive comparison of the algorithm we developed with other popular methods, often employed in the literature, for solving Schrödinger-like equations.
- Experiment.
  - In Chapter 8, we describe the experiment performed on a optical system modeled by the Newton–Schrödinger equation.
  - In Chapter 9, we discuss the analysis of the data collected during the measurements and we present the experimental results.

Part I

THEORETICAL ASPECTS

2

DOMAINS OF APPLICATION OF THE NEWTON–SCHRÖDINGER EQUATION

In this chapter, we introduce the Newton–Schrödinger equation and discuss its physical applications, focusing in particular on self-gravitating systems and optics. First, we write the equation in the case where it describes a single particle, then we discuss the many-body case, sketching-out the derivation of the mean-field approximation. Second, we explain how this equation can be used to describe collisionless matter, considering some applications in astrophysics and cosmology. Finally, we write the Newton–Schrödinger equation in the optical environment and we explain how it can be derived from Maxwell equations under appropriate approximations.

2.1 THE SINGLE-PARTICLE NEWTON-SCHRÖDINGER EQUATION

The Newton-Schrödinger equation can be used to describe the quantum evolution of a single particle. The interaction is purely classical, i. e. Newtonian, and the wavefunction ψ satisfies

$$i\hbar\frac{\partial\psi}{\partial t} + \frac{\hbar^2}{2m}\nabla^2\psi - mV\psi = 0 \tag{2.1a}$$

$$\nabla^2 V = 4\pi G m |\psi|^2, \tag{2.1b}$$

which is a Schrödinger equation coupled with a Poisson equation for the potential V, whose source is the probability density $|\psi|^2$ obtained from the wavefunction; G is the gravitational constant, ∇^2 is the 3-dimensional Laplace operator, $\hbar$ the reduced Planck constant and m the mass of the particle.

This equation has been employed by Diosi [3] in 1984 and then by Penrose [4, 5] in 1996 and 1998 to describe the phenomenon of the quantum wavefunction collapse, which takes place whenever a measurement is performed for a given quantum system. In their works, they tried to describe the quantum state reduction mechanism as a consequence of a self-gravitational interaction. This interaction is supposed to be fundamentally classical and, for this reason, the Schrödinger equation has been coupled to the Poisson equation in the context of the wavefunction collapse. Entering into the details of this description for the phenomenon of the wavefunction collapse is, however, not in the purposes of this thesis. We rather focus on the introduction of the equation in the simple case of a single particle and then discuss, in the next section, the N particles case.

2.2 THE MANY-BODY NEWTON–SCHRÖDINGER EQUATION

Historically the Newton–Schrödinger equation was introduced in 1969 by Ruffini and Bonazzola [1] in a very different physical context compared to the wavefunction collapse. In their work, they introduced the equation to describe a many-body system

of self-gravitating bosons as the weak field limit of general relativity. The resulting state is a gravitationally bounded Bose–Einstein condensate, called "Boson star" [2].

In order to obtain this equation, the starting point is the Schrödinger equation for N identical particles. In the case where all particles have the same mass m, the equation is

$$i\hbar \frac{\Psi_N}{\partial t} = \widehat{H}\Psi_N, \tag{2.2}$$

where Ψ_N is the many-body wavefunction $\Psi_N = \Psi_N(\mathbf{x}_1, \mathbf{x}_2, ..., \mathbf{x}_N, t)$, $\mathbf{x}_\ell$ being the position of particle ℓ, with $1 \leqslant \ell \leqslant N$, $\widehat{H}$ is the quantum Hamiltonian and the "hat" notation is used to stress that the underneath quantity is an operator. The Hamiltonian includes a kinetic term $\widehat{K}$ and a potential term $\widehat{V}$ due to gravity, therefore $\widehat{H} = \widehat{K} + \widehat{V}$, with

$$\widehat{K} = -\frac{\hbar^2}{2m}\sum_{\ell=1}^{N} \nabla_\ell^2 \tag{2.3}$$

where in three dimension $\nabla_\ell^2 = \frac{\partial^2}{\partial x_\ell^2} + \frac{\partial^2}{\partial y_\ell^2} + \frac{\partial^2}{\partial z_\ell^2}$.

Interpreting the modulus squared of the wavefunction as the mass density, as done by Ruffini and Bonazzola [1], the interaction term is given by

$$\hat{V} = G m^2 \sum_{\ell \neq j} \frac{1}{|\mathbf{x}_\ell - \mathbf{x}_j|} \tag{2.4}$$

Plugging (2.4) in (2.2), the N-body Schrödinger equation reads

$$i\hbar \frac{\Psi_N}{\partial t} = -\frac{\hbar^2}{2m}\sum_{\ell=1}^{N} \nabla_\ell^2 \Psi_N, + G m^2 \sum_{\ell \neq j} \frac{1}{|\mathbf{x}_\ell - \mathbf{x}_j|}\Psi_N, \tag{2.5}$$

2.2.1 *Mean-field limit*

In most cases one is interested into studying a system where the number of particles N is very large, making the solution of the N-body Newton–Schrödinger equation practically impossible to achieve. For this reason, the Hartree approximation is often employed, allowing to switch from the N-particles wavefunction $\Psi_N(\mathbf{x}_1, \mathbf{x}_2, ..., \mathbf{x}_N, t)$, to a mean-field wavefunction $\psi(\mathbf{x}, t)$, in the limit of a very large number of particles, i. e. $N \to \infty$. This approximation starts from the assumption that the at $t = 0$, the N-body wavefunction can be written in a factorized form, namely

$$\Psi_N(\mathbf{x}_1, \mathbf{x}_2, ..., \mathbf{x}_N, t = 0) = \prod_{\ell=1}^{N} \psi(\mathbf{x}_\ell, t = 0), \tag{2.6}$$

and leads to a mean-field solution $\psi(\mathbf{x}, t)$ that for all $t > 0$ obeys to the Hartree equation

$$i\hbar \frac{\partial \psi}{\partial t} = -\frac{\hbar^2}{2m}\nabla^2\psi - G m^2 \int d\mathbf{x}' U(|\mathbf{x} - \mathbf{x}'|)\,|\psi(\mathbf{x}', t)|^2\,\psi(\mathbf{x}, t), \tag{2.7}$$

where $U(|x-x'|) = \frac{1}{|x-x'|}$. Despite being formally identical the the single particle case, (2.7) describes a quantum system of N self-gravitating bosons, in the limit $N \to \infty$, as a mean-field approximation.

Here, we sketch out the derivation of this equation, which requires the implementation of the Bogoliubov–Born–Green–Kirkwood–Yvon (BBGKY) quantum hierarchy in the limit $N \to \infty$. Interested readers can consult [31–33] for further details. This derivation is performed with the the N-body density matrix ρ_N, defined as

$$\rho_N\left(x_1, ..., x_N, x_1', ..., x_N', t\right) = \Psi_N^*\left(x_1, ..., x_N, t\right)\Psi_N\left(x_1', ..., x_N', t\right), \tag{2.8}$$

where "$*$" denotes the complex conjugation. We fix the notation:

$$\mathbf{X}_n = (x_1, x_2, \ ..., x_n) \qquad \forall\, 1 \leqslant n \leqslant N \tag{2.9a}$$

$$\mathbf{X}_N^n = (x_{n+1}, x_{n+2}, \ ..., x_N) \qquad \forall\, 1 \leqslant n < N. \tag{2.9b}$$

For simplicity, we consider the adimensional N-body Newton–Schrödinger equation

$$i\,\frac{\Psi_N}{\partial t} = \left(-\frac{1}{2}\sum_{\ell=1}^{N}\nabla_\ell^2 + \frac{1}{N}\sum_{\ell\neq j} U\left(\left|x_\ell - x_j\right|\right)\right)\Psi_N, \tag{2.10}$$

where the $1/N$ factor, also known as "weak-coupling scaling", is due to the extensivity of the potential. Here the wavefunction is normalized to unity, namely

$$\int dX_n |\Psi_N(X_n, t)|^2 = 1 \qquad \forall\, t \in \mathbb{R}. \tag{2.11}$$

If one defines the sequence of n-marginals of ρ_N,

$$\rho_{N,n}\left(X_n, Y_N, t\right) = \int \rho_N\left(X_n, Z_N^n, Y_N, Z_N^n, t\right)\, dZ_N^n, \qquad 1 \leqslant n < N, \tag{2.12}$$

with $\rho_{N,N} = \rho_N$ and $\rho_{N,n} = 0\ \forall\, n > N$, then the following "N-body Schrödinger hierarchy" is satisfied:

$$\begin{aligned} i\hbar\,\frac{\partial \rho_{N,n}\left(X_n, Y_n, t\right)}{\partial t} &= -\frac{\hbar^2}{2m}\left(\nabla_{X_n}^2 - \nabla_{Y_n}^2\right)\rho_{N,n}\left(X_n, Y_n, t\right) \\ &\quad + \frac{n-N}{N}\mathcal{C}_{n,n+1}\rho_{N,n+1}\left(X_n, Y_n, t\right) \\ &\quad + \frac{1}{N}\sum_{1\leqslant k\leqslant \ell\leqslant n}\left[U(|x_k - x_\ell|) - U(|y_k - y_\ell|)\right]\rho_{N,n}\left(X_n, Y_n, t\right), \end{aligned} \tag{2.13}$$

where $\mathcal{C}_{n,n+1}$ is an operator, defined as

$$\begin{aligned} \mathcal{C}_{n,n+1}\rho_{N,n+1}\left(X_n, Y_n, t\right) &= \sum_{k=1}^{N}\int\left[U(|x_k - z|) - U(|y_k - z|)\right] \\ &\quad \times \rho_{N,n+1}\left(X_n, z, Y_n, z, t\right) dz. \end{aligned} \tag{2.14}$$

Fixing n, and formally taking the limit $N \to \infty$ (see [31] for the details of this operation) in (2.13) leads to

$$\begin{aligned} i\hbar\,\frac{\partial \rho_n\left(X_n, Y_n, t\right)}{\partial t} &= -\frac{\hbar^2}{2m}\left(\nabla_{X_n}^2 - \nabla_{Y_n}^2\right)\rho_n\left(X_n, Y_n, t\right) \\ &\quad + \mathcal{C}_{n,n+1}\rho_{n+1}\left(X_n, Y_n, t\right), \end{aligned} \tag{2.15}$$

which also goes under the name of "infinite Schrödinger hierarchy".

One can show [33] that if $\psi(\mathbf{x}, t)$ is a solution of

$$i\frac{\partial\psi}{\partial t} = -\frac{1}{2}\nabla^2\psi - \int dx' U(|x-x'|)\,|\psi(x', t)|^2\,\psi(x, t), \tag{2.16}$$

and the factorized initial condition $\Psi_N(\mathbf{X}_N, t = 0) = \prod_{\ell=1}^{N}\psi(x_\ell)$ is assumed to satisfy

$$\int \Psi_N\left(\mathbf{X}_n, \mathbf{Z}_N^n, \mathbf{Y}_n, \mathbf{Z}_N^n, t = 0\right) d\mathbf{Z}_N^n \to \rho_n\left(\mathbf{X}_n, \mathbf{Y}_n, t = 0\right) \tag{2.17}$$

as $N \to \infty$, then

$$\rho_n\left(\mathbf{X}_n, \mathbf{Y}_n, t\right) = \prod_{\ell=1}^{n}\psi^*\left(x_\ell, t\right)\psi\left(y_\ell, t\right) \tag{2.18}$$

is a solution of the infinite hierarchy (2.15), as rigorously proved in [34–36].

This implies that the sequence of n-marginals $\rho_{N,n}$ converges as $N \to \infty$ to $\rho_n\left(\mathbf{X}_n, \mathbf{Y}_n, t\right)$, built on the solution of

$$i\frac{\partial\psi}{\partial t} = -\frac{1}{2}\nabla^2\psi - \int dx' U(|x-x'|)\,|\psi(x', t)|^2\,\psi(x, t), \tag{2.19}$$

which is the mean-field Newton–Schrödinger equation, describing a quantum system of N self-gravitating bosons in the limit $N \to \infty$.

2.3 THE NEWTON–SCHRÖDINGER EQUATION AS A NUMERICAL METHOD IN ASTROPHYSICS

In astrophysics, plasma physics and cosmology, the Newton–Schrödinger equation is often employed as a model for simulating numerically collisionless matter. In this context, matter is modeled as a continuous fluid by smoothing out the graininess of the discrete particle distribution. If the interparticle spacing is negligible with respect to the size of the structures of interest, the collisionless matter fluid can be described with a continuous phase-space distribution $f(\mathbf{x}, \mathbf{v})$.

Usually, this distribution is obtained with the so called "N-body simulation" [37], where a coarse-grain is applied to the distribution function which is then statistically described by N virtual superparticles [38]. Here, Newton equations are used to evaluate the N positions and velocities of the particles,

$$\ddot{x}_i = \sum_{j=1}^{N} F_{ij}, \qquad F_{ij} = \begin{cases} 0 & \text{if } i = j, \\ G\,m\,\frac{1}{|x_i - x_j|^2} & \text{if } i \neq j \end{cases}, \tag{2.20}$$

and then the coarse-grained phase-space distribution is approximated with

$$f_N(\mathbf{x}, \mathbf{v}, t) = \sum_{i=1}^{N}\delta\left(\mathbf{x} - \mathbf{x}_i(t)\right)\,\delta\left(\mathbf{v} - \dot{\mathbf{x}}_i(t)\right), \tag{2.21}$$

which is also known as Klimontovich phase-space distribution [39]. This method however is limited by the presence of finite N effects, which arise from the initial time [40].

Finite N effects can be avoided with a mean-field approach, resulting in the collisionless Boltzmann equation. The latter, which is also known as Vlasov–Poisson equation [14], reads

$$\frac{\partial f}{\partial t} = \sum_{i=1}^{3} \frac{\partial V}{\partial x_i} \frac{\partial f}{\partial v_i} - v_i \frac{\partial f}{\partial x_i} \tag{2.22a}$$

$$\nabla^2 V = 4\pi G m^2 \int d\boldsymbol{v}\, f(\boldsymbol{x}, \boldsymbol{v}, t)\,, \tag{2.22b}$$

where $\boldsymbol{x} = (x_1, x_2, x_3)$, $\boldsymbol{v} = (v_1, v_2, v_3)$ are the position and velocity coordinates and V is the gravitational potential. However, solving (2.22) is in general a hard numerical task because of the computational cost required to compute the 6-dimensional phase-space distribution. In addition, the latter often gives birth to fine-grained structures [41] which represent a further numerical challenge. For these reasons alternative methods have been proposed and used.

The Newton–Schrödinger equation, on the other hand, represents a valid and attractive model to describe collisionless matter as a continuous field [6]. Furthermore, it is able to compete with the N-body simulations in terms of computational time. Here the Newton–Schrödinger equation must be considered in the context of a many-body self gravitating system in the Hartree approximation,

$$i\hbar \frac{\partial \psi}{\partial t} + \frac{\hbar^2}{2m} \nabla^2 \psi - m V \psi = 0 \tag{2.23a}$$

$$\nabla^2 V = 4\pi G m |\psi|^2\,, \tag{2.23b}$$

where the modulus squared of the wavefunction is interpreted as a mass density. The latter, being only a function of the 3-dimensional space variable $\boldsymbol{x}$, determines the advantage in terms of computational cost with respect to the Vlasov–Poisson equation.

At the same time, a phase-space distribution can be built from the wavefunction ψ. However, because of the uncertainty principle, simultaneous values of position and velocity are not allowed in the quantum mechanics framework. For this reason, the quantum phase-space function results in quasi-probability distributions. There are many possible definitions to define such quasi-probability distributions, like the Wigner or the Husimi functions [42]. The Wigner distribution function [43] is not positive-defined, while the Husimi representation [44] does not provide the correct charge and current density when integrated; for these reasons they are quasi-probability distributions. However, this approach remains valid as long as $\frac{\hbar}{m}$ is interpreted as a parameter, whose manipulation, in the limit $\frac{\hbar}{m} \to 0$, allows to recover the classical behavior, as we explain in the next section.

2.3.1 *Classical limit of the Newton–Schrödinger equation*

As we already mentioned, formally, the classical limit of the Newton–Schrödinger equation can be recovered by sending $\frac{\hbar}{m} \to 0$. Indeed, as this parameter gets smaller the dynamics of the equation becomes more similar to the classical one [45].

In the case of the Husimi representation [44] for example, the quantum phase-space distribution is

$$f_H(\mathbf{x}, \mathbf{p}, t) = \left| \left(\frac{1}{2\pi\hbar}\right)^{3/2} \left(\frac{1}{\pi\eta^2}\right)^{3/4} \times \int dx\, \psi(\mathbf{x}, t)\, \exp\left[-\frac{(\mathbf{x}-\mathbf{r})^2}{2\eta^2} - i\frac{\mathbf{p}\cdot(\mathbf{r}-\mathbf{x}/2)}{\hbar}\right]\right|^2, \tag{2.24}$$

where η is a parameter that corresponds to the resolution in phase-space. This parameter, for a system whose typical size of spatial variation is L and whose typical momentum is P, must satisfy $\frac{\hbar}{P} \ll \eta \ll L$ [46].

As done in [47], one can prove that the quantum phase-space distribution f_H defined in (2.24) verifies

$$\frac{\partial f_H}{\partial t} = \sum_{i=1}^{3} \left(m \frac{\partial V}{\partial x_i} \frac{\partial f_H}{\partial v_i} - \frac{p_i}{m} \frac{\partial f_H}{\partial x_i} \right) + O\left(\frac{\eta^2}{L^2}\right) \frac{\partial f_H}{\partial t} + O\left(\frac{\hbar^2}{\eta^2 P^2}\right) \frac{\partial f_H}{\partial t} \tag{2.25}$$

which, taken into account that by definition $\frac{\hbar}{P} \ll \eta \ll L$, in the limit $\hbar/m \to 0$ coincides with the Vlasov equation (2.22) .

In Figure 2.1, three different simulations where the parameter $\hbar/m$ has been changed, are shown, taking respectively the values 10^{-1}, 10^{-2} and 10^{-3}. Specifically, we plot the density, $\rho = |\psi|^2$, obtained from an one-dimensional self-gravitating system simulated with the Newton–Schrödinger equation with the same gaussian initial condition. As the value of $\hbar/m$ decreases, the phase-space evolution displays a more similar behavior to the classical system, with filaments which become more distinguishable and more numerous.

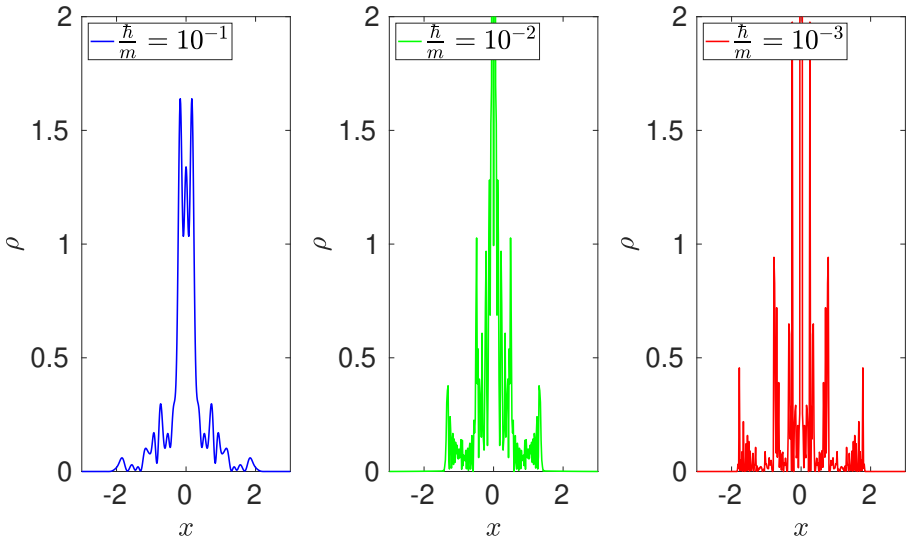

Figure 2.1 – Snapshots of $\rho = |\psi|^2$ at $t = 10 t_{dyn}$ (time is expressed in units of $t_{dyn} = \frac{\sigma}{\sqrt{mG}}$, where σ is the standard deviation of the gaussian initial condition) for simulations with different values of $\hbar/m$. The density is normalised to 1 and the horizontal axis is in adimensional units.

2.3.2 *Fuzzy Dark Matter*

The Newton–Schrödinger equation in astrophysics, is also applied in the description of dark matter. The true nature of this hypothetical form of matter, which is estimated to account for approximately 85% of the matter in the Universe, is still unknown. However, most cosmologists agree on the Cold Dark Matter (CDM) model [48–51], according to which dark matter is characterized by collisionless particles which are cold, namely with very low velocity dispersion. According to the CDM model, dark matter tends to form structures in a hierarchical way, with small objects first collapsing because of the self-gravitational interaction and then merging to form more massive and larger objects. There are many candidates for Cold Dark Matter particles, such as WIMPs (Weakly Interacting Massive Particles) [52, 53], MACHOs (Massive compact halo objects) [54] and axions, in the contest of the Fuzzy Dark Matter model [7, 8]. For the latter in particular, dark matter is found in a state of a Bose–Einstein condensate which can be well modeled by a complex scalar field $\psi(\mathbf{r}, t)$ obeying to the Newton–Schrödinger equation in the mean-field approximation (see (2.2.1))

$$i\hbar \frac{\partial \psi}{\partial t} + \frac{\hbar^2}{2m} \nabla^2 \psi - m V \psi = 0 \tag{2.26a}$$

$$\nabla^2 V = 4\pi G |\psi|^2 , \tag{2.26b}$$

where m the mass of the dark matter particle, called the axion. Here ψ is normalised such that

$$\int |\psi|^2 d\mathbf{r} = M, \tag{2.27}$$

where M is the total mass of the system.

The hypothesis that dark matter is composed by an ultralight bosonic field, the axion, is indeed one of the most attractive possibilities [7] to explain several problems which appear in the field of structure formation, such as the non observation of "cuspy" haloes which is pointed out in N-body simulations [8, 55–59], the "too big to fail" problem [60] and the missing satellites problem [61, 62]. The model is motivated from particle physics, solving the strong CP problem of the standard model of elementary particles [63]. In this context, fuzzy dark matter is naturally produced with very low velocity dispersion, being in the state of a Bose-Einstein condensate. Regarding structure formation, it presents very similar properties at large scales, compared to the standard (classical) cold dark matter models. The main difference resides in the small scales properties, in which a quantum pressure appears. This is due to the fact that the quantum pressure, naturally present in the Newton–Schrödinger equation, allows to explain the homogeneous distribution of dark matter near the center of galaxies [8], while the classical picture, which relies on N-body simulations, fails in justifying this feature. This quantum pressure is due to the Heisenberg uncertainty principle: the mass of the axion is expected to be so small ($\sim 10^{-22}$ eV) so that its De Broglie wavelength is estimated to be around 1kpc, a galactic scale, the size of our galaxy being estimated around 30 kpc.

2.3.3 *Large scale structure formation of the Universe*

Another version of the Newton–Schrödinger equation, has an important application in cosmology to simulate the formation of large-scale structures in the early Universe. The main difference from the previous case is an additional term in the Poisson equation, which is related to the expansion of the Universe, together with the scale factor $a(t)$. For a cosmological model where gravitational effects are weak and can be well described with the Newtonian potential, the nonrelativistic field ψ satisfies

$$i\hbar\frac{\partial\psi}{\partial t} + \frac{\hbar^2}{2ma}\nabla^2\psi - amV\psi = 0 \tag{2.28a}$$

$$\nabla^2 V = 4\pi G\rho_0 a^2\left(|\psi|^2 - 1\right), \tag{2.28b}$$

where $a(t)$, with $a(t_0) = 1$, is the scale factor, t_0 being the current age of the Universe; ρ_0 is the critical density, namely the average density of matter required for the Universe to just halt its expansion, and the wavefunction is normalized to unity. The explicit expression of the scale factor depends on the particular cosmological model considered, for example, for the Einstein–De Sitter Universe one has $a(t) = (\frac{t}{t_0})^{\frac{3}{2}}$.

Usually the cosmological initial condition consists of a constant density with some small fluctuation

$$\psi(\mathbf{x}, t = 0) = \sqrt{\rho_0 + \delta\rho(\mathbf{x})}e^{i\theta_0(\mathbf{x})}, \tag{2.29}$$

where θ_0 is related to the initial velocity $\boldsymbol{v}_0$, specifically $\nabla\theta \propto \boldsymbol{v}$, field and ρ_0 is the background constant density. The fluctuations term, $\delta\rho(\mathbf{x})$, is generated as

$$\delta\rho(\mathbf{x}) = \mathcal{F}^{-1}[R(\mathbf{k})\sqrt{P(\mathbf{k})}], \tag{2.30}$$

where $R(\mathbf{k})$ is a gaussian random field, with zero average and unitary variance, while $P(\mathbf{k})$ is called the power spectrum.

2.3.3.1 *Power spectrum in the linear regime*

There exists an analytical solution of (2.28) in the regime where $\delta\rho \ll \rho_0$. To derive it, we consider for simplicity the case of a static Universe, i. e. $a(t) = 1\ \forall t \geqslant t_0$. The adimensional equation (see Appendix A) reads

$$i\frac{\partial\psi}{\partial t} + \frac{1}{2}\nabla^2\psi - V\psi = 0 \tag{2.31a}$$

$$\nabla^2 V = g\left(|\psi|^2 - 1\right), \tag{2.31b}$$

where $g = 4\pi G\rho_0 L^4\left(\frac{m}{\hbar}\right)^2$ and L is arbitrary spatial scale chosen for the adimensionalization.

The starting point is performing a Madelung transformation [64]

$$\psi = \sqrt{\rho}e^{i\theta}, \tag{2.32}$$

where ρ and θ are two real functions of space and time.

Plugging (2.32) inside the Schrödinger equation and taking its imaginary part, yields

$$\partial_t \sqrt{\rho} = -\frac{1}{2}\left[2(\nabla\sqrt{\rho})\cdot(\nabla\theta) + (\nabla^2\theta)\sqrt{\rho}\right], \tag{2.33}$$

which can be written as a continuity equation if one defines the velocity field $\boldsymbol{v} = \nabla\theta$

$$\partial_t \rho + \nabla\cdot(\rho\boldsymbol{v}) = 0. \tag{2.34}$$

The real part of the equation on the other hand, yields

$$\partial_t \theta = -\left[\frac{(\nabla\theta)^2}{2} - V - \frac{1}{2}\frac{\nabla^2\sqrt{\rho}}{\sqrt{\rho}}\right]. \tag{2.35}$$

Applying the gradient to this equation, one obtains

$$\partial_t \boldsymbol{v} + (\boldsymbol{v}\cdot\nabla)\boldsymbol{v} - \nabla V - \left[\frac{(\nabla\theta)^2}{2} - V - \frac{1}{2}\nabla\left(\frac{\nabla^2\sqrt{\rho}}{\sqrt{\rho}}\right)\right] = 0. \tag{2.36}$$

Linearising (2.34) and (2.36) for $\delta\rho = \rho - 1 \ll 1$, the system together with the Poisson equation for the potential V becomes

$$\partial_t \delta\rho + \nabla\cdot\boldsymbol{v} = 0 \tag{2.37a}$$

$$\partial_t \boldsymbol{v} - \nabla V - \frac{1}{4}\nabla\left(\nabla^2\delta\rho\right) = 0 \tag{2.37b}$$

$$\nabla V = g\,\delta\rho. \tag{2.37c}$$

These three equations can be combined taking the time derivative of the first one and the spatial derivative of the second one,

$$\partial_t^2\delta\rho - g\delta\rho + \frac{1}{4}\nabla^2\left(\nabla^2\delta\rho\right) = 0, \tag{2.38}$$

which can be easily solved in Fourier space,

$$\partial_t^2\widehat{\delta\rho} = \left(g - \frac{k^4}{4}\right)\widehat{\delta\rho}, \tag{2.39}$$

where Fourier transforms are denoted with a "hat".

The solutions depend on the value of the Jeans wavenumber $k_J = \sqrt[4]{4g}$, in particular they are stable for $k > k_J$ and unstable for $k \leqslant k_J$.

In Figure 2.2 we plot the one dimensional Power Spectrum $P(k,t) = \left\langle \left|\widehat{\delta\rho}(k,t)\right|^2 \right\rangle$ in the linear regime and compare it with the simulations; the agreement is quite good up to $t = 3t_{dyn}$.

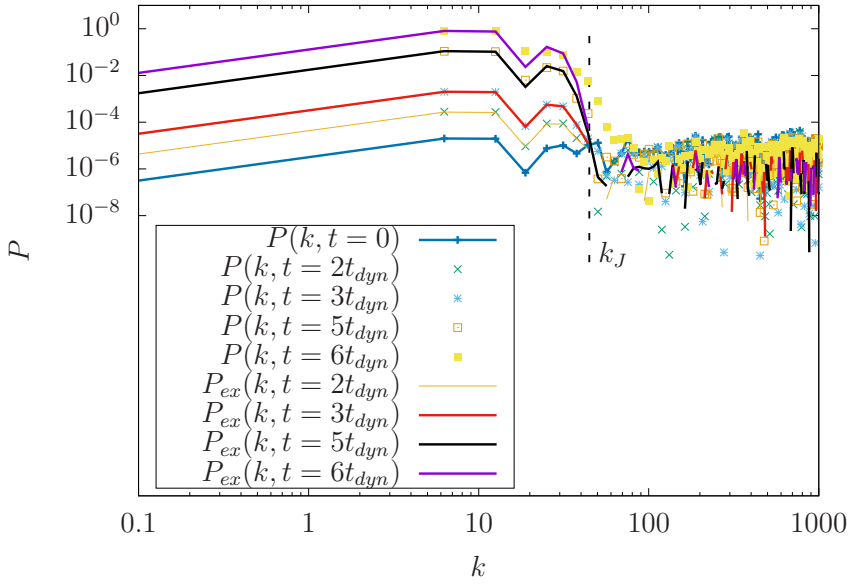

Figure 2.2 – Power Spectrum comparisons for the simulations of the one dimensional cosmological Schrödinger-Newton equation. Time is expressed in units of $t_{dyn} = \left(G\,\rho_0\,L^4\,\left(\frac{m}{\hbar}\right)^2\right)^{-1/2}$.The subscript "ex" denotes the exact analytical solution in the linear regime.

2.4 THE NEWTON–SCHRÖDINGER EQUATION IN OPTICS

In optics, the Newton–Schrödinger equation describes the evolution of the field $\mathcal{E}$ of an optical beam, propagating through a nonlinear and nonlocal medium

$$i\,\frac{\partial \mathcal{E}}{\partial z} + \frac{1}{2\,k}\,\nabla_\perp^2\,\mathcal{E} + k_0\,\Delta n\,\mathcal{E} = 0 \tag{2.40a}$$

$$\nabla_\perp^2 \Delta n = -\frac{\alpha\,\beta}{\kappa}\,|\mathcal{E}|^2\,, \tag{2.40b}$$

where z is the propagation direction of the beam, $\nabla_\perp^2 = \frac{\partial^2}{\partial x^2} + \frac{\partial^2}{\partial y^2}$ is the 2-dimensional transverse Laplace operator, $k = n_b\,k_0$ and k_0 are the wave-numbers of the beam, inside the medium and in void respectively, n_b is the medium background refractive index, Δn is the variation of the refractive index, α the absorption coefficient, β is the medium thermo-optic coefficient and κ the thermal conductivity.

The nonlocality is due to the variation of the refractive index with the intensity of the beam $I = |\mathcal{E}|^2$, described by (2.40b) and resulting in a self-focusing interaction. As we shall see next, (2.40b) is the result of heat-like equation in the stationary regime, where the heat source is due to the laser increasing the temperature of the medium while propagating through it. This system is schematically represented in Figure 2.3.

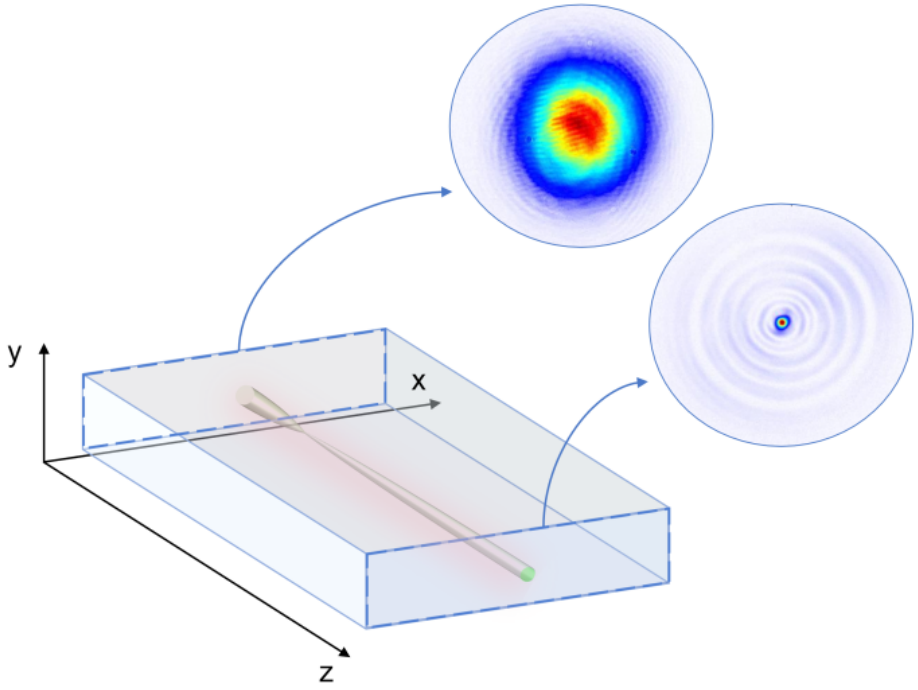

Figure 2.3 – Illustration of the beam propagating inside the self-focusing thermo-optical medium.

2.4.1 *From Maxwell equations to the optical Newton–Schrödinger equation*

The optical Newton–Schrödinger equation can be derived directly from Maxwell equations with proper approximations. Here we list and explain the most important of these assumptions, following the approach described in [65]. We consider the case of a continuous wave beam, propagating inside a nonlinear optical medium.

From Maxwell equations, it is known that the electric-field vector $\mathbf{E}$ obeys to

$$\nabla^2 \mathbf{E} - \frac{1}{c^2}\frac{\partial^2 \mathbf{E}}{\partial t^2} = \frac{1}{\epsilon_0 c^2}\frac{\partial^2 \mathbf{P}}{\partial t^2}, \tag{2.41}$$

where c is the speed of light in the medium considered, ϵ_0 is the vacuum permittivity and $\mathbf{P}$ is the induced polarization vector. The latter can always be split in a linear part $\mathbf{P}_L$ and a nonlinear one $\mathbf{P}_{NL}$

$$\mathbf{P}(\mathbf{r}, t) = \mathbf{P}_L(\mathbf{r}, t) + \mathbf{P}_{NL}(\mathbf{r}, t), \tag{2.42}$$

which are related to the electric field through the susceptibility tensors [66], i. e. $\chi^{(1)}$ and $\chi^{(3)}$

$$\mathbf{P}_L(\mathbf{r},t) = \epsilon \int_{-\infty}^{\infty} \chi^{(1)}(t-t') \cdot \mathbf{E}(\mathbf{r},t')\, dt' \tag{2.43a}$$

$$\mathbf{P}_{NL}(\mathbf{r},t) = \epsilon \int_{-\infty}^{\infty} \chi^{(3)}(t-t_1,t-t_2,t-t_3)\times \times \mathbf{E}(\mathbf{r},t_1)\,\mathbf{E}(\mathbf{r},t_2)\,\mathbf{E}(\mathbf{r},t_3)\, dt_1\, dt_2\, dt_3. \tag{2.43b}$$

These equations can be remarkably simplified by taking into account some assumptions, listed and justified below.

— The nonlinear response is assumed to be instantaneous so that the time dependence of $\chi^{(3)}$ is given by the product of three delta functions of the form $\delta(t-t_i)$. Than (2.43b) reduces to

$$\mathbf{P}_{NL}(\mathbf{r},t) = \epsilon\, \mathbf{E}(\mathbf{r},t)\,\mathbf{E}(\mathbf{r},t)\,\mathbf{E}(\mathbf{r},t). \tag{2.44}$$

This corresponds to neglecting the contribution of molecular vibrations to $\chi^{(3)}$.

— $\mathbf{P}_{NL}$ can be treated as a small perturbation to $\mathbf{P}_L$ because nonlinear changes in the refractive index are always $\frac{\Delta n}{n} \ll 1$ for media with this kind of nonlinearity.

— The optical field is assumed to maintain its polarization along the medium, so that a scalar approach can be used, this is valid in the isotropic materials case.

— We make the ansatz

$$\mathbf{E}(\mathbf{r},t) = \frac{1}{2}\hat{p}[\mathcal{E}(\mathbf{r},t)e^{-i\omega_0 t} + c.c.] \tag{2.45}$$

where ω_0 is the carrier frequency, $\hat{p}$ is the polarization unit vector, $k = k_0 n_b = \frac{2\pi n_b}{\lambda}$ is the propagation constant in terms of the optical wavelength $\lambda = \frac{2\pi c}{\omega_0}$, c.c. denotes the complex conjugated and $\mathcal{E}(\mathbf{r},t)$ is called envelope function. The polarization components $\mathbf{P}_L(\mathbf{r},t)$ and $\mathbf{P}_{NL}(\mathbf{r},t)$ can also be expressed in a similar way:

$$\mathbf{P}_L(\mathbf{r},t) = \frac{1}{2}\hat{p}[P_L(\mathbf{r},t)e^{-i\omega_0 t} + c.c.] \tag{2.46}$$

$$\mathbf{P}_{NL}(\mathbf{r},t) = \frac{1}{2}\hat{p}[P_{NL}(\mathbf{r},t)e^{-i\omega_0 t} + c.c.] \tag{2.47}$$

— When (2.45) is substituted in (2.44), the envelope function of $\mathbf{P}_{NL}$ is found to have a term oscillating at ω_0 and another term oscillating at the third-harmonic frequency, $3\omega_0$. The latter term necessitates phase matching and can be neglected. With this slowly varying envelope approximation, it is found that [65]

$$P_{NL}(\mathbf{r},t) \approx \epsilon\, \epsilon_{NL}\, \mathcal{E}(\mathbf{r},t), \tag{2.48}$$

where the nonlinear contribution to the dielectric constant is defined as

$$\epsilon_{NL} \overset{\text{def}}{=} \frac{3}{4}\chi^{(3)}\,|\mathcal{E}(\mathbf{r},t)|^2. \tag{2.49}$$

— When a perturbative approach is employed, the dielectric constant, which includes both linear and nonlinear refractive index and absorption effects, is approximated as [67]

$$\epsilon = n_b^2 + 2\, n_b\, n_{nl}(I) + n_b\, \frac{i\,\alpha}{\omega_0}. \tag{2.50}$$

In the latter expression, α is the absorption coefficient, $n_{nl}(I)$ indicates the nonlinear component of the refractive index, that is a function of the light beam intensity $I = |\mathcal{E}|^2$ and n_b is the background refractive index. The full refractive index is defined as

$$n = n_b + n_{nl}(I) \tag{2.51}$$

— The thermo-optical nonlinearity can be included by assuming that the nonlinear part of the refractive index varies with temperature [68] according to

$$n_{nl} = \frac{dn}{dT}\, T_l \tag{2.52}$$

where T_l represents the laser induced change in temperature. The quantity $\beta = \frac{dn}{dT}$ is a constant called the medium thermo-optic coefficient. Assuming that T_l obeys to the heat-transport equation, one has

$$\rho_0 C \frac{\partial T_l}{\partial t} - \kappa \nabla^2 T_l = \alpha I, \tag{2.53}$$

where $\rho_0 C$ denotes the heat capacity per unit volume.

— The paraxial approximation [69] is applied, assuming that the beam propagates in the z direction and diffract or self-focuses in the transverse plan $\mathbf{r}_\perp = (x, y)$. This means that within a distance $\Delta z = \lambda$, the change $\Delta\mathcal{E}$ is much smaller than $\mathcal{E}$ itself. Therefore one has

$$\begin{aligned} &\triangle\mathcal{E} \ll \mathcal{E} \Leftrightarrow \triangle z \ll \lambda \quad \Rightarrow \frac{\partial \mathcal{E}}{\partial z} \ll \frac{\mathcal{E}}{\lambda} = \frac{\mathcal{E} k}{2\pi} \\ &\Rightarrow \frac{\partial \mathcal{E}}{\partial z} \ll k\mathcal{E}, \quad \frac{\partial^2 \mathcal{E}}{\partial z^2} \ll k^2 \mathcal{E}. \end{aligned} \tag{2.54}$$

The condition $\frac{\partial^2 \mathcal{E}}{\partial z^2} \ll k^2\mathcal{E}$ implies that, once the ansatz (2.45) is plugged into (2.41), one formally gets $\nabla^2 \approx \nabla_\perp + 2i\,k\frac{\partial}{\partial_z}$.

Taking into account these assumptions, with some algebraic manipulations, plugging the ansatz for $\mathbf{E}$ and $\mathbf{P}$ into (2.41) leads to the Paraxial Helmholtz equation

$$2ik\frac{\partial \mathcal{E}}{\partial z} + \nabla_\perp^2 \mathcal{E} + 2k k_0 \Delta n \mathcal{E} = 0 \tag{2.55}$$

which, with the definition $\Delta n = n - n_b$, corresponds to (2.40).

2.4.2 *Absorption and time dependence*

To model a real optical medium, (2.40) should incorporate a time dependence and the contribution of the absorption, which in general is not negligible. In this case, the Newton–Schrödinger equation, must be written as

$$i\,\frac{\partial \mathcal{E}}{\partial z} + \frac{1}{2\,k}\,\nabla_\perp^2 \mathcal{E} + k_0\,\Delta n\,\mathcal{E} + i\,\frac{\alpha}{2}\,\mathcal{E} = 0 \tag{2.56a}$$

$$\frac{\rho_0\, C}{\kappa}\,\frac{\partial \Delta n}{\partial t} - \nabla_\perp^2 \Delta n = \frac{\alpha\,\beta}{\kappa}\,|\mathcal{E}|^2, \tag{2.56b}$$

The time dependence implies that for a beam of radius s, there exists a thermal diffusion time τ, which may be estimated as

$$\frac{1}{\tau} = \frac{\kappa}{s^2 \rho_0 C}. \tag{2.57}$$

This can directly be observed switching to Fourier space, which, for (2.56b) yields

$$\frac{\rho_0 C}{\kappa} \frac{\partial \widehat{\Delta n}}{\partial t} + k^2 \nabla_\perp^2 \widehat{\Delta n} = \frac{\alpha \beta}{\kappa} \widehat{I}, \tag{2.58}$$

whose solution is

$$\widehat{\Delta n}(\mathbf{k}, t) = \frac{\alpha \beta}{\kappa} \widehat{I} \left(1 - e^{-\frac{\kappa}{\rho_0 C} k^2 t}\right). \tag{2.59}$$

Hence, the $\frac{\rho_0 C}{\kappa} \frac{\partial \Delta n}{\partial t}$ term in the heat equation can be neglected if one waits long enough, such that the stationary regime is reached, namely for $t \gg \tau$.

On the other hand, the presence of the absorption introduces an exponential drop of the total power P of the beam

$$\int d\mathbf{r}_\perp |\mathcal{E}(\mathbf{r}_\perp, z)|^2 = e^{-\alpha z} P, \tag{2.60}$$

which weakly influences the dynamics in the case where a propagation length $z \ll \alpha^{-1}$ is considered.

3

DYNAMICS OF LONG RANGE INTERACTING SYSTEMS

In this chapter, we introduce the main features of the dynamics of classical long-range interacting systems, focusing in particular on self-gravitating systems. As mentioned in Section 2.3.1, quantum long-range interacting systems display the same features when approaching the classical limit, namely when $\frac{\hbar}{m} \to 0$. In addition, when this limit is not perfectly reached, but the long range interacting potential still dominates over quantum effects, similar dynamical features take place. Indeed, we shall see how in this regime, one has both the classical solution and the quantum part (also known as soliton). First, we give the definition of long-range force and long range potential, mentioning, under a statistical mechanics point of view, some of the most important aspects of this interaction. Second, we describe the equilibrium state to which this kind of systems evolve, explaining the main mechanisms that rules this process. Finally, we discuss the virial theorem and give some examples of how it applies to the Newton–Schrödinger equation, both for the quantum regime and the classical limit.

3.1 LONG RANGE INTERACTING SYSTEMS

Self-gravitating systems are characterized by an interaction, the gravitational one, which is known to be long-range [70]. The formal definition of long range interaction comes from statistical mechanics: in a d-dimensional space, a system is called long-range if it interacts with a potential $U(r \to \infty) \sim 1/r^{\gamma}$, decaying with the interparticle distance r, with an exponent γ smaller then the dimensionality d of the embedding space [71–73]. However, as specified in [74], some of the features of long range interacting systems, like the existence of quasi-stationary states, are not ensured by the large distance behavior of the interaction alone. This requires a classification of pair interactions based on the convergence properties of the forces acting on particles as a function of system size [75]. Specifically, one should distinguish between the $\gamma > d-1$ and the $\gamma \leqslant d-1$ cases. In the former, also known as "dynamically short-range" case, the dominant contribution to the force at a given site arises from particles in a finite neighborhood around it. For $\gamma \leqslant d-1$ on the other hand, the dominant contribution to the force comes from the mean field due to the bulk potential. This is also known as "dynamically long-range" case. Both those cases share the same features for the dynamics at the statistical equilibrium. However for $\gamma > d-1$ the dynamics before the equilibrium is driven by short range interactions.

Beyond astrophysics [70, 76], other physical examples of systems belonging to this category can be found in: (i) two-dimensional hydrodynamics such as geophysical flows and vortex models [77–79], (ii) in atomic and nuclear physics such as quantum spin models [80], dipolar excitons [81], cold atom models [82], colloids at interfaces [83] and in (iii) plasma physics, e.g. magnetically confined plasmas [84].

In the next sections, we explain the most important dynamical features typical of these systems. Indeed, because of the long-range nature of the interaction, for which

every elementary constituent is subjected to a force whose major contribute is not only given by the neighboring ones. In this kind of systems the energy is non-additive [73]. The non-additivity implies that long-range interacting systems manifest some very unusual and counter-intuitive properties like inequivalence of statistical ensembles and possible apparition of negative specific-heat in the microcanonical ensemble [73, 85].

3.1.1 *Formation of the quasi-stationary State*

The long range nature of the force has important consequences for the macroscopic dynamics. Starting from an arbitrary initial condition, these systems give rapidly birth to a generic formation of out-of-equilibrium quasi stationary states [86, 87]. Then they slowly relax the Maxwell-Boltzmann thermodynamic equilibrium, in a time which scales generically with the number of elementary constituents [15]. One speaks of out-of-equilibrium states because the quasi-stationary state is not extremum of the free energy or a meta-stable state. In addition, the reason why it is called "quasi-stationary", is that during this transient the time evolution is very slow compared with the dynamics of the thermodynamic equilibrium, allowing to define weakly varying macroscopic observables.

Examples of such quasi-stationary states are galaxies, for which the time needed to reach the thermodynamic equilibrium is typically larger than the age of the Universe.

The quasi-stationary state formation process is called collisionless relaxation, and is a generic combination of two phenomena [15]:

1. Mixing, which is caused by the motion of particles in a non-harmonic potential created self-consistently by the distribution of particles itself, which tends to mix the phase space.
2. Violent relaxation, which mix the energy of particles because the potential created by the distribution of particles is not stationary in time.

The mixing phenomenon can be directly observed looking at the phase-space distribution of the system $f(\mathbf{x}, \mathbf{v}, t)$, as shown in Figure 3.1. This phase-space distribution, is defined such that $f(\mathbf{x}, \mathbf{v}, t)d\mathbf{x}d\mathbf{v}$ represents the probability of finding a particle in the volume $d\mathbf{x}$ within a velocity $d\mathbf{v}$ at time t. This quantity, in the limit where the the number of particles is very large and collisions can be neglected, follows an incompressible evolution in phase-space, namely

$$\frac{df}{dt} = 0. \tag{3.1}$$

Applying the chain rule to (3.1), one obtains

$$\frac{df}{dt} = \frac{\partial f}{\partial t} + \dot{\mathbf{x}} \cdot \nabla_{\mathbf{x}} f + \dot{\mathbf{v}} \cdot \nabla_{\mathbf{v}} f = 0, \tag{3.2}$$

where $\nabla_{\mathbf{x}}$ and $\nabla_{\mathbf{v}}$, respectively, denote the gradient with respect to position and velocity variables. Plugging Newton equation $\dot{\mathbf{v}} = \frac{\mathbf{F}}{m}$, where $\mathbf{F}(\mathbf{x}, t)$ is the force at the position $\mathbf{x}$ at time t,to (3.2) yields

$$\frac{\partial f}{\partial t} + \dot{\mathbf{x}} \cdot \nabla_{\mathbf{x}} f + \frac{\mathbf{F}}{m} \cdot \nabla_{\mathbf{v}} f = 0, \tag{3.3}$$

which is the Vlasov equation (see Section 2.3).

In general, this equation cannot be analytically solved. All one can say about the stationary phase-space is that, for a given initial condition, the solution is any function Q of the energy, i. e.,

$$f(\mathbf{x}, \mathbf{v}, t \to \infty) = Q\left(\frac{m}{2}v^2 + V\right), \tag{3.4}$$

as it can be found by imposing $\partial f/\partial t = 0$. Here, V is the mean-field potential, given by $\mathbf{F} = -\nabla V$ and related to the interacting one by $V(\mathbf{x}, t) = \int d\mathbf{v}'\, d\mathbf{x}'\, U(|\mathbf{x} - \mathbf{x}'|)\, f(\mathbf{x}, \mathbf{v}')$.

Mathematically, the relation between the quasi-stationary state and the Maxwell-Boltzmann equilibrium distribution can be explained by a kinetic theory, using an expansion of the classical BBGKY hierarchy in powers of $1/N$ as $N \to \infty$ [88–91]. Specifically, the quasi-stationary state is obtained when the limit $N \to \infty$ is taken before the $t \to \infty$ one, and the Boltzmann equilibrium is obtained when the limit $t \to \infty$ is taken before the $N \to \infty$ limit.

In Figure 3.1 and Figure 3.3, we illustrate for a classical one-dimensional self-gravitating system, the evolution of phase space with time. It exhibits a "filamentation" from the very beginning, which shows the presence of the mixing phenomenon. Then it reaches a quasi-stationary state, where it slowly evolves with time.

3.1.2 *Entropy*

We now explain another feature of long-range interacting systems, namely the fact that their entropy does not increase with time. In order to do that, we first define the entropy of the system,

$$S(t) = C_1 - C_2 \int dx\, dv\, f\, \ln f, \tag{3.5}$$

where C_1 and C_2 are two constants and f is the phase-space distribution. From (3.1) it follows that the entropy does not evolve with time

$$\frac{\partial S}{\partial t} = 0. \tag{3.6}$$

Even though the microscopic entropy does not change, usually one is rather interested in a macroscopic entropy when describing such systems. In fact long-range systems contain both short-range and long-range interactions. This is due to the rate at which long-range interactions drop, which is slower than the rate at which the interparticle distance increases. For this reason, short-range interaction features, like collisions, will always appear at very small scales. In addition, the lack of information concerning the dynamics at small scales always determines an increase of the macroscopic entropy. For this reason, when long range interactions dominate, a physically more relevant entropy can be defined, performing a coarse-graining over these scales. This macroscopic entropy is obtained averaging f over small cells in the (x, v) space. It is defined as

$$\bar{S}(t) = C_1 - C_2 \int dx\, dv\, \bar{f}\, \ln \bar{f}, \tag{3.7}$$

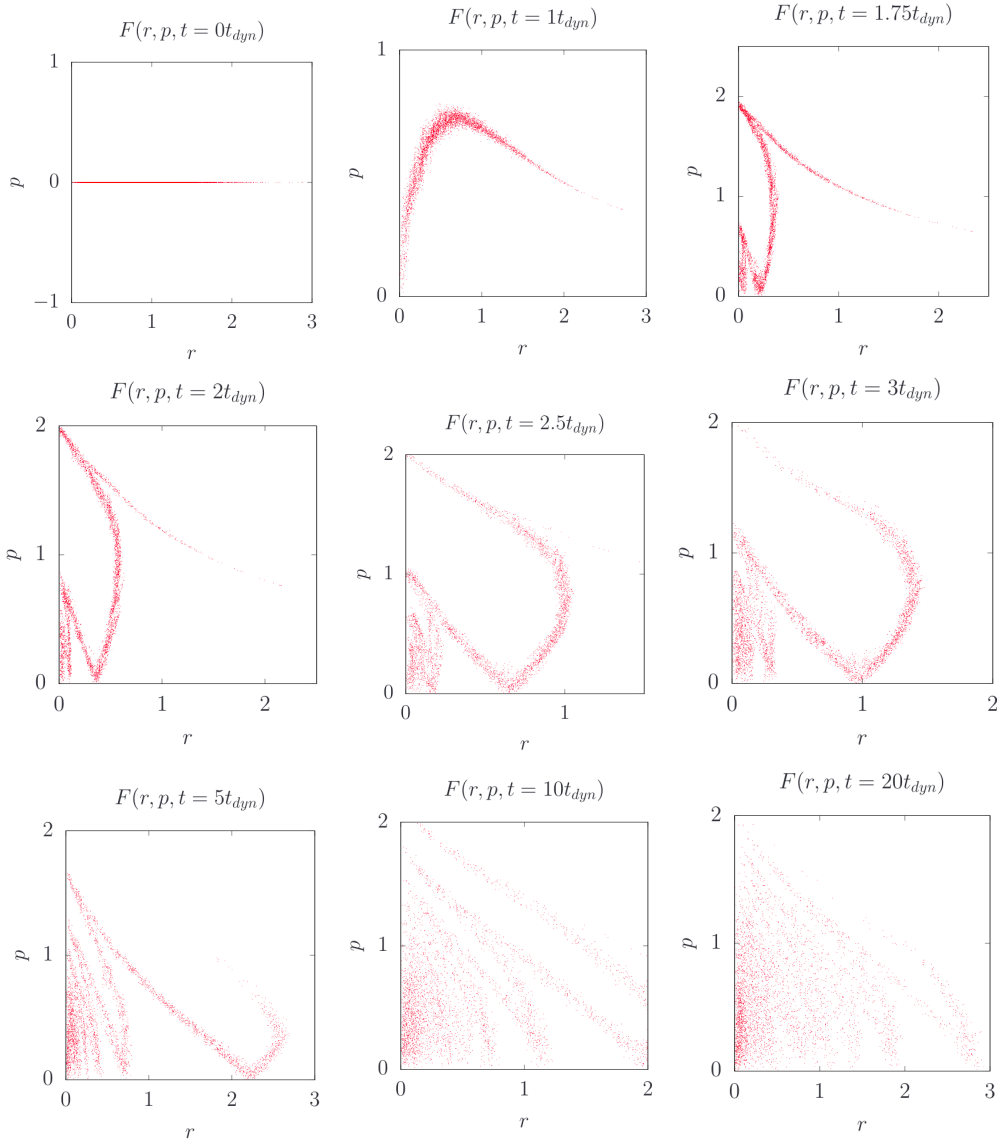

Figure 3.1 – Evolution of phase-space with time (horizontal axis is the position x and the vertical one the velocity v) of an one-dimensional classical self-gravitating system. Time is expressed in units of $t_{dyn} = \frac{\sigma}{\sqrt{m\,G}}$, where σ is the standard deviation of the gaussian initial condition for the matter density distribution.

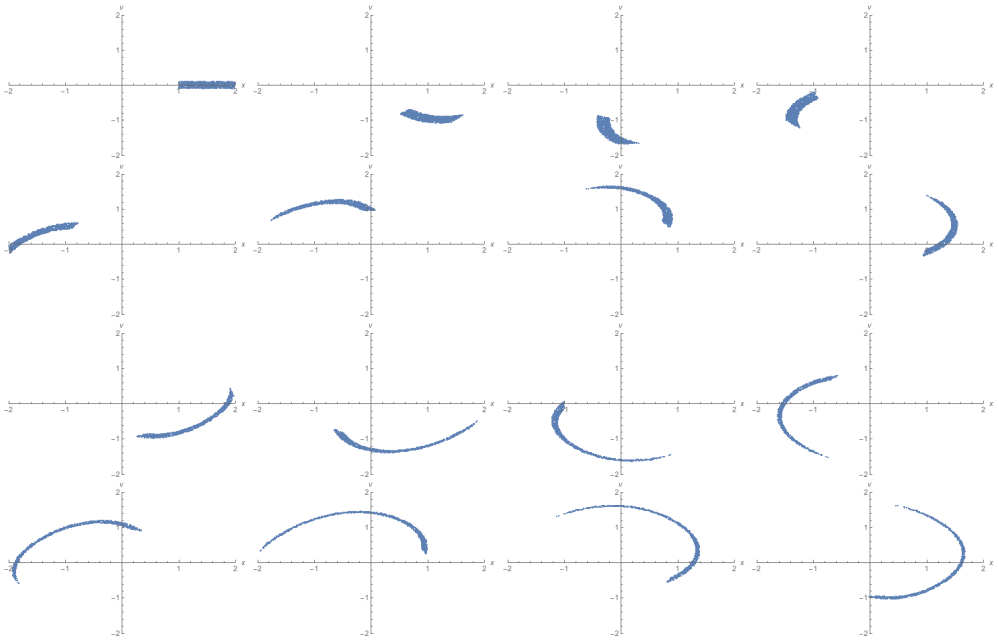

Figure 3.2 – Evolution of the phase space at early times for times for 1000 particles and $t = n$, $n \in \mathbb{N}$.

where $\bar{f}$ is the coarse-grained distribution. Phase space and coarse-grained phase space are normalized to unity, i. e.,

$$\int dx\, dv\, f = \int dx\, dv\, \bar{f} = 1. \tag{3.8}$$

In the next section, we shall see with an example that the coarse-grained entropy does increase with time.

3.1.2.1 *A pedagogical example*

Let us consider a very simple example, focusing on a system where only mixing takes place. The system under investigation is a set of non-interacting real classical oscillators. The equation of motion of each oscillator is

$$\ddot{x}(t) = \sin(x(t)). \tag{3.9}$$

Let us look at the evolution of the phase-space solving (3.9) for a set of particles which are homogeneously distributed in phase space in the region $1 \leqslant x \leqslant 2$ and velocity $-1/10 \leqslant v \leqslant 1/10$. The evolution for early times appear in Figure 3.2. The volume of phase-space is rigorously conserved, and so is the entropy (3.6).

In Figure 3.3, we plot the evolution of the phase-space, starting from the last plot of Figure 3.2, with much larger time-interval between the plots. We observe the filamentation of the phase-space. The volume of phase-space is still rigorously conserved, and so is the entropy (3.6).

In Figure 3.4, we show the phase-space at a very large time. The filamentation of the phase-space continues to go on at smaller and smaller scales, beyond the resolution of the simulation and, more importantly, beyond the resolution in which

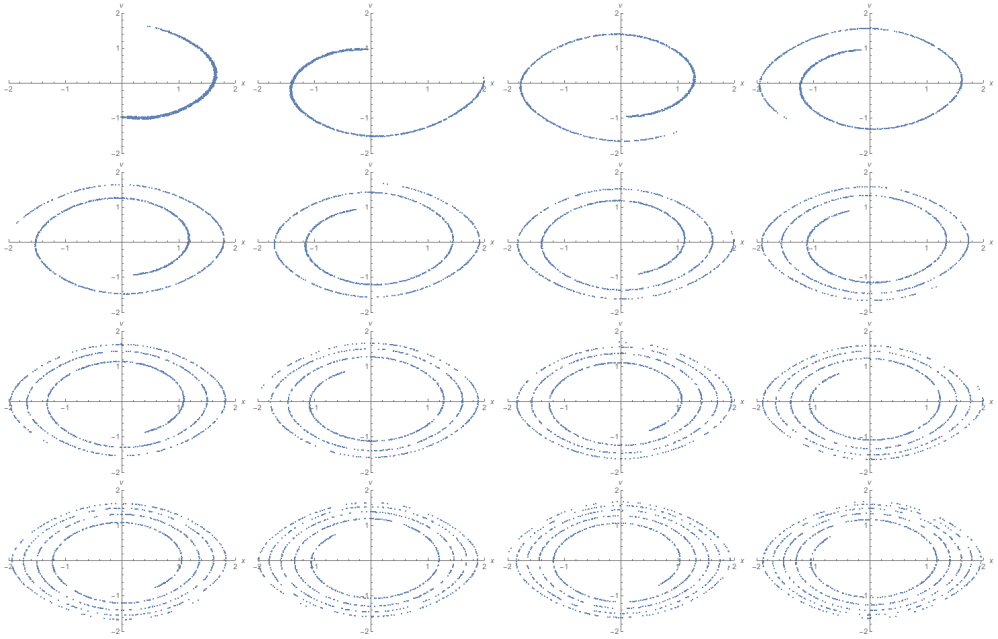

Figure 3.3 – Evolution of the phase space at large times for 1000 particles and times $t = 10n$, $n \in \mathbb{N}$, starting from $t = 16$.

we are interested in. In a similar way of equilibrium statistical physics, in which one is not interested in all the details of the system but only in macroscopic quantities.

In our very simple particular case, we can compute the stationary state using that (i) we observe in the simulation that the stationary phase-space is homogeneous and (ii) the initial velocities are negligible. Then, stationary phase-space is bounded by the two curves $1/2v^2 - (\cos x - \cos(1))$ and $1/2v^2 - (\cos x - \cos(2))$, as it can be seen in Figure 3.5.

As discussed in Section 3.1.2, the microscopic entropy does not change, only the macroscopic coarse-grained one varies with time. To explicitly see that, we start by observing that because of the normalization, we have that $f(x, v, t = 0)$ is zero everywhere except for the region $1 \leqslant x \leqslant 2$, $-1/10 \leqslant v \leqslant 1/10$ in which $f(x, v) = \frac{1}{5}$.

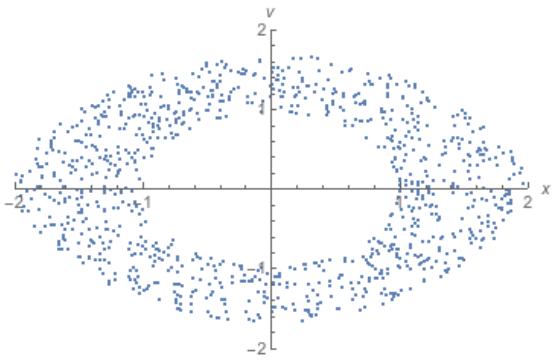

Figure 3.4 – Phase space for 1000 particles at time $t = 1000$.

.

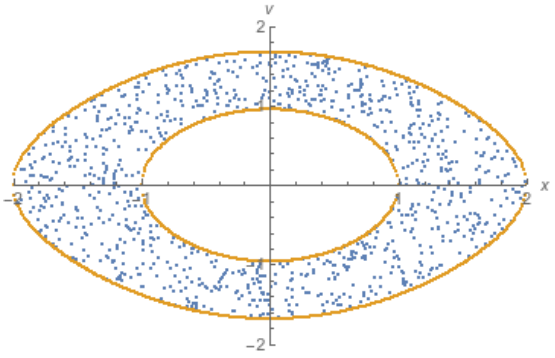

Figure 3.5 – Phase space for 1000 particles at time $t = 1000$.

.

For the stationary regime, $\bar{f}$ is zero outside the regions bounded by the curves in Figure 3.5 and $\bar{f} \approx 0.14$ between the curves. Then

$$S(0) = \bar{S}(0) = C_1 - C_2 \ln(1/5) \approx C_1 + 1.6\, C_2 \tag{3.10}$$

and

$$\bar{S}(t \to \infty) = C_1 - C_2 \ln(0.14) \approx C_1 + 1.95\, C_2. \tag{3.11}$$

Therefore the coarse-grained entropy has increased $\bar{S}(t \to \infty) > \bar{S}(0)$, even though Boltzmann entropy has remained constant $S(t \to \infty) = S(0)$.

3.1.3 *Violent relaxation*

In the last example, we illustrated the mixing phenomenon, which is the simplest mechanism which causes relaxation in gravitational systems. The violent relaxation mechanism, on the other hand, requires, an exchange of energy in order to take place. Since for a classical system one has

$$\begin{aligned}
\frac{dE}{dt} &= \frac{d}{dt}\left(\frac{1}{2}\, m v^2 + V(\mathbf{x})\right) \\
&= \nabla_{\boldsymbol{v}} E \cdot \frac{\partial \boldsymbol{v}}{\partial t} + \frac{dV}{dt} \\
&= -m\boldsymbol{v} \cdot \frac{\nabla V}{m} + \frac{dV}{dt} \\
&= -\boldsymbol{v} \cdot \nabla V + \frac{\partial V}{\partial t} + \nabla V \cdot \boldsymbol{v} \\
&= \frac{\partial V}{\partial t},
\end{aligned} \tag{3.12}$$

it is easy to see that an exchange of energy between the particle and the potential can take place only with a time varying potential. It is possible to explore whether a given system is exhibiting an energy exchange looking at its energy distribution. This quantity can be obtained by constructing the histogram $\nu(E, t)$

$$\nu(E, t) = \int d\mathbf{r}\, \delta\left[E - E(\mathbf{r}, t)\right]\, \rho(\mathbf{r}, t), \tag{3.13}$$

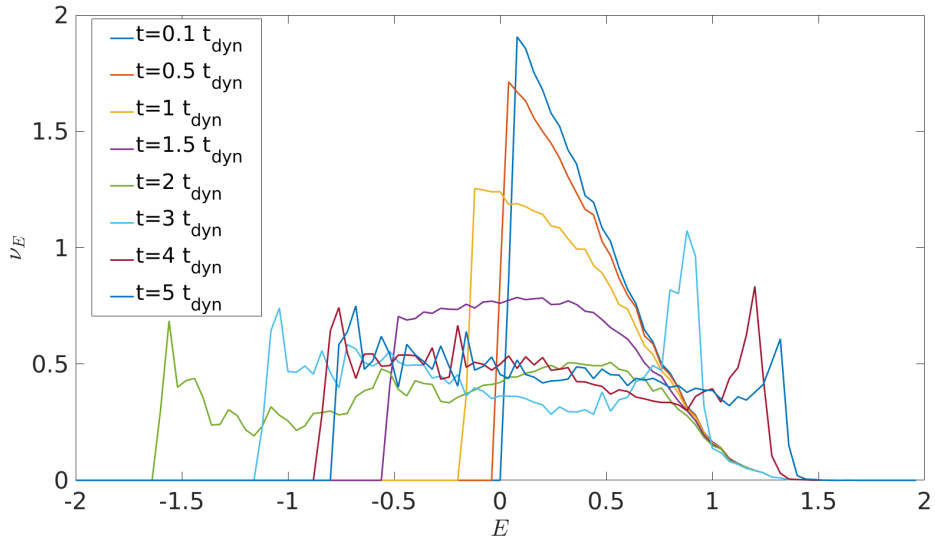

Figure 3.6 – Snapshots of the energy distribution as a function of time for a classical 2-dimensional self-gravitating systems of $N = 65536$ particles. Time is expressed in units of $t_{dyn} = \frac{\sigma}{\sqrt{m\,G}}$, where σ is the standard deviation of the gaussian initial condition for the matter density distribution. On the horizontal axis the energy is expressed in the units where $m = G = 1$ while on the vertical axis ν_E represents the normalized number of particles with energy E.

where $E(\mathbf{x}, t)$ is the total energy density, and $\rho(\mathbf{r}, t)$ is the mass density.

In Figure 3.6, we show the time evolution of the energy distribution obtained from a N-body simulation of a 2-dimensional self-gravitating system of $N = 65536$ particles. From the plots, it is clear how the violent relaxation starts at the more negative energies, which correspond to the particles that are closer to the center. This is also the region where fast particles cross the slow ones for the first time. This phenomenon, known as shell-crossing [92], leads to the formation of caustics singularities in the density field, as the velocity field of the solution of the Vlasov–Poisson equations becomes multi-valued.

As a last remark, it is important to stress that the violent relaxation mechanism requires a potential that needs to be both non-harmonic, which triggers the mixing, and time-dependent. Indeed, it is possible to construct a potential which depends on time that nevertheless present an invariant energy distribution [93].

3.2 VIRIAL THEOREM

The virial theorem is a way to characterize the stationarity of a system. For this reasons, it can be employed also to describe the quasi-stationary state of long range interacting systems. We start from its explanation in the classical case, and then focus on the quantum version. Then, we explain the relation between the two versions, focusing on the particular case of the Newton-Schrödinger equation and its classical limit.

3.2.1 *Classical virial theorem*

The virial theorem in its classical version, provides a relation between the time average of kinetic and potential energy. Specifically, for a system of N particles, the theorem states

$$2\,\overline{K} = \overline{\sum_{i=0}^{N} \mathbf{r}_i \cdot \nabla_i V_i}, \tag{3.14}$$

where K is the total kinetic energy, $\mathbf{r}_i$ is the position of the i^{th} particle, ∇_i denotes the gradient with respect to coordinates $\mathbf{r}_i$, $V_i = V(\mathbf{r}_i)$ is the bulk potential experienced by particle i^{th} and the bar indicates a time average. The relation between the interacting potential U and the bulk (mean field) one is, for a system of N particles

$$V(\mathbf{r}_i) = \sum_{j=1,\, j\neq i}^{N} U(\left|\mathbf{r}_i - \mathbf{r}_j\right|). \tag{3.15}$$

In the case of an interacting potential which decays as a power law with the inter-particle distance, $U(r) = \alpha r^{-n}$, with $n > 0$, the theorem takes the form

$$2\,\overline{K} = -n\,\overline{V}. \tag{3.16}$$

For example, in the case of 3-dimensional gravity ($n = 1$) one has

$$2\,\overline{K} = -\overline{V}. \tag{3.17}$$

In the case of 2-dimensional gravity, the interacting potential is a logarithm and the virial theorem cannot be applied in the power-law form. Indeed, for a a 2-dimensional system of N self-gravitating particles with unitary mass, one has

$$V = \sum_{i,j=1,\, j\neq i}^{N} U(\left|\mathbf{r}_i - \mathbf{r}_j\right|) = \sum_{i,j=1,\, j\neq i}^{N} \log\left|\mathbf{r}_i - \mathbf{r}_j\right|, \tag{3.18}$$

and therefore

$$\mathbf{r}_i \cdot \nabla_i V_i = \sum_{j=1,\, j\neq i}^{N} \mathbf{r}_i \cdot \nabla_i \log\left|\mathbf{r}_i - \mathbf{r}_j\right| = \sum_{j=1,\, j\neq i}^{N} \mathbf{r}_i \cdot \frac{\mathbf{r}_i - \mathbf{r}_j}{\left|\mathbf{r}_i - \mathbf{r}_j\right|^2}, \tag{3.19}$$

which, using $\mathbf{r}_i \cdot (\mathbf{r}_i - \mathbf{r}_j) + \mathbf{r}_j \cdot (\mathbf{r}_j - \mathbf{r}_i) = \left|\mathbf{r}_i - \mathbf{r}_j\right|^2$ leads to

$$2\,\overline{K} = \frac{N^2}{2}. \tag{3.20}$$

In Figure 3.7, we show for a 2-dimensional system of $N = 4096$ particles self-interacting through classical gravity and initially distributed with a gaussian density, the total kinetic energy as a function of time. The process through which this quantity oscillates, with an amplitude which decreases with time, around the value $\overline{K} = \frac{1}{4}\overline{V}$ is called virialization. We rescale the total kinetic energy on the vertical axis with the virialization value $K_v = \frac{\overline{\mathbf{r}\cdot\nabla V}}{2}$, in such a way that it oscillates around 1. This value

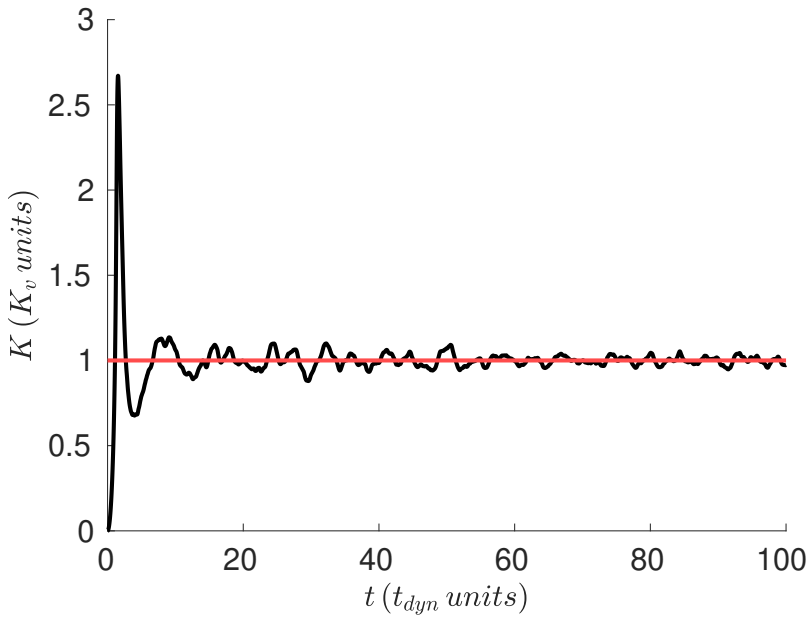

Figure 3.7 – Total kinetic energy in units of the virialized value $K_v = \frac{\overline{\mathbf{r}\cdot\nabla V}}{2}$, as a function of time for a classical 2-dimensional self-gravitating systems of $N = 4096$ particles. Time is expressed in units of $t_{dyn} = \frac{\sigma}{\sqrt{m\,G}}$, where σ is the standard deviation of the gaussian initial condition for the matter density distribution.

is also used to defined the virial ratio, i.e. the ratio between the initial value of the kinetic energy K_0 and K_v,

$$\Gamma_v = \frac{K_0}{K_v}. \tag{3.21}$$

The value of this ratio allows to discriminate between different types of initial dynamics: the $\Gamma_v > 1$ case corresponds to the “hot initial condition", because the initial kinetic energy is larger then the virial value and therefore the dynamics is initially dominated by the kinetic pressure. On the other hand, the $\Gamma_v < 1$ case corresponds to “cold initial conditions", where the dynamics is characterized by an initial gravitational collapse, as the case of Figure 3.7.

3.2.2 *Quantum virial theorem*

So far in this chapter we discussed classical systems, we conclude by presenting the quantum formulation of the virial theorem and showing how in the limit $\hbar/m$ one recovers the classical behavior. For a quantum system the formulation of the theorem is analogue, with the prescription that time-averages must be substituted with averages over the state of the system, which must by an eigenfunction of the Hamiltonian. Specifically, the quantum virial theorem [94] states that, if the system is in an eigenstate of the Hamiltonian,

$$\langle 2\hat{K}\rangle_\psi = \langle \hat{\mathbf{r}}\cdot\nabla\hat{V}\rangle_\psi, \tag{3.22}$$

where $\hat{K}$ is the kinetic energy operator, $\hat{V}$ is the potential operator, and ψ is an eigenstate of the Hamiltonian. Averages of a given operator $\hat{O}$ over a given state ψ are denoted as

$$\langle \hat{O} \rangle_\psi \stackrel{\text{def}}{=} \int d\mathbf{r}\, \psi^*(\mathbf{r}, t)\, \hat{O}\psi(\mathbf{r}, t). \tag{3.23}$$

3.2.3 *Application to the Schrödinger–Newton equation*

In the particular case of the Schrödinger–Newton system, where the potential obeys to Poisson equation, it is possible to evaluate the right hand side of (3.22) exploiting $U(\mathbf{r}, \mathbf{r}')$, the Green function of the 2-dimensional Laplace operator. Since the latter is $U(\mathbf{r}, \mathbf{r}') = \frac{1}{2\pi} \log|\mathbf{r} - \mathbf{r}'|$, one has

$$\begin{aligned} \hat{V} &= 2\pi G m^2 \int U(\mathbf{r}, \mathbf{r}')\ |\psi(\mathbf{r}', z)|^2\ d\mathbf{r}' \\ &= G m^2 \int \log|\mathbf{r} - \mathbf{r}'|\ |\psi(\mathbf{r}', z)|^2\ d\mathbf{r}'. \end{aligned} \tag{3.24}$$

Subsequently, after applying some manipulations (see Section 3.2.1), one finds the value to which the kinetic energy relaxes

$$K_\nu = \frac{G m^2}{4} \tag{3.25}$$

In Figure 3.8, we show the virialization of the kinetic energy for the 2-dimensional Newton–Schrödinger equation initialized with a gaussian wavefunction $\psi(\mathbf{r}, t = 0) = e^{-\frac{r^2}{2\sigma^2}}/\sqrt{\pi\sigma^2}$, for different values of $\frac{\hbar}{m}$. The gaussian is not an eigenfunction of the Newton–Schrödinger Hamiltonian, so the result of the quantum virial theorem in principle is not valid in this case. However, we observe that, as the value of $\hbar/m$ gets smaller, the total kinetic energy of the system behaves in a more similar way to the classical case, displaying oscillations around the virialization value, as shown in Figure 3.9. This behavior is due to the classical limit of the Newton–Schrödinger equation, explained in Section 2.3.1.

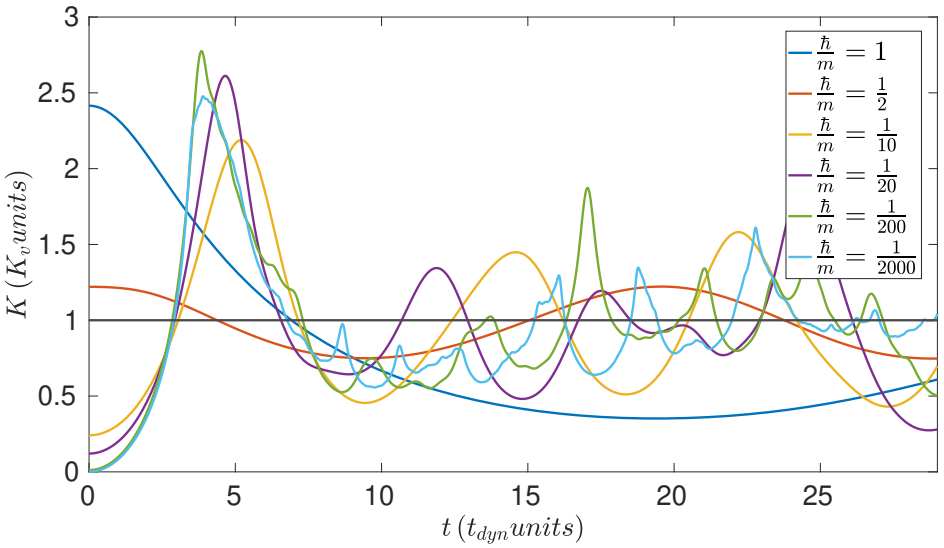

Figure 3.8 – Total kinetic energy in units of the virialized value $K_v = \frac{G\,m^2}{4}$, as a function of time for the 2-dimensional Newton–Schrödinger equation. Time is expressed in units of $t_{dyn} = \frac{\sigma}{\sqrt{m\,G}}$, where σ is the standard deviation of the gaussian initial condition.

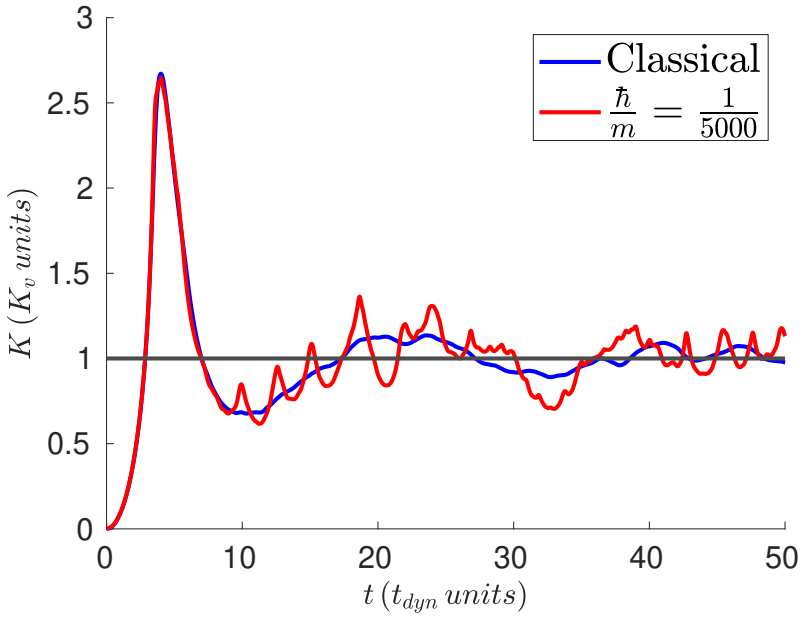

Figure 3.9 – Total kinetic energy in units of the virialized value $K_v = \frac{G\,m^2}{4}$, as a function of time for the 2-dimensional Newton–Schrödinger equation and for a classical (N-body) 2-dimensional self-gravitating systems of $N = 4096$ particles. Time is expressed in units of $t_{dyn} = \frac{\sigma}{\sqrt{m\,G}}$, where σ is the standard deviation of the gaussian initial condition for the matter density distribution, which is the same for both simulations.

4

THEORETICAL PREPARATION OF THE EXPERIMENT

In this chapter, we discuss some theoretical results obtained for the Schrödinger-Newton equation in the context of the preparation of the experiment. First, we show the mapping which must be applied to obtain the full mathematical correspondence between optics and self-gravitating systems through the Schrödinger-Newton equation. Second, we list the most important scales along with their physical interpretation for both the optical and the gravitational domain of application. Third, we define the solitonic solutions of the equation. Finally, we introduce a variational model which is able to provide an analytical approximation for the early part of the dynamics.

4.1 MATHEMATICAL CORRESPONDENCE

To the purpose of describing the mapping which must be applied in order to obtain the full correspondence between the the gravitational framework of Schrödinger-Newton equation and optics, let us start considering both equations. On the one hand, the Schrödinger-Newton equation, describing a system of self-gravitating particles of mass m

$$\begin{aligned} i\hbar\,\partial_t\psi + \frac{\hbar^2}{2m}\nabla^2\psi + m\,\Phi\,\psi = 0 \\ \nabla^2\Phi = -4\pi G\,|\psi|^2, \end{aligned} \tag{4.1}$$

with the wavefunction normalized to the total mass $\int |\psi|^2\,d\mathbf{r} = M$.

On the other hand, the Paraxial-Helmholtz equation for an optical beam propagating through a medium with a thermo-optic nonlinearity

$$\begin{aligned} i\,\partial_z\mathcal{E} + \frac{1}{2k}\nabla_\perp^2\,\mathcal{E} + k_0\,\Delta n\,\mathcal{E} = 0 \\ \nabla_\perp^2\Delta n = -\frac{\alpha\beta}{\kappa}\,|\mathcal{E}|^2, \end{aligned} \tag{4.2}$$

with the optical field normalized to the beam power $\int |\mathcal{E}|^2\,d\mathbf{r}_\perp = P$.

It is clear that, in the case where we consider the two dimensional version of (4.1), namely where the Laplacian is $\nabla = \frac{\partial^2}{\partial x^2} + \frac{\partial^2}{\partial y^2}$, the two equations are formally equivalent under a mathematical point of view. Regarding the physical parameters, the correspondence remains valid as long as the time variable in the gravitational context is mapped into the propagation coordinate of the optical system. If this is taken into account, then the time evolution of the self-gravitating mass density $\rho = |\psi|^2$, corresponds to the propagation of a laser beam, with intensity $I = |\mathcal{E}|^2$, through the

thermo-optical medium. To be more specific, the correspondence between the two systems is given by the following mapping:

$$\begin{aligned}
&\hbar \leftrightarrow 1\\
&t \leftrightarrow z\\
&\psi \leftrightarrow \mathcal{E}\\
&m \leftrightarrow k\\
&\Phi \leftrightarrow k_0\,\Delta_n\\
&4\pi G \leftrightarrow \frac{\alpha\,\beta}{\kappa\,n_b}\\
&M \leftrightarrow P.
\end{aligned} \tag{4.3}$$

4.2 IMPORTANT SCALES

We describe the most relevant physical scales of the system; the knowledge of these scales is crucial for preparing the experiment, correctly tuning the experimental parameters in order to observe the violent relaxation. First, we focus on the spatial scales, and then we consider the dynamical ones. We derive each quantity for the two-dimensional version of the equation in the gravitational context, and then give the results for the optical environment using the mapping (4.3).

4.2.1 *Spatial scales*

The Schrödinger-Newton equation has in general two physically relevant spatial scales. These scales also appear in the context of the Schrödinger equation in quantum mechanics

$$i\,\hbar\partial_t\psi + \frac{\hbar^2}{2\,m}\,\nabla^2\,\psi - V\,\psi = 0, \tag{4.4}$$

where V is a general potential, and ψ is the wavefunction. We choose the first of the two relevant spatial scales to be the average size of the system, defined as

$$R = \langle r\rangle = \frac{\int d\mathbf{r}\,\psi^*\,r\,\psi}{\int d\mathbf{r}\,|\psi|^2}, \tag{4.5}$$

where r is the modulus of the position vector. The second important spatial scale is the De Broglie wavelength,

$$\lambda_{DB} = \frac{h}{\langle p\rangle} = \frac{h\int d\mathbf{r}\,|\psi|^2}{\left|-i\,\hbar\int d\mathbf{r}\,\psi^*\,\nabla\psi\right|}, \tag{4.6}$$

where p is the modulus of the momentum operator, which in coordinate space is defined as $\mathbf{p} = -i\,\hbar\,\nabla$. This λ_{DB} can also be interpreted, in addition to the wave-particle duality, as the inverse of the average size of the system in Fourier space. To

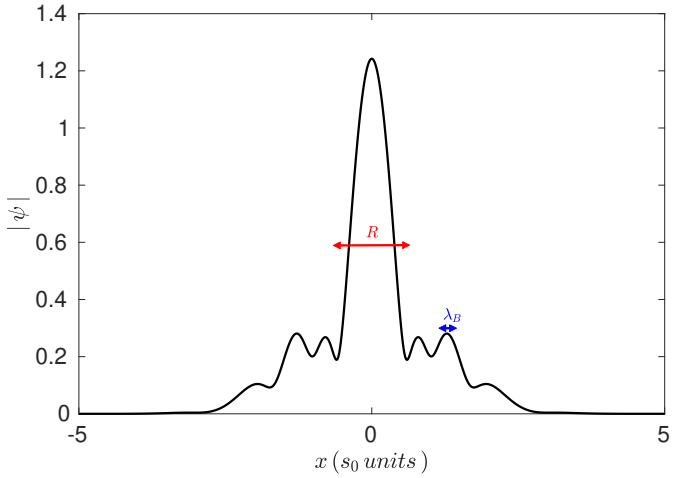

Figure 4.1 – Example of the interplay between the two spatial scales, the average size of the system R and the De-Broglie wavelength λ_{DB} for a snapshot of the solution of the Newton–Schrödinger equation in one dimension. The initial condition is a gaussian $\psi(x, t = 0) = e^{-\frac{x^2}{2s_0^2}}$. The x-axis is in units of s_0.

see this, it is sufficient to consider the definition of the De Broglie wavelength in (4.6), in k-space

$$\lambda_{DB} = \frac{h}{\langle p \rangle} = \frac{h \int dk \left|\widehat{\psi}\right|^2}{\int dk\, \widehat{\psi}^* \hbar k \widehat{\psi}} = \frac{2\pi \int dk \left|\widehat{\psi}\right|^2}{\int dk \left|\widehat{\psi}\right|^2 k}, \tag{4.7}$$

where k is the modulus of the wavevector.

Notice that there exists at least one case where those two scales are essentially the same, which is the gaussian wavefunction. Indeed, considering $\psi(r) = e^{-r^2/(2\sigma^2)}$, one has $R \propto \sigma$ and $\lambda_{DB} \propto \sigma$, which is related with the very well known saturation of the Heisenberg uncertainty relation for a gaussian wavepacket. An example of the interplay between these two spatial case is showed in Figure 4.1.

4.2.1.1 *A pedagogical example*

Here we discuss a pedagogical example which clarifies the multiscale nature of the equation. We consider a one dimensional wavefunction, which is qualitatively very similar to the one we deal with in the experimental setup

$$\psi(x) = \mathcal{N} e^{-\frac{x^2}{2\sigma^2}} \cos\frac{x}{\mu}, \tag{4.8}$$

where $\mathcal{N}$ is the normalization constant, defined in such a way that $\int dx |\psi(x)|^2 = 1$, σ is the standard deviation of the gaussian and μ is related to the oscillation frequency.

Evaluating R, using (4.6), one has

$$R = \int dx\, |x|\, |\psi(x)|^2 = \frac{2 e^{\frac{\sigma^2}{\mu^2}} \sigma \left[\mu - \sigma D\left(\frac{\sigma}{\lambda}\right)\right]}{\left(1 + e^{\frac{\sigma^2}{\mu^2}}\right)\sqrt{\pi}\,\sigma}, \tag{4.9}$$

where $D(y) = e^{-y^2}\int_0^y e^{t^2}dt$ is the Dawson function, whose asymptotic behaviors are the following: $D(y) \approx_{y\to 0} y$ and $D(y) \approx_{y\to\infty} 0$.

Whereas evaluating λ_{DB} according to (4.7) yields

$$\lambda_{DB} = \frac{2\pi}{\int dk \left|\widehat{\psi}\right|^2 k} = \frac{2\pi\left(1+e^{\frac{\sigma^2}{\mu^2}}\right)\sqrt{\pi}\,\sigma\,\mu}{2\mu + e^{\frac{\sigma^2}{\mu^2}}\sqrt{\pi}\,\sigma\,\operatorname{erf}\frac{\sigma}{\mu}}, \tag{4.10}$$

where the Fourier transform of ψ, $\widehat{\psi}(k) = \frac{e^{-\frac{\sigma^2(k\mu-1)^2}{2\mu^2}} + e^{-\frac{\sigma^2(k\mu+1)^2}{2\mu^2}}}{\sqrt{2\left(1+e^{-\sigma^2/\mu^2}\right)\sqrt{\pi}/\sigma}}$ has been used.

From (4.9)-(4.10), it is straightforward to notice that in the case where $\mu \ll \sigma$, one has $R \approx \sigma$ and $\lambda_{DB} \approx \mu$. This confirms how R is indeed related to the average size of the system and λ_{DB} to the minimal size of its spatial fluctuations.

4.2.2 *Classicality*

We now define a very useful parameter which is employed to describe and identify the different physical regimes of the Schrödinger–Newton equation. This parameter points out how much the quantum effects are negligible compared to the effect due to the gravitational interaction, thus, how close one is to the semiclassical regime of the system. In the optical framework on the other hand, it can be interpreted as a parameter which quantifies how much the self-focusing interaction is dominating over diffraction.

This parameter is defined as

$$\chi = \frac{\lambda_{DB}}{R}, \tag{4.11}$$

which is the ratio between the two spatial scales we introduced, λ_{DB} and R, such that the more the De Broglie wavelength is small compared to the average size of the system, the more the quantum pressure related to the Heisenberg uncertainty relation can be neglected. In general this is a dynamical quantity, because both R and λ_{DB} change with time. However, near the quasi-stationary state, it can be approximated with a constant. One way to do that, is defining the typical De Broglie wavelength as the scale at which the kinetic and the potential energy are of the same magnitude. In the case of two spatial dimensions, one has

$$\frac{\hbar^2}{m\lambda_{DBeq}^2} \approx m\,G\,M \qquad \Rightarrow \qquad \lambda_{DBeq} = \frac{\hbar}{m}\frac{1}{\sqrt{G\,M}}. \tag{4.12}$$

Through numerical simulations, we observe that the typical average size of the system reamins of the same order of magnitude compared with the initial size. For this reason we take $R_{typ} = \sigma$. In this way, one obtains for the expression of χ

$$\chi = \frac{\hbar}{m}\frac{1}{\sqrt{G\,M\,\sigma}}. \tag{4.13}$$

In the optical system, the values of $\lambda_{DB,eq}$ and χ can be obtained either by doing the same computations, or by using the mapping defined in (4.3), leading to

$$\lambda_{DB} = \sqrt{\frac{2\pi\kappa n_b}{k^2\,\alpha\,\beta\,P}} \qquad \chi = \sqrt{\frac{2\pi\kappa n_b}{k^2\,\alpha\,\beta\,P\,\sigma^2}}. \tag{4.14}$$

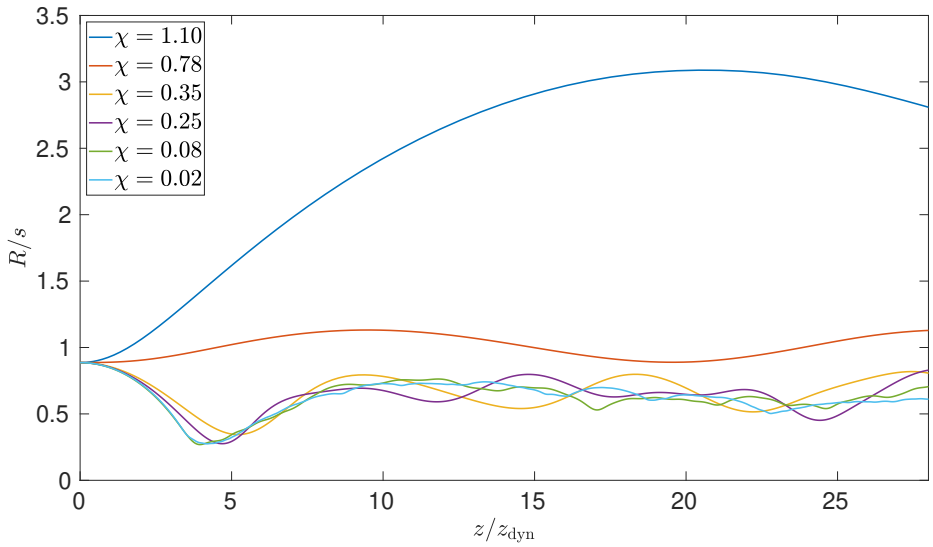

Figure 4.2 – Plot of the average size of the laser beam $< r >= R$ as a function of the longitudinal coordinate z in units of z_{dyn}, for different values of χ.

In Figure 4.2, we show how varying χ affects the dynamics of the average size of the system, obtained from the numerical simulations for the optical version of the Newton–Schrödinger equation. When $\chi \gtrsim 1$, analogue quantum effects start being important, with the system initially expanding because of the quantum pressure (or diffraction in the optical framework) dominating over gravity (self-focusing interaction). Whereas, in the semi-classical regime, with $\chi \ll 1$, the dynamics is dominated by an initial collapse.

4.2.3 *Dynamical scales*

Here, we focus on the dynamical scales of the system. As for the spatial case, the Schrödinger-Newton equation is characterized by two time-scales: one related to the quantum pressure (or diffraction in optics) and the other one coming from the gravitational (self-focusing) interaction.

The first one can be defined considering the magnitude of the term containing the time derivative inside the equation, namely $i\hbar\partial_t\psi$ and comparing it to the kinetic energy $-\frac{\hbar^2}{2m}\nabla^2\psi$. Thus one has

$$\frac{\hbar}{t_k} \approx \frac{\hbar^2}{m\lambda_{DB}^2} \qquad \Rightarrow \qquad t_k \approx \frac{m}{\hbar}\lambda_{DB}^2. \tag{4.15}$$

The time-scale related to the gravitational interaction on the other hand, can be estimated comparing the term containing the time derivative to the potential term, $mV\psi$

$$\frac{\hbar}{t_G} \approx m\,V, \tag{4.16}$$

where V is evaluated via the Green's integral

$$V(\mathbf{r},t) = 2\pi G \int d\mathbf{r}' G(\mathbf{r},\mathbf{r}')\,|\psi(\mathbf{r}',t)|^2 \approx G\,M. \tag{4.17}$$

Combining (4.16) and (4.17) one obtains

$$t_G \approx \frac{\hbar}{m}\frac{1}{G\,M}. \tag{4.18}$$

Notice how if on the one hand t_k is proportional to the ratio $\frac{m}{\hbar}$, on the other hand $t_G \propto \frac{\hbar}{m}$, meaning that when the classical limit is considered, i.e. formally $\frac{\hbar}{m} \to 0$, the former goes to infinity and the latter goes to zero. Whenever close to the classical limit, a more meaningful way to quantify the typical scale of the gravitational interaction, which we call t_{dyn}, is exploiting Newton's law, namely

$$m\,\ddot{\mathbf{r}} = -\nabla V. \tag{4.19}$$

In this way, using that $\nabla V \approx -\frac{G\,M\,m}{R}$, one has

$$\frac{m\,R}{t_{dyn}^2} \approx \frac{G\,M\,m}{R} \qquad \Rightarrow \qquad t_{dyn} = \frac{R}{\sqrt{G\,M}}. \tag{4.20}$$

In the optical system, the quantity t_{dyn} is related to the propagation scale z. It can be obtained using the mapping (4.3), leading to

$$z_{dyn} = \sqrt{\frac{n_b\,\kappa}{\alpha\,\beta}}\frac{R}{P}. \tag{4.21}$$

4.2.4 *Virial Ratio*

Another important dynamical scale is the virial ratio Γ_v, defined in Section 3.2 as the ratio between the initial value of the kinetic energy K_0 and the value of equilibrium, given by the virial theorem. As explained in Section 3.2.2, the theorem states that for any eigenstate of the Hamiltonian, the kinetic energy satisfies

$$K_v = -\frac{1}{2}\langle \mathbf{r}\cdot\nabla V\rangle, \tag{4.22}$$

In order to evaluate this quantity, one first needs to compute $V = -m\,\Phi$ in a suitable form. The computations are done for the adimensionalized equation in the form of (A.4), with $f = 0$ and $h = 0$ (see Appendix A). Since the Green function U of the two dimensional Laplace operator is $U(\mathbf{r},\mathbf{r}') = \log|\mathbf{r}-\mathbf{r}'|$ [95], one has

$$\begin{aligned}\langle -\mathbf{r}\cdot\nabla V\rangle &= 2\,\pi\,G\,m\Big\langle \int \mathbf{r}\cdot\nabla U(\mathbf{r},\mathbf{r}')\;|\psi(\mathbf{r}',t)|^2\;\,d\mathbf{r}'\Big\rangle \\ &= G\,m\iint \frac{\mathbf{r}\cdot(\mathbf{r}-\mathbf{r}')}{|\mathbf{r}-\mathbf{r}'|^2}\,|\psi(\mathbf{r}',t)|^2\;|\psi(\mathbf{r},t)|^2\;\,d\mathbf{r}'\,d\mathbf{r}.\end{aligned} \tag{4.23}$$

Interchanging $\mathbf{r}\leftrightarrow\mathbf{r}'$ and exploiting the identity $\mathbf{r}\cdot(\mathbf{r}-\mathbf{r}')+\mathbf{r}'\cdot(\mathbf{r}'-\mathbf{r}) = |\mathbf{r}-\mathbf{r}'|^2$, together with the normalization of ψ, one obtains

$$\langle -\mathbf{r}\cdot\nabla V\rangle = \frac{G\,M^2\,m}{2}. \tag{4.24}$$

Therefore

$$K_v = \frac{G\,M^2\,m}{4}, \tag{4.25}$$

independently of the initial condition.

For a Gaussian initial condition, $\psi(\mathbf{r}, t = 0) = \sqrt{M}/\left(\sigma\sqrt{\pi}\right) e^{-r^2/(2\sigma^2)}$, one has for the initial kinetic energy

$$K_0 = \frac{-\hbar^2}{2m}\int \psi^*(\mathbf{r}, t = 0)\,\nabla^2\psi(\mathbf{r}, t = 0)\,d\mathbf{r} = \frac{\hbar^2 M}{2m\sigma^2} \tag{4.26}$$

Therefore the virial ratio in this case is

$$\Gamma_v = \frac{K_0}{K_v} = 2\chi^2, \tag{4.27}$$

which shows how in two spatial dimensions the virial ratio is directly related to the parameter χ.

As shown in Figure 4.3, where the same quantities as those of Figure 3.8 are plotted in terms of Γ_v, for $\Gamma_v < 1$ the system initially collapses while for $\Gamma_v > 1$ it initially expands before collapsing. Specifically, the $\Gamma_v > 1$ case corresponds to "hot initial condition" in the gravitational framework, because the initial kinetic energy is larger then the virial value and therefore the dynamics is initially be dominated by the kinetic pressure. On the other hand, the $\Gamma_v < 1$ case corresponds to "cold initial conditions", where the dynamics is characterized by an initial collapse.

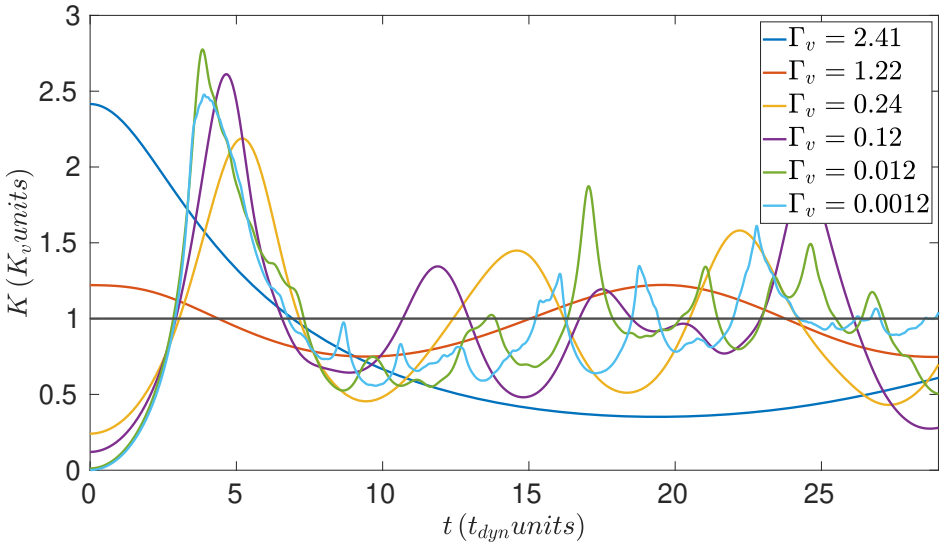

Figure 4.3 – Total kinetic energy in units of the virialized value $K_v = (4\chi^2)^{-1}$, as a function of time for the 2-dimensional Newton–Schrödinger equation.

4.3 THE SOLITON PROFILE

As discussed in Section 3.2, self-gravitating systems undergo a virialization process. In the quantum regime, as described by the quantum virial theorem, the virialization takes place only when the system is in an eigenstate of the Hamiltonian. However, as mentioned in Section 3.2.2), as the system approaches the classical limit, namely as $\frac{\hbar}{m} \to 0$, the classical virialization behavior is recovered. Here, we show that in the case of the Newton–Schrödinger equation it is possible to compute the

density profile of the stationary state in the center of the structure by looking for time-independent solutions of the equation. These time-independent solutions of the Schrödinger–Newton equation are usually called "solitons" [8, 96]. To derive it, as done in [97], we consider the equation in the form

$$\begin{aligned} -\frac{\hbar^2}{2m}\nabla^2\psi + m\,V\psi &= E\,\psi \\ \nabla^2 V &= 4\pi G\,|\psi|^2, \end{aligned} \tag{4.28}$$

which can be obtained applying the separation of variables method to the time-dependent Schrödinger equation. Here ψ and V are only functions of the spatial coordinates; in addition we focus on real and spherically symmetric functions, i.e. $V = V(r)$ and $\psi = \psi(r)$ with $\psi \in \mathbb{R}$.

With the change of variable

$$\begin{aligned} \psi &= a\,S \\ E - V &= b\,W, \end{aligned} \tag{4.29}$$

where $a = \frac{\hbar}{\sqrt{4\pi G m^3}}$ and $b = \frac{\hbar}{m}$, the equations become

$$\begin{aligned} \frac{1}{2}\nabla^2 S + S\,W &= 0 \\ \nabla^2 W &= -S^2. \end{aligned} \tag{4.30}$$

These equations are characterized by a scale invariance property: if $S(r)$ and $V(r)$ are solutions of the system, then the same is true also for $\zeta^2 S(r/\zeta)$ and $\zeta^2 V(r/\zeta)$, with ζ being a nonzero scalar. This rescaling can be used to impose a posteriori the normalization of S.

We look for solutions that are finite and smooth everywhere, which implies

$$\begin{aligned} \lim_{r\to\infty} S(r) &= 0 \\ \left.\frac{\partial S}{\partial r}\right|_{r=0} &= 0 \\ \left.\frac{\partial W}{\partial r}\right|_{r=0} &= 0. \end{aligned} \tag{4.31}$$

To obtain these solutions, we employ a numerical shooting method as done by Moroz et al. in [97], then we compare the virialized inner density profile outputted by time-dependent numerical simulations with the solitonic solution $S(r)$. In Figure 4.4 we show the time-average, $\overline{|\psi|}$, of the modulus of the virialized solution profile $|\psi|$ and the soliton $S(r)$. We observe how $\overline{|\psi|}$ can be well fitted by $S(r)$ near the origin. Moreover, the agreement gets more accurate in the cases where $\chi \gtrsim 1$, see Figure 4.5. This is due to the fact that the closer one is to the deep quantum regime, the larger the magnitude of the De Broglie wavelength λ_{DB} gets and subsequently the size of the central soliton increases. On the other hand, as the χ parameter increases, the systems gets closer to the classical limit and the size of the central solitonic structure decreases as a consequence of the quantum pressure becoming weaker. For this reason, outer

regions are not solution of the soliton, but solution of the classical evolution [8], and in the deep quantum regime they disappear.

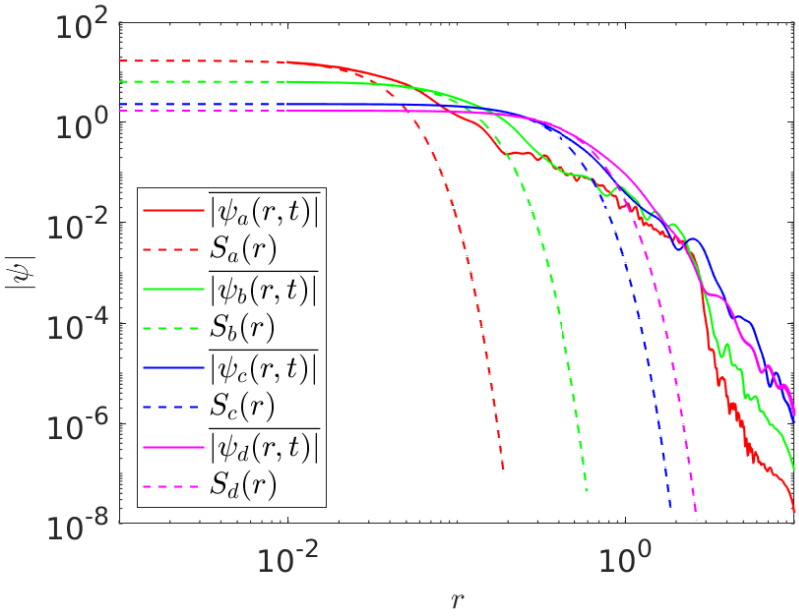

Figure 4.4 – Comparison between $\overline{|\psi|}$ and the soliton solution $S(r)$ in the cases: $\chi_a = 0.02$, $\chi_b = 0.08$, $\chi_c = 0.25$, $\chi_d = 0.35$. The plot is in adimensional units.

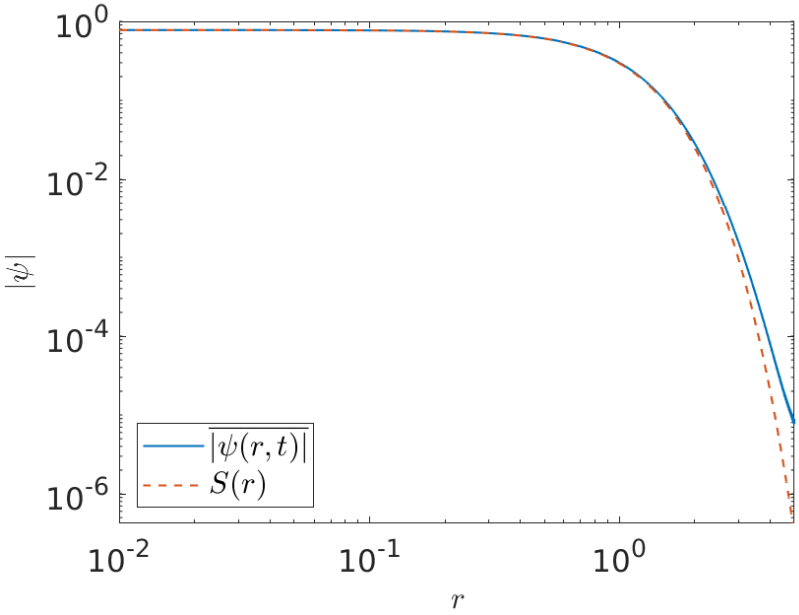

Figure 4.5 – Comparison between $\overline{|\psi|}$ and the soliton solution $S(r)$ in the $\chi = 0.78$ case. The plot is in adimensional units.

4.4 VARIATIONAL MODEL

In this section, we introduce a variational approach in order to derive an analytical solution of the Schrödinger-Newton equation. This method so far has only been presented in three dimensions [98], we derive here the two dimensional version in order to apply it to the case of interest in optics. The results allow to obtain an approximated analytical solution, which we often employed in order to make some rapid test or prediction on the system. We start introducing the hydrodynamical picture of the Schrödinger–Newton equation, which can be obtained with the Madelung Transformation, and then we employ a gaussian ansatz to build the variational model. The results obtained are finally compared with the numerical solution.

4.4.1 *Hydrodynamical picture*

Let us consider the Schrödinger–Newton equation

$$\begin{aligned} i\hbar\,\partial_t\psi + \frac{\hbar^2}{2m}\nabla^2\psi - m\,V\,\psi = 0 \\ \nabla^2 V = 4\pi G|\psi|^2. \end{aligned} \tag{4.32}$$

and let us apply the Madelung transformation [99]. This transformation consists of separating the modulus and phase fields of the the wavefunction, hence switching from a complex variable $\psi(\mathbf{r},t)$ to two real variables $\rho(\mathbf{r},t)$ and $S(\mathbf{r},t)$. This change of variable is defined as

$$\psi(\mathbf{r},t) = \sqrt{\rho(\mathbf{r},t)}\,e^{i\,S(\mathbf{r},t)}. \tag{4.33}$$

Plugging (4.33) in (4.32) and separating the real and imaginary part, yields

$$\frac{\partial\rho}{\partial t} - \frac{\hbar}{m}\nabla\rho\cdot\nabla S + \frac{\hbar}{m}\nabla^2 S\rho = 0 \tag{4.34}$$

$$\frac{\partial S}{\partial t} - \frac{\hbar}{2m}\left(\frac{\nabla^2\sqrt{\rho}}{\sqrt{\rho}} - |\nabla S|^2\right) + \frac{m}{\hbar}V = 0 \tag{4.35}$$

$$\nabla^2 V = 4\pi G\,\rho. \tag{4.36}$$

Introducing the quantity $\mathbf{u} = \frac{\hbar}{m}\nabla S$, which physically has the dimension of a velocity, and applying the gradient to (4.36), one gets

$$\frac{\partial\rho}{\partial t} + \nabla(\rho\cdot\mathbf{u}) = 0 \tag{4.37}$$

$$\frac{\partial\mathbf{u}}{\partial t} + \mathbf{u}(\nabla\cdot\mathbf{u}) = -\nabla V + \frac{\hbar}{2m}\nabla\left(\frac{\nabla^2\sqrt{\rho}}{\sqrt{\rho}}\right) \tag{4.38}$$

$$\nabla^2 V = 4\pi G\,\rho. \tag{4.39}$$

This result can be interpreted as an equivalence between the Schrödinger-Newton system and a hydrodynamical system. Indeed, (4.37) and (4.38) represent respectively the continuity and the Euler equation for a fluid with density ρ, velocity field $\mathbf{u}$ and subjected to a potential V, given by (4.39). The $\frac{1}{2}\nabla(\frac{\nabla^2\sqrt{\rho}}{\sqrt{\rho}})$ term can be interpreted as a pressure. In particular, since it comes from the kinetic energy term of the Schrödinger

equation, one can interpret it as a kinetic pressure due to Heisenberg uncertainty relation.

It is convenient at this point, to derive a Lagrangian density associated with this system. To do that, we write a Lagrangian density as done in [98] for the three dimensional case and check that it actually gives back (4.37),(4.38),(4.39)) when one writes the equations of motion associated with it. The Lagrangian density is

$$\mathcal{L}(\rho, S, V) = \frac{\hbar}{m}\frac{\rho}{2}(\nabla S)^2 + \rho\frac{\partial S}{\partial t} + \frac{\hbar}{m}\frac{|\nabla\rho|^2}{8\rho} + \frac{m}{\hbar}\frac{|\nabla V|^2}{8\pi G} + \frac{m}{\hbar}\rho V. \tag{4.40}$$

Indeed, writing the Euler-Lagrange equations associated with $\mathcal{L}$, leads to

$$\begin{aligned}
\frac{\partial\mathcal{L}}{\partial\rho} &= \nabla\cdot\left(\frac{\partial\mathcal{L}}{\partial(\nabla\rho)}\right) + \frac{\partial}{\partial t}\left(\frac{\partial\mathcal{L}}{\partial(\frac{\partial\rho}{\partial t})}\right)\\
\frac{\partial\mathcal{L}}{\partial S} &= \nabla\cdot\left(\frac{\partial\mathcal{L}}{\partial(\nabla S)}\right) + \frac{\partial}{\partial t}\left(\frac{\partial\mathcal{L}}{\partial(\frac{\partial S}{\partial t})}\right)\\
\frac{\partial\mathcal{L}}{\partial V} &= \nabla\cdot\left(\frac{\partial\mathcal{L}}{\partial(\nabla V)}\right) + \frac{\partial}{\partial t}\left(\frac{\partial\mathcal{L}}{\partial(\frac{\partial V}{\partial t})}\right).
\end{aligned} \tag{4.41}$$

The first equation gives back Euler equation, the second one gives back continuity equation and the third one, Poisson equation.

4.4.2 *Gaussian ansatz*

We know try to explicitly solve (4.37),(4.38),(4.39), through a gaussian ansatz for the function ρ,

$$\rho(\mathbf{r}, t) = \mathcal{N} e^{-\frac{r^2}{R(t)^2}}, \tag{4.42}$$

where $\mathcal{N}$ is a normalization constant, fixed in such a way that

$$\int d\mathbf{r}\,\rho(\mathbf{r}, t) = M \qquad \Leftrightarrow \qquad \mathcal{N} = \frac{M}{\pi R(z)^2} \tag{4.43}$$

given that we are considering the case of two spatial dimensions.

With this ansatz (4.39), can be solved analytically. Its general solution is

$$V(r, t) = a - G M\, Ei\left(-\frac{r^2}{R(t)^2}\right) + b\,\log(r) \tag{4.44}$$

where Ei is a special function, called Exponential-Integral function, defined as

$$Ei(r) = \int_{-r}^{\infty}\frac{e^{-t}}{t}\,dt. \tag{4.45}$$

Since the integration constants a is just a global constant which does not change the physics, it can be set to zero. The other integration constant, b, is chosen in such a way that the potential is finite at the origin. This choice is motivated from the fact that in the optical setup we are interested in, the potential corresponds to a variation

of refraction index and it cannot be singular at the origin. Considering the Taylor expansion of the Exponential-Integral function near the origin

$$\mathrm{Ei}(-r^2) = \gamma + 2\,\log r + O\left(r^2\right), \tag{4.46}$$

where γ is the Euler's constant, with numerical value $\gamma \approx 0.577216$, one gets that the potential has finite value at the origin for $b = 2G$. This choice of the integration constants lead to

$$V(r,t) = -G\,M\,\mathrm{Ei}\left(-\frac{r^2}{R(t)^2}\right) + 2\,G\,M\,\log(r). \tag{4.47}$$

Concerning the continuity equation, it is exactly solved by the velocity field $\mathbf{u}(\mathbf{r},t) = \frac{\dot{R}(t)}{R(t)}\mathbf{r}$, as it can be easily checked by substitution. The phase function is therefore

$$S(\mathbf{r},t) = \frac{m}{2\hbar}\frac{\dot{R}(t)}{R(t)}\,r^2 \tag{4.48}$$

where the dot denotes a derivative with respect to time.

Plugging (4.42),(4.47),(4.48) in (4.41), one gets the Lagrangian density associated with the gaussian ansatz, which at this point only depends on $\mathbf{r} = (x,y)$ and time. Since the information about the $\mathbf{r}$ dependence are already contained in the ansatz, it is possible to switch from the Lagrangian density $\mathcal{L}$ to the Lagrangian, integrating the spatial variables. However, this operation must be done carefully because the term $\int \frac{m}{\hbar}\frac{|\nabla V|^2}{8\pi G}d\mathbf{r}$ is not bounded. For this reason, the Lagrangian density is split in two parts

$$\mathcal{L}(r,t) = \mathcal{L}_1(r,t) + \mathcal{L}_2(r,t) \tag{4.49}$$

$$\mathcal{L}_1(r,t) = \frac{\hbar}{m}\frac{\rho}{2}(\nabla S)^2 + \rho\frac{\partial S}{\partial t} + \frac{\hbar}{m}\frac{|\nabla\rho|^2}{8\rho} + \frac{m}{\hbar}\rho\,V \tag{4.50}$$

$$\mathcal{L}_2(r,t) = \frac{m}{\hbar}\frac{|\nabla V|^2}{8\,\pi\,G}. \tag{4.51}$$

The first term $\mathcal{L}_1$ can be directly integrated with respect to $\mathbf{r}$. Concerning the second term, $\mathcal{L}_2$, first we write the equation of motions associated with it and then we integrate them with respect to spatial variables. This ensures all the integrals not to be divergent.

The equation of motion can therefore be written as

$$\ddot{R} = \frac{\hbar^2}{m^2}\frac{1}{R^3} - \frac{M\,G}{R} \tag{4.52}$$

which represents, in the Newtonian picture, the equation of motion of a point-like particle of mass m evolving in an external potential $\Phi(R) = -\frac{\hbar^2}{2\,m}\frac{1}{R^2} + m\,M\,G\,\log R$. The first term of this potential is repulsive and associated with a kinetic pressure, while the second term, is attractive and associated with two dimensional gravity. For small values of R the first term dominates on the second one, while when R is large, gravity is the dominant interaction.

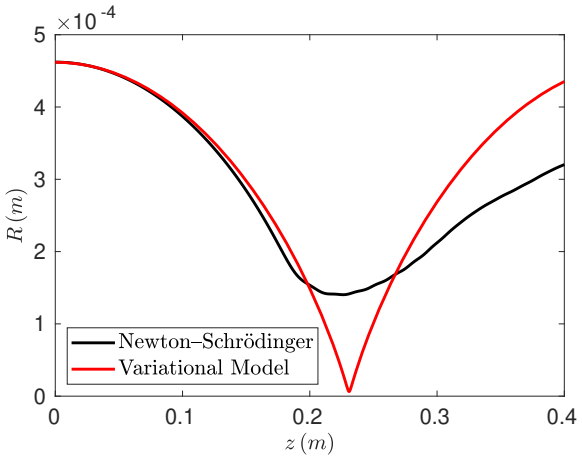

Figure 4.6 – Comparison for the function $R(z)$ between the variational model and the Newton–Schrödinger equation.

4.4.2.1 *Application to the optical setup*

This variational model can be useful in the optical framework of the Newton–Schrödinger equation, when a gaussian beam initial condition is considered. Indeed, in this case one expects the real solution to be not so different from a Gaussian for a small propagation distance.

The variational model in the optical framework can be derived applying the mapping defined by Equation 4.3, with

$$I(\mathbf{r}_\perp, z) = \frac{P}{\pi R^2(z)} e^{-\frac{r_\perp}{R^2(z)}}. \tag{4.53}$$

In this case the variational approach yields

$$\ddot{R} = \frac{1}{k^2}\frac{1}{R^3} - \frac{P\,\alpha\,\beta}{2\,\pi\,\kappa\,n_b}\frac{1}{R} \tag{4.54}$$

where dots indicate derivatives with respect to z.

4.4.3 *Comparison with numerical solution*

Even though equation (4.54) can be analytically solved only for the inverse function $z(R)$, the so obtained solution $z(R)$ cannot be inverted analytically, for this reason we solve the equation numerically.

In Figure 4.6 we show the comparison for the function $R(z)$ between the variational model and the Newton–Schrödinger equation. For the latter, $R(z)$ as been evaluated as

$$R(z) \overset{\text{def}}{=} \frac{2}{\sqrt{\pi}}\langle\sqrt{x^2+y^2}\rangle = \frac{2}{\sqrt{\pi}}\frac{\iint dx\,dy\,I(x,y,z)\sqrt{x^2+y^2}}{\iint dx\,dy\,I(x,y,z)} \tag{4.55}$$

given that plugging equation (4.53) into (4.55) returns $R(z)$.

As shown in Figure 4.7, the model approximates accurately the solution only in the early phase of the dynamics, for values of propagation distance much smaller than

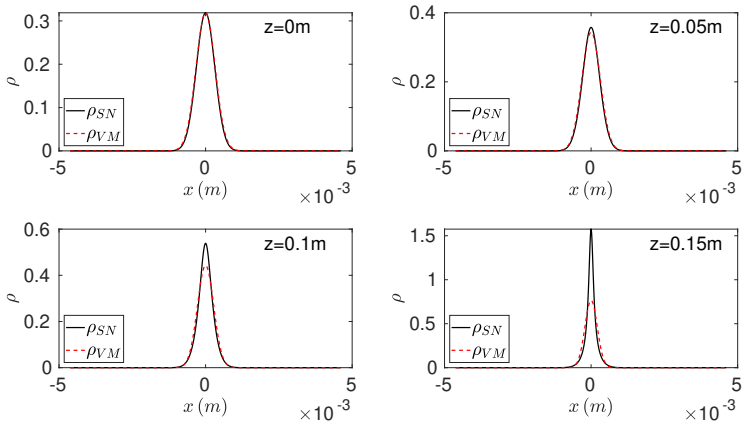

Figure 4.7 – Comparison of several snapshots of $\rho(x, y = 0, z)$ in the early part of the dynamics between the variational model ρ_{VM} and the Newton–Schrödinger equation ρ_{SN}.

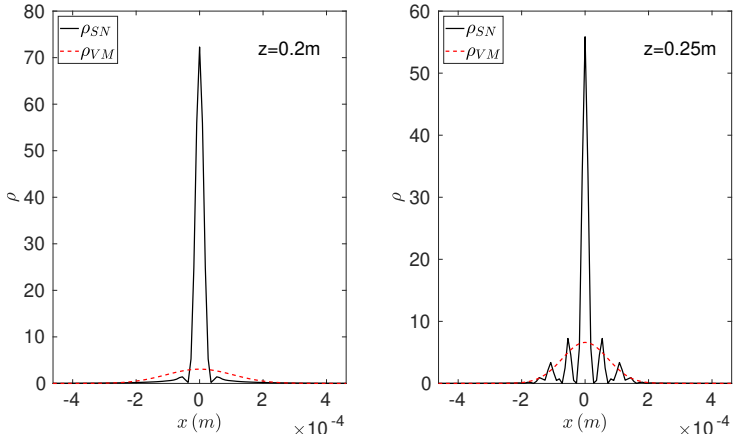

Figure 4.8 – Comparison of several snapshots of $\rho(x, y = 0, z)$ near the collapse between the variational model ρ_{VM} and the Newton–Schrödinger equation ρ_{SN}.

$z_c \approx 0.2\,m$, the minimum point of $R(z)$, which is associated with the collapse. This is due the to fact that for $z \ll z_c$ the solution is not far from a gaussian, and then as z increases it develops some more complicated features which break the gaussian profile, as shown in Figure 4.8.

Part II

NUMERICAL ASPECTS

5 NUMERICAL METHODS

The Newton–Schrödinger equation is a system of nonlinear and nonlocal partial differential equations whose solution can generally be evaluated with a numerical method. In this chapter we list and explain the different numerical algorithms exploited during this thesis work, to solve not only the Newton–Schrödinger system but also other Schrödinger-like equations with different potential terms. First, we discuss the spatial resolution, focusing on spectral methods based on fast Fourier transform techniques. Second, we consider the temporal resolution. For the latter, there are essentially two families of methods commonly employed to solve this kind of equations: the integrating factor technique and the Split-Step algorithm. Finally, we explain how those methods work, both in the case of fixed and adaptive time-steps. The comparisons between all the different numerical schemes considered, the advantages and disadvantages of each method together with an improvement of the integrating factor algorithm, are then discussed in the next chapters.

5.1 NUMERICAL SPATIAL RESOLUTION

The numerical spatial resolution of Schrödinger-like equations, can be addressed with several categories of numerical methods. Among the most popular ones, one can find finite difference methods [100] and spectral (or pseudo-spectral) methods [101–103]. While a finite difference scheme often introduces excessive numerical errors, spectral methods are known to be more efficient, combining very high accuracy with a small computational cost. In addition, spectral methods are characterized by an exponential error decay rate, which is much faster if compared to the polynomial one, typical of finite difference schemes. Moreover, methods belonging to the spectral family are quite advantageous and flexible whenever higher order derivatives and different types of partial differential equations are considered. In the context of meteorology, ocean waves, seismology and turbulence for example, they are well known to be a robust and successful numerical tool [103]. These are the main reasons why, in this thesis, we choose to focus on spectral methods rather than finite difference techniques, for the spatial numerical resolution of the equations considered. The details of this chosen methods, are explained in the next sections.

5.1.1 *Spectral and pseudo-spectral Fourier methods*

When solving a differential equation with a spectral method, the solution $\psi(\mathbf{x})$ is decomposed as

$$\psi(\mathbf{x}) = \sum_{n=0}^{N} a_n \phi_n(\mathbf{x}), \tag{5.1}$$

where ϕ_n are some differentiable functions which represent a basis and a_n are the coefficients. In the context of a numerical solution the series (5.1) is obviously trun-

cated, resulting in a approximation. The derivative with respect to the variable $\mathbf{x}$ are then evaluated analytically by means of this decomposition. In this way, every time a spatial derivative is computed, the information coming from the entire domain is taken into account. This is a crucial advantage compared to finite difference methods, which compute derivatives exploiting information coming only from a few neighborhood points. The coefficients a_n can be calculated following several approaches, interested readers can consult [104] for further details. We focus on the pseudo-spectral method case, for which those coefficients are evaluated in some fixed points of the domain. In particular we use pseudo-spectral Fourier methods, which employ a decomposition with trigonometric series, allowing to exploit the Fast-Fourier-Transform algorithm. In the next paragraph, we briefly illustrate how this method works.

5.1.1.1 *Fast Fourier transform*

The fast Fourier transform algorithm computes the discrete Fourier transform of a function, in an efficient way. If one considers the definition of the discrete Fourier transform for the N-dimensional vector $\mathbf{x} = (x_0, x_1, ..., x_{N-1})$,

$$X_k = \sum_{n=0}^{N-1} x_n \, e^{-\frac{2\pi i n}{N} k} \qquad k \in \{0, 1, 2, ..., N-1\}, \tag{5.2}$$

and devise the algorithm by simply applying this procedure, the number of operations needed for the computation is $\mathcal{O}(N^2)$. Nevertheless, because of the symmetry of the discrete Fourier transform, it is possible to divide the sum (5.2) of N terms into two sums of $\frac{N}{2}$ terms each,

$$X_k = \sum_{n=0}^{N/2-1} x_{2n} \, e^{-\frac{2\pi i n}{N/2} k} + e^{\frac{2\pi i k}{N}} \sum_{n=0}^{N/2-1} x_{2n+1} \, e^{-\frac{2\pi i n}{N/2} k},$$

separating the contributes of the odd even and even index values. This allows to compute the discrete Fourier transform recursively in $\mathcal{O}(N \log N)$ operations and is known as Cooley-Tukey fast Fourier transform algorithm [105]. Here, to evaluate the Fourier transforms which appears in all the numerical algorithms we consider, we use the FFTW library implementation [106].

5.1.2 *Spatial discretization in Fourier space and Nyquist frequency*

The spatial discretization in Fourier space is in general subjected to some constraints. First, in order to achieve a proper sampling of the signal, the discretization must incorporate a large enough number of points N. If the physical space is characterized by N points, over a domain of size L, then the discretization step is by definition

$$\Delta x = \frac{L}{N}, \tag{5.3}$$

and each site x_n, with $n \in \{0, 1, ..., N-1\}$ satisfies

$$x_n = \Delta x \, n = \frac{L}{N} n. \tag{5.4}$$

The second constraint is that the step of the spatial discretization in Fourier space must be defined as

$$\Delta k = \frac{2\pi}{L}, \tag{5.5}$$

which also defines the fundamental frequency.

Each mode k_n verifies

$$k_n = \Delta k\, n = \frac{2\pi}{L} n. \tag{5.6}$$

Moreover, there exists a critical frequency, called the Nyquist frequency, defined as $k_{Nyquist} = \frac{1}{2\Delta x}$, for which the maximal frequency of the signal k_{max} must satisfy

$$k_{max} < k_{Nyquist}. \tag{5.7}$$

Therefore positive frequencies $k_n^{(+)}$ and negative ones $k_n^{(-)}$ must obey to

$$\begin{aligned} 0 \leqslant k_n^{(+)} &\leqslant k_{Nyquist}, \quad n \in \{0, 1, ..., [N/2]-1\} \\ -k_{Nyquist} \leqslant k_n^{(-)} &\leqslant 0, \quad n \in \{[N/2]+1, ..., N-1\}, \end{aligned} \tag{5.8}$$

where squared brackets denote the integer part. This taken into account, we define the numerical Fourier modes as

$$k_n = \begin{cases} \frac{2\pi}{L} n & \text{if } n \in \{0, 1, ..., [N/2]-1\}, \\ \frac{2\pi}{L} (n - N) & \text{if } n \in \{[N/2]+1, ..., N-1\}, \end{cases} \tag{5.9}$$

where the $n = \left[\frac{N}{2}\right]$ case corresponds to the Nyquist frequency, whose corresponding signal value must be put to zero.

5.1.3 *Aliasing errors*

While dealing with a spectral method, a particular category of numerical errors, known as aliasing errors [101], must be considered and treated properly. The origin of these errors is the truncated decomposition, defined in (5.1), for which a discrete sum of a Fourier transform is truncated in a finite number of modes. If for example a simple product between two functions in physical space is considered, it is easy to check that the discretization of the product does not correspond to the product of the discretised functions. Looking at the Fourier space, one has indeed a convolution in the first case and a circular convolution in the second one. This is the source of aliasing errors, which would destabilize the numerical solution for high wave-numbers in Fourier space, if not treated properly.

A very simple way to avoid this kind of errors is the zero-padding technique with the $\frac{4}{2}$-rule [102]. This anti-aliasing procedure deals with extending the spectrum of the solution, i.e., the sizes of the discretization grid, of a factor 2 and then artificially imposing all the frequency in the extended region to be zero. In the case where one needs to numerically evaluate with a spectral method the modulus square of a given signal, say $|\psi|^2$ for example, this nonlinearity will be subjected to the filtering described in Algorithm 1.

Algorithm 1 : dealiasing

1: ψ
2: $\mathrm{FFT}[\psi]$
3: $\mathrm{FFT}[\psi] \leftarrow \mathrm{FFT}[\psi]_f$
4: $\mathrm{FFT}^{-1}[\mathrm{FFT}[\psi]_f]$
5: $|\psi|^2 \leftarrow \mathrm{FFT}^{-1}[\mathrm{FFT}[\psi]_f]^* \mathrm{FFT}^{-1}[\mathrm{FFT}[\psi]_f]$.

Here the subscript f, which stands for "filtered", denotes the zero-padding filter with the $\frac{4}{2}$-rule, FFT indicates the Fast-Fourier-Transform and the "star" notation is related to complex conjugation. In Figure 5.1 we show an example of dealiasing for the $|\psi|^2$ nonlinearity, for a simulation where the Fourier transform is repeated 100 times, by coming back to real space with an inverse one.

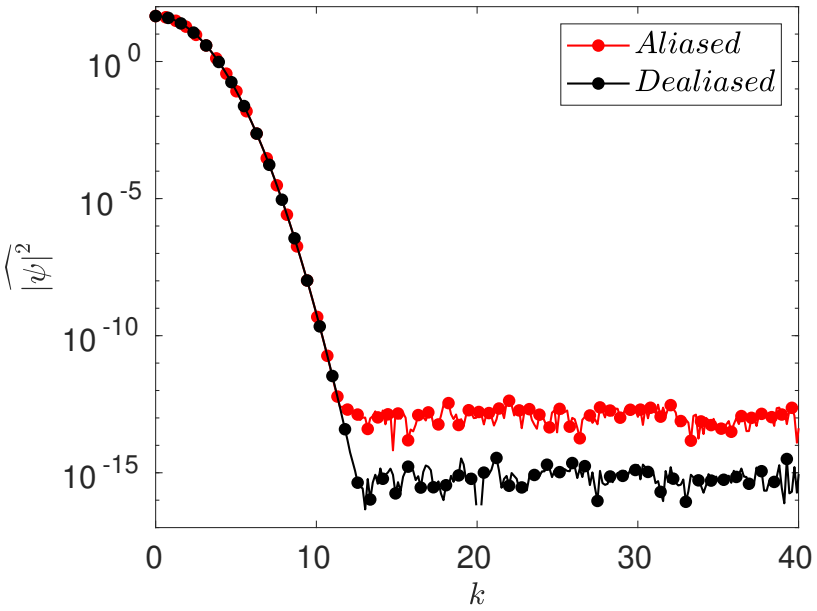

Figure 5.1 – Fourier transform of $|\psi|^2 = |e^{-\frac{x^2}{2}}|^2$ with the aliasing treatment (red line) and without it (black line). The aliasing treatment is the one described in Algorithm 1 with the $\frac{4}{2}$-rule. 10^{-16} is the machine precision.

5.1.4 *Resolution of Poisson's equation*

We now discuss in detail the pseudo-spectral Fourier method employed to obtain the solution ϕ of the Poisson equation,

$$\nabla^2 \phi(\mathbf{x}) = \rho(\mathbf{x}), \tag{5.10}$$

which appears in the Schrödinger–Newton system. Here, we assume that both the function ϕ and ρ are defined on an open set of $\mathbb{R}^d$, for some integer $d \geqslant 1$. In addition, we assume that the source ρ is well known.

When a pseudo-spectral Fourier method is employed, the Poisson equation in Fourier space becomes,

$$\widehat{\phi}(\mathbf{k}) = \widehat{G}(\mathbf{k})\widehat{\rho}(\mathbf{k}), \tag{5.11}$$

where the hat indicates Fourier transform of the underneath function, which is defined, in d dimensions, for the generic function $f(\mathbf{x})$ as

$$\widehat{f}(\mathbf{k}) = \int d^d x\, f(\mathbf{x}) \exp(i\mathbf{k}\cdot\mathbf{x}). \tag{5.12}$$

The function $\widehat{G}(\mathbf{k})$ is the Fourier transform of the Green function of the Laplace operator, defined as

$$\nabla^2 G(\mathbf{x}) = \delta(\mathbf{x}). \tag{5.13}$$

In general, boundary conditions must be taken into account when computing G. In (5.13) we considered the free-space Green function. Switching to Fourier space, (5.13) reads

$$\widehat{G}(\mathbf{k}) = -\frac{1}{|\mathbf{k}|^2}. \tag{5.14}$$

The original function is retrieved applying the inverse Fourier transform

$$f(\mathbf{x}) = \frac{1}{(2\pi)^d} \int d^d k\, \widehat{f}(\mathbf{k}) \exp(-i\mathbf{k}\cdot\mathbf{x}). \tag{5.15}$$

It is in principle simple to calculate the solution of the Poisson equation by calculating the inverse Fourier transform of (5.11). However, one has to be careful when the density source has not zero average, i.e.

$$M = \int d^d x\, \rho(\mathbf{x}) \neq 0. \tag{5.16}$$

This is due to the fact that $\widehat{\rho}(\mathbf{k} = 0) = M$ gives a numerical divergence for $\mathbf{k} = 0$ which needs to be treated carefully. It is a tricky task if in addition the system is subjected to open boundary conditions, i.e.,

$$\phi(r \to \infty) \sim MG(r), \tag{5.17}$$

where $r = |\mathbf{x}|$. Two main families of methods appear in the literature: the one due to Hockney [38] and the one due to James [107]. We focus on the former, providing a simple pedagogical example in $d = 1$; readers interested to James method can also consult [108] for a more compact description.

In Hockney's method the divergence is regularized in $\mathbf{k} = 0$ doubling, for each spatial dimension, the simulation box, and modifying the Green's function in an appropriate manner. In one spatial dimension (see [38] and [109] for a straightforward generalization to $d = 2$ and $d = 3$ respectively) the Green's function, for an original simulation box of size L centered in $x = L/2$, is modified as

$$G_H(x) = \begin{cases} G(x) & 0 \leqslant x \leqslant L \\ G(2L - x) & L < x \leqslant 2L \end{cases} \tag{5.18}$$

When this modified Green function is repeated periodically, with period $2L$, the correct potential is reproduced in the region $[0, L]$. The singularity in Fourier space at $k = 0$ is then artificially removed, imposing $\hat{G}(k) = 0$. The potential is calculated computing the discrete Fourier transform of (5.18) (using a fast Fourier transform technique). For a spatial discretization with N points, in one dimension $x_n = L\,n/N$, $k_m = 2\pi\,m/L$ (where n and m are integers) the Fourier coefficients are

$$\widehat{G}_m = \sum_{n=0}^{N-1} G_n \exp\left(i\frac{2\pi}{N}mn\right), \tag{5.19}$$

with $G_n = G(x_n)$ and $\widehat{G}_m = \widehat{G}(k_m)$. The inverse discrete Fourier transform is

$$G_n = \frac{1}{N}\sum_{n=0}^{N-1} \widehat{G}_m \exp\left(-i\frac{2\pi}{N}mn\right). \tag{5.20}$$

The potential ϕ_n is calculated performing the inverse discrete Fourier transform (5.20) of

$$\widehat{\phi}_m = \widehat{G}_m\,\widehat{\rho}_m, \tag{5.21}$$

where $\widehat{\phi}_m$ and $\widehat{\rho}_m$ are defined analogously to $\widehat{G}_m$. Note that this doubling procedure leads to a use of 2^d more points than using only the original simulation box. In Figure 5.2 this method is illustrated for a Gaussian density

$$\rho(x) = \frac{1}{\sqrt{2\pi\sigma^2}}\exp\left(-\frac{(x-x_0)^2}{2\sigma^2},\right) \tag{5.22}$$

whose potential is known analytically,

$$\phi(x) = \frac{1}{2}(x-x_0)\,\mathrm{erf}\left(\frac{x-x_0}{\sqrt{2}\sigma}\right) + \frac{\sigma}{\sqrt{2\pi}}\exp\left(-\frac{(x-x_0)^2}{2\sigma^2}\right), \tag{5.23}$$

with $L = 1$, $x_0 = 1/3$ and $\sigma = 0.04$. We observe that the correct potential is obtained in the interval $x \in [0, L]$.

5.2 NUMERICAL TIME RESOLUTION

Like the spatial integration, also the time integration can be performed with different numerical schemes. In general a temporal integrator can be either explicit or implicit. In the case of explicit methods, the information about the system at the present instant of time is used to evaluate the solution at a larger time. For implicit schemes on the other hand, the solution is evaluated considering the information about the system at a present instant of time and at the successive one. Albeit implicit methods usually allow more stability also when dealing with stiff equations, they are computationally more expensive, this is why in this thesis we consider only explicit methods.

For the the Schrödinger equation, there are two main families of methods that are usually employed to recover the numerical solution: the integrating factor technique, which is essentially a change of variable allowing the equation to be solved with an

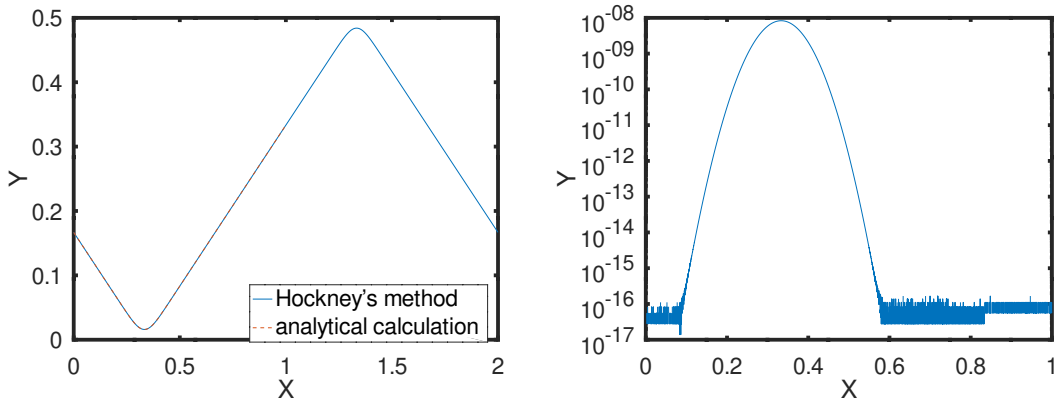

Figure 5.2 – Left: computation of $\phi(x)$ for the density (5.22) with the Hockney's method and with the analytical solution (5.23). Right: relative difference between numerical and analytical solution for a grid of $N = 10^5$ points. 10^{-16} is the machine precision

integrator that typically relies on some Runge-Kutta scheme, and Splitting methods. Both of those families can carry on the numerical integration either by using a fixed time-step, or with an adaptive one.

For each class of the aforementioned numerical methods, we start by describing how it can be derived in a general framework, and then we proceed by explaining how it can be applied in the particular case of the Schrödinger equation. We explain how one can switch from the fixed time-step scheme to the adaptive one and list the particular numerical algorithms we relied on.

5.2.1 *Integrating factor*

The integrating factor, or Lawson transform [27, 110], is a numerical method which allows to simplify the temporal resolution of a given differential equation exploiting a change of variable. It can be applied whenever one deals with a partial differential equation of the form

$$\partial_t \psi = f(\psi(\mathbf{r}, t), t). \tag{5.24}$$

The right hand side is split into linear and nonlinear parts, so the equation is rewritten

$$\partial_t \psi + \mathcal{L}\psi = \mathcal{N}(\mathbf{r}, t, \psi), \tag{5.25}$$

where $\mathcal{L}$ is an easily computable autonomous linear operator and $\mathcal{N} \overset{\text{def}}{=} F + \mathcal{L}\psi$ is the remaining (usually) nonlinear part. At the n-th time-step, with $t \in [t_n, t_{n+1}]$, considering the change of dependent variable

$$\phi \overset{\text{def}}{=} \exp[(t - t_n)\mathcal{L}]\psi, \tag{5.26}$$

one has

$$\psi_t = \exp[(t_n - t)\mathcal{L}](\phi_t - \mathcal{L}\phi) \tag{5.27}$$

so $\phi = \psi$ at $t = t_n$. The equation (5.25) is rewritten

$$\phi_t \;=\; \exp[\,(t - t_n)\,\mathcal{L}\,]\,\mathcal{N}. \tag{5.28}$$

The operator $\mathcal{L}$ being well chosen, the stiffness of (5.25) is considerably reduced and the equation (5.28) is (hopefully) well approximated by algebraic polynomials for $t \in [t_n; t_{n+1}]$. Thus, standard time-stepping methods, such as an adaptive Runge–Kutta method [111, 112], can be used to efficiently solve (5.28). In Figure 5.3 we show the advantages of the integrating factor technique, comparing the solution of (5.24) with a direct integration, namely in the form of (5.25) and without the exponential change of variable (5.28). As expected the integrating factor allows to improve remarkably the accuracy of the simulation, conserving the energy with zero machine precision and guaranteeing at the same time a much larger time-step, resulting in a smaller global computational time.

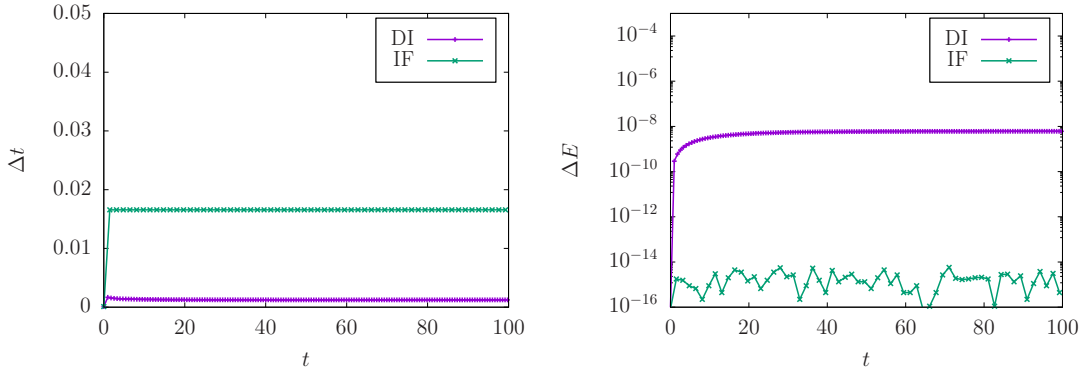

Figure 5.3 – Comparison of the solution of one-dimensional nonlinear Schrödinger, solved with the Dormand & Prince adaptive Runge-Kutta algorithm with a direct integration (DI), namely in the form of (5.25) and with the integrating factor (IF), i.e. (5.28). Left: time-step Δt as a function of time. Right: error on the conservation of energy ΔE as a function of time. The exact definition of ΔE, together with the details of the numerical simulation can be found in Section 7.2 and Section 7.3.1 respectively.

5.2.2 *Modified integrating factor*

If properly chosen, the integrating factor is able to reduce the stiffness of the equation, making the numerical integration more efficient. In addition, the magnitude of the nonlinear part of (5.28) also contributes to the efficiency of the numerical integration. Specifically, if $\mathcal{N}$ is zero, $\partial_t \phi = 0$ and the integrating factor technique is exact. Thus, the efficiency of the algorithm is expected to increase as the magnitude of $\mathcal{N}$ gets smaller, and subsequently the overall computational time should be reduced. For this reason, one possible strategy to improve the integrating factor is minimizing the magnitude of $\mathcal{N}$ at each time-step.

The modified integrating factor method [113] consists in subtracting from both sides of (5.25) a polynomial in time, $P(t)$,

$$\psi'(t) \;+\; \mathcal{L}\,\psi(t) \;-\; P(t) \;=\; \mathcal{N}(t, \psi(t)) - P(t). \tag{5.29}$$

To keep exactly the same numerical result compared to the standard integrating factor method, the degree of this polynomial must not be larger than the order of the numerical integrator employed. Performing the change of variable

$$\psi(t) = e^{-\mathcal{L}(t-t_0)}\phi(t) + \int_{t_0}^{t} e^{\mathcal{L}(t'-t)}P(t')\,dt', \tag{5.30}$$

equation (5.29) reads

$$\phi'(t) \;=\; e^{\mathcal{L}(t-t_0)}\,(\mathcal{N}(t,\psi(t)) - P(t)). \tag{5.31}$$

The time derivative of (5.30) being

$$\psi'(t) \;= -\mathcal{L}\,e^{-\mathcal{L}(t-t_0)}\phi(t) \;+\; e^{-\mathcal{L}(t-t_0)}\,\phi'(t) \tag{5.32}$$

$$-\int_{t_0}^{t} \mathcal{L}\,e^{\mathcal{L}(t'-t)}\,P(t')\,dt' \;+\; P(t). \tag{5.33}$$

We choose $P(t)$ such that the right hand side is zero at the initial time t_0, namely $\phi'(t_0) = 0$. Hence,

$$P(t) = \sum_{\ell=0}^{p} \frac{(t-t_0)^\ell}{\ell!}\left[\psi^{(\ell+1)}(t_0) + \mathcal{L}\psi^{(\ell)}(t_0)\right], \tag{5.34}$$

where p is the order of the method employed to numerically integrate the equation. Using (5.25) one can easily check that this form of $P(t)$ satisfies $P(t_0) = \mathcal{N}(t_0, \psi(t_0))$. The terms of the sum with $\ell > 0$ require to evaluate the higher order derivatives of ψ, which can be calculated using an approximation, like the Dense Output method [111].

In order to keep the computational cost of the method as low as possible, we choose to truncate the sum at the 0^{th} order, i.e.,

$$P(t) = \psi'(t_0) + \mathcal{L}\psi(t_0) = \mathcal{N}(t_0, \psi(t_0)). \tag{5.35}$$

Therefore the modified integrating factor method deals with solving (5.32) imposing (5.35) at the beginning of each time-iteration.

As discussed in Chapter 7, the improvement of this method compared to the standard integrating factor technique depends on the system. For example, as shown in Figure 5.4, the improvement is remarkable in the nonlinear Schrödinger equation case, and quite negligible for the Newton-Schrödinger equation.

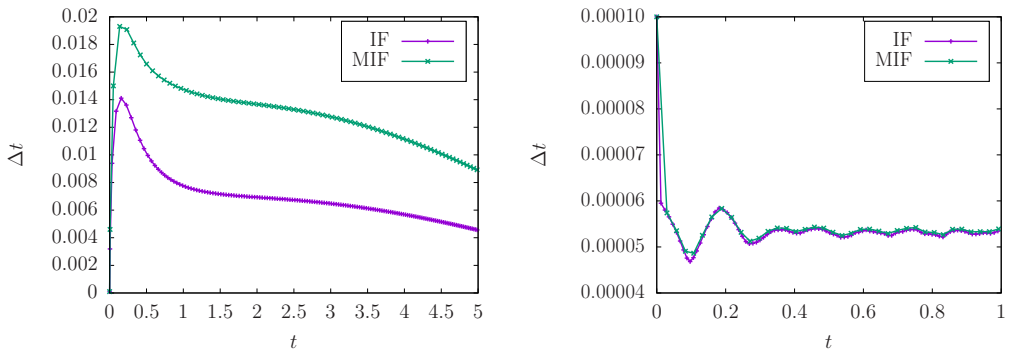

Figure 5.4 – Time-step as a function of time for the modified Integraing factor method compared with the standard integrating factor, applied to the two dimensional nonlinear Schrödinger (left) and Newton-Schrödinger equations (right) with the adaptive Dormand & Prince solver.

5.2.2.1 *Fixed time-steps explicit Runge–Kutta methods*

A temporal Runge–Kutta integrator of order q with standard time-stepping methods, is a numerical algorithm which allows to obtain the exact numerical solution of a differential equation for a polynomial whose order is smaller or equal to q. For an equation of the form

$$\partial_t \phi = f(\phi(\mathbf{r}, t), t). \tag{5.36}$$

the explicit Runge–Kutta schemes is denoted as

$$\phi_{\ell+1} = \phi_\ell + h \sum_{i=0}^{s} b_i k_i, \tag{5.37}$$

where s is the number of stages needed to evaluate the solution, h is the time step, ℓ indicates the number of iterations. The quantities k_i are defined as

$$\begin{aligned}
k_1 &= h f(t_\ell, \phi_\ell) \\
k_2 &= h f(t_\ell + c_2 h, \phi_\ell + h a_{2,1} k_1) \\
k_3 &= h f(t_\ell + c_3 h, \phi_\ell + h(a_{3,1} k_1 + a_{3,2} k_2)) \\
&\vdots \\
k_s &= h f(t_\ell + c_s h, \phi_\ell + h(a_{s,1} k_1 + a_{s,2} k_2 + \dots a_{s,s-1} k_{s-1})),
\end{aligned} \tag{5.38}$$

where the coefficients a_i, b_i and c_i are expressed by some known relations whose derivation can be found in [111]. This coefficient are usually arranged in the so-called Butcher tableau [111] attached to the method. The latter takes the form

$$\begin{array}{c|cccc}
0 & & & & \\
c_2 & a_{2,1} & & & \\
c_3 & a_{3,1} & a_{3,2} & & \\
\vdots & \vdots & \vdots & \ddots & \\
c_s & a_{s,1} & a_{s,2} & \dots & a_{s,s-1} \\
\hline
 & b_1 & b_2 & \dots & b_{s-1} \quad b_s.
\end{array}$$

For example, for a 4^{th} order Runge–Kutta method, the corresponding Butcher tableau is

$$\begin{array}{c|cccc} 0 & & & & \\ \frac{1}{2} & \frac{1}{2} & & & \\ \frac{1}{2} & 0 & \frac{1}{2} & & \\ 1 & 0 & 0 & 1 & \\ \hline & \frac{1}{6} & \frac{1}{3} & \frac{1}{3} & \frac{1}{6}. \end{array}$$

Thus one has

$$\phi_{\ell+1} = \phi_\ell + \frac{1}{6}(k_1 + 2k_2 + 2k_3 + k_4), \tag{5.39}$$

where the quantities k_i, $i \in \{1, 2, 3, 4\}$, are

$$\begin{aligned} k_1 &= h f(t_\ell, \phi_\ell) \\ k_2 &= h f(t_\ell + \frac{h}{2}, \phi_\ell + \frac{k_1}{2}) \\ k_3 &= h f(t_\ell + \frac{h}{2}, \phi_\ell + \frac{k_2}{2}) \\ k_4 &= h f(t_\ell + h, \phi_\ell + k_3). \end{aligned} \tag{5.40}$$

5.2.2.2 *Application to the Schrödinger equation*

We now show how to apply the integrating factor technique to the Schrödinger equation. We consider its adimensional form without loss of generality (see Appendix A), and we discuss the case of a general potential V,

$$i\partial_t\psi + \frac{1}{2}\nabla^2\psi - V\psi = 0. \tag{5.41}$$

The kinetic energy term, i.e. $\frac{1}{2}\nabla^2\psi$, represents the linear part, while, in the Schrödinger-Newton equation for example, the potential acts on the wavefunction as a nonlinear operator. Switching to Fourier space in position the equation becomes

$$i\frac{\partial\widehat{\psi}}{\partial t} - \frac{1}{2}k^2\widehat{\psi} - \widehat{V\psi} = 0. \tag{5.42}$$

Therefore the system is now in a form where the application of the integrating factor method is straightforward. Setting $\phi(\mathbf{k}, t) = \widehat{\psi}(\mathbf{k}, t)e^{i\frac{k^2}{2}(t-t_0)}$, one obtains

$$\frac{\partial\phi}{\partial t} = -ie^{i\frac{k^2}{2}(t-t_0)}\widehat{V\psi}. \tag{5.43}$$

5.2.2.3 *Adaptive Runge–Kutta integrators*

Adaptive Runge–Kutta methods [111, 112], also known as embedded Runge–Kutta methods, allow to numerically solve a differential equation with a time-step which is not fixed but changes in a smart way with the dynamics. For the time stepping, embedded Runge–Kutta methods estimate an error of quadrature comparing the results of two orders of the time integrator [111]. For a solver of order N with an embedded $(N-1)$-order scheme (hereafter schemes of orders $\{N, N-1\}$), at the n-th time step, the error Δ_n is

$$\Delta_n \stackrel{\text{def}}{=} \sqrt{\frac{1}{M}\sum_{m=0}^{M-1}\left(\frac{\left|\phi(k_m,t_n)-\widetilde{\phi}(k_m,t_n)\right|}{\mathrm{TOL}+\max\left(|\phi(k_m,t_n)|,\left|\widetilde{\phi}(k_m,t_n)\right|\right)\times \mathrm{TOL}}\right)^2}, \tag{5.44}$$

where M is the number of spatial nodes, $\phi(k_m,t_n)$ is the N-th order solution at the m-th Fourier mode, the "tilde" notation indicating the solution at order $N-1$, and TOL is the tolerance (parameter determining the precision of the time-integration). The time step h_n is accepted if the error Δ_n is smaller than than the tolerance TOL, otherwise h_n is reduced and this step is recomputed. h_n being accepted, the next time step h_{n+1} is obtained assuming the largest error equal to the tolerance. The latter is set as a free parameter at the beginning of the simulation and the smaller its value is, the better the accuracy gets; in contrast, the time-step decreases, slowing down the simulation. In Figure 5.5 we display this interplay between speed and accuracy when the tolerance is changed: it confirms how decreasing the tolerance improves the precision of the simulations, in particular zero machine precision is achieved for the error on the energy conservation with a tolerance of 10^{-9}. The computational cost of this small tolerance is however relatively small in this case: switching from $\mathrm{tol} = 10^{-7}$ to $\mathrm{tol} = 10^{-9}$, leads to an average time step which is only about 2.5 smaller

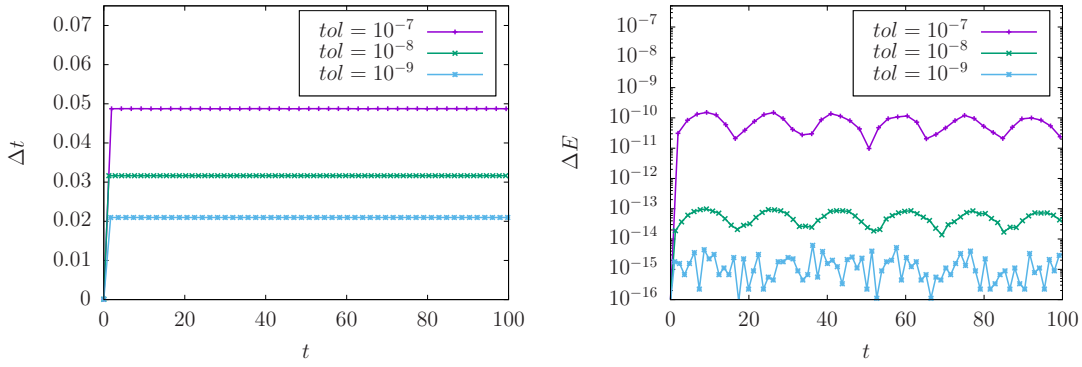

Figure 5.5 – Comparison of the solution of the one-dimensional nonlinear Schrödinger, solved with the Dormand & Prince adaptive Runge-Kutta algorithm with the integrating factor technique for different values of tolerances. Left plot: time-step Δt as a function of time. Right plot: error on the conservation of energy ΔE as a function of time.

As standard time-stepping methods, also adaptive Runge-Kutta methods are attached with a Butcher tableau representing all the coefficients which characterize the scheme. For an equation of the form

$$\partial_t \phi = f(\phi(\mathbf{r}, t), t), \tag{5.45}$$

the explicit embedded Runge–Kutta scheme is denoted as

$$\begin{aligned} \phi_{\ell+1} &= \phi_\ell + h \sum_{i=0}^{s} b_i k_i \\ \tilde{\phi}_{\ell+1} &= \phi_\ell + h \sum_{i=0}^{s} \tilde{b}_i k_i, \end{aligned} \tag{5.46}$$

where s is the number of stages needed to evaluate the solution, h is the time step, ℓ indicates the number of iterations and k_i are defined as

$$\begin{aligned} k_1 &= h f(t_\ell, \phi_\ell) \\ k_2 &= h f(t_\ell + c_2 h, \phi_\ell + h a_{2,1} k_1) \\ k_3 &= h f(t_\ell + c_3 h, \phi_\ell + h (a_{3,1} k_1 + a_{3,2} k_2)) \\ &\vdots \\ k_s &= h f(t_\ell + c_s h, \phi_\ell + h (a_{s,1} k_1 + a_{s,2} k_2 + \dots a_{s,s-1} k_{s-1})). \end{aligned} \tag{5.47}$$

The latter Butcher tableau encompassing the values of the coefficients a_i, b_i, $\tilde{b}_i$ and c_i in this case is

$$\begin{array}{c|cccc} 0 & & & & \\ c_2 & a_{2,1} & & & \\ c_3 & a_{3,1} & a_{3,2} & & \\ \vdots & \vdots & \vdots & \ddots & \\ c_s & a_{s,1} & a_{s,2} & \dots & a_{s,s-1} \\ \hline & b_1 & b_2 & \dots & b_{s-1} \quad b_s \\ & \tilde{b}_1 & \tilde{b}_2 & \dots & \tilde{b}_{s-1} \quad \tilde{b}_s. \end{array}$$

Popular integrators we use in this thesis are the Dormand & Prince 5(4) [114], Tsitouras 5(4) [115] and Fehlberg 7(8) [111].

PI STEP-CONTROL In order to avoid an excess of rejected time steps, we use the Proportional Integral (PI) Step Control [116], which chooses the optimal time step h_{n+1} as

$$h_{n+1} = h_n \Delta_n^{-b} \Delta_{n-1}^{c}, \tag{5.48}$$

where $b = 0.7/p$, $c = 0.4/p$, p being the order of the chosen integrator [117]. Interested readers should refer to [116] for details on this classical procedure.

DORMAND & PRINCE The Dormand & Prince method [114], is a 5^{th} order solver, embedded with a 4^{th} order scheme. The corresponding Butcher tableau is

$$
\begin{array}{c|ccccccc}
0 & & & & & & & \\
\frac{1}{5} & \frac{1}{5} & & & & & & \\
\frac{3}{10} & \frac{3}{40} & \frac{9}{40} & & & & & \\
\frac{4}{5} & \frac{44}{45} & -\frac{56}{15} & \frac{32}{9} & & & & \\
\frac{8}{9} & \frac{19372}{6561} & -\frac{25360}{2187} & \frac{64448}{6561} & -\frac{212}{729} & & & \\
1 & \frac{9017}{3168} & -\frac{355}{33} & \frac{46732}{5247} & \frac{49}{176} & -\frac{5103}{18656} & & \\
1 & \frac{35}{384} & \frac{500}{1113} & \frac{500}{1113} & \frac{125}{192} & -\frac{2187}{6784} & \frac{11}{84} & \\
\hline
 & \frac{35}{384} & 0 & \frac{500}{1113} & \frac{125}{192} & -\frac{2187}{6784} & \frac{11}{84} & 0 \\
 & \frac{5179}{57600} & 0 & \frac{7571}{16695} & \frac{393}{640} & -\frac{92097}{339200} & \frac{187}{2100} & \frac{1}{40}.
\end{array}
$$

Thus the solutions are

$$
\begin{aligned}
\phi_{l+1} &= \phi_l + \frac{35}{384}\,k_1 + \frac{500}{1113}\,k_3 + \frac{125}{192}\,k_4 - \frac{2187}{6784}\,k_5 \\
&\quad + \frac{11}{84}\,k_6 \\
\tilde{\phi}_{l+1} &= \phi_l + \frac{5179}{57600}\,k_1 + \frac{7571}{16695}\,k_3 + \frac{393}{640}\,k_4 - \frac{92097}{339200}\,k_5 \\
&\quad + \frac{187}{2100}\,k_6 + \frac{1}{40}\,k_7,
\end{aligned}
\tag{5.49}
$$

where

$$
\begin{aligned}
k_1 &= h\,f(t_l,\, \phi_l) \\
k_2 &= h\,f(t_l + \frac{1}{5}\,h,\, \phi_l + \frac{1}{5}\,k_1) \\
k_3 &= h\,f(t_l + \frac{3}{10}\,h,\, \phi_l + \frac{3}{40}\,k_1 + \frac{9}{40}\,k_2) \\
k_4 &= h\,f(t_l + \frac{4}{5}\,h,\, \phi_l + \frac{44}{45}\,k_1 - \frac{56}{15}\,k_2 + \frac{32}{9}\,k_3) \\
k_5 &= h\,f(t_l + \frac{8}{9}\,h,\, \phi_l + \frac{19372}{6561}\,k_1 - \frac{25360}{2187}\,k_2 + \frac{64448}{6561}\,k_3 - \frac{212}{729}\,k_4) \\
k_6 &= h\,f(t_l + h,\, \phi_l + \frac{9017}{3168}\,k_1 - \frac{355}{33}\,k_2 + \frac{46732}{5247}\,k_3 + \frac{49}{176}\,k_4 - \frac{5103}{18656}\,k_5) \\
k_7 &= h\,f(t_l + h,\, \phi_l + \frac{35}{384}\,k_1 + \frac{500}{1113}\,k_3 + \frac{125}{192}\,k_4 - \frac{2187}{6784}\,k_5 + \frac{11}{84}\,k_6).
\end{aligned}
\tag{5.50}
$$

TSITOURAS The Tsitouras method [115], is another 5^{th} order solver, embedded with a 4^{th} order scheme. Even though this algorithm is of the same order of the Dormand & Prince one, depending on the equation considered it can provide a greater computational speed by keeping the same accuracy compared with the other 5(4) method we described. The corresponding coefficients of Butcher tableau are listed in Appendix B.

FEHLBERG The Fehlberg method [111], is a 7^{th} order solver, embedded with a 8^{th} order scheme. We employ this high order scheme to establish reference simulation which is used for further discussions and comparisons on the accuracy of the other methods described so far. The corresponding Butcher tableau is

0													
$\frac{2}{27}$	$\frac{2}{27}$												
$\frac{1}{9}$	$\frac{1}{36}$	$\frac{1}{12}$											
$\frac{1}{6}$	$\frac{1}{24}$	0	$\frac{1}{8}$										
$\frac{5}{12}$	$\frac{5}{12}$	0	$-\frac{25}{16}$	$\frac{25}{16}$									
$\frac{1}{2}$	$\frac{1}{20}$	0	0	$\frac{1}{4}$	$\frac{1}{5}$								
$\frac{5}{6}$	$-\frac{25}{108}$	0	0	$\frac{125}{108}$	$-\frac{65}{27}$	$\frac{125}{54}$							
$\frac{1}{6}$	$\frac{31}{300}$	0	0	0	$\frac{61}{225}$	$-\frac{2}{9}$	$\frac{13}{900}$						
$\frac{2}{3}$	2	0	0	$-\frac{53}{6}$	$\frac{704}{45}$	$\frac{-107}{9}$	$\frac{67}{90}$	3					
$\frac{1}{3}$	$-\frac{91}{108}$	0	0	$\frac{23}{108}$	$\frac{-976}{135}$	$\frac{311}{54}$	$-\frac{19}{60}$	$\frac{17}{6}$	$-\frac{1}{12}$				
1	$\frac{2383}{4100}$	0	0	$-\frac{341}{164}$	$\frac{4496}{1025}$	$-\frac{301}{82}$	$\frac{2133}{4100}$	$\frac{45}{82}$	$\frac{45}{164}$	$\frac{18}{41}$			
0	$\frac{3}{205}$	0	0	0	0	$-\frac{6}{41}$	$-\frac{3}{205}$	$-\frac{3}{41}$	$\frac{3}{41}$	$\frac{6}{41}$	0		
1	$-\frac{1777}{4100}$	0	0	$-\frac{341}{164}$	$\frac{4496}{1025}$	$-\frac{289}{82}$	$\frac{2193}{4100}$	$\frac{51}{82}$	$\frac{33}{164}$	$\frac{12}{41}$	0	1	
	$\frac{41}{840}$	0	0	0	0	$\frac{34}{105}$	$\frac{9}{35}$	$\frac{9}{35}$	$\frac{9}{280}$	$\frac{9}{280}$	$\frac{41}{840}$	0	0
	0	0	0	0	0	$\frac{34}{105}$	$\frac{9}{35}$	$\frac{9}{35}$	$\frac{9}{280}$	$\frac{9}{280}$	0	$\frac{41}{840}$	$\frac{41}{840}$

5.2.3 *Splitting methods*

The Split-Step method [28] can be applied to any differential equation of the form

$$\frac{\partial \psi(\mathbf{r}, t)}{\partial t} = \widehat{D}\psi(\mathbf{r}, t), \tag{5.51}$$

where $\widehat{D}$ is a differential operator, which can be split in two terms

$$\widehat{D} = \widehat{F} + \widehat{R}, \tag{5.52}$$

in such a way that the differential equations

$$\begin{aligned} \frac{\partial \psi_F(\mathbf{r},t)}{\partial t} &= \widehat{F}\psi_F(\mathbf{r},t) \\ \frac{\partial \psi_R(\mathbf{r},t)}{\partial t} &= \widehat{R}\psi_R(\mathbf{r},t), \end{aligned} \tag{5.53}$$

can be easily solved, as long as $\widehat{D}$ does not depend on time and $\widehat{D}\psi(\mathbf{r},t)$ is continuous with continuous derivatives. In this case, one formally has

$$\begin{aligned} \psi_F(\mathbf{r},t) &= e^{\widehat{F}t}\psi(\mathbf{r},0) \\ \psi_R(\mathbf{r},t) &= e^{\widehat{R}t}\psi(\mathbf{r},0), \end{aligned} \tag{5.54}$$

where the exponential of an operator must be interpreted as a series

$$e^{\widehat{D}t} = \sum_{n=1}^{\infty} t^n \frac{\widehat{D}^n}{n!}. \tag{5.55}$$

The Split-Step method, applied in a time interval $[0,t]$, deals with subdividing the interval in N small steps of size h and applying in each step the two operators $\widehat{F}$ and $\widehat{R}$ separately. For example, a simple splitting method can be derived from (5.55), using

$$e^{\widehat{D}t} = e^{(\widehat{F}+\widehat{R})t} = e^{\widehat{F}t}e^{\widehat{R}t} + \mathcal{O}(t^2). \tag{5.56}$$

and then applying this to the solution of the equation

$$\begin{aligned} \psi(\mathbf{r},t_{n+1}) &= e^{\widehat{F}h}e^{\widehat{R}h}\psi(\mathbf{r},t_n) \qquad n \in \{0,1,2,...,N-1\}, \\ t_{n+1} &= t_n + h_n, \qquad t_0 = 0, \qquad t_{N-1} = t. \end{aligned} \tag{5.57}$$

5.2.3.1 *Local Truncation Error: Symmetric 2^{nd} order Split-Step example*

The error of this method is related to the $\mathcal{O}(t^2)$ term in (5.56), also known as local truncation error. The latter is zero in the case where $\widehat{F}$ and $\widehat{R}$ commute, i.e.

$$[\widehat{F},\widehat{R}] = \widehat{F}\widehat{R} - \widehat{R}\widehat{F} = 0$$

which, as discussed in the next paragraph, is in general not true in the Schrödinger equation case. It is possible though, to reduce the local truncation error, considering a more accurate splitting

$$e^{\widehat{D}t} = e^{\frac{\widehat{F}}{2}t}e^{\widehat{R}t}e^{\frac{\widehat{F}}{2}t} + \mathcal{O}(t^3) = e^{\frac{\widehat{R}}{2}t}e^{\widehat{F}t}e^{\frac{\widehat{R}}{2}t} + \mathcal{O}(t^3) \tag{5.58}$$

as can be easily proved considering the series in (5.55) up to second order. This is called symmetric 2^{nd} order Split-Step method and follows the ideas of other similar algorithms as the Leap-Frog one, often employed in molecular dynamics simulations [118]. Moreover, when many steps are applied successively, the algorithm efficiency can be increased by merging two consecutive iterations, yielding

$$\psi(\mathbf{r},t_{k+1}) = e^{\frac{\widehat{F}}{2}h}e^{\widehat{R}h}e^{\widehat{F}h}e^{\widehat{R}h}e^{\frac{\widehat{F}}{2}h}\psi(\mathbf{r},t_k). \tag{5.59}$$

5.2.3.2 *Adaptation to the Schrödinger equation*

In the particular case of the Schrödinger equation, the operator $\widehat{D}$ coincides with the Hamiltonian $\widehat{H} = \widehat{K} + \widehat{V}$, which is split in the kinetic energy term $\widehat{K}$ and the potential one $\widehat{V}$. The assumptions according to which $\widehat{D}\psi(\mathbf{r}, t) \in C^1$ is , in the Schrödinger equation case, true, as it models a physical system and therefore the wave function together with its derivatives have to be continuous.

In the case where $\widehat{D}$ is time dependent, the solution is more complicated. However, as discussed in the next paragraph, such operator is usually evaluated over small steps where it can be assumed almost constant. In order to analyse in detail how the method works, let us consider the Schrödinger equation for a general Hamiltonian,

$$i\partial_t \psi = \widehat{H}\psi. \tag{5.60}$$

The solution of (5.60) is given by

$$\psi(\mathbf{r}, t) = e^{-i\widehat{H}(t-t_0)}\psi(\mathbf{r}, t_0). \tag{5.61}$$

Except for very few cases where an analytical solution is known, it is not possible to apply the operator $e^{-i\widehat{H}(t-t_0)}$ to $\psi(\mathbf{r}, t_0)$. Moreover, since $\widehat{K}$ and $\widehat{V}$ do not commute, one has

$$e^{-i\widehat{H}(t-t_0)} \neq e^{-i\widehat{K}(t-t_0)}e^{-i\widehat{V}(t-t_0)}, \tag{5.62}$$

so it is not possible to simply apply the kinetic and the potential energy operators separately. Nevertheless it is possible to approximate at a given order the quantity $e^{-i\widehat{H}(t-t_0)}$ as a product of a sequence of the potential and the kinetic term separated with appropriated coefficients. For example up to order 2 in $(t - t_0)$ one has

$$e^{-i\widehat{H}(t-t_0)} = e^{-i\widehat{K}(\frac{(t-t_0)}{2}}e^{-i\widehat{V}(t-t_0)}e^{-iK\frac{(t-t_0)}{2}} + O\left((t-t_0)^3\right), \tag{5.63}$$

which is also known as Trotter Splitting formula [119] and corresponds to the Split-Step order 2 integration method. At higher order the problem, also known as Suzuki-Trotter expansion [120], is in general more complicated and there exist more than one solution, which can be determined with the Baker – Campbell – Hausdorff formula [119]. In this thesis we consider the Split-Step order 2 (SS2), order 4 (SS4) and order 6 (SS6), together with and adaptive scheme, all these algorithms are described in Appendix B.

SCHRÖDINGER–NEWTON WITH TIME-DEPENDENT POTENTIAL In order to apply this algorithm to the case of a time-dependent potential one can still identify $\widehat{D}$ with the Hamiltonian of the system, $\widehat{F}$ with the kinetic energy and $\widehat{R}$ with the potential energy operators. Since the latter is time-dependent, instead of (5.54) one can write

$$\psi(\mathbf{r}, t) = e^{\int_0^t dt' \widehat{R}(t')}\psi(\mathbf{r}, 0). \tag{5.64}$$

However, if a time step small enough compared with the variation of the potential is chosen, the integral can reasonably be approximated as a product between the integrand and the step, thus (5.54) remains valid. In this way one can evolve the

wavefunction according to the usual quantum time evolution operator $\widehat{U}(t, t_0 = 0) = e^{-i\widehat{H}t}$, considering the kinetic $\widehat{K}$ and the potential $\widehat{V}$ contribute in the Hamiltonian $\widehat{H}$ separately. The advantage of this is that the $\widehat{K}$ and $\widehat{V}$ operators are local, respectively in Fourier and in real space, thus

$$\begin{aligned} e^{-i\widehat{K}h}\psi &= \mathcal{F}^{-1}[e^{-iKh}\widetilde{\psi}(\mathbf{k}, t)] = \mathcal{F}^{-1}[e^{-i\frac{k^2}{2}h}\widetilde{\psi}(\mathbf{k}, t)] \\ e^{-i\widehat{V}h}\psi &= e^{-iVh}\psi(\mathbf{r}, t) \end{aligned} \tag{5.65}$$

being $\widetilde{\psi}(\mathbf{k}, t)$ the Fourier transform in $\mathbf{r}$ of ψ, k^2 the modulus square of the wave vector, V the potential and $\mathcal{F}^{-1}$ denoting the inverse Fourier transform.

5.2.3.3 *Adaptive time-step*

It is also possible to design an adaptive time-step scheme with this method. Here, we use and adaptive embedded splitting pair [121] of order 4(3). It is characterized by a fourth order splitting solver derived by Blanes and Moan [122] embedded with third order scheme constructed by Thalhammer and Abhau [121, 123]. In the same spirit of adaptive Runge-Kutta schemes, the step selection consists in re-modulating the time-step as a function of the difference between the solution at the two consecutive orders and the tolerance TOL

$$h_{opt} = h_n \min\left\{\alpha\left(\frac{tol}{\Delta_n}\right)^{\frac{1}{4}}, \beta\right\} \tag{5.66}$$

where we set $\alpha = 0.9$, $\beta = 3$ and

$$\Delta_n = \sqrt{\frac{\sum_{i=1}^{N}\left|\psi(\mathbf{x}_i, t_n) - \widetilde{\psi}(\mathbf{x}_i, t_n)\right|^2}{\sum_{j=1}^{N}\left|\psi(\mathbf{x}_j, t_n)\right|^2}}. \tag{5.67}$$

In this case ψ denotes the solution at the 4^{th} order and $\widetilde{\psi}$ at the 3^{rd} one. Hereafter will denote this algorithm as "SSa". The pseudo-code and the coefficients of this algorithm are shown in Appendix B.

6

NEW NUMERICAL METHOD

In this chapter, we introduce a new numerical method to integrate Schrödinger-like equations, based on an optimization of the integrating factor technique. As explained in Section 5.2.2.2, for the Schrödinger equation,

$$i\,\partial_t\,\psi \;+\; \tfrac{1}{2}\,\nabla^2\psi \;-\; V\,\psi \;=\; 0, \tag{6.1}$$

the integrating factor, allows to analytically integrate the linear part, i.e. $\frac{1}{2}\,\nabla^2\psi$. In this way, the stiffness of the equation is reduced, thus making the numerical integration more efficient. This is done performing the change of variable $\phi(\mathbf{k},\,t) = \widehat{\psi}(\mathbf{k},\,t)e^{i\,\frac{k^2}{2}\,(t-t_0)}$, which yields

$$\partial_t\,\phi \;=\; -i\,e^{i\,\frac{k^2}{2}\,(t-t_0)}\,\widehat{V\psi}. \tag{6.2}$$

The new method we present here, is based on a the same principles of the modified integrating factor, explained in Section 5.2.2, namely the fact that the efficiency of the algorithm is expected to further increase as the magnitude of the nonlinear term, $\mathcal{N} = -i\,e^{i\,\frac{k^2}{2}\,(t-t_0)}\,\widehat{V\psi}$, gets smaller. However the approach used here is very different, as it exploits a gauge invariance of the Schrödinger equation. Indeed, if at a given time t, ψ is a solution of (6.1), then $\Psi \overset{\text{def}}{=} \psi\,e^{-i\,\mathcal{C}\,t}$ is a solution of

$$i\,\partial_t\,\Psi \;+\; \tfrac{1}{2}\,\nabla^2\Psi \;-\; (V+\mathcal{C})\;\Psi \;=\; 0, \tag{6.3}$$

as one can easily verify. Thus, at each time-step, adding a constant $\mathcal{C}_n$ to V in (6.1), modifies the solution as

$$\psi(t_n) \;\to\; \psi(t_n)\,e^{-i\varphi}, \qquad \varphi \;\overset{\text{def}}{=}\; \sum_{j=1}^{n} \mathcal{C}_j\,h_j, \tag{6.4}$$

where $h_j \overset{\text{def}}{=} t_{j+1} - t_j$ is the j-th time-step. Of course, at the end of the computations, the operation (6.4) can be easily reverted if the original phase is relevant.

In this chapter, we derive some analytic formulas giving an optimal $\mathcal{C}_n$ in order to maximise the time-step, i.e., to minimize the overall computational time of the numerical resolution. Using this procedure, we observed up to a five-fold speed increase (the overall computational time is divided by about five) compared to taking $\mathcal{C}_n = 0$. Of course, the speed-up varies depending on the initial condition, of the (spatial and temporal) numerical schemes and on the choice of gauge corresponding to $\mathcal{C}_n = 0$. Two strategies are presented. In Section 6.1, a first natural approach to derive a suitable $\mathcal{C}_n$ is based on the analytical structure of the equation and it is independent of the numerical algorithm employed for its resolution. More precisely, $\mathcal{C}_n$ is obtained minimizing a norm of the right-hand side of the equation (5.25). This provides an easy manner to obtain a formula that is moreover computationally cheap. This expression is however only near optimal, so a better expression is subsequently

derived. Considering both the equations and the numerical algorithms, a second optimal expression for $\mathcal{C}_n$ is derived in Section 6.2. This approach consists in minimizing exactly the numerical error and thus explicitly dependents on the numerical scheme. This provides a more accurate, but computationally expansive, solution. Finally, the advances of these special choices are illustrated numerically in Section 6.3.

6.1 NEAR OPTIMAL $\mathcal{C}_n$

As mentioned above, if properly chosen, the integrating factor is able to reduce the stiffness of the equation, making the numerical integration more efficient. In addition, the magnitude of the nonlinear part of (5.28) also contributes to the efficiency of the numerical integration. Specifically, if $\mathcal{N}$ is zero, $\partial_t \phi = 0$ and the integrating factor technique is exact. Thus, the efficiency of the algorithm is expected to increase as the magnitude of $\mathcal{N}$ gets smaller, and subsequently the overall computational time should be reduced. Here, we show how to choose the arbitrary constant $\mathcal{C}_n$ in order to reduce the magnitude of the nonlinear part $\mathcal{N}$. In the case of the Schrödinger equation, one has

$$\mathcal{N}(\mathbf{k}, t; \phi; \mathcal{C}_n) \;=\; -i \exp\left[\tfrac{i}{2} k^2 (t - t_n)\right] \mathcal{F}\{(V + \mathcal{C}_n)\, \psi\}, \tag{6.5}$$

where $\mathcal{F}$ denotes the Fourier transform and

$$\psi(\mathbf{x}, t) = \mathcal{F}^{-1}\{\exp\left[-\tfrac{i}{2} k^2 (t - t_n)\right] \phi(\mathbf{k}, t)\}. \tag{6.6}$$

A natural strategy is to minimise the L_2-norm, namely

$$\mathcal{G}_n(\mathcal{C}_n) \stackrel{\text{def}}{=} \frac{1}{M} \sum_{m=-[M/2]}^{[M/2]-1} |\mathcal{N}(\mathbf{k}_m, t_n; \phi; \mathcal{C}_n)|^2, \tag{6.7}$$

where M is the number of spatial modes, square brackets denote the integer part and $\mathbf{k}_m$ is the m-th Fourier mode. The explicit expression of $\mathcal{G}_n$ can be found exploiting the definition of the discrete Fourier transform. For simplicity, we do the calculations in one dimension (1D) without loss of generality, since the final result is independent of the spatial dimension d. From Parseval theorem, one obtains

$$\mathcal{G}_n(\mathcal{C}_n) \;=\; \sum_{\ell=-[M/2]}^{[M/2]-1} (V_\ell + \mathcal{C}_n)^2 \, |\psi_\ell|^2, \tag{6.8}$$

where $\psi_\ell \stackrel{\text{def}}{=} \psi(\mathbf{x}_\ell)$ and $V_\ell \stackrel{\text{def}}{=} V(\mathbf{x}_\ell)$ at time t_n. Since the function $\mathcal{G}_n(\mathcal{C}_n)$ is a second-order polynomial in $\mathcal{C}_n$, it admits an unique minimum, which is obtained from the equation $dG_n(\mathcal{C}_n)/d\mathcal{C}_n = 0$, yielding

$$\mathcal{C}_n \;=\; -\left(\sum_{\ell=-[M/2]}^{[M/2]-1} V_\ell \, |\psi_\ell|^2\right) \Bigg/ \left(\sum_{\ell=-[M/2]}^{[M/2]-1} |\psi_\ell|^2\right) \stackrel{\text{def}}{=} \tilde{\mathcal{C}}_n. \tag{6.9}$$

Therefore, at each time step n, $\tilde{\mathcal{C}}_n$, which is the value of $\mathcal{C}_n$ minimizing the L_2-norm of $\mathcal{N}$, is obtained from (6.9). We show below that even though this approach is not unique (i.e., different norms could be considered), the provided solution is quite advantageous compared to others, being computationally cheap and independent on the order of the numerical scheme.

6.2 OPTIMAL $\mathcal{C}_n$

We show here another way to choose the arbitrary constant $\mathcal{C}_n$ in order to improve the algorithm efficiency and reduce the overall computational time. This approach is based on the principles of the adaptive time-step procedure, where, as explained in Section 5.2.2.3, at each time step n, an error Δ_n between two approximated solutions of different orders is estimated. Since the smaller this quantity the larger the time-step, minimizing Δ_n allows to choose a larger time-step, speeding-up the numerical integration and keeping roughly the same numerical error. More specifically, the error Δ_n depends on the arbitrary constant $\mathcal{C}_n$, hence the minimization can be performed (see below) choosing an appropriate $\mathcal{C}_n$. Although the determination of $\mathcal{C}_n$ can be formally presented for any embedded Runge–Kutta schemes, this results in very cumbersome calculations with little insights. Thus, for brevity and clarity, we illustrate the method with the Heun method (that is a second-order Runge–Kutta method with an embedded first-order explicit Euler scheme for the time stepping [124]). We then sketch-out how this procedure can be implemented for generic embedded Runge–Kutta methods.

6.2.1 *Optimum time step*

Since the constant $\mathcal{C}_n$ can be chosen freely, we seek for the value of $\mathcal{C}_n$ providing the largest time-step. This can be done considering the step-control formula introduced in 5.2.2.3, thus maximizing the right-hand side of

$$h_{n+1} \;=\; h_n\,\Delta_n^{-b}\,\Delta_{n-1}^{c}. \tag{6.10}$$

Since h_n and Δ_{n-1} are determined at the previous time-step, only Δ_n in (6.10) depends on $\mathcal{C}_n$. Thus, in order to maximize h_{n+1}, Δ_n must be minimized, i.e., one must solve $d\Delta_n/d\mathcal{C}_n = 0$. This derivation being characterized by cumbersome algebra for general embedded Runge–Kutta schemes, we illustrate the case of the Heun algorithm (that is a second-order Runge–Kutta method with an embedded first-order explicit Euler scheme for the time stepping [124]), the principle being the same for higher order integrators. Also for simplicity, we give the calculations in one dimension (1D) without loss of generality, since the final result is independent of the spatial dimension.

6.2.1.1 *Optimum $\mathcal{C}_n$ for Heun's method*

Heun's method consists, here, in solving the initial value problem (for $t \geqslant t_n$)

$$i\,\partial_t\,\phi \;=\; f(\mathbf{k},t;\phi;\mathcal{C}_n) \;=\; -i\,\exp\!\left[\,\tfrac{i}{2}\,k^2\,(t-t_n)\,\right]\mathcal{F}\{\,(V+\mathcal{C}_n)\,\psi\,\}, \tag{6.11}$$

and

$$\phi(\mathbf{k},t) \;\stackrel{\text{def}}{=}\; \exp\!\left[\,\tfrac{i}{2}\,k^2\,(t-t_n)\,\right]\mathcal{F}\{\psi(\mathbf{x},t)\}. \tag{6.12}$$

Hereafter, for brevity, we denote

$$\begin{aligned}
\phi_n \;&=\; \phi_n(\mathbf{k}) \;\stackrel{\text{def}}{=}\; \phi(\mathbf{k},t_n), \\
\psi_n \;&=\; \psi_n(\mathbf{x}) \stackrel{\text{def}}{=}\; \psi(\mathbf{x},t_n), \\
V_n \;&=\; V_n(\mathbf{x}) \stackrel{\text{def}}{=} V(\mathbf{x},t_n).
\end{aligned} \tag{6.13}$$

At time $t = t_{n+1}$, the first- and second-order (in h_n) approximations of ϕ, respectively $\widetilde{\phi}_{n+1}$ and ϕ_{n+1}, are

$$\begin{aligned}
\widetilde{\phi}_{n+1} &= \phi_n + h_n f(\mathbf{k}, t_n; \phi_n; \mathcal{C}_n), && (6.14)\\
\phi_{n+1} &= \phi_n + \tfrac{1}{2} h_n [f(\mathbf{k}, t_n; \phi_n; \mathcal{C}_n) \\
&\quad f(\mathbf{k}, t_n + h_n; \phi_n + h_n f(\mathbf{k}, t_n; \phi_n; \mathcal{C}_n); \mathcal{C}_n)]. && (6.15)
\end{aligned}$$

The next time-step h_{n+1} is chosen using equation (6.10). For our equation, the difference between the first- and second-order approximations $\Delta\phi_{n+1} \stackrel{\text{def}}{=} \left|\phi_{n+1} - \widetilde{\phi}_{n+1}\right|$ is such that

$$\begin{aligned}
(\Delta\phi_{n+1})^2 &= \tfrac{1}{4} h_n^2 \, | f(\mathbf{k}, t_n; \phi_n; \mathcal{C}_n) \\
&\quad - f(\mathbf{k}, t_n + h_n; \phi_n + h_n f(\mathbf{k}, t_n; \phi_n; \mathcal{C}_n); \mathcal{C}_n) \, |^2 \\
&= \tfrac{1}{4} h_n^2 \Big| f(\mathbf{k}, t_n; \phi_n; \mathcal{C}_n) + i e^{i k^2 h_n/2} \times \\
&\quad \mathcal{F}\left\{ (V_{n+1} + \mathcal{C}_n) \mathcal{F}^{-1}\left\{ e^{-i k^2 h_n/2} \left(\phi_n + h_n f(\mathbf{k}, t_n; \phi_n; \mathcal{C}_n)\right)\right\}\right\} \Big|^2 , \qquad (6.16)
\end{aligned}$$

where $V_{n+1} = V(\mathbf{x}, t_n + h_n)$. We note that the absolute value in (6.16) is of first-order in h_n, as one can easily check with a Taylor expansion around $h_n = 0$, so $(\Delta\phi_{n+1})^2 = O(h_n^4)$. More precisely, after some elementary algebra, one finds

$$\begin{aligned}
(\Delta\phi_{n+1})^2 &= \tfrac{1}{4} h_n^4 \, \Big| \mathcal{F}\left\{ (V_n + \mathcal{C}_n)^2 \psi_n \right\} + i \mathcal{F}\{ \partial_t V_n \, \psi_n \} \qquad (6.17)\\
&\quad + \mathcal{F}\{ \partial_x V_n \, \partial_x \psi_n \} + \tfrac{1}{2} \mathcal{F}\{ \partial_{xx} V_n \, \psi_n \} \Big|^2 + O(h_n^5) ,
\end{aligned}$$

which, defining

$$\begin{aligned}
\alpha(\mathbf{x}, t; \mathcal{C}_n) &\stackrel{\text{def}}{=} (V_n + \mathcal{C}_n)^2 \psi_n , \\
\beta(\mathbf{x}, t) &\stackrel{\text{def}}{=} i \, \partial_t V_n \, \psi_n + \partial_x V_n \, \partial_x \psi_n + \tfrac{1}{2} \partial_{xx} V_n \, \psi_n , \qquad (6.18)
\end{aligned}$$

can be rewritten as

$$(\Delta\phi_{n+1})^2 = \tfrac{1}{4} h_n^4 \, |\mathcal{F}\{\alpha(\mathcal{C}_n) + \beta\}|^2 + O(h_n^5) . \qquad (6.19)$$

Introducing the mean quadratic error

$$E_n(\mathcal{C}_n) \stackrel{\text{def}}{=} \frac{1}{M} \sum_{m=-[M/2]}^{[M/2]-1} \Delta\phi_{n+1}^2(k_m, t_n; \mathcal{C}_n), \qquad (6.20)$$

substituting (6.19) into (6.20) and exploiting the definition of the discrete Fourier transform, one obtains (using Parseval theorem)

$$\begin{aligned}
E_n(\mathcal{C}_n) &= \frac{1}{M} \sum_{m=-[M/2]}^{[M/2]-1} \left| \sum_{\ell=-[M/2]}^{[M/2]-1} e^{-2i\pi m \ell / M} (\alpha_\ell(\mathcal{C}_n) + \beta_\ell) \right|^2 \times \\
&\quad \tfrac{1}{4} h_n^4 + O(h_n^5) \\
&= \sum_{\ell=-[M/2]}^{[M/2]-1} |\alpha_\ell(\mathcal{C}_n) + \beta_\ell|^2 \, \tfrac{1}{4} h_n^4 + O(h_n^5) . \qquad (6.21)
\end{aligned}$$

The minimum of $E_n(\mathcal{C}_n)$, obtained from the equation $dE_n(\mathcal{C}_n)/d\mathcal{C}_n = 0$, is such that

$$\sum_{\ell=-[M/2]}^{[M/2]-1} \frac{d\,|\alpha_\ell(\mathcal{C}_n)|^2}{d\mathcal{C}_n} + 2\,\mathrm{Re}\left(\frac{d\alpha_\ell(\mathcal{C}_n)}{d\mathcal{C}_n}\beta_\ell^*\right) = 0, \tag{6.22}$$

Therefore, the optimum $\hat{\mathcal{C}}_n$ providing the largest h_{n+1}, in the case of Heun's method, is a solution of (6.22).

6.2.1.2 *Optimum $\mathcal{C}_n$ for generic embedded Runge–Kutta schemes*

The optimum $\mathcal{C}_n$ for general embedded Runge–Kutta schemes can be obtained following the same principles illustrated above with the Heun algorithm. However, the algebraic calculations get rapidly cumbersome, leading to expensive computations that, in most cases, exceeds the time gained with a larger step. Here, we sketch-out the procedure for generic embedded Runge–Kutta methods, considering solvers of order N with an embedded $(N-1)$-order scheme (for other embedded or extrapolation methods, the procedure is completely analogue). For a s-stage method, the error $\Delta\phi_{n+1}$ can be written as [116]

$$\begin{aligned}(\Delta\phi_{n+1})^2 &= \left|\sum_{\ell=1}^{s} d_\ell\, w_\ell\right|^2, \quad d_\ell \stackrel{\text{def}}{=} a_{s,\ell} - b_\ell,\\ w_\ell &\stackrel{\text{def}}{=} h_n\, f\left(\mathbf{k}, t_n + c_\ell\, h_n; \phi_n + \sum_{r=1}^{\ell-1} a_{\ell,r}\, w_r; \mathcal{C}_n\right),\end{aligned} \tag{6.23}$$

where $a_{\ell,r}$, b_ℓ and c_ℓ are the coefficients of the Butcher tableau which characterizes the integrator [116]. Using Taylor expansions and un-nesting the scheme, it is possible to prove that a result with a similar structure compared with (6.19) is obtained. In this case, the number of stages s appears as exponent in the function α, which takes the form $\alpha(\mathbf{x}, t; \mathcal{C}_n) = (V_n + \mathcal{C}_n)^{2s}\,\psi_n$. The function β, on the other hand, becomes explicitly dependent on $\mathcal{C}_n$, involving a number of terms growing exponentially with s. For this reason, even though the exact result can always be achieved, the computational time needed to minimize the error (5.44) is often larger than the time gained with a larger step, especially for higher order schemes ($s > 3$). In the next section, we show how, for practical applications, an exact solution is not necessary to improve the algorithm, and (6.9) represents a fast and accurate method.

6.3 NUMERICAL EXAMPLES

Here, we consider numerical examples where we apply this method, focusing on both the Schrödinger–Newton (SN) and Nonlinear Schrödinger (NLS) equations solved with the Dormand and Prince 5(4) integrator [114] in one and two spatial dimensions. In all cases, we set open boundary conditions for the potential, while the initial conditions and the value of the physical parameters are chosen to be very close to regimes of physical interest, as described in [17–19].

For the one-dimensional NLS, we considered the case $g = -1$ (see 1.4) and we used $\psi(x, t = 0) = \sqrt{2}\,\mathrm{sech}\left(\sqrt{2}\,x\right)$ as initial condition. We discretized the space with $N = 2048$ points, in a computational box of length $L = 80$. The two-dimensional

NLS, which is often employed in optics to model self-focusing beams in a medium with a cubic non-linearity [125, 126], presents a finite time (blow-up) singularity [127]. Specifically, whenever the initial condition ψ_0 satisfies $E_g = \int d\mathbf{r}\, \psi_0 \left(-\frac{1}{2}\nabla^2 + \frac{g}{2}|\psi_0|^2\right) \psi_0^* < 0$, the norm of the solution, or of one of its derivatives, becomes unbounded in finite time. For this reason, we stop the simulation at $t_{fin} = 5$, i.e., before the singularity occurs. We set $\psi(\mathbf{r}, t = 0) = e^{-r^2/2}/\sqrt{\pi}$ as initial condition and we consider the $g = -6$ case, for which the corresponding initial energy is $E(g = -6) \approx 0.02$, hence quite close to the singular regime; for the spatial discretization we used $L = 120$ and $N = 4096^2$ (squared box with side $L = 120$ discretized with 4096×4096 nodes). For both the one and two dimensional SN equations, we set $g = 500$ and considered a Gaussian initial condition, $\psi(\mathbf{x}, t = 0) = \mathcal{N} e^{-|\mathbf{x}|^2/2}$ where $\mathcal{N}$ is the normalisation factor, fixed such that $\int d\mathbf{x}\, |\psi(\mathbf{x}, t = 0)|^2 = 1$. The parameters of the spatial discretization are $L = 20$ and $N = 2048$ in 1D, while for the 2D case we set $L = 20$ and $N = 1024^2$.

The gain factor provided by the method depends on the optimal value of $\mathcal{C}_n$ compared to the $\mathcal{C}_n = 0$ case, which changes from case to case as a function of the boundary conditions for the potential and of the profile of the solution. Specifically, since the gain factor is evaluated with respect to the $\mathcal{C}_n = 0$ case, the more the optimal value of $\mathcal{C}_n$ is far from zero, the larger the gain factor gets.

For the one-dimensional NLS, some analytical stationary solutions are known. We then use one of these solutions (see (7.8)) as initial condition. For all other cases (SN and NLS 2D), no such stationary solutions are known, so we use gaussian initial conditions.

In Figure 6.1, we show the average time-step $h_{av} = \sum_{n=1}^{N_h} h_n / N_h$, for an entire simulation with N_h time steps, as a function of $\mathcal{C}_n$ for the one-dimensional SN and NLS equations. These plots are generated taking $\mathcal{C}_n$ constant for the entire simulations, in order to better appreciate the strong dependence of the time-step on the choice of the gauge for the potential. In Figure 6.2, we report the result of simulations performed choosing the near optimal $\mathcal{C}_n = \tilde{\mathcal{C}}_n$ at each time-step. Note that, for the one-dimensional NLS, the solution being stationary, h_n and the optimum $\mathcal{C}_n$ do not change in time, that is not the case in 2D. We show the time-step h_n as a function of time for the one-dimensional SN and NLS equations, comparing the $\mathcal{C}_n = 0$ case with $\mathcal{C}_n = \tilde{\mathcal{C}}_n$. In both cases, the time-step chosen by the algorithm with the optimisation of the gauge constant proves to be larger, compared to the $\mathcal{C}_n = 0$ case. In Table 6.1, we show the number of time-loops $N_{\Delta t}$ required to run each simulation and the time T needed to run the simulation (in seconds) for the cases $\mathcal{C}_n = 0$ and $\mathcal{C} = \tilde{\mathcal{C}}_n$. For NLS, in the one dimensional case we achieve roughly a 30% improvement in terms of speed gain between the $\mathcal{C} = 0$ and $\mathcal{C} = \tilde{\mathcal{C}}_n$ cases, while in two dimensions the speed gain is only approximately 10% since, here, the value of $\tilde{\mathcal{C}}_n$ is very close to zero. As long as the SN equation is concerned, (6.9) proved to reduce remarkably both the number of time loops and the effective time for the total simulation, providing up to a factor 5 of improvement with respect to the $\mathcal{C}_n = 0$ case in 1D and up to a factor 3 in 2D.

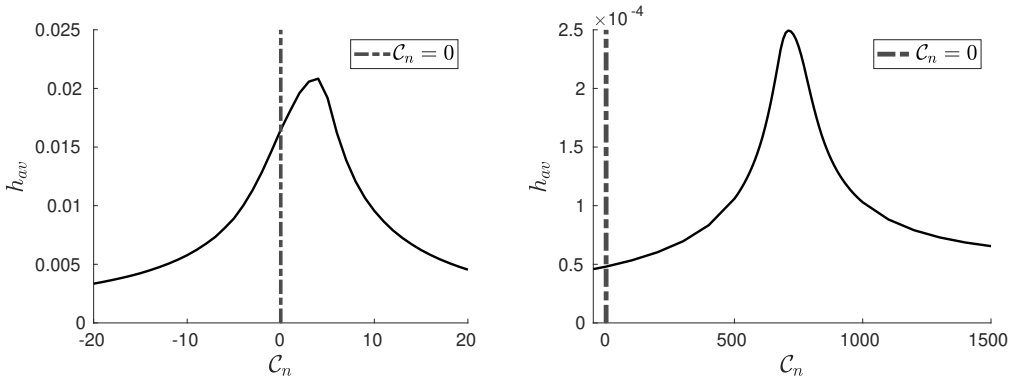

Figure 6.1 – Average time-step $h_{av} = \frac{1}{N_h}\sum_{n=1}^{N_h} h_n$ with a constant $\mathcal{C}_n$ for the IF method applied to the one dimensional NLS (left) and SN (right) equations.

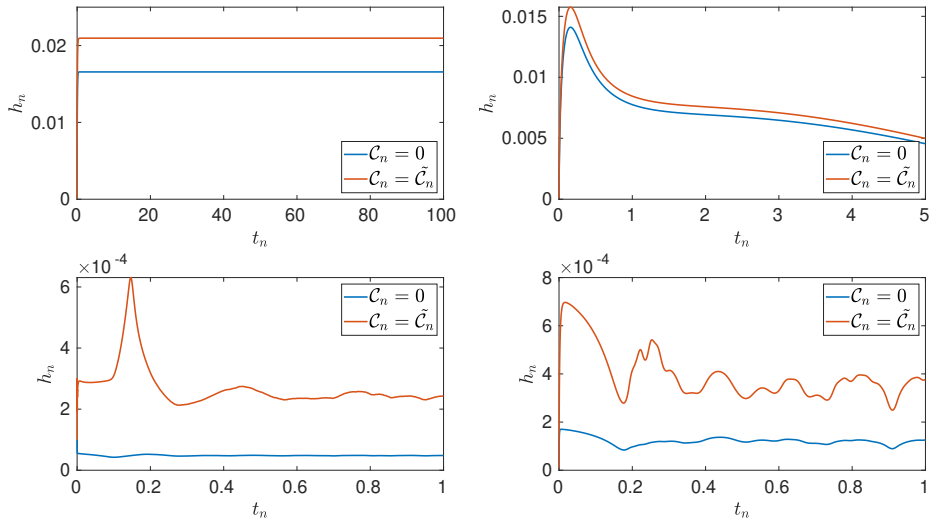

Figure 6.2 – Comparison between $\mathcal{C}_n = \tilde{\mathcal{C}}_n$ and $\mathcal{C}_n = 0$ for time-step h_n as a function of time, for the IF method applied to the NLS_{1D} (top left), NLS_{2D} (top right), SN_{1D} (bottom left) and SN_{2D} (bottom down).

Eq.	SN_{1D}	SN_{1D}	SN_{2D}	SN_{2D}	NLS_{1D}	NLS_{1D}	NLS_{2D}	NLS_{2D}
$\mathcal{C}$	0	$\tilde{\mathcal{C}}_n$	0	$\tilde{\mathcal{C}}_n$	0	$\tilde{\mathcal{C}}_n$	0	$\tilde{\mathcal{C}}_n$
$N_{\Delta t}$	20819	3871	8382	2682	6047	4781	754	690
T(s)	66.7	12.1	12856	4736	18.9	14.5	23769	22843

Table 6.1 – Comparisons for the SN and the NLS equations, in one and two spatial dimensions, between different values of $\mathcal{C}_n$.

7

NUMERICAL COMPARISON OF THE DIFFERENT TIME-INTEGRATORS

In this chapter, we present a large and detailed comparison about the implementation of all methods previously described: Splitting algorithms, the integrating factor technique, the modified integrating factor and the new method we developed. The comparisons are done considering both speed and precision for each algorithm, simulating systems with different interactions, boundary and initial conditions. First, we explain one of the key differences between the two categories of methods under consideration, focusing on the fact that Splitting algorithms are symplectic integrators and therefore time-reversible, while methods belonging to the integrating factor family are not. This is a key point which must be taken into account when comparing these algorithms. Second, we discuss the different estimators we use to determine the precision of the different integrators. Finally, we test the methods on different equations, comparing their accuracy and computational speed in each case. In particular, we focus on the Nonlinear Schrödinger, the Newton–Schrödinger and the Gross–Pitaevskii–Poisson equations, in one and two spatial dimensions, considering different physical regimes and exploring both the open and periodic boundary conditions case. The results of the one and two dimensional cases are shown to be very similar, hence analogue conclusions are expected also in 3D.

7.1 TIME REVERSIBILITY AND SYMPLECTIC INTEGRATORS

One of the most important differences between Splitting algorithms and methods belonging to the Runge–Kutta family, to which the integrating factor is closely related, is that the former are symplectic integrators [128, 129]. This property implies that Splitting methods are in general designed both to conserve the energy and to be time-reversible, namely numerical errors related to the conservation of this constant of motion remain stable.

Here, in order to better understand the meaning of this feature, we apply to both the Split-Step method and the integrating factor algorithm time inversion tests. In each of these tests, the simulation starts at initial time t_0 and is run up to a final instant t_{fin}, then time is reversed until it reaches back the initial value. The tests were made for the Nonlinear Schrödinger equation, with the second order Split-Step integrator and the Dormand & Prince adaptive algorithm combined with the integrating factor, although analogue results are obtained independently of the differential equation considered and the order of the integrators.

To estimate the error on the conservation of energy, we start from the quantity

$$\Delta E_i = \left| \frac{E_{t_i}}{E(t_{in})} - 1 \right|, \tag{7.1}$$

where t_{in} is the initial time and t_i denotes the i^{th} time-step of the numerical integration. The energy E for the Schrödinger equation, being defined as

$$E = \frac{1}{2}\int dr\, \psi^*(-\nabla^2 + V)\psi. \tag{7.2}$$

Since ΔE varies with time, to the purpose of estimating the precision of each algorithm, we consider

$$\widehat{\Delta E} = \max_i \left[\Delta E_i\right], \tag{7.3}$$

namely we take the maximal energy difference with respect to the initial value, during the whole simulation.

As shown in Figure 7.1, the error on the energy conservation remains relatively stable with the Split-Step algorithm and when time is reversed it retraces the forward pattern. The Dorman & Prince integrator on the other hand exhibits a clear increasing trend, pointing out a weak stability as long as this particular type of numerical error is considered.

However, as shown in Figure 7.2, this trend reduces as the tolerance is decreased, down to a very small value, whose magnitude depends on the particular equation considered. For the Nonlinear Schrödinger equation for example, we find that with a tolerance $TOL = 10^{-9}$, double machine precision is achieved.

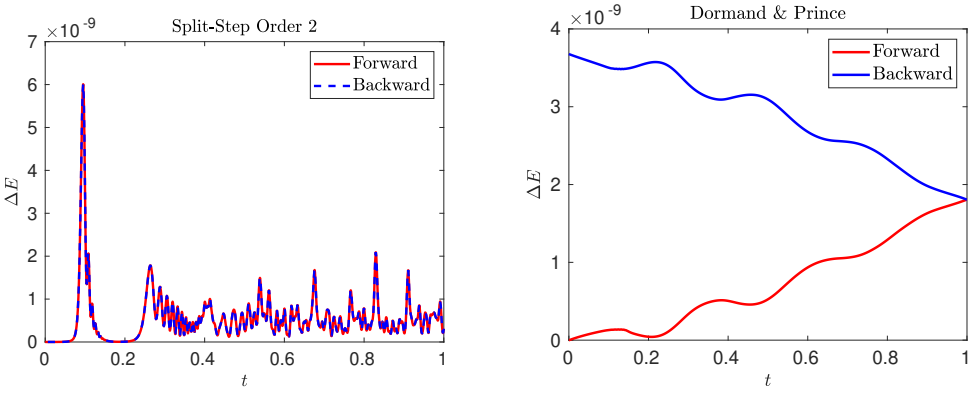

Figure 7.1 – Time-reversion plots of the energy error, $\Delta E = \left|\frac{E}{E_0} - 1\right|$, as a function of time for different numerical methods: Split-Step order 2 and Dormand & Prince (with tolerance 10^{-10}), for the Schrödinger–Newton equation.

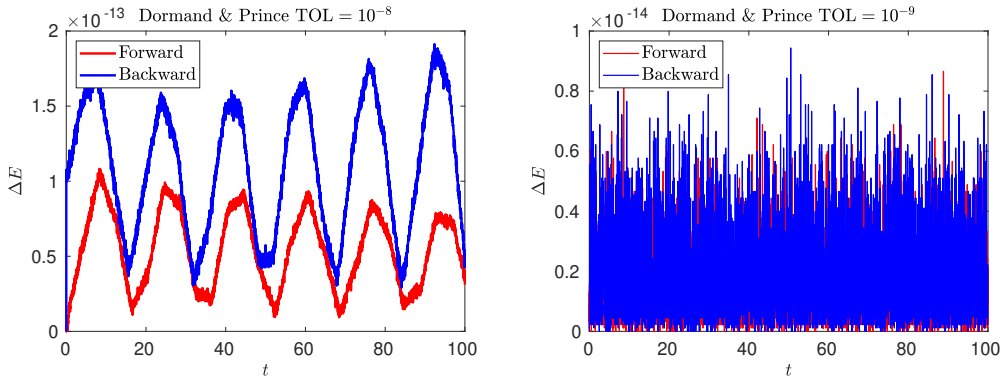

Figure 7.2 – Time-reversion plots of the energy error, $\Delta E = \left|\frac{E}{E_0} - 1\right|$, as a function of time for different numerical methods: Dormand & Prince, with tolerances 10^{-8} and 10^{-9}.

7.2 ESTIMATORS OF THE PRECISION OF THE TIME-INTEGRATION ALGORITHMS

For the comparison between all algorithms, we estimate the precision of the time-integration, looking not only at the error on the conservation of energy, but also at other types of the numerical errors, related to the solution. These precision estimators are listed below.

1. The error on the energy conservation, as defined in (7.3).
2. Another constant of motion for the considered equation, is the mass,

$$M = \int d\mathbf{r}\, |\psi|^2. \tag{7.4}$$

   This quantity is automatically conserved with machine precision when using splitting algorithms, while it is not in general the case with the integrating factor. For this reason, when the latter technique is employed, we impose mass conservation at each time-step, multiplying the solution ψ by $M_0/\int d\mathbf{r}\, |\psi|^2$, where M_0 is the initial mass.
3. The error on the solution performing time inversion tests. This quantity is obtained by running a simulation up to a given time t_{fin}, then reversing the time and evolving back to the initial instant. The error is monitored using the L_∞-norm of the difference between the solution at the initial time at beginning of the simulation and at the end of it. Denoting the "backward" solution by $\Delta\psi_{rev}$, one has

$$\Delta\psi_{rev} = \max_i \left[|\psi(x_i, t_{in}) - \psi_{backward}(x_i, t_{in})|\right]. \tag{7.5}$$

4. The two estimators described above favorize time-splitting algorithms because they are symplectic and reversible integrators whereas the integrating factor is not. For this reason, we also compare the result of the simulations with a "reference one", very accurate, using an adaptive Fehlberg integrator of order 7

embedded within an order 8 scheme, with a very small tolerance, $\mathtt{tol} = 10^{-14}$. Defining this estimator as $\Delta\psi_{ref}$, one has

$$\Delta\psi_{ref} = \max_i \left[\left| \psi(x_i, t_f) - \psi_{F7(8)}(x_i, t_{fin}) \right| \right], \tag{7.6}$$

where ψ is the numerical solution provided by the particular method considered and $\psi_{F7(8)}$ is the one outputted by the Fehlberg 7(8) integrator.

7.3 NUMERICAL COMPARISONS

We start by implementing and comparing the numerical methods on the 1D Nonlinear Schrödinger equation, which is used as benchmark since in this case an analytical solution is known. We then focus on the 1D Newton–Schrödinger equation, with open and periodic boundary conditions. Then we switch to the 2D case for the Nonlinear and Newton–Schrödinger equations, the latter for both open and periodic boundary conditions. Finally, we present the results for the two dimensional Gross–Pitaevskii–Poisson equation, which can be regarded as a hybrid version of the Newton–Schrödinger and Nonlinear Schrödinger systems.

For brevity we use the following shorthand notation.

1. NLS: Nonlinear Schrödinger equation
2. SN: Newton–Schrödinger equation
3. GPP: Gross–Pitaevskii–Poisson equation
4. SS2: Split-Step order 2
5. SS2: Split-Step order 4
6. SS2: Split-Step order 6
7. SSa: Adaptive Split-Step order 4(3)
8. IF: Integratig factor
9. MIF: Modified integratig factor
10. IFC: Integratig factor with optimal gauge condition for the potential

7.3.1 *1d Nonlinear Schrödinger equation*

In order to validate the code and verify the accuracy of the algorithms, we first consider the case of the one dimensional nonlinear Schrödinger equation

$$i\frac{\partial\psi}{\partial t} + \frac{1}{2}\frac{\partial^2\psi}{\partial x^2} + |\psi|^2\psi = 0, \tag{7.7}$$

where the potential is simply given by $V(x,t) = -|\psi(x,t)|^2$. In this case there is a simple analytical solution, which is called the soliton

$$\psi(x,t) = \sqrt{2}\,\mathrm{sech}\left(\sqrt{2}x\right) e^{it}, \tag{7.8}$$

In the simulations, we discretised space with $N = 2048$ points, in a box of length $L = 80$ and we used the analytical solution at $t = 0$ as initial condition.

We run a first set of simulations in order to compare the efficiency of the different variants of the integrating factor: IF, MIF, and IFC. For these simulations we use the Dormand & Prince integrator, which resulted to perform better for this system than the ones of the Tsitouras family. The results, using a fixed tolerance $\mathtt{tol} = 10^{-9}$, are shown in Figure 7.3. The MIF is in this case the most efficient one in terms of number of time-loops employed whereas the IFC method is the fastest one. The details of the comparisons are illustrated in Table 7.1.

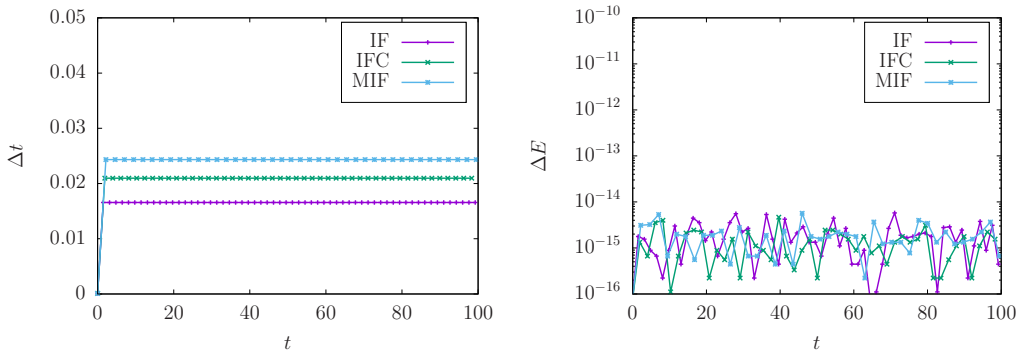

Figure 7.3 – Comparisons for the 1D nonlinear Schrödinger equation of the time-step (left) and the error on the energy conservation (right) with the Dormand & Prince integrator and at fixed tolerance, $\mathtt{tol} = 10^{-9}$.

Method	$N_{\Delta t}$	$\Delta\psi_{rev}$	$\Delta\psi_{ref}$	T(s)
MIF	4122	$3.3 \cdot 10^{-10}$	$6.3 \cdot 10^{-10}$	17.1
IFC	4781	$1.2 \cdot 10^{-9}$	$7.8 \cdot 10^{-10}$	14.5
IF	6047	$3.6 \cdot 10^{-10}$	$3.8 \cdot 10^{-10}$	18.9

Table 7.1 – Comparisons for the 1D nonlinear Schrödinger equation of different methods with the Dormand & Prince integrator at fixed tolerance, $\mathtt{tol} = 10^{-9}$. $N_{\Delta t}$ denotes the number of time-loops required and T is the time needed to run the simulation, in seconds.

We present a second set of simulations, in order to compare the Split-Step integrators with the IFC (the fastest of the previous methods) looking at the energy conservation error, the error on the solution and the total time needed to run each simulation. The results are illustrated in Figure 7.4 and Table 7.2. We observe that the IFC solver is the fastest one by at least a factor 2, presenting at the same time the best results to all the indicators: it uses a larger time-step, presents equal or better energy conservation, returns a slightly worse $\Delta\psi_{rev}$ and it is one of the best, if compared to the reference simulation. We conclude that in this case the IFC solver is best one.

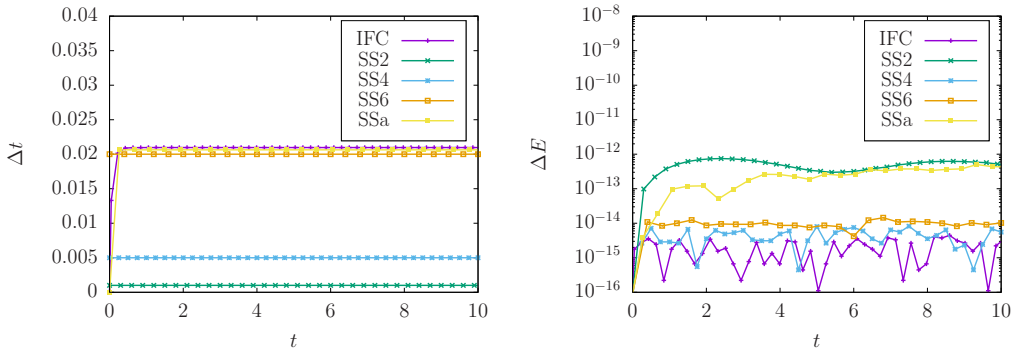

Figure 7.4 – Comparisons for the 1D nonlinear Schrödinger equation of different methods between the time-step (left) and the error on the energy conservation (right) for the IFC method and the Split-Step solvers.

Method	Δt	$\widehat{\Delta E}$	$\Delta\psi_{rev}$	$\Delta\psi_{ref}$	T(s)
SS2	10^{-3}	$7.5 \cdot 10^{-13}$	$6.3 \cdot 10^{-10}$	$1.1 \cdot 10^{-4}$	86.7
SS4	$5 \cdot 10^{-3}$	10^{-15}	$8.2 \cdot 10^{-10}$	$5.8 \cdot 10^{-7}$	38.1
SS6	$2 \cdot 10^{-2}$	10^{-15}	$2.0 \cdot 10^{-10}$	$3.7 \cdot 10^{-9}$	29.3
SSa, tol $= 10^{-6}$	$2.1 \cdot 10^{-2}$	$1.6 \cdot 10^{-12}$	$3.5 \cdot 10^{-10}$	$6.5 \cdot 10^{-10}$	34.0
IFC, tol $= 10^{-9}$	$2.1 \cdot 10^{-2}$	10^{-15}	$1.2 \cdot 10^{-9}$	$7.8 \cdot 10^{-10}$	14.5

Table 7.2 – Comparison for the 1D nonlinear Schrödinger equation between the IFC method and the Split-Step solvers. T is the total time required to run each simulation, measured in seconds. The Δt for the adaptive algorithms is the averaged one.

7.3.2 *1D Schrödinger-Newton equation*

We now focus on the SN system, starting from the case of a single spatial dimension,

$$\begin{aligned} i\frac{\partial\psi}{\partial t} + \frac{1}{2}\frac{\partial^2\psi}{\partial x^2} - V\psi = 0 \\ \frac{\partial^2 V}{\partial x^2} = g\,|\psi|^2 . \end{aligned} \tag{7.9}$$

The solutions of (7.9) depend on the initial condition and on the single parameter g. We set $\psi(x, t = 0) = e^{-x^2/2}/\sqrt[4]{\pi}$ as initial condition. The potential V is calculated using the Hockney's method [38]. We perform a set of tests with the different integrating methods for $g = 10$, which corresponds to a system in the quantum regime, i.e., with an associated De Broglie wavelength of the order of the size of the system, and $g = 500$, which corresponds to a system closer to the semiclassical regime, with an associated De Broglie wavelength about 20 times smaller than the size of the system. Snapshots of the evolution of this system are plotted in Figure 7.5: the initial condition oscillates, exhibiting a complex dynamics. This is particularly evident in the semiclassical regime, where high frequency oscillations appear in the wavefunction (see last row of the figure). The simulation is run in a box of length $L = 80$,

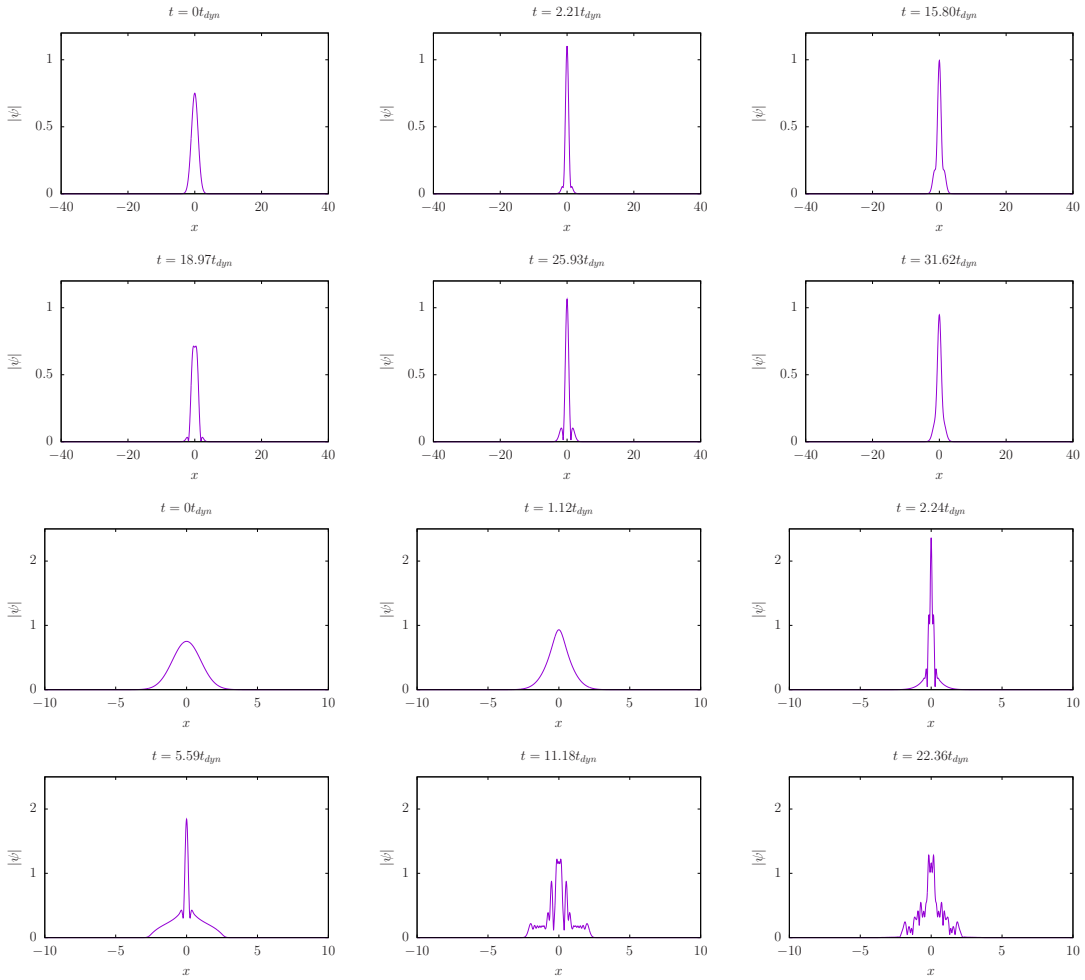

Figure 7.5 – Snapshots of the modulus of the solution of the 1D Newton–Schrödinger equation $|\psi|$. The upper panel (first six plots) corresponds to the $g = 10$ case while the lower one is associated with $g = 500$.

discretised into $N = 2048$ points in the $g = 10$ case, while for $g = 500$ we set $L = 20$ and $N = 2048$. The characteristic time of dynamics is defined as $t_{dyn} = |g|^{-1/2}$.

In this case, we use the Tsitouras solver for integrating factor algorithms, which resulted to perform better than the Dormand and Prince one. In Figure 7.6 we show its efficiency for the different methods IF, MIF and IFC. We observe oscillations in Δt, which corresponds to spatial oscillations of the system during the evolution. Thanks to the time-adaptive integrator, we do not observe such oscillations in the energy conservation ΔE, as the integrator automatically chooses the optimal time-step for the chosen accuracy. There is no sensible difference between the standard IF method and the MIF, however the IFC performs much better: the average time step is around one order of magnitude larger whereas it attains a better energy conservation, for the simulations in the two regimes, $g = 10$ and $g = 500$. Table 7.3 confirms these results: for similar errors in the inversion test and in the one comparing with a reference simulation, $\Delta\psi_{rev}$ and $\Delta\psi_{ref}$ respectively, the IFC is about one order of magnitude faster.

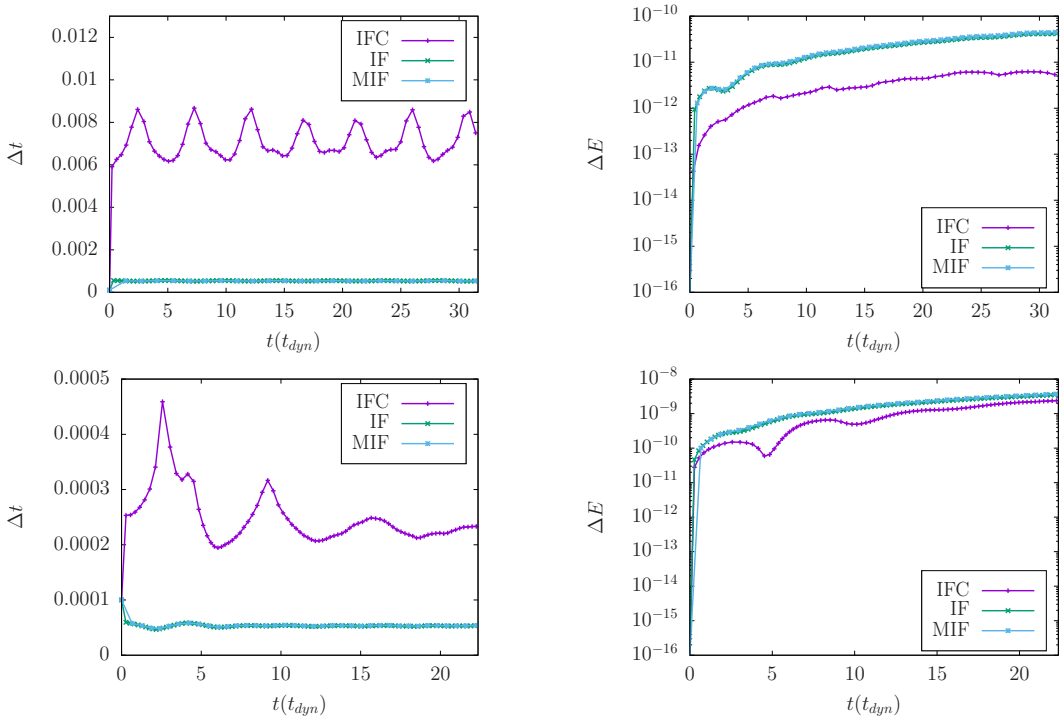

Figure 7.6 – Comparisons of the time-step and the error on the energy conservation for the 1D Newton–Schrödinger equation with the Tsitouras integrator at fixed tolerance, $\mathrm{tol} = 10^{-10}$ with the IF, IFC and MIF methods and for both the cases $g = 10$ (upper plots) and $g = 500$ (lower plots).

g	Method	$N_{\Delta t}$	$\Delta\psi_{rev}$	$\Delta\psi_{ref}$	T(s)
10	MIF	27425	$1.4 \cdot 10^{-10}$	$3.3 \cdot 10^{-11}$	111.5
	IF	27484	$1.3 \cdot 10^{-10}$	$3.3 \cdot 10^{-11}$	52.5
	IFC	1592	$1.3 \cdot 10^{-10}$	$3.3 \cdot 10^{-11}$	5.0
500	MIF	18639	$1.1 \cdot 10^{-8}$	$1.5 \cdot 10^{-7}$	77.8
	IF	18784	$1.0 \cdot 10^{-8}$	$1.4 \cdot 10^{-7}$	52.5
	IFC	3915	$2.3 \cdot 10^{-8}$	$1.5 \cdot 10^{-8}$	11.9

Table 7.3 – Comparisons for the 1D Newton–Schrödinger equation between different methods for the Tsitouras integrator at fixed tolerance, $\mathrm{tol} = 10^{-10}$. $N_{\Delta t}$ denotes the number of time-loops required and T is the time needed to run the simulation, in seconds.

In Figure 7.7 and Table 7.4, we compare the Split-Step integrators with the IFC, looking at the energy conservation error, the error on the solution and the total time needed to run each simulation. In this case splitting algorithms are the most efficient ones, even though the IFC is able to compete, providing the same order of magnitude for the accuracy parameters.

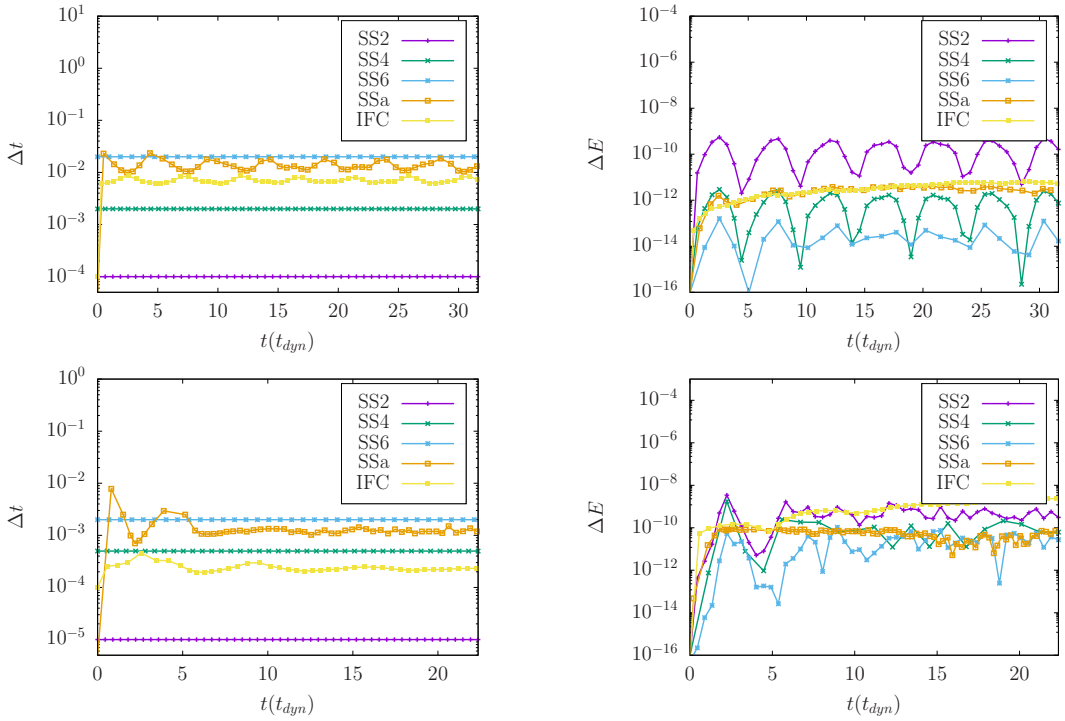

Figure 7.7 – Comparison for the 1D Newton–Schrödinger equation between the time-step and the error on the energy conservation for the IFC method and the Split-Step solvers for both the cases $g = 10$ (upper plots) and $g = 500$ (lower plots).

g	Method	Δt	$\widehat{\Delta E}$	$\Delta\psi_{rev}$	$\Delta\psi_{ref}$	T(s)
10	SS2	10^{-4}	$5.5 \cdot 10^{-10}$	$4.5 \cdot 10^{-11}$	$4.5 \cdot 10^{-9}$	123.3
	SS4	$2 \cdot 10^{-3}$	$2.9 \cdot 10^{-12}$	$2.5 \cdot 10^{-12}$	$5.5 \cdot 10^{-11}$	11.1
	SS6	$2 \cdot 10^{-2}$	$1.5 \cdot 10^{-13}$	$4.0 \cdot 10^{-12}$	$1.1 \cdot 10^{-11}$	3.5
	SSa	$1.5 \cdot 10^{-2}$	$4.2 \cdot 10^{-12}$	$8.5 \cdot 10^{-11}$	$5.9 \cdot 10^{-11}$	6.4
	IFC	$7.5 \cdot 10^{-3}$	$1.8 \cdot 10^{-12}$	$1.3 \cdot 10^{-10}$	$3.3 \cdot 10^{-11}$	5.0
500	SS2	10^{-5}	$6.0 \cdot 10^{-9}$	$1.1 \cdot 10^{-10}$	$5.2 \cdot 10^{-8}$	120.0
	SS4	$5 \cdot 10^{-4}$	$2.5 \cdot 10^{-9}$	$4.9 \cdot 10^{-12}$	$1.3 \cdot 10^{-7}$	5.4
	SS6	$2 \cdot 10^{-3}$	$1.8 \cdot 10^{-10}$	$2.8 \cdot 10^{-11}$	$7.6 \cdot 10^{-8}$	3.5
	SSa	$2 \cdot 10^{-3}$	$1.0 \cdot 10^{-10}$	$6.4 \cdot 10^{-8}$	$2.9 \cdot 10^{-8}$	6.7
	IFC	$3.5 \cdot 10^{-4}$	$1.8 \cdot 10^{-9}$	$2.3 \cdot 10^{-8}$	$1.5 \cdot 10^{-8}$	11.9

Table 7.4 – Comparison for the 1D Newton–Schrödinger equation between the IFC method and the Split-Step solvers. The SSa simulations and IFC have been performed with a tolerance $tol = 10^{-7}$ and $tol = 10^{-10}$ respectively for $g = 10$ and $tol = 10^{-6}$ and $tol = 10^{-10}$ respectively for $g = 500$. The Δt for the adaptive algorithms is the averaged one. T is the total time required to run each simulation, measured in seconds.

7.3.2.1 *Periodical case*

We now switch to cosmological version of the SN system, introduced in Section 2.3.3. We consider the simplest case of a static universe taking $a = 1$; we do not expect modifications of our conclusions for a different cosmological model. In one dimension the equations reads

$$i\frac{\partial\psi}{\partial t} + \frac{1}{2}\frac{\partial^2\psi}{\partial x^2} - V\psi = 0 \tag{7.10a}$$

$$\frac{\partial^2 V}{\partial x^2} = g(|\psi|^2 - 1), \tag{7.10b}$$

where the wavefunction $|\psi|^2$ is normalized to unity. The potential V, with periodic boundary conditions, is obtained by calculating the inverse of the Laplacian in Fourier space and transforming back the result to real space. We take cold initial conditions (see [45, 130]), namely,

$$\psi(x, t = 0) = \sqrt{\rho_0 + \delta\rho(x)}e^{i\theta(x)}, \tag{7.11}$$

where θ is related to the initial velocity field (see Section 2.3.3), which we set to zero for simplicity, ρ_0 is the background constant density and $\delta\rho(x)$ the density fluctuations, generated as

$$\delta\rho(x) = \mathcal{F}^{-1}[R(k)\sqrt{P(k)}], \tag{7.12}$$

where $R(k)$ is a Gaussian random field, with zero average and variance unity and P is the power spectrum (see Section 2.3.3). In addition, the initial condition are numerically initialized by applying an additional filter $F(k)$ in Fourier space with the aim of setting to zero all the modes which correspond to a space scale comparable or smaller with respect to the grid-step

$$F(k) = \frac{1}{\cosh\left[(k/k_F)^{10}\right]}, \tag{7.13}$$

with $k_F = k_N/8$, where k_N is the Nyquist wavelength, defined in Section 5.1.2. Thus, our initial condition is

$$\psi(x, t = 0) = \mathcal{F}^{-1}\left[F(k)\mathcal{F}\left[\sqrt{\rho_0 + \delta\rho(x)}\right]\right]. \tag{7.14}$$

In the simulations, we discretize space with $N = 1024$ points, in a box of length $L = 1$ and we use a constant power spectrum as initial condition. We show the results of simulations in the semiclassical regime taking $g = 10^6$ (we do not observe differences in the performance in the quantum regime, i.e., for smaller values of g) and $\rho_0 = 1$. The reason why we set the parameter g to such a large value is because the semiclassical limit we are interested in can be taken by formally sending to zero the value of the reduced Plank constant, and the coupling constant g turns out to be proportional to the inverse of this quantity, namely $g \propto \frac{1}{\hbar^2}$.

The Dormand & Prince solver resulted to be the faster than the Tsitouras one in this case. In Figure 7.8 we show the typical evolution of the system in the cosmological context: the initial condition is spatially homogeneous with small fluctuations. The

fluctuations grow due to the gravitational interaction, up to be dominated by the finite size of the simulation box. The characteristic time of dynamics is defined as $t_{dyn} = |g|^{-1/2}$.

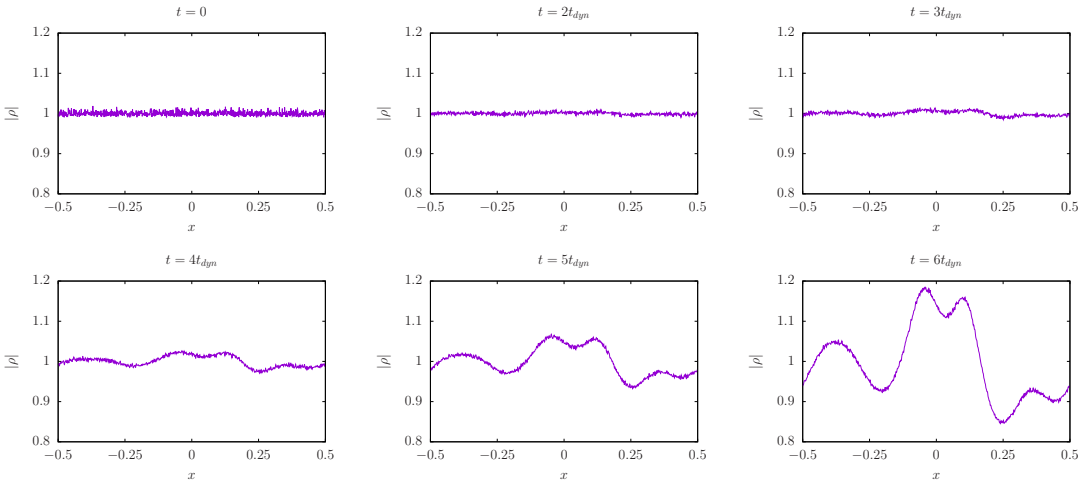

Figure 7.8 – Snapshots of the modulus squared of the solution of the 1D SN equation (periodical case) $|\psi|^2$.

In Figure 7.9 we observe that the IF and IFC are the best integrators among the integrating factor family methods. There is a little difference between them because in this case the $\tilde{C}_n \approx 0$. We observe for $t \gtrsim 5t_{dyn}$ that the time-step decreases; this is due to the fact that the dynamics switches from a regime where the largest scales are still linear, to a regime where all the scales are nonlinear[131]. It indicates, along with Figure 7.9 that the IF family integrator is particularly efficient in the weakly non-linear regime, which is the regime of interest in cosmological simulations.

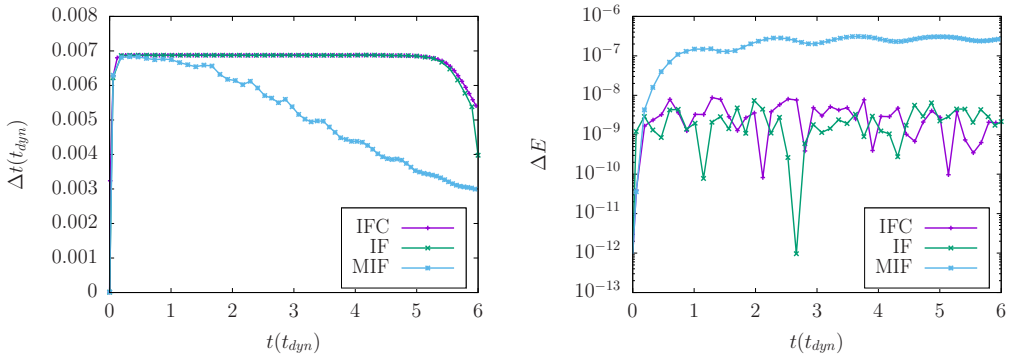

Figure 7.9 – Comparison for the 1D SN equation (periodical case) of the time-step (left plots) and the error on the energy conservation (right plots) for the Dormand & Prince integrator and at fixed tolerance, $tol = 10^{-12}$.

Method	$N_{\Delta t}$	$\Delta\psi_{rev}$	$\Delta\psi_{ref}$	T(s)
MIF	1258	$1.8 \cdot 10^{-9}$	$4.5 \cdot 10^{-10}$	2.7
IFC	898	$1.8 \cdot 10^{-10}$	$6.7 \cdot 10^{-11}$	1.3
IF	901	$3.5 \cdot 10^{-9}$	$7.0 \cdot 10^{-11}$	1.3

Table 7.5 – Comparisons for the 1D SN equation (periodical case) of different methods for the Dormand & Prince integrator at fixed tolerance, $tol = 10^{-12}$. $N_{\Delta t}$ denotes the number of time-loops required and T is the time needed to run the simulation, in seconds.

In Figure 7.10 we compare the Split-Step integrators with the IFC. We observe that the Split-Step integrators (except SS2) perform in the same manner in the weakly non-linear and strongly non-linear regime. We observe that IFC outperforms the tested Split-Step integrators in the first regime, whereas, in the second one it becomes equally efficient compared to the split-step methods. This is consistent with the observation of Section 7.3.2: since the dynamics corresponds to a highly non-linear regime, the Split-Step method is more performing than the IFC one. Looking to Table 7.6 it is clear that, for the whole simulation, in this case the IFC is the most performing integration method.

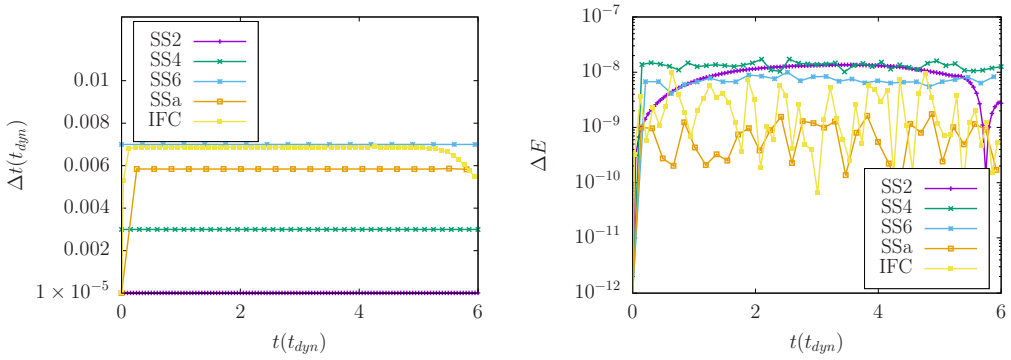

Figure 7.10 – Comparison for the 1D SN equation (periodical case) between the time-step (left plot) and the error on the energy conservation (right plot) for the IFC method and the Split-Step solvers. The $\Delta E(t)$ plots is in a logarithmic scale.

Method	$\Delta t(t_{dyn})$	$\widehat{\Delta E}$	$\Delta\psi_{rev}$	$\Delta\psi_{ref}$	T(s)
SS2	10^{-5}	$1.6 \cdot 10^{-8}$	$8.3 \cdot 10^{-9}$	$8.5 \cdot 10^{-10}$	276.5
SS4	$3 \cdot 10^{-3}$	$1.9 \cdot 10^{-8}$	$1.3 \cdot 10^{-9}$	$1.5 \cdot 10^{-11}$	1.8
SS6	$7 \cdot 10^{-3}$	$1.1 \cdot 10^{-8}$	$1.1 \cdot 10^{-8}$	$3.1 \cdot 10^{-11}$	2.3
SSa, $tol = 10^{-9}$	$5.8 \cdot 10^{-3}$	$2.3 \cdot 10^{-9}$	$3.3 \cdot 10^{-9}$	$1.2 \cdot 10^{-11}$	4.3
IFC, $tol = 10^{-12}$	$6.5 \cdot 10^{-3}$	$1.1 \cdot 10^{-8}$	$1.8 \cdot 10^{-10}$	$6.7 \cdot 10^{-11}$	1.3

Table 7.6 – Comparison for the 1D SN equation (periodical case) between the IFC method and the Split-Step solvers. T is the total time required to run each simulation, measured in seconds. The Δt for adaptive algorithms is the averaged one.

7.3.3 *2D Nonlinear Schrödinger equation*

In the 2D NLS case, one has

$$i\frac{\partial\psi}{\partial t}+\frac{1}{2}\nabla^2\psi-g\left|\psi\right|^2\psi=0. \tag{7.15}$$

As mentioned in Section 6.3, the dynamics of (7.15) presents a finite time (blow-up) singularity [127]. More specifically, whenever the initial condition ψ_0 satisfies $E_g=\int d\mathbf{r}\,\psi_0,\left(-\frac{1}{2}\nabla^2+\frac{g}{2}\left|\psi_0\right|^2\right)\psi_0^*<0$, the norm of the solution, or of one of its derivatives, becomes unbounded in finite time.

We take as initial condition $\psi(\mathbf{r},t=0)=e^{-r^2/2}/\sqrt{\pi}$ and we study the cases $g=-1$ and $g=-6$, for which the corresponding initial energies are $E_{g=-1}\approx 0.42$ and $E_{g=-6}\approx 0.02$, hence the latter being associated with an initial energy which is closer to the singular regime. We run the simulation in a box of side $L=80$, discretized into $N=1024^2$ points in the $g=-1$ case, while for $g=-6$ we set $L=120$ and $N=4096^2$, the characteristic time of dynamics is defined as $t_{dyn}=|g|^{-1/2}$. In this case, we use the Dormand & Prince solver for the integrating factor. In Figure 7.11, snapshots of the modulus of the solution in the two cases are shown. We observe that, as expected, the final size of the system with $g=-6$ is much smaller than the one with $g=-1$ because the system is closer to the blow-up singularity. The results of the comparison between the different methods based on the integrating factor are shown in Figure 7.12) and table Table 7.7. Here, the MIF proved to be very efficient in the case where the dynamic is closer to the singular regime, i.e. $g=-6$, reducing substantially both computational time and number of time loops required to perform the numerical integration.

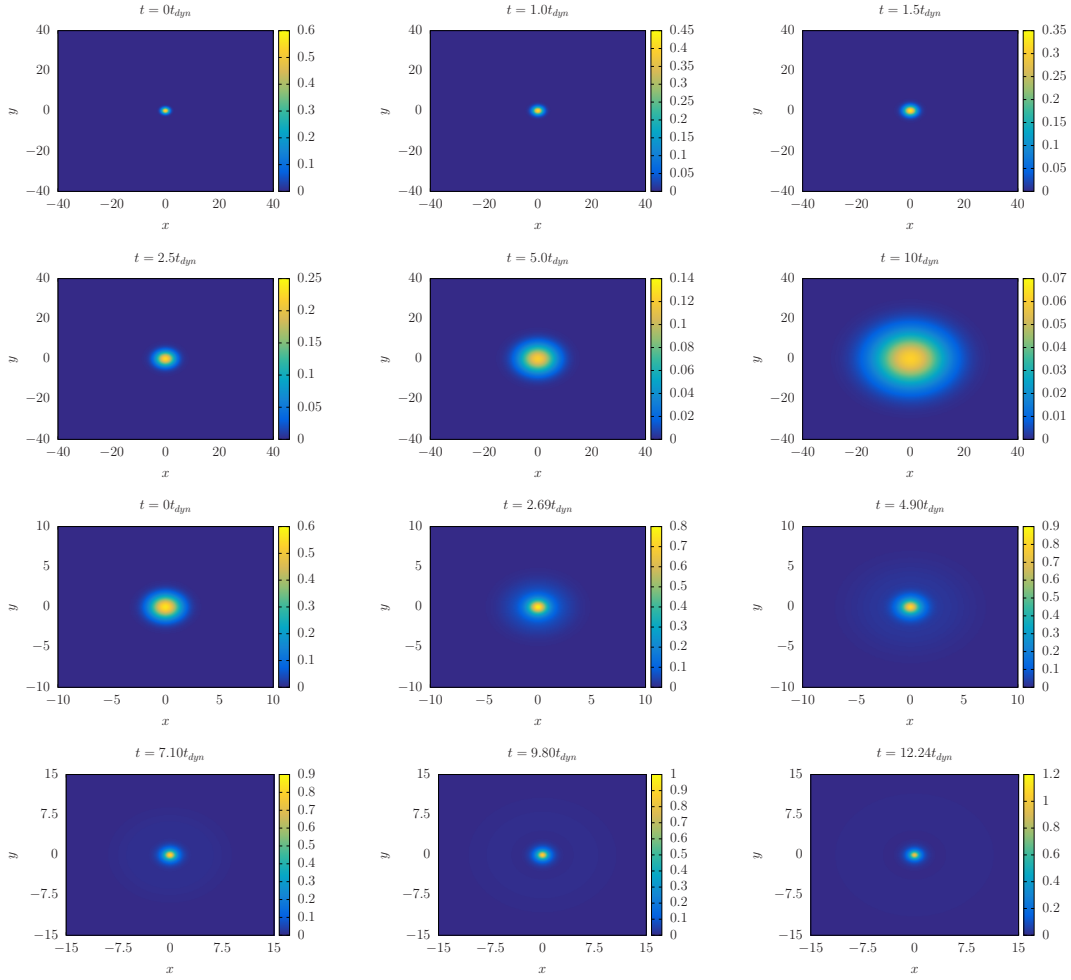

Figure 7.11 – Snapshots of the modulus of the solution of the 2D NLS equation $|\psi|$. The upper panel (first six plots) corresponds to the $g = -1$ case while the lower one is associated with $g = -6$.

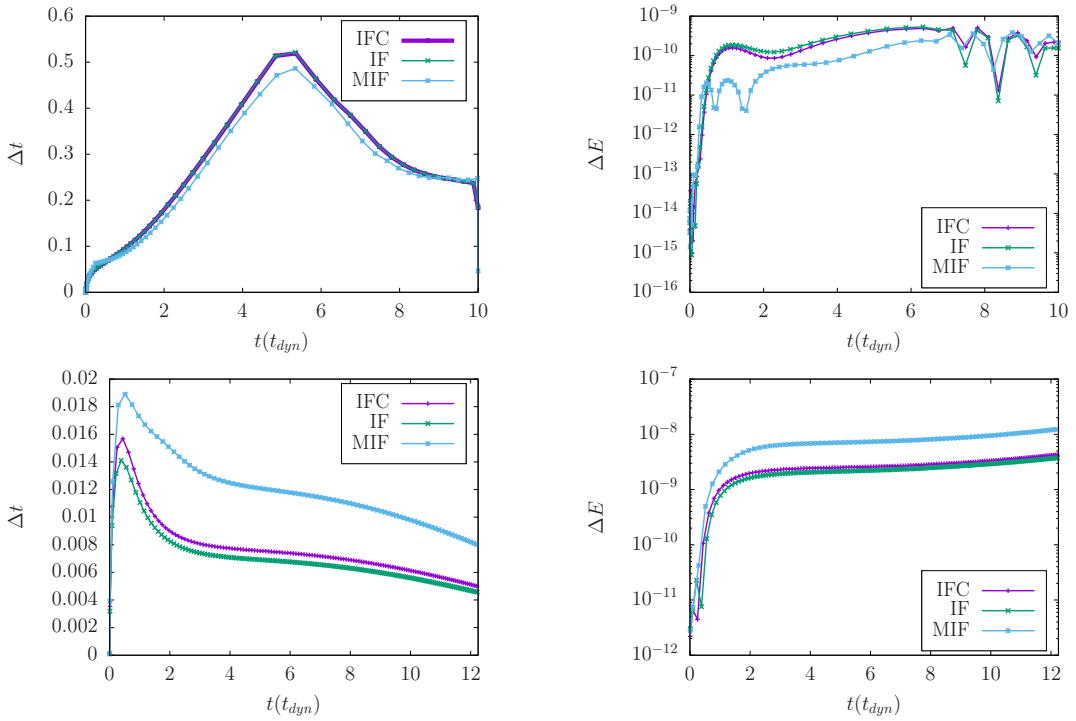

Figure 7.12 – Comparison for the 2D NLS equation of the time-step (left panel) and the error on the energy conservation (right panel) for the Dormand & Prince integrator and at fixed tolerance, $\mathrm{tol} = 10^{-10}$. The top row corresponds to the $g = -1$ case while the bottom one corresponds to $g = -6$. The last time-step is chosen in such a way that the final time is the same in all simulations, in order to ensure that $\Delta\psi_{rev}$ and $\Delta\psi_{ref}$ are evaluated properly, which explain the step which appears for the last time point in Δt.

g	Method	$N_{\Delta t}$	$\Delta\psi_{rev}$	$\Delta\psi_{ref}$	T(s)
-1	MIF	57	$2.5 \cdot 10^{-9}$	$5.0 \cdot 10^{-11}$	241
	IF	55	$3.0 \cdot 10^{-10}$	$2.1 \cdot 10^{-11}$	155
	IFC	55	$3.0 \cdot 10^{-10}$	$1.6 \cdot 10^{-11}$	169
-6	MIF	439	$3.0 \cdot 10^{-9}$	$9.4 \cdot 10^{-9}$	20541
	IF	754	$1.5 \cdot 10^{-10}$	$2.5 \cdot 10^{-9}$	23769
	IFC	690	$1.3 \cdot 10^{-10}$	$3.5 \cdot 10^{-9}$	22843

Table 7.7 – Comparisons for the 2D NLS equation between different methods for the Dormand & Prince integrator and at fixed tolerance, $\mathrm{tol} = 10^{-10}$ for the $g = -1$ case and for $\mathrm{tol} = 10^{-11}$ for $g = -6$. $N_{\Delta t}$ denotes the number of time-loops required and T is the time needed to run the simulation, in seconds.

Finally we compare the Split-Step integrators with the IFC, looking at the energy conservation error, the error on the solution and the total time needed to run each simulation. The results are illustrated in Figure 7.13 and Table 7.8.

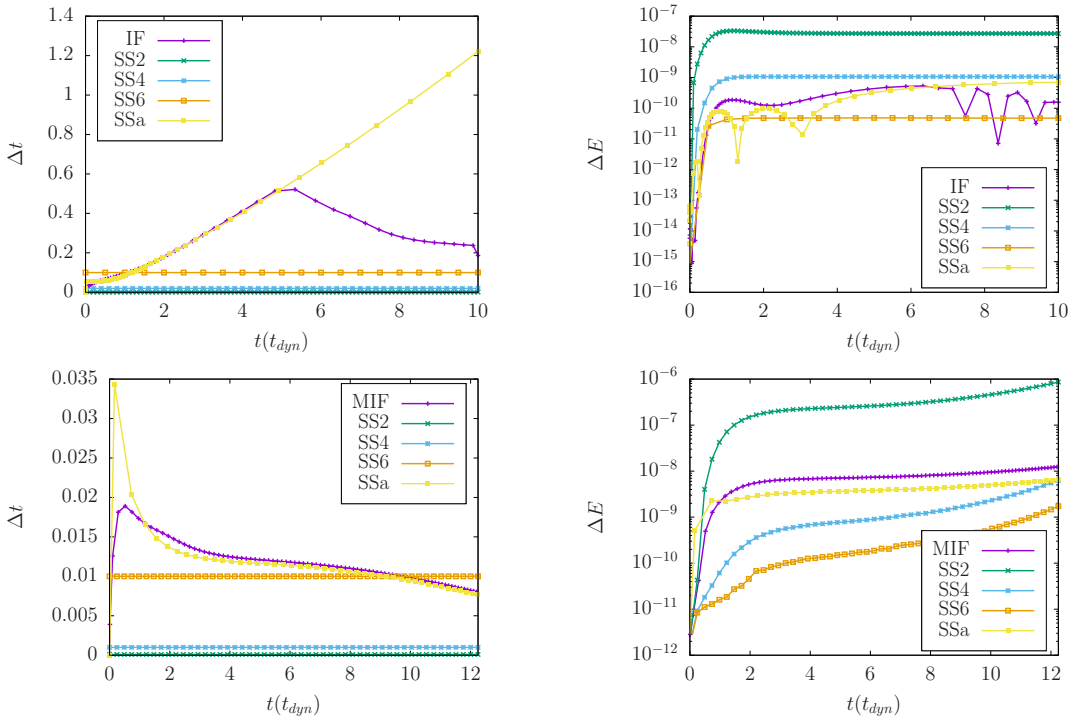

Figure 7.13 – Comparison for the 2D NLS equation between the time-step (left panel) and the error on the energy conservation (right panel) for the IFC method and the Split-Step solvers. The last time-step is chosen in such a way that the final time is the same in all simulations, in order to ensure that $\Delta\psi_{rev}$ and $\Delta\psi_{ref}$ are evaluated properly, which explain the step which appears for the last time point in Δt.

g	Method	Δt	$\widehat{\Delta E}$	$\Delta\psi_{rev}$	$\Delta\psi_{ref}$	T(s)
-1	SS2	10^{-3}	$3.3 \cdot 10^{-8}$	$4.5 \cdot 10^{-8}$	$5.0 \cdot 10^{-10}$	6939
	SS4	$2 \cdot 10^{-2}$	$1.1 \cdot 10^{-9}$	$3.5 \cdot 10^{-13}$	$7.0 \cdot 10^{-11}$	830
	SS6	10^{-1}	$4.5 \cdot 10^{-11}$	$2.5 \cdot 10^{-14}$	$6.2 \cdot 10^{-11}$	445
	SSa	$6 \cdot 10^{-1}$	$7.0 \cdot 10^{-10}$	$3.0 \cdot 10^{-10}$	$2.5 \cdot 10^{-11}$	267
	IF	$5 \cdot 10^{-1}$	$4.5 \cdot 10^{-10}$	$3.0 \cdot 10^{-10}$	$2.1 \cdot 10^{-11}$	155
-6	SS2	10^{-4}	$8.8 \cdot 10^{-7}$	$1.4 \cdot 10^{-11}$	$7.9 \cdot 10^{-7}$	405012
	SS4	10^{-3}	$6.3 \cdot 10^{-9}$	$2.5 \cdot 10^{-12}$	$3.7 \cdot 10^{-9}$	82891
	SS6	10^{-2}	$1.7 \cdot 10^{-9}$	$1.6 \cdot 10^{-12}$	$1.8 \cdot 10^{-9}$	24453
	SSa	$1.5 \cdot 10^{-2}$	$6.5 \cdot 10^{-9}$	$1.4 \cdot 10^{-10}$	$5.4 \cdot 10^{-9}$	29117
	MIF	$1.1 \cdot 10^{-2}$	$9.2 \cdot 10^{-9}$	$3.0 \cdot 10^{-9}$	$9.4 \cdot 10^{-9}$	20541

Table 7.8 – Comparisons for the 2D NLS equation between different methods for the Dormand & Prince integrator. The Δt for adaptive algorithms is the averaged one. T is the total time required to run each simulation, measured in seconds. The tolerances of the integrator SS4(3) is $tol = 10^{-6}$, for the IF integrator $tol = 10^{-10}$ and for the MIFC one $tol = 10^{-11}$.

Here, the gain factor between the splitting algorithms and the methods relying on the integrating factor, namely the IFC and MIF is remarkable.

7.3.4 *2D Schrödinger-Newton equation*

In the 2D SN case, one has

$$\begin{aligned} i\frac{\partial\psi}{\partial t} + \frac{1}{2}\nabla^2\psi - V\psi = 0 \\ \nabla^2 V = g\,|\psi|^2\,. \end{aligned} \tag{7.16}$$

We simulate two analogous systems than in the 1d case: Gaussian initial conditions $\psi(\mathbf{r}, t = 0) = e^{-r^2/2}/\sqrt{\pi}$ and two values of the coupling constant, $g = 10$ and $g = 500$. The former corresponds to a system in the quantum regime and the latter is closer to the semiclassical one. The potential V, as in the 1D case, is calculated using the Hockney method [38]. We run the simulation in a box of side $L = 40$, discretized into $N = 1024^2$ points in the $g = 10$ case, while for $g = 500$ we set $L = 20$ and $N = 1024^2$, the characteristic time of dynamics is defined as $t_{dyn} = |g|^{-1/2}$. In Figure 7.14, snapshots of the modulus of the solution in the two cases are shown. We observe for $g = 500$, as in the 1D case, a more complex dynamics with the formation of rings.

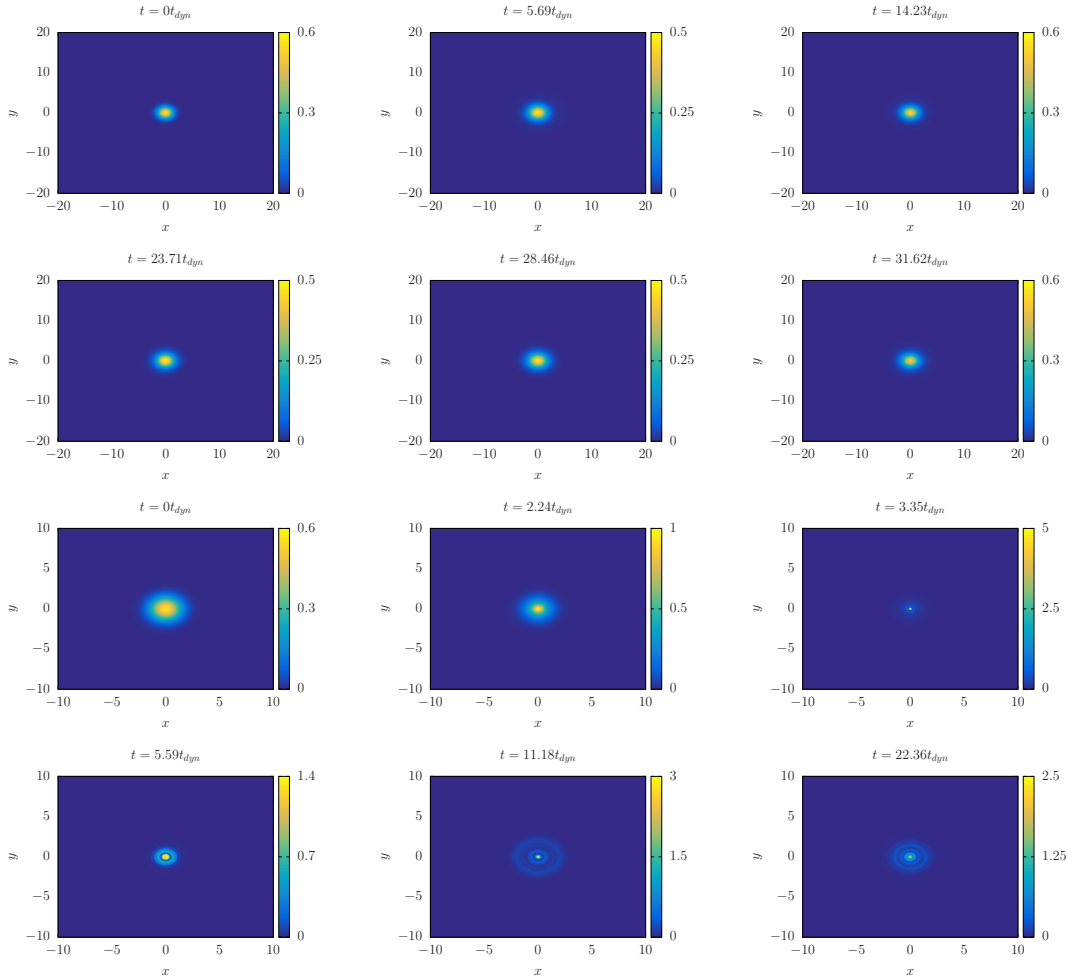

Figure 7.14 – Snapshots of the modulus of the solution of the 2D SN equation $|\psi|$. The upper panel (first six plots) corresponds to the $g = 10$ case while the lower one is associated with $g = 500$.

Here, we used the Tsitouras solver for the integrating factor methods. The results of the comparison between the different methods based on the integrating factor are shown in Figure 7.15 and Table 7.9.

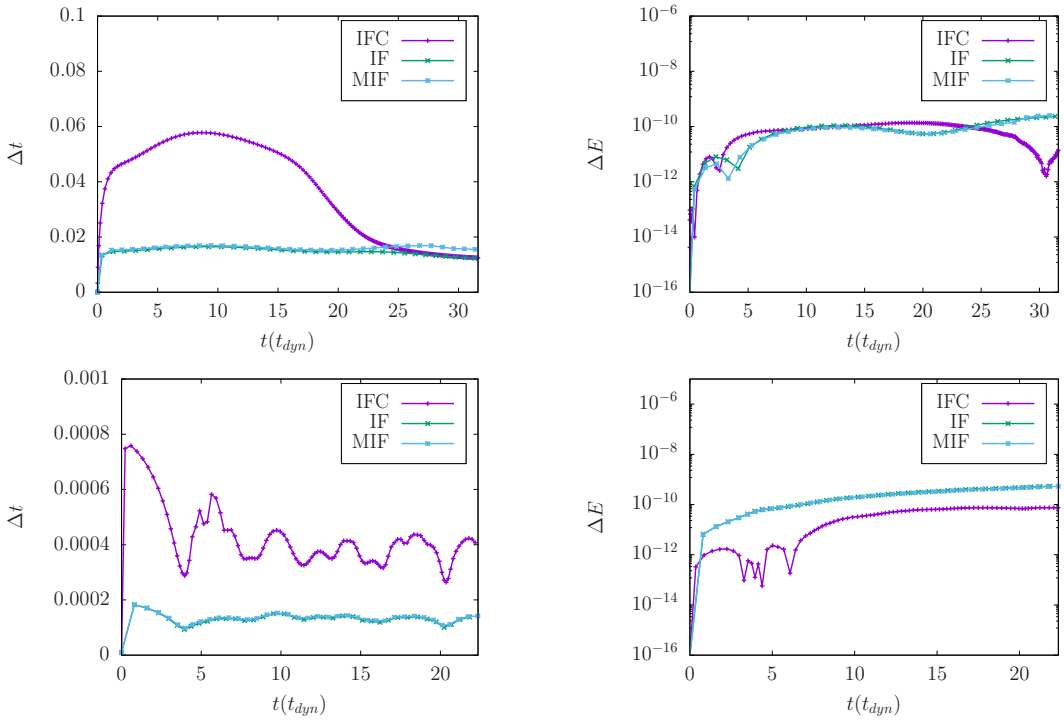

Figure 7.15 – Comparisons for the 2D SN equation between the time-step and the error on the energy conservation with the IF, IFC and MIF methods and for both the cases $g = 10$ ($tol = 10^{-10}$, upper plots) and $g = 500$ ($tol = 10^{-12}$, lower plots).

g	Method	$N_{\Delta t}$	$\Delta\psi_{rev}$	$\Delta\psi_{ref}$	T(s)
10	MIF	637	$1.0 \cdot 10^{-7}$	$4.0 \cdot 10^{-8}$	2798
	IF	689	$9.5 \cdot 10^{-8}$	$2.5 \cdot 10^{-8}$	2028
	IFC	376	$5.8 \cdot 10^{-8}$	$2.9 \cdot 10^{-8}$	1172
500	MIF	7403	$1.2 \cdot 10^{-9}$	$9.1 \cdot 10^{-9}$	25541
	IF	7572	$1.2 \cdot 10^{-9}$	$9.0 \cdot 10^{-9}$	17947
	IFC	2462	$3.0 \cdot 10^{-10}$	$1.6 \cdot 10^{-9}$	6637

Table 7.9 – Comparisons for the 2D SN equation between different methods. $N_{\Delta t}$ denotes the number of time-loops required and T is the time needed to run the simulation, in seconds.

In Table 7.10 and Figure 7.16 we compare the Split-Step integrators with the IFC, looking at the energy conservation error, the error on the solution and the total time needed to run each simulation.

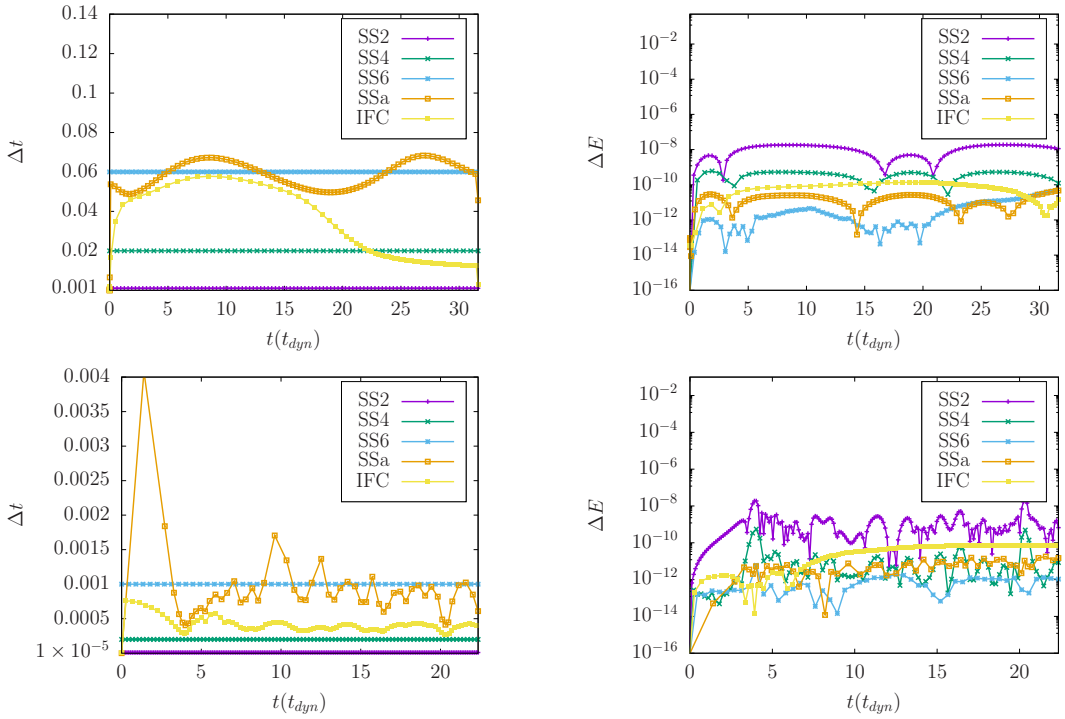

Figure 7.16 – Comparison for the 2D SN equation between the time-step and the error on the energy conservation with the IFC method and the Split-Step solvers for both the cases $g = 10$ (upper plots) and $g = 500$ (lower plots).

g	Method	Δt	$\widehat{\Delta E}$	$\Delta\psi_{rev}$	$\Delta\psi_{ref}$	T(s)
10	SS2	10^{-3}	$1.8 \cdot 10^{-8}$	$3.5 \cdot 10^{-12}$	$1.0 \cdot 10^{-7}$	9070
	SS4	$2 \cdot 10^{-2}$	$6.0 \cdot 10^{-10}$	$1.4 \cdot 10^{-11}$	$3.8 \cdot 10^{-8}$	959
	SS6	$6 \cdot 10^{-2}$	$4.6 \cdot 10^{-11}$	$1.6 \cdot 10^{-7}$	$4.1 \cdot 10^{-8}$	932
	SSa	$6 \cdot 10^{-2}$	$4.7 \cdot 10^{-11}$	$1.4 \cdot 10^{-7}$	$3.9 \cdot 10^{-8}$	1174
	IFC	10^{-2}	$1.3 \cdot 10^{-10}$	$5.8 \cdot 10^{-8}$	$2.9 \cdot 10^{-8}$	1172
500	SS2	10^{-5}	$2.0 \cdot 10^{-8}$	$3.1 \cdot 10^{-10}$	$9.1 \cdot 10^{-8}$	84030
	SS4	$2 \cdot 10^{-4}$	$5.6 \cdot 10^{-10}$	$2.8 \cdot 10^{-11}$	$7.0 \cdot 10^{-9}$	8401
	SS6	10^{-3}	$6.1 \cdot 10^{-12}$	$9.1 \cdot 10^{-11}$	$4.1 \cdot 10^{-9}$	5143
	SSa	$2 \cdot 10^{-3}$	$1.9 \cdot 10^{-11}$	$2.0 \cdot 10^{-11}$	$3.9 \cdot 10^{-9}$	6676
	IFC	$4.5 \cdot 10^{-4}$	$7.5 \cdot 10^{-11}$	$3.0 \cdot 10^{-10}$	$1.6 \cdot 10^{-9}$	6637

Table 7.10 – Comparison for the 2D SN equation between the IFC method and the Split-Step solvers. The Δt for adaptive algorithms is the averaged one. The tolerance for the SSa algorithm is $tol = 10^{-6}$ and $tol = 10^{-7}$ for $g = 10$ and $g = 500$ respectively, and for the IFC algorithm $tol = 10^{-10}$ and $tol = 10^{-12}$ for $g = 10$ and $g = 500$ respectively.

The results are similar to the one dimensional case: the adaptive splitting algorithms proved to be as efficient as the IFC. Here, the *SS4* and *SS6* performed better if compared to the adaptive integrators. This is due the fact that, for this particular system, the extra computational cost due to the implementation of the adaptive-step

is not fully compensated by the time-gain in terms of computational speed. Indeed, splitting algorithms with fixed time-step require a smaller number of computational operations to be implemented. For this reason, here, choosing a "proper" fixed time-step still results in a slightly faster numerical integration compared to an adaptive scheme. However, for systems with a more complicated dynamics, the implementation of an adaptive time-step is crucial to achieve an efficient numerical integration.

7.3.4.1 *Periodical case*

For the 2D periodical case, we run the simulations in a box of side $L = 1$ with $N = 1024^2$, again by using a constant power spectrum as initial condition with the parameter $g = 10^6$, $\rho_0 = 1$ and a zero initial velocity field. In Figure 7.17 some snapshots of the modulus squared of the solution are shown, expressing time in units of $t_{dyn} = 1/\sqrt{g}$.

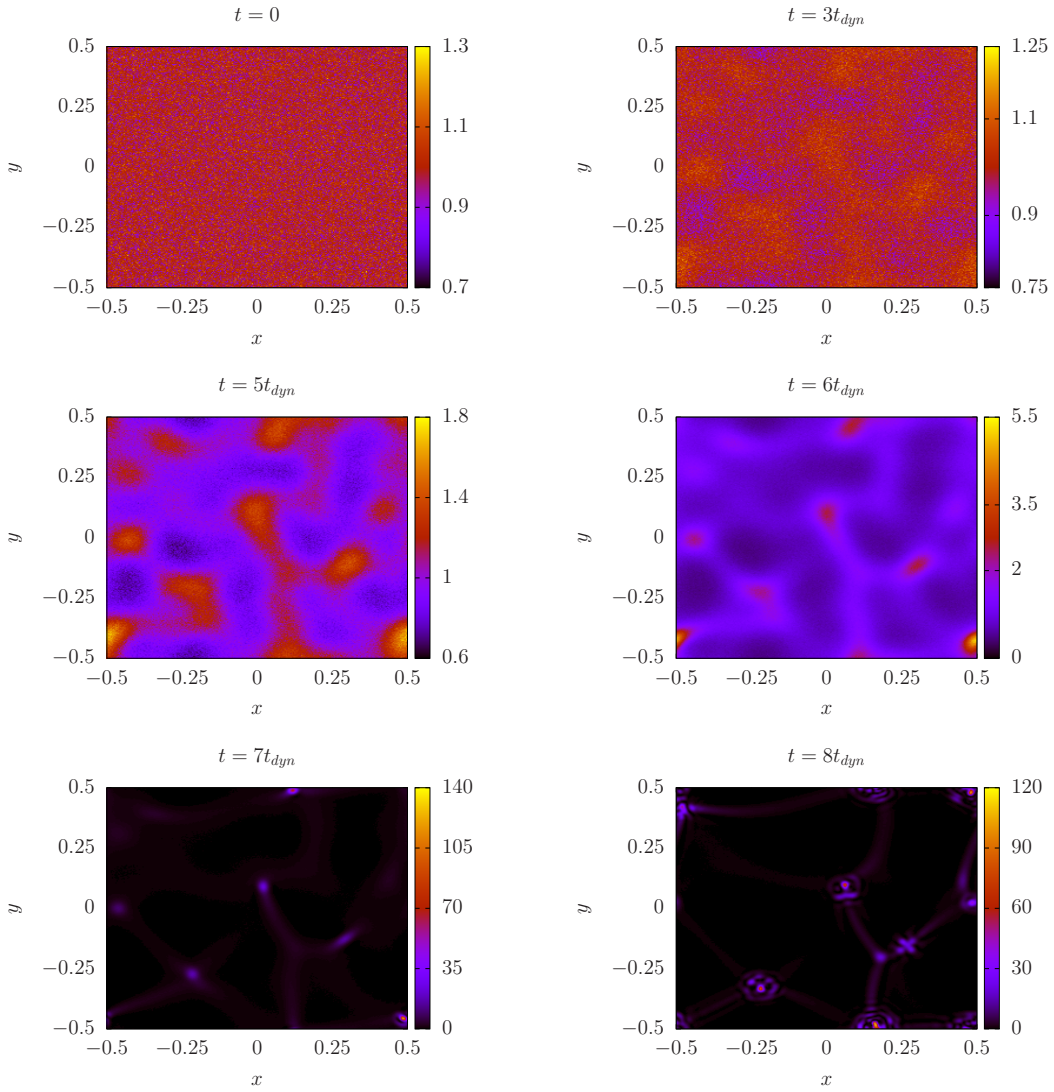

Figure 7.17 – Snapshots of the modulus squared of the solution of the 2D SN equation (periodical case) $|\psi|^2$.

Here we used the Dormand & Prince solver for the adaptive time-step case, the results of the comparison between the different methods based on the integrating factor are shown in Figure 7.18 and Table 7.11.

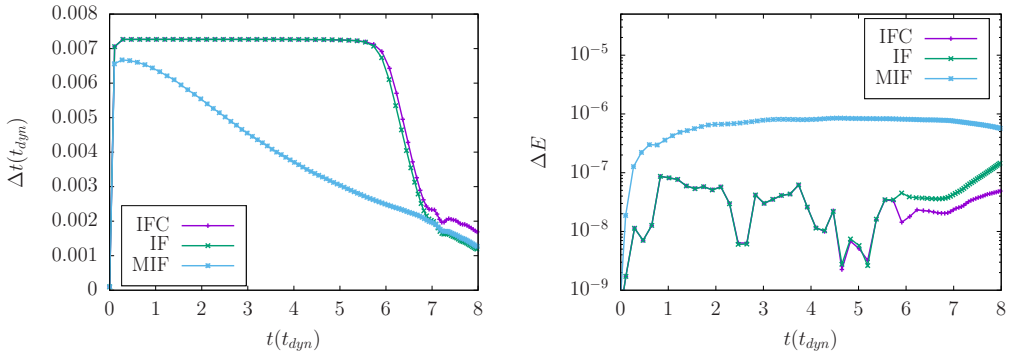

Figure 7.18 – Comparison for the 2D SN equation (periodical case) of the time-step (left plots) and the error on the energy conservation (right plots) for the Dormand & Prince integrator and at fixed tolerance, $\mathrm{tol} = 10^{-12}$.

Method	$N_{\Delta t}$	$\Delta\psi_{rev}$	$\Delta\psi_{ref}$	T(s)
MIF	1882	$2.8 \cdot 10^{-6}$	$8.3 \cdot 10^{-6}$	5050
IF	1135	$4.6 \cdot 10^{-6}$	$8.9 \cdot 10^{-7}$	2147
IFC	1104	$4.6 \cdot 10^{-6}$	$8.9 \cdot 10^{-7}$	2232

Table 7.11 – Comparisons for the 2D SN equation (periodical case) of different methods for the Dormand & Prince integrator at fixed tolerance, $\mathrm{tol} = 10^{-12}$. $N_{\Delta t}$ denotes the number of time-loops required and T is the time needed to run the simulation, in seconds.

In table Table 7.12 and Figure 7.19, we compare the Split-Step integrators with the IFC, looking at the energy conservation error, the error on the solution and the total time needed to run each simulation.

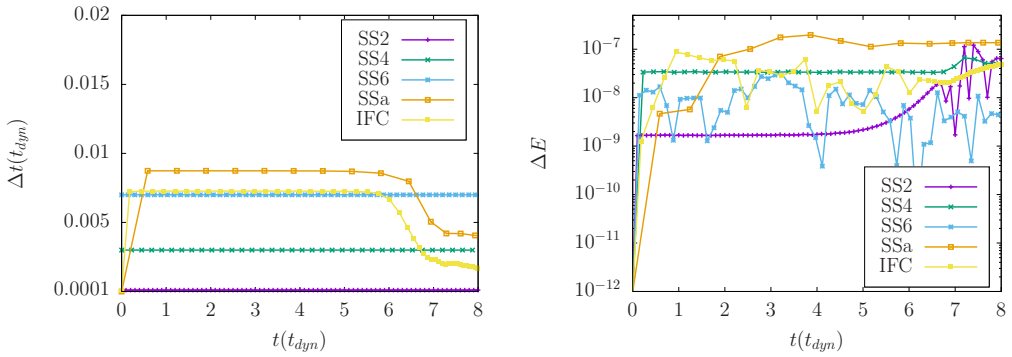

Figure 7.19 – Comparison for the 2D SN equation (periodical case) between the time-step (left plot) and the error on the energy conservation (right plot) for the IFC method and the Split-Step solvers. The $\Delta E(t)$ plots is in a logarithmic scale.

Method	$\Delta t(t_{dyn})$	$\widehat{\Delta E}$	$\Delta\psi_{rev}$	$\Delta\psi_{ref}$	T(s)
SS2	10^{-4}	$1.8\cdot10^{-8}$	$4.5\cdot10^{-9}$	$1.0\cdot10^{-5}$	31711
SS4	$3\cdot10^{-3}$	$4.2\cdot10^{-8}$	$3.1\cdot10^{-6}$	$5.3\cdot10^{-6}$	2485
SS6	$7\cdot10^{-3}$	$3.5\cdot10^{-8}$	$4.5\cdot10^{-10}$	$5.1\cdot10^{-6}$	3046
SSa, tol $=10^{-7}$	$8\cdot10^{-3}$	$2.3\cdot10^{-7}$	$8.5\cdot10^{-7}$	$1.2\cdot10^{-6}$	3362
IF, tol $=10^{-12}$	$6\cdot10^{-3}$	$9.5\cdot10^{-8}$	$4.6\cdot10^{-6}$	$8.9\cdot10^{-7}$	2147

Table 7.12 – Comparison for the 2D SN equation (periodical case) between the IFC method and the Split-Step solvers. T is the total time required to run each simulation, measured in seconds. The Δt for adaptive algorithms is the averaged one.

Here we obtain the same result than in one dimension, with the IFC being the most efficient method.

7.3.5 *Gross–Pitaevskii–Poisson equation*

We conclude by presenting the results for the 2D Gross–Pitaevskii–Poisson equation, which is a combination of the NLS and SN equations

$$
\begin{aligned}
&i\,\partial_t\psi + \frac{1}{2}\nabla^2\psi - V\psi = 0\\
&V = V_1 + V_2\\
&\nabla^2 V_1 = g_1\,|\psi|^2\\
&V_2 = g_2\,|\psi|^2\,.
\end{aligned}
$$

In the case of open boundary conditions, we would expect the split-step or the integrating factors to outperform one the other, depending on the values of g_1 and g_2. We set them to $g_1 = -3$ and $g_2 = 100$ which are very close to the one typically employed when simulating the collapse of a self-gravitating Bose-Einstein condensate with attractive self-interaction [24]. The numerical parameters are $N = 2048^2$, $L = 40$ and $t_f = 5$ while the initial condition is a Gaussian, $\psi(r, t = 0) = e^{-\frac{r^2}{2}}/\sqrt{\pi}$. In Table 7.13 comparisons between the most efficient methods tested for the NLS (SS6 or SSa, depending on the parameters) and the SN (IFC method) are shown. For the values of g_1 and g_2 we use, the IFC method outperforms the split-step solvers. Moreover, we observe that for our particular initial condition, the smaller the $\frac{g_1}{g_2}$ ratio is, the better the IFC performs with respect to the splitting methods, with a robust difference already appearing for $\frac{g_1}{g_2} \lessapprox 0.1$.

Method	Δt	$\widehat{\Delta E}$	$\Delta\psi_{rev}$	$\Delta\psi_{ref}$	T(s)
SS6	$2.5\cdot10^{-3}$	$1.2\cdot10^{-9}$	$4.5\cdot10^{-11}$	$4.5\cdot10^{-8}$	32753
SSa, tol $=10^{-7}$	$4\cdot10^{-3}$	$2.4\cdot10^{-11}$	$2.2\cdot10^{-8}$	$1.4\cdot10^{-8}$	63315
IFC, tol $=10^{-11}$	$2\cdot10^{-3}$	$7.7\cdot10^{-10}$	$6.2\cdot10^{-8}$	$2.3\cdot10^{-8}$	28273

Table 7.13 – Comparison for the 2D Gross–Pitaevskii–Poisson equation between the IFC and the Split-Step methods. T is the total time required to run each simulation, measured in seconds.

Part III

EXPERIMENT

8 DESCRIPTION OF THE EXPERIMENT

In this chapter, we describe the experiment we performed to observe the violent relaxation mechanism in an optical setup. First, we outline the main goals of the experiment. Second, we illustrate the experimental setup and procedure. Finally, we discuss some additional elements one needs to incorporate in the Newton–Schrödinger equation to model more accurately the system.

8.1 GOAL

The goals of this experiment, are the following.

1. Provide a quantitative comparison between theory and experiment, comparing the measurements with the prediction of the Newton-Schrödinger model.
2. Observe experimentally the violent relaxation mechanism.
3. Observe characteristic phenomena of long range interacting systems, such as the formation of a quasi stationary state, mixing and shell-crossing.

To our knowledge, none of the aforementioned goals has been achieved so far, except for qualitative comparisons, which have been already done in other experiments [132, 133]. Indeed, experiments with these kind of systems with long range interactions, which mimic the gravitational one, are difficult to realize. For instance, possible physical environments for the observation of violent relaxation are: cold classical atoms [134], different kind of Bose gases [135–137] such as trapped electron plasma [138–145], quasi-two-dimensional superfluids [78, 146], and atomic gases [147]. However, because of the presence of the stochastic noise, in all of these systems it is only possible to observe the thermodynamic equilibrium, not the violent relaxation mechanism. This mechanism is similar to to Landau damping in plasma physics, where there is an exchange of energy between the electromagnetic wave generated by the particles of the plasma and the particles themselves [148]. Landau damping has been observed, for repulsive interactions, in plasma experiments [140–143, 149–151] and in space plasma turbulence [144]. Moreover, some theoretical works about the possible observation of such phenomena in electron rings are described in [152, 153].

8.2 EXPERIMENTAL SETUP AND PROCEDURE

To achieve the experimental goals, one need to measure the laser beam optical field $\mathcal{E}$. This is in general a complex quantity, hence the information about both the intensity profile $I(\mathbf{r}_\perp, z) = |\mathcal{E}(\mathbf{r}_\perp, z)|^2$ and the phase $\theta(\mathbf{r}_\perp, z) = \arg \mathcal{E}(\mathbf{r}_\perp, z)$ are needed.

The experimental setup is summarized in Figure 8.1: a continuous-wave laser with a Gaussian profile centered at $\lambda = 532\,\mathrm{nm}$ passes through a 90 T : 10 R non-polarizing beam splitter, where the reflected part becomes the reference beam (a), and the transmitted part becomes the target beam (b). Whereas (a) goes through a telescope with a 4:1 magnification factor so that a significantly large profile in the (x, y) plane is

obtained (in order to have a good approximation of a reference plane wave), (b) goes through a telescope with a 1:2 magnification factor and then shines onto three slab of lead-doped glass (each one with height $D = 5\,mm$, length $l_0 = 100\,mm$ and width $W = 40\,mm$), which is a self-focusing nonlinear optical medium with the following optical parameters: thermal conductivity $\kappa = 0.7\,W m^{-1} K^{-1}$, background refractive index $n_b = 1.8$, absorption coefficient $\alpha = 1\,m^{-1}$, and thermo-optic coefficient $\beta = \frac{\partial n}{\partial T} = 1.4 \cdot 10^{-5} K^{-1}$.

The sets of beam intensity profiles and interferograms are collected for powers ranging from $0.19\,W$ to $5.47\,W$, with a $0.25\,W$ step. The experimental values of the beam intensity at the output facet of the medium are obtained by means of an imaging technique. Specifically, after the $l = 300\,mm$ nonlinear propagation, the output facet of the medium is imaged onto a CMOS camera. The collection of information on the phase of the same beam requires a tool called *Off-Axis Digital Holography*, which is fully explained in [154]. In the Off-Axis Digital Holography technique, a target beam and a reference plane wave are imaged together onto a detector, creating an interference pattern in direct space (x, y): this interferogram has intensity fringes whose number and tilt depend on the angle α between the directions of propagation z_1 and z_2 of the target beam and the reference wave, and the relative polarization of the two beams is tuned by using one $\lambda/2$ waveplate in order to have the highest visibility of the fringes. When a Fourier transform is operated on this interference profile, two identical copies of the Fourier transform of the target beam are observed in the (k_x, k_y) plane at a distance from the $(k_x = 0, k_y = 0)$ point that depends on the angle α; one of these Fourier transforms copies is then inversely transformed to direct space, resulting in a complex matrix $A(x, y) = A_0(x, y) e^{i\theta(x,y)}$, where $A_0(x, y)$ and $\theta(x, y)$ are the retrieved amplitude and phase profiles of the target beam, respectively. It is possible to switch from collecting the interferograms to collecting the intensities simply by stopping the reference beam.

8.3 EXACT MODELING OF THE EXPERIMENTAL SETUP

We now discuss some aspects of the experimental setup which need to be incorporated in the model, together with the range of validity of the approximations employed so far. First, we discuss the role of dissipations, such as absorption and back-reflections. Then, we explain how the dynamics along the propagation direction can be reconstructed by only performing measurements at the end of the material interface and not inside it. Finally, we discuss the contribute of boundary effects.

8.3.1 *Absorption and back-reflections*

In this experimental setup, there are dissipation effects, due to the absorption and back-reflections, which need to be taken into account in the model. As discussed in Section 2.4.2, absorption can be modeled adding an extra term in the equation describing the propagation of the laser beam

$$i \frac{\partial \mathcal{E}}{\partial z} + \frac{1}{2k} \nabla_\perp^2 \mathcal{E} + k_0 \Delta n \, \mathcal{E} + i \frac{\alpha}{2} \mathcal{E} = 0, \tag{8.1}$$

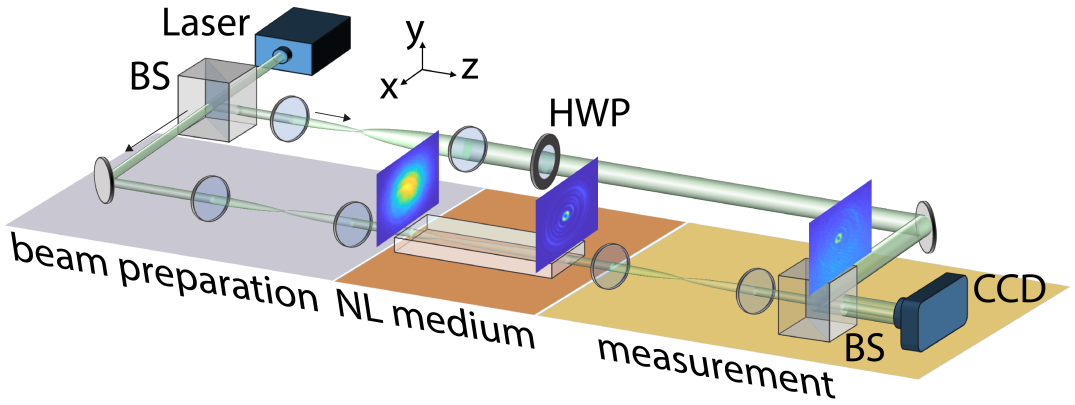

Figure 8.1 – Illustration of the experimental setup for obtaining the intensity and phase profiles of a beam undergoing an optical analogue evolution of the Newton–Schrödinger equation. A continuous-wave laser with a Gaussian profile centered at $\lambda = 532\,\mathrm{nm}$ passes through a 90 T : 10 R non-polarizing beam splitter, where the reflected part becomes the reference beam (a), and the transmitted part becomes the target beam (b). Whereas (a) goes through a telescope with a 4:1 magnification factor so that a significantly large profile in the (x, y) plane is obtained (in order to have a good approximation of a reference plane wave), (b) goes through a telescope with a 1:2 magnification factor and then shines onto three slab of lead-doped glass.

which introduces an exponential drop of the total power P of the beam,

$$\iint d\mathbf{r}_\perp \, |\mathcal{E}(\mathbf{r}_\perp, z)|^2 = e^{-\alpha z} P. \tag{8.2}$$

In our setup configuration, the value of the absorption coefficient is $\alpha = 0.01\,\mathrm{cm}^{-1}$, while the total propagation length is $z_{fin} = 30\,\mathrm{cm}$. Hence the contribute of absorption is expected to attenuate the total power by a factor $e^{-0.3} \approx 0.74$.

Another important dissipation effect, which must be taken into account, is the contribute of back-reflections. The latter comes from the experimental configuration as well. Specifically, given that the medium is obtained by combining three identical samples, each one with length $l = 100\mathrm{mm}$, and transmittance of the transverse surface $T = 0.92$, power drops take place at each facet through which the beam propagates. These power drops can be incorporated in the model, multiplying the intensity by a factor $T = 0.92$ at the values of z where a back-reflection is taking place. Thus, the intensity is multiplied by the following function

$$B_R(z) = \begin{cases} T & \text{if } z = 0 \\ T^3 & \text{if } z = 10\,\mathrm{cm} \\ T^5 & \text{if } z = 20\,\mathrm{cm} \\ T^6 & \text{if } z = 30\,\mathrm{cm}. \end{cases} \tag{8.3}$$

However, taking into account only back-reflections which take place during the actual propagation inside the medium, the $z = 0$ and $z = 30\,\mathrm{cm}$ contributions can be excluded. This results in an attenuation by a factor $T^4 \approx 0.72$, during the propagation

length. Regarding the total power injected in the medium, it is reduced of a factor $T^6 \approx 0.6$.

Therefore, the combination of these two effects, absorption and back-reflections, reduces the total power of roughly 50%. However, this dissipation does not prevent the violent relaxation mechanism to take place. Indeed, in the astrophysical picture of the Newton–Schrödinger equation, power loss along the propagation direction are mapped into mass loss in time. Specifically, the absorption would corresponds to a global loss of mass in the system of amount $M(t) = M(0)\exp(-\alpha t)$ and each reflection in the experiment would determine mass loss of amount $1 - T$, which do not alter the presence of violent relaxation in the system.

8.3.2 *Reconstructing the dynamics along the propagation direction*

To reconstruct the dynamics along the propagation direction, one should in principle measure the laser beam optical field $\mathcal{E}(\mathbf{r}_\perp, z)$ at different values of the propagation coordinate z. This would result in performing measurements inside the medium as well, which can however be avoided exploiting a scaling symmetry of the equation which model the system. Indeed, if $\mathcal{E}(\mathbf{r}_\perp, z)$ and $\Delta n(\mathbf{r}_\perp, z)$ are solutions of

$$\begin{aligned} i\frac{\partial \mathcal{E}}{\partial z} + \frac{1}{2k}\nabla_\perp^2 \mathcal{E} + k_0 \Delta n\, \mathcal{E} &= 0 \\ \nabla_\perp^2 \Delta n &= -\frac{\alpha\beta}{\kappa}|\mathcal{E}|^2 , \end{aligned} \tag{8.4}$$

then, $\gamma\,\mathcal{E}(\gamma\,\mathbf{r}_\perp, \gamma^2 z)$ and $\gamma\,\Delta n(\gamma\,\mathbf{r}_\perp, \gamma^2 z)$ are solutions of (8.4) as well, for any value of γ. This scaling symmetry implies that changing the power and the width of the laser beam, is equivalent to explore different values of z. Notice how, in presence of losses, like absorption, this scaling symmetry does not hold anymore. However, in our experimental regime, a mapping between power and propagation length can still be applied. This is discussed in Appendix C, where we show that the undergoing physics in this system in not significantly changed by the presence of losses.

In addition, for small values of the χ parameter, defined in Section 4.2.2,

$$\chi = \frac{\lambda_B}{s} = \sqrt{\frac{2\pi\kappa n_b}{k^2\alpha\beta P s^2}} \tag{8.5}$$

it is possible to explore different values of z only by changing the power, leaving the width of the laser beam unaltered. This is due to the fact that, as Figure 8.2 shows, for $\chi \ll 1$, the dynamics of the system does not display significant differences when varying χ, especially before the collapse. Therefore, at small χ, the full dynamics along the propagation length z can be reconstructed by only performing the measurements at the output facet of the medium.

An example of this procedure is illustrated in Figure 8.3, where the power axis must be interpreted as a quantity playing the role of the longitudinal coordinate z.

8.4 ROLE OF THE LONGITUDINAL NONLOCALITY

Another important element, which has been studied in [155] and must be taken into account when modeling this optical system, is the role of the longitudinal nonlocality. Here, we discuss a simple example, addressed to our experimental setup. The

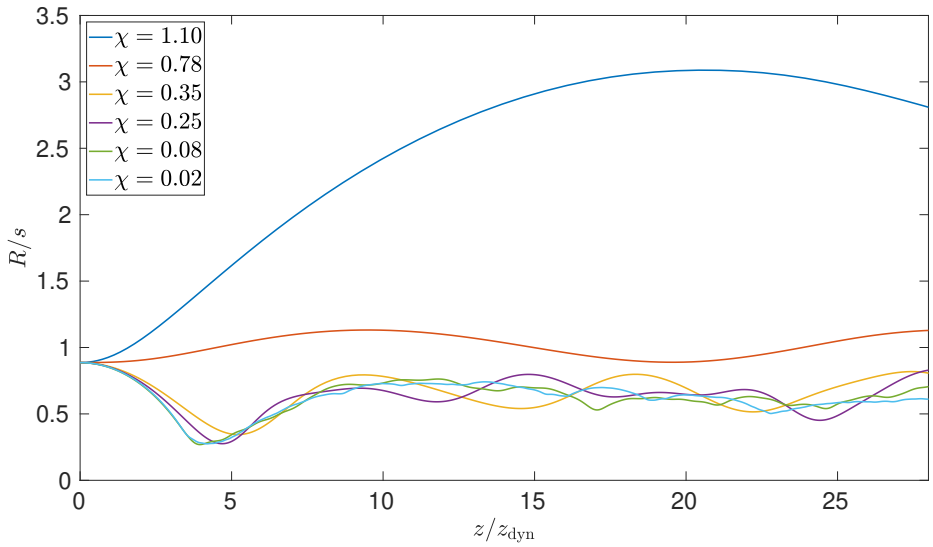

Figure 8.2 – Plot of the average size of the laser beam $< r >= R$ as a function of the longitudinal coordinate z in units of z_{dyn}, for different values of χ.

problem, discussed in Section 2.4.1, concerns the range of validity of neglecting the ∂_z^2 term in the heat equation. The latter, in the stationary regime, reads

$$\kappa\nabla^2(\Delta T)_{3d}(\mathbf{r}) = -\alpha I(\mathbf{r}), \tag{8.6}$$

where $(\Delta T)_{3d}$ is the change in temperature, related to the refractive index variation Δn through the medium thermo-optic coefficient, $\Delta T = \beta\Delta n$. The problem is three-dimensional, so the Laplace operator in (8.6) is, in Cartesian coordinates,

$$\nabla^2 = \partial_x^2 + \partial_y^2 + \partial_z^2. \tag{8.7}$$

In the current model, it is assumed that the derivative along the propagation axis z is much smaller than the one in the transverse plane (x, y), i.e., defining $\nabla_\perp^2 = \partial_x^2 + \partial_y^2$, one has that $\nabla_\perp^2 \gg \partial_z^2$. When this paraxial approximation is applied (see Section 2.4.1), (8.6) can be written as

$$\kappa\nabla_\perp^2(\Delta T)_{2d}(\mathbf{r}_\perp, z) = -\alpha I(\mathbf{r}_\perp, z). \tag{8.8}$$

Using (8.8) instead of (8.6) is equivalent to assume that, when calculating $\Delta T(\mathbf{r}_\perp, z_0)$ for a given z_0 with (8.6), $I(\mathbf{r}_\perp, z) = I(\mathbf{r}_\perp, z_0)\ \forall z$. This coincides with assuming that the the system is spatially infinite along the direction z.

In order to better understand the paraxial approximation, let us perform an explicit calculation for a Gaussian beam of size $s = 300\mu m$ and a propagation medium of $L = 30cm$. For simplicity, we assume that the intensity is

$$I(\mathbf{r}_\perp, z) = \frac{1}{2\pi s^2}\exp\left(-\frac{r_\perp^2}{2s^2}\right), \tag{8.9}$$

for all $z \in [0, L]$. One can calculate $(\Delta T)_{3d}$ with the Green integral

$$\nabla^2(\Delta T)_{3d}(\mathbf{r}) = -\frac{\alpha}{\kappa}\int_D d\mathbf{r}'\frac{I(\mathbf{r}')}{|\mathbf{r}-\mathbf{r}'|}, \tag{8.10}$$

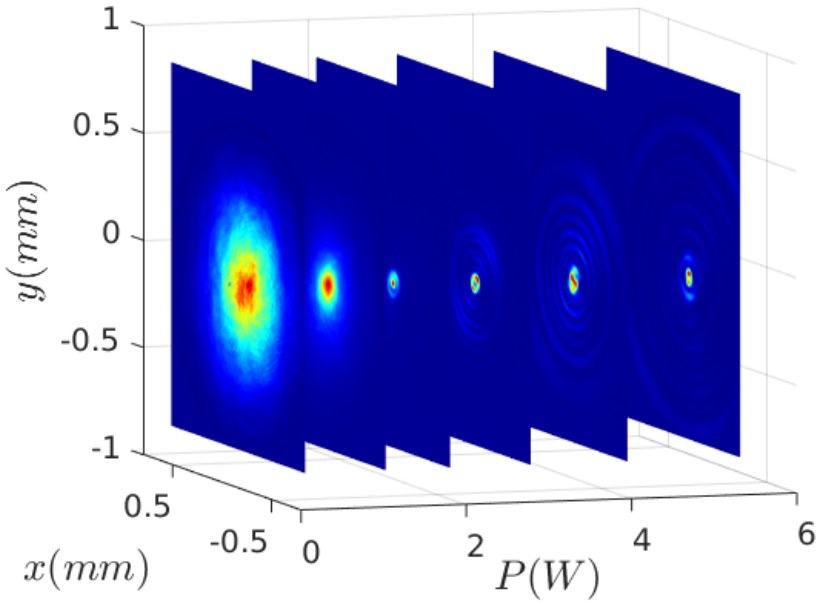

Figure 8.3 – Intensity profile measurements at the end of the material interface for different powers.

where D is the whole glass. Using cylindrical coordinates $(\boldsymbol{\rho}, z)$, such that $\mathbf{r} = \rho\hat{r} + z\hat{z}$ and choosing $\boldsymbol{\rho}$ to be parallel with the x axis, one has

$$|\mathbf{r} - \mathbf{r}'| = \sqrt{|\boldsymbol{\rho} - \boldsymbol{\rho}'| + (z - z')^2} = \sqrt{\rho^2 + \rho'^2 - 2\rho\rho'\cos\phi + (z - z')^2}. \tag{8.11}$$

In this system of coordinates (8.10) reads

$$\begin{aligned} \nabla^2(\Delta T)_{3d}(\rho, z) &= -\frac{\alpha}{2\kappa\pi\sigma^2}\int_0^L dz' \int_0^\infty d\rho'\rho' e^{-\rho'^2/2\sigma^2} \\ &\times \int_0^{2\pi} d\phi \frac{1}{\sqrt{\rho^2 + \rho'^2 - 2\rho\rho'\cos\phi + (z - z')^2}}. \end{aligned} \tag{8.12}$$

Integrating over ϕ one obtains

$$\begin{aligned} \nabla^2(\Delta T)_{3d}(\rho, z) &= -\frac{\alpha}{\kappa\pi\sigma^2}\int_0^L dz' \int_0^\infty d\rho'\rho' e^{-\rho'^2/2\sigma^2} \\ &\times \left[\frac{K\left(-\frac{4\rho\rho'}{(z-z')^2+(\rho-\rho')^2}\right)}{\sqrt{(\rho - \rho')^2 + (z - z')^2}} + \frac{K\left(\frac{4\rho\rho'}{(z-z')^2+(\rho+\rho')^2}\right)}{\sqrt{(\rho + \rho')^2 + (z - z')^2}}\right]. \end{aligned} \tag{8.13}$$

The remaining integrals in (8.13) have to be performed numerically.

Before looking to some numerical examples, it is interesting to understand how the solution of (8.8) can be obtained from (8.10). Changing the order of integration, the integrals of (8.12) are modified into

$$\begin{aligned} \nabla^2(\Delta T)_{2d}(\rho) &= -\frac{\alpha}{2\kappa\pi\sigma^2}\int_0^\infty d\rho'\rho' e^{-\rho'^2/2\sigma^2} \\ &\times \int_0^{2\pi} d\phi \int_{-\infty}^\infty dz' \frac{1}{\sqrt{\rho^2 + \rho'^2 - 2\rho\rho'\cos\phi + z'^2}}, \end{aligned} \tag{8.14}$$

where the dependence on z has been removed because $(\Delta T)_{2d}$ does not depend on it anymore [1].

Since we are implicitly imposing the potential of a distribution which is spatially extended up to infinity, to be zero at infinity, the integral about z' in (8.14) is not convergent. However, this divergence can be treated by removing an (infinite) constant,

$$\lim_{L\to\infty}\int_{-L}^{L} dz' \frac{1}{\sqrt{|\boldsymbol{\rho}-\boldsymbol{\rho}'|+z'^2}} = \lim_{L\to\infty} 2\ln\left(\frac{\sqrt{|\boldsymbol{\rho}-\boldsymbol{\rho}'|^2+L^2}+L}{|\boldsymbol{\rho}-\boldsymbol{\rho}'|}\right). \tag{8.15}$$

Performing an expansion at first order around $L\to\infty$ one obtains

$$\lim_{L\to\infty}\int_{-L}^{L} dz' \frac{1}{\sqrt{|\boldsymbol{\rho}-\boldsymbol{\rho}'|+z'^2}} = \lim_{L\to\infty} 2\ln\left(\frac{2L}{|\boldsymbol{\rho}-\boldsymbol{\rho}'|}\right) + \mathcal{O}\left(\frac{1}{L^2}\right). \tag{8.16}$$

Once the limit is taken, one has

$$\int_{-\infty}^{\infty} dz' \frac{1}{\sqrt{|\boldsymbol{\rho}-\boldsymbol{\rho}'|+z'^2}} = -2\ln\left(|\boldsymbol{\rho}-\boldsymbol{\rho}'|\right) + 2\lim_{L\to\infty}\ln(2L), \tag{8.17}$$

which is the Green's kernel of our two-dimensional problem, except the (infinite) constant which has been removed. Since the chosen intensity is normalized to unity, (8.14) yields

$$\begin{aligned}\nabla^2(\Delta T)_{2d}(\rho) &= \frac{\alpha}{\kappa\pi\sigma^2}\lim_{L\to\infty}\ln(2L) \\ &- \frac{\alpha}{\kappa\pi\sigma^2}\int_0^{\infty} d\rho'\rho' e^{-\rho'^2/2\sigma^2}\int_0^{2\pi} d\phi \ln\left(\rho^2+\rho'^2-2\rho\rho'\cos\phi\right).\end{aligned} \tag{8.18}$$

In this particular case it is possible to obtain an analytical solution of (8.18),

$$\begin{aligned}\nabla^2(\Delta T)_{2d}(\rho) &= \frac{\alpha}{\kappa\pi\sigma^2}\lim_{L\to\infty}\ln(2L) \\ &- \frac{\alpha}{\kappa\pi\sigma^2}\left[\mathrm{Ei}\left(-\frac{\rho^2}{2\sigma^2}\right)-2\log(\rho)\right].\end{aligned} \tag{8.19}$$

In Figure 8.4 we show the ratio $(\Delta T)_{3d}/(\Delta T)_{2d}$, removing appropriately the divergence in $(\Delta T)_{2d}$, for the whole crystal along z (note that the z axis is divided by L). Length is in units of the initial radius of the beam (s"="300μm). We observe a not negligible discrepancy for a relatively large part of the material. However, if one looks to the gradient of (ΔT), since this quantity is less long-range than (ΔT), the discrepancy is much smaller. Indeed, Figure 8.6 and Figure 8.5 show that the direction of the gradient is correct except up to $z \approx L/10$ at each side of the sample.

For small values of the parameter χ, namely when the semiclassical limit is approached, the relevant quantity is not ΔT, but the the gradient of ΔT. Indeed for a classical system, the meaningful quantity is the force, namely the gradient of the potential, not the potential itself. For this reason the role of the longitudinal nonlocality can be safely neglected in our experimental configuration.

1. In our physical problem ΔT depends indeed on z, what we actually do when calculating $\Delta T(\rho, z_0)$ is to replace (implicitly) in (8.14) $I(\rho', z')$ by $I(\rho', z_0)$.

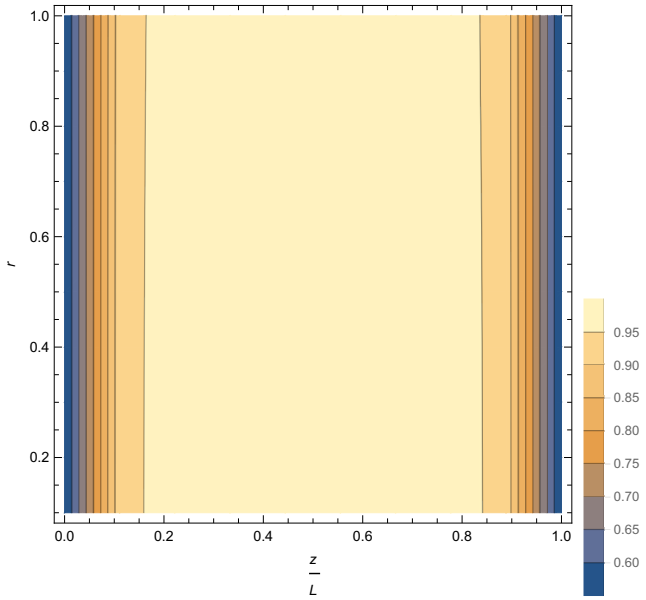

Figure 8.4 – Ratio $(\Delta T)_{3d}/(\Delta T)_{2d}$ for the whole crystal along z (note that the z axis is divided by L). Length is in units of the initial radius of the beam (i.e. 1"="300μm).

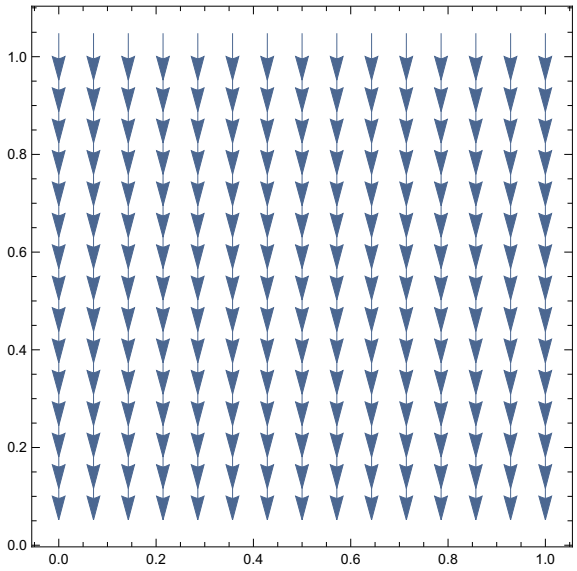

Figure 8.5 – Normalized to unity gradient of $(\Delta T)_{2d}$ Length is in units of the initial radius of the beam (i.e. 1"="300μm). Horizontal axis z/L, vertical axis ρ.

8.5 BOUNDARY CONDITIONS

When solving the Newton–Schrödinger equation, proper boundary conditions must be incorporated both for the field $\mathcal{E}$ and the variation of the refractive index Δn. Concerning the former, for a Gaussian beam initial condition, the intensity is expected to be zero very far from the center of the signal. In the case of a medium with infinite size one would simply have $\mathcal{E}(r_\perp \to \infty, z) \to 0 \,\forall\, z$, while, for our setup, since

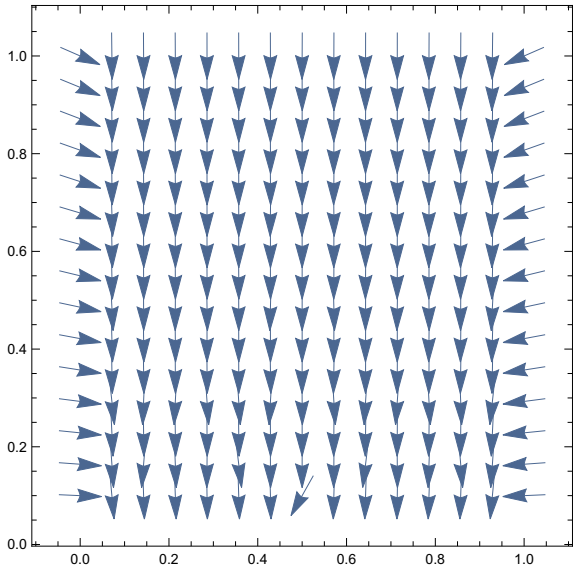

Figure 8.6 – Normalized to unity gradient of $(\Delta T)_{3d}$ Length is in units of the initial radius of the beam (i.e. 1"="300μm). Horizontal axis z/L, vertical axis ρ.

the medium transverse section is much large then the size of the laser beam, open boundary conditions can be set for $\mathcal{E}$.

Boundary conditions for the refractive index variation on the other hand, require a deeper discussion. Indeed, in the case of a sample with finite sizes, the temperature distribution at the edges of the thermo-optical medium must be taken into account. To do that, one should in principle measure the temperature along the boundaries of the medium, which in general can also be non-uniform in z and asymmetrical. This might lead, because of the nonlocality, to important effects for the beam profile, as typically happens in nonlocal media [155–157]. For example, asymmetric boundary conditions can produce, starting from a radially symmetric initial condition, an elliptic soliton beam [12]. However, as we shall see next, in our setup configuration these boundary effects can be safely neglected.

Boundary conditions for Δn can be of several nature: for example in the case where the edges of the medium are kept at a fixed temperature, Dirichlet boundary conditions should be used; if there is a prescribed heat flux from the medium to the external environment, Neumann's boundary conditions must be taken into account. In the most general case one has a linear combination of the two, which goes under the name of Robin boundary condition or convective boundary condition

$$a\,\Delta n(\mathbf{r}_\perp, z) + b\,\frac{\partial \Delta n}{\partial \hat{n}}(\mathbf{r}_\perp, z) = f(\mathbf{r}_\perp, z) \quad \forall\, \mathbf{r}_\perp \in \partial\Omega, \tag{8.20}$$

where a and b are some nonzero constants, $\frac{\partial}{\partial \hat{n}}$ is the derivative in the direction $\hat{n}$ perpendicular to the boundaries which are denoted as $\partial\Omega$ and f is a given function.

8.5.1 *Distributed loss model*

In the case where the boundary conditions are symmetrical and uniform in z, as an alternative, one can consider a phenomenological model which incorporates thermal

losses due to the presence of the boundaries [158]. In this way, the refractive-index equation is modified into a screened Poisson equation

$$\nabla_\perp^2 \Delta n - \frac{1}{\sigma^2}\Delta n = -\frac{\alpha\beta}{\kappa}|\mathcal{E}|^2 \tag{8.21}$$

where σ is the non-locality degree which represents the interaction length scale set by thermal diffusion. Defining the response function $R(\mathbf{r}_\perp)$ as

$$\Delta n(\mathbf{r}_\perp, z) = \iint d\mathbf{r}'_\perp \, R(\mathbf{r}_\perp - \mathbf{r}'_\perp)\, |\mathcal{E}(\mathbf{r}'_\perp, z)|^2, \tag{8.22}$$

it is easy to check that for the distributed loss model case, the response function is a modified Bessel function of the second kind

$$R(\mathbf{r}_\perp) \propto K_0\left(\frac{\mathbf{r}_\perp}{\sigma}\right), \tag{8.23}$$

which avoids the logarithmic divergence of the 2-dimensional Poisson equation in the open boundary conditions case. In Fourier space, since $\widehat{\Delta n}(\mathbf{k}_\perp, z) = \widehat{R}(\mathbf{k}_\perp)\,\widehat{I}(\mathbf{k}_\perp, z)$, one has

$$\widehat{\Delta n} = \frac{\alpha\beta\sigma^2}{\kappa}\frac{\widehat{|\mathcal{E}|^2}}{1+\sigma^2 k^2}. \tag{8.24}$$

Notice that in the limit $\sigma \to \infty$ the infinite space model is recovered, with (8.24) becoming the standard Poisson equation and the modified Bessel function of the second kind, tending to the logarithm

$$R(\mathbf{r}_\perp) = K_0\left(\frac{r_\perp}{\sigma}\right) = -\log\frac{r_\perp}{\sigma} + \text{const} + O\left(\frac{r_\perp^2}{\sigma^2}\right). \tag{8.25}$$

This approximation is more accurate for a laser beam whose width w is much smaller compared to the shortest side D of the medium. The nonlocal degree is then approximated with half the characteristic size of the medium, i.e. $\sigma \approx D/2$.

In Figure 8.7, we compare the dynamics of the system for different boundary conditions: Dirichlet, Neumann and open boundary conditions. In our configuration, where the boundaries are sufficiently far from the laser beam, there are minimal differences between the open boundary conditions case and the distribution loss model. Hence, for simplicity, the latter can be used when simulating the system as long as $s \ll D$, which is our case.

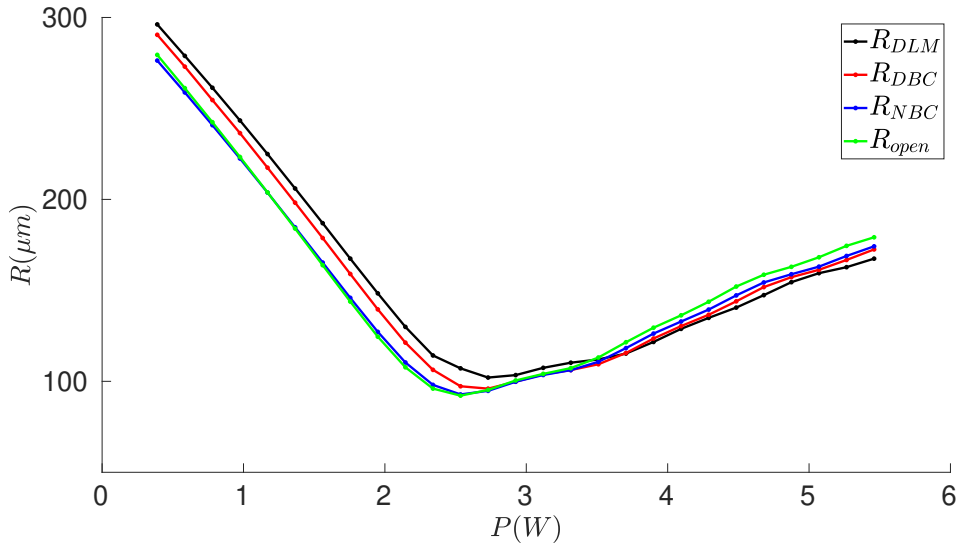

Figure 8.7 – Comparison between the outputs of the Newton–Schrödinger equation simulation with the Distributed loss Model (DLM) and Dirichlet (DBC), Neumann (NBC) and open boundary conditions (open) for the average size of the beam profile as a function of power.

9 EXPERIMENTAL RESULTS

In this chapter, we present the results of the experiment. First, we discuss the analysis of the data collected during the measurements, explaining how the noise is treated and how the initial condition is interpolated. Second, we compare the experimental data with simulations, both in real space for the intensity profile and the average beam size, and in phase-space with the Wigner distribution. Finally, we show the most important indicators for the violent relaxation mechanism: mixing, shell-crossing and energy exchange.

9.1 NOISE TREATMENT

The experimental intensity profiles are characterized by a background noise. The latter results as an offset different from zero at large distances from the main body of the beam, as shown in Figure 9.1 where one-dimensional slices of the intensity profile are plotted. This noise is relatively small and hardly appreciable if the two-dimensional intensity profiles are plotted, as shown in Figure 9.2. However, it becomes very important when integral quantities, such as the average beam size $R(z) = \int dxdy\sqrt{x^2+y^2}I(x,y,z)/P$ are evaluated.

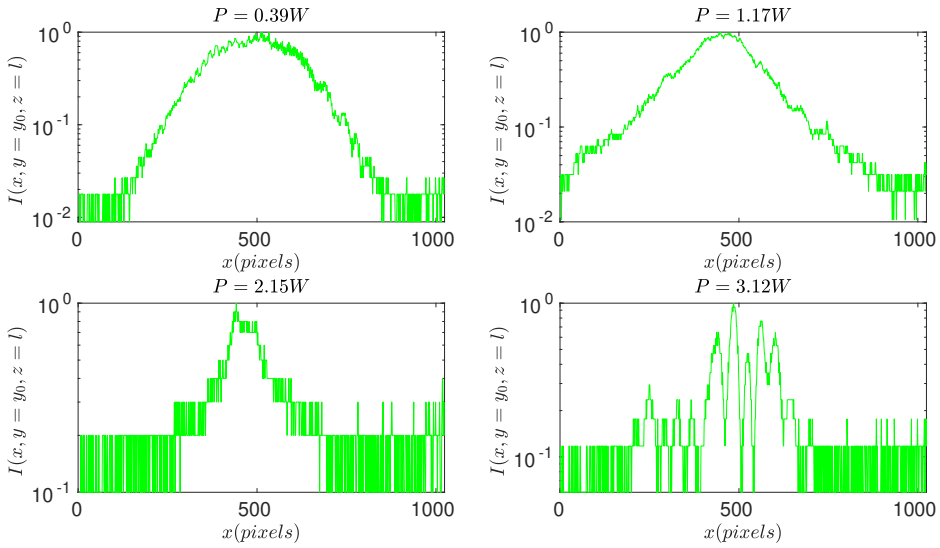

Figure 9.1 – Row data of one dimensional slices of the laser beam intensity profile for different values of power, acquired with an imaging technique. The x-axis is in units of camera pixels, with 1 pixel= 5.3µm. The vertical axis, which is in a logarithmic scale, has been renormalized to the maximal value of intensity.

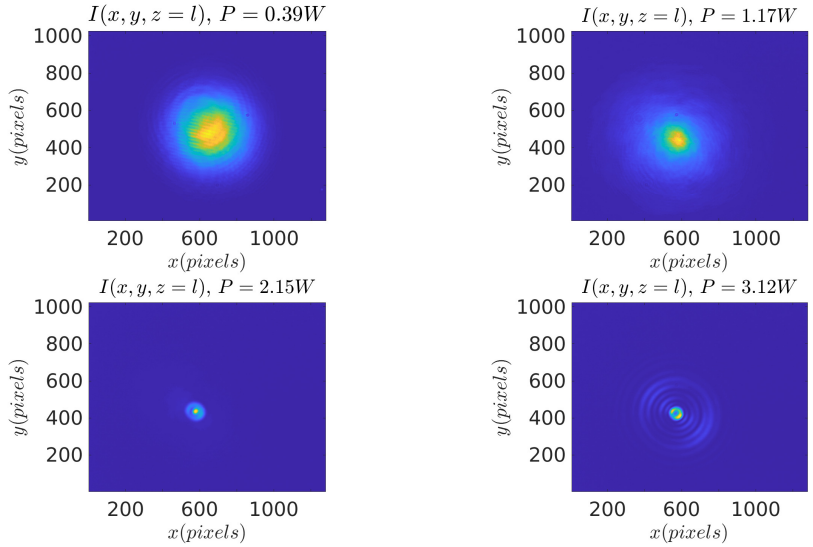

Figure 9.2 – Row data of the laser beam intensity profile for different values of power, acquired with an imaging technique. The x and y-axes are in units of camera pixels, with 1 pixel$= 5.3\mu m$.

It is important to carefully treat the noise, in order to avoid cutting the weak intensity contributions to the signal. The technique we apply for noise treatment consists in averaging out the intensity coming from some pixels that are at the edge of the (x, y) beam profiles. This average is then used as an estimate for the background noise and then subtracted from the whole experimental data. A noise mask is then applied, i.e. the intensity points far from the main body of the beam profile are set to zero. This noise treatment procedure is crucial to obtain robust results when evaluating integral quantities, such as the average beam size for example.

As long as the interferogram data are concerned, a noise treatment is not needed. This is due to the fact that the Off Axis Digital Holography technique, selecting a small window around the Fourier transform of the beam, automatically filters all high-frequency contributions to the signal.

9.2 INTERPOLATION OF THE INITIAL CONDITION

To correctly simulate the beam propagation in the thermo-optical medium, the exact profile of the injected beam is needed. This quantity is employed as initial condition for the numerical simulation of the Newton-Schrödinger equation, which is used for quantitative comparisons with the experimental data. In order to obtain this information, we interpolate the input beam injected into the sample with a Gaussian field and an initial phase

$$\mathcal{E}_{fit}(x, y, z = 0) = Ae^{-\frac{(x-x_0)^2+(y-y_0)^2}{2s^2}} e^{-ik\frac{(x-x_0)^2+(y-y_0)^2}{2f}}, \tag{9.1}$$

being A, x_0, y_0, s, f, the best fit parameters. The fitting curve resulted into profile with $s = 350\,\mu m$ and an initial phase $f = -1m$.

9.3 REAL-SPACE COMPARISONS

For the real-space comparisons, we consider both the intensity profile and the average size of the beam. The former is analyzed considering a slice of the beam intensity profile as a function of one transverse coordinate for numerical simulation and experiment. We observe a good qualitative agreement, as shown in Figure Figure 9.3.

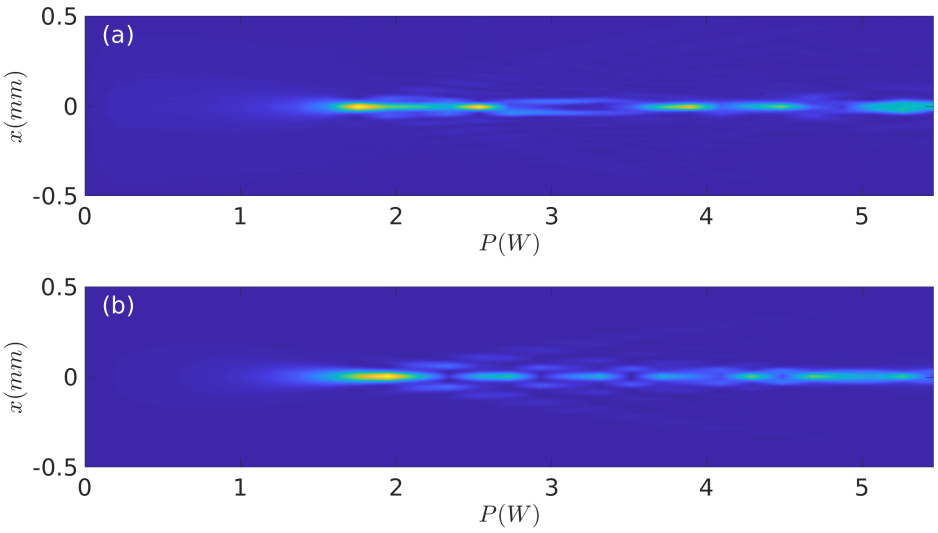

Figure 9.3 – $y = 0$ slice of the beam intensity profile as a function of one transverse coordinate x and power, obtained from experimental data (a) and the numerical simulation (b).

The global dynamics of the system is studied following the evolution of the average size of the beam profile, with the quantity

$$R(z) = \frac{1}{P_{y_0}} \int I(x, y = 0, z)\, |x|\, dx, \tag{9.2}$$

with $P_{y_0} = \int I(x, y = 0, z) dx$. The reason why we choose the one dimensional version of R, integrating over the $y = 0$ slice of the intensity profile instead of the full one, is that in this way a larger weight is given to the central part of the beam compared with the peripheral regions. The latter are indeed harder to experimentally measure with good accuracy, given that their relative intensity compared to the maximum one is very small.

In Figure 9.4, we show how varying χ affects the dynamics of the average size of the beam, obtained from the numerical simulations the Newton–Schrödinger equation. When $\chi \gtrsim 1$, diffraction effects start being important, as the beam width increases. Whereas, for small values of χ, the dynamics is dominated by the self-focusing collapse of the laser beam. The latter represents the regime where the semi-classical limit is approached.

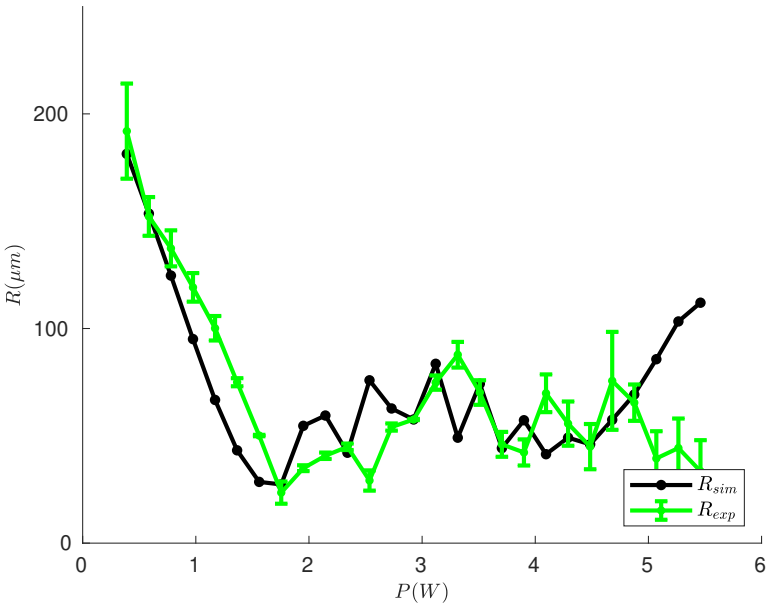

Figure 9.5 – Comparison between experiment and simulation of the average size of the beam profile as a function of power.

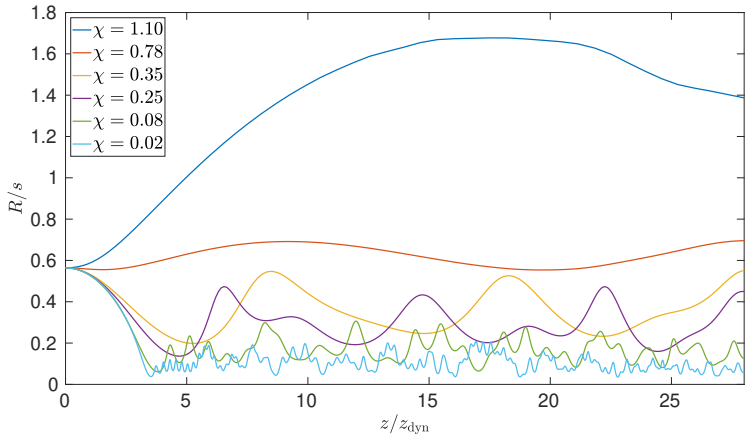

Figure 9.4 – Plot of the average size of the laser beam over the $y = 0$ slice of the intensity profile as a function of the longitudinal coordinate z in units of z_{dyn}, for different values of χ.

The evolution of R as a function of the input power (which can be mapped in z) in both the experimental case and the numerical simulation, is shown in Figure 9.5. Before the maximal collapse, the agreement is very good which indicates that the physics is well modeled by the Newton-Schrödinger equation. After the collapse, at large values of powers, the agreement is relatively good but not perfect. This is an expected feature since the oscillations predicted by the simulation are known to be chaotic [159], thus with a strong dependence on experimental parameters, such as the medium length and off-centering, as discussed in the next section.

9.3.1 *Medium length and off-centering*

The optical medium of our experimental setup is made of 3 identical samples, each of 100mm length, however the exact propagation distance covered by the beam is slightly larger. This is due to the fact that, at each interface between two samples, in order to avoid the back reflected beam to superpose with the incident one, a very small angle is introduced between the normal directions of the two facets. For this reason the propagation length inside the thermo-optical medium is expected to be a few millimeters larger. Simulations show how this quantity, which has not been directly measured, has an important influence on the behavior of the R(P) curve. As shown in Figure 9.6, where a difference of 1cm is taken into account, this parameter does not change significantly the results before the collapse. However, the difference becomes relatively important at large values of power, where a phase difference in the nonlinear oscillations appears.

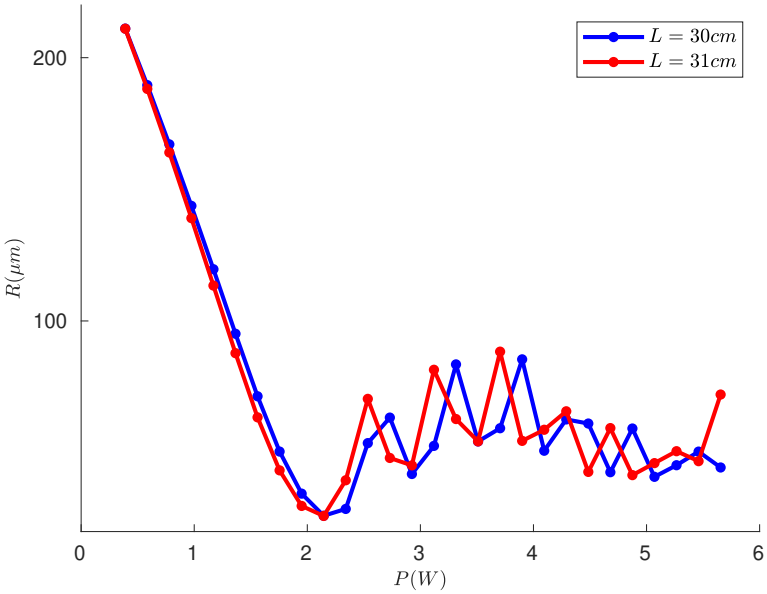

Figure 9.6 – Comparison of the average size of the beam profile as a function of power between two simulations, with media of lengths 30cm and 31cm.

Another parameter which is observed to strongly influence the behavior of the R(P) curve, is the off-centering, namely the correct identification of the pixel containing the center of the beam intensity profile. This is relatively easy, as long as the beam maintains a gaussian profile, with a single central peak. In this case, which is related to small values of power, the center can be simply identified with the pixel of the camera image corresponding to the maximal intensity. However after the collapse, several peaks appear and the central one does not always coincide with the maximal intensity, because of the presence of rings and oscillations. For this reason, identifying the exact position of the beam profile center could be more problematic, leading to another possible source of error which has some small - but still non negligible - consequences for the average size of the beam profile curve as a function of power, as shown in Figure 9.7.

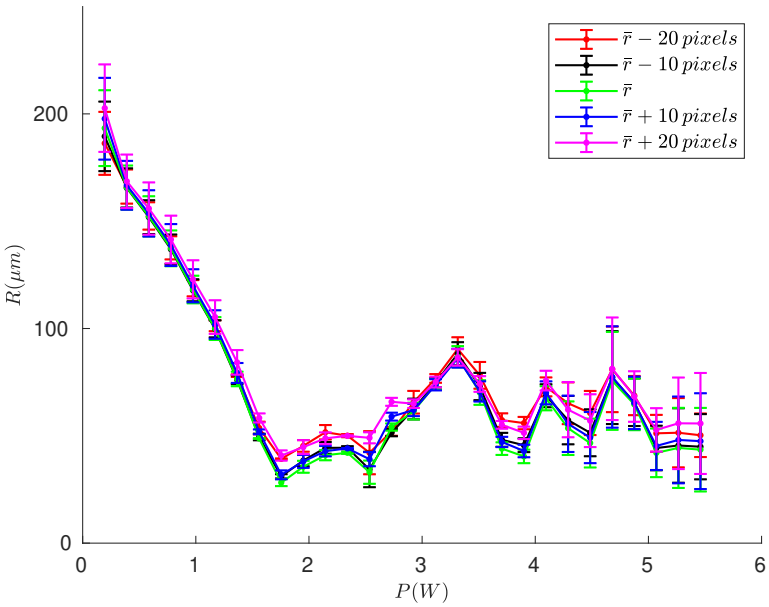

Figure 9.7 – Comparison of the experimental average size of the beam profile as a function of power with different off-centering.

9.4 PHASE-SPACE COMPARISONS

The existence of mixing in the system is studied experimentally and numerically, looking at the evolution of the phase space. To do that we use the Wigner distribution [43]

$$F(\mathbf{r}, \mathbf{k}, z) = \int d^2r' \, \mathcal{E}\left(\mathbf{r} + \frac{\mathbf{r}'}{2}, z\right) \mathcal{E}^*\left(\mathbf{r} - \frac{\mathbf{r}'}{2}, z\right) e^{i\mathbf{k}\cdot\mathbf{r}'}, \tag{9.3}$$

where $\mathcal{E}$ is the complex field (amplitude and phase) of the beam, obtained experimentally from the interferograms.

As done with the $R(P)$ quantity, also in this case we consider a one dimensional version of the Wigner distribution, by integrating over the $y = 0$ slice of the beam field instead of the full one

$$F(x, k_x, z) = \int dx' \, \mathcal{E}\left(x + \frac{x'}{2}, y = 0, z\right) \mathcal{E}^*\left(x - \frac{x'}{2}, y = 0, z\right) e^{ik_x x'}. \tag{9.4}$$

The results, which are shown in Figure 9.8, are in good agreement with simulations: at the beginning, the system has a Gaussian distribution in space and a very narrow dispersion along the k-axis, then phase mixing starts first "rolling up" phase space and then forming characteristic filaments (see e.g. [16]). The observed behavior of the evolution of phase space is the one expected when the violent relaxation process is present. The differences for the evolution of phase space and intensity profile with or without violent relaxation are discussed in details in the next section.

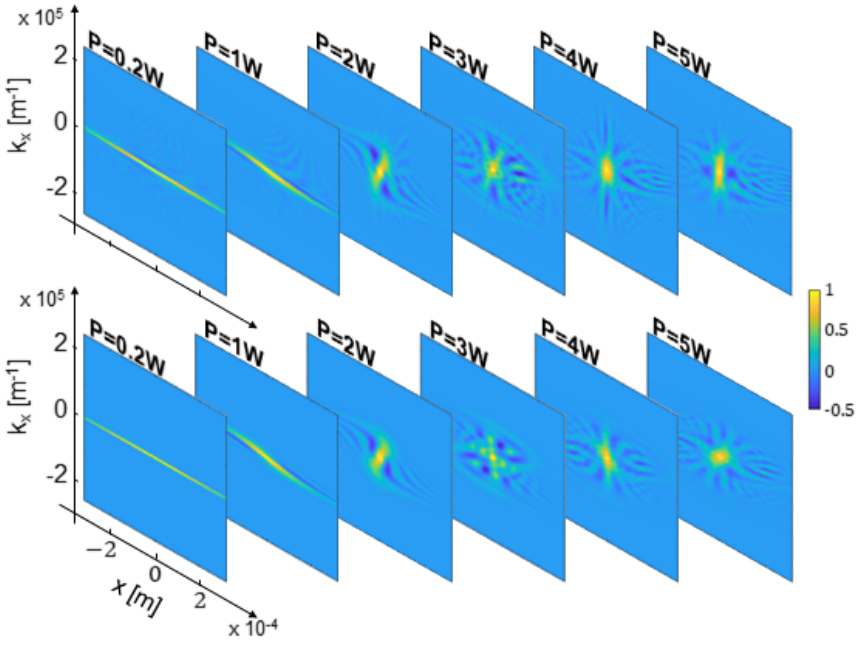

Figure 9.8 – Results of experiment (first row) and simulation (second row) for the $y = 0, k_y = 0$ profiles of the Wigner distribution.

9.4.1 *Differences of the evolution of phase space and intensity profile with or without violent relaxation*

As discussed in Section 3.1.1, if the mechanism of mixing process is driven by the existence of a (static) an-harmonic potential, the violent relaxation mechanism on the other hand requires the presence of a z-dependence on the potential. To better show the differences between this two cases, we look at the evolution of Newton-Schrödinger model, which presents phase-space mixing and violent relaxation, and the Snyder-Mitchell model [160], which only presents phase mixing. The Snyder-Mitchell model consist in a Schrödinger equation coupled with a nonlinear refractive-index profile calculated using the input beam profile $\mathcal{E}_0 = \mathcal{E}(\vec{r}_\perp, z = 0)$, namely

$$\begin{aligned} i\partial_z \mathcal{E} + \frac{1}{2k}\nabla_\perp^2 \mathcal{E} + k_0 \Delta n \mathcal{E} &= 0 \\ \nabla_\perp^2 \Delta n &= -\frac{\alpha\beta}{\kappa} I_0, \end{aligned} \tag{9.5}$$

where $I_0 = |\mathcal{E}_0|^2$.

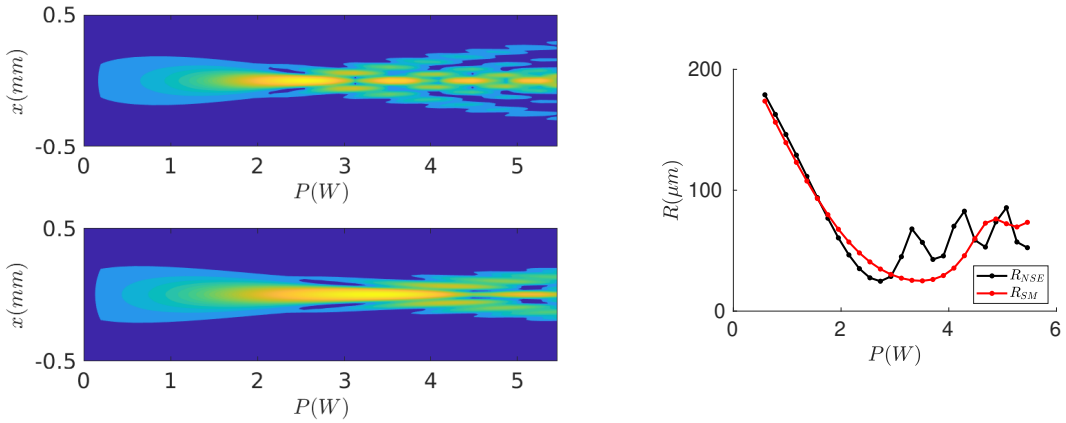

Figure 9.9 – Left plots: $y = 0$ slice of the beam intensity profile as a function of one transverse coordinate x and power, obtained from the Newton-Schrödinger equation (SN) (top left) and Snyder-Mitchell (SM) model (bottom left); both plots are in logarithmic color-scale. Right plot: comparison between the outputs of the Newton-Schrödinger equation simulation (black curve) and SM model (red curve) for the one dimensional average size of the beam profile as a function of power.

Figure 9.9 shows a quantitative comparison between the Newton-Schrödinger equation and the Snyder-Mitchell model: the dynamics is qualitatively similar, showing in both cases a collapse followed by nonlinear oscillations. At small power the difference between the structure of the output intensity profile is quite small, while after the minimum of the $R(P)$ curve, the dynamics of the two systems starts to differ in an important way. In particular one can see for the Newton-Schrödinger model an oscillating peak surrounded by concentric rings, while for the Snyder-Mitchell system the rings are less extended and the peak less pronounced, as shown in Figure 9.10. Indeed, the Newton-Schrödinger equation output intensity profile is in agreement with the one observed in the experiment, as at large power it is characterized by an autonomous central oscillating soliton surrounded by rings. On the other hand, the Snyder-Mitchell result is quite different, being more similar to a Fresnel diffraction pattern from a circular aperture.

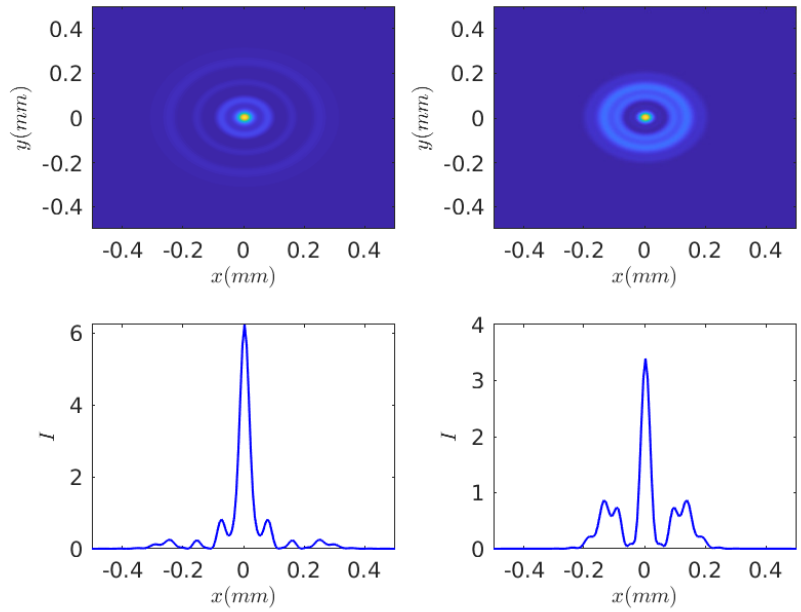

Figure 9.10 – Left plots: intensity profile predicted by the Newton-Schrödinger model as a function of the two transverse spatial coordinates (top left) and $y = 0$ slice (bottom left). Right plots: intensity profile predicted by the Snyder-Mitchell model as a function of the two transverse spatial coordinates (top right) and $y = 0$ slice (bottom right). All plots are at P=5.46W, as in both cases the central peak is at an absolute maximum at that power.

We arrive at the same conclusions looking at the phase-space dynamics, shown in Figure 9.11. At the beginning, the two models are very similar. At large powers, and in particular after the collapse ($P \approx 2W$), the Newton-Schrödinger model exhibits a more complicated dynamics (akin to the experimental Wigner distribution) compared with Snyder-Mitchell.

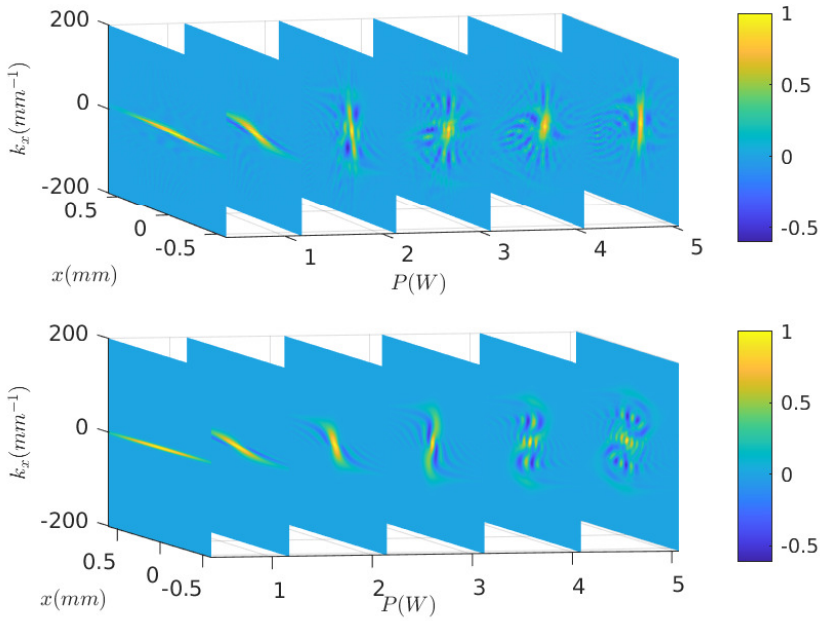

Figure 9.11 – Results of the NSE simulation (first row) and Snyder-Mitchell model (second row) for the $y = 0, k_y = 0$ profiles of the Wigner distribution.

9.4.2 *Shell-crossing*

Another typical feature of the dynamics of long range interacting system, essential for the violent relaxation mechanism, is the shell crossing phenomenon [15]. As explained in Section 3.1.3, during shell crossing the potential changes abruptly, leading to an exchange of energy between shells. This happens because different shells reach the center at different times.

In the optical framework, this corresponds to different "shells" of the intensity profile of the beam which self-focus by experiencing a potential well which changes during the propagation.

To observe the shell crossing phenomenology in the experiment, we study the map of the radial velocity distribution. The latter is obtained evaluating the gradient of the phase of the optical beam $\mathcal{E}$. Before doing this, the phase, measured with the holography technique, must be unwrapped, to prevent discontinuities associated with the its periodical behavior, which are not physical.

In Figure 9.12, we plot different snapshots of the evolution of the for experimental the velocity field. The color indicates the magnitude (with the sign) of the radial velocity. Specifically, we assign different red colors to the inward flux (red regions are collapsing toward the center) and blue colors to the outward flux (blue regions are going away from the center). At the beginning everything is red, since the system is self-focusing, then, after the collapse ($P \approx 1.8W$) the velocity flux starts going outward, exhibiting both rings going toward the center and rings going away from it. This corresponds to the shell crossing phenomenon [161], as we observe that there are shells which are going inwards, while other are going outwards.

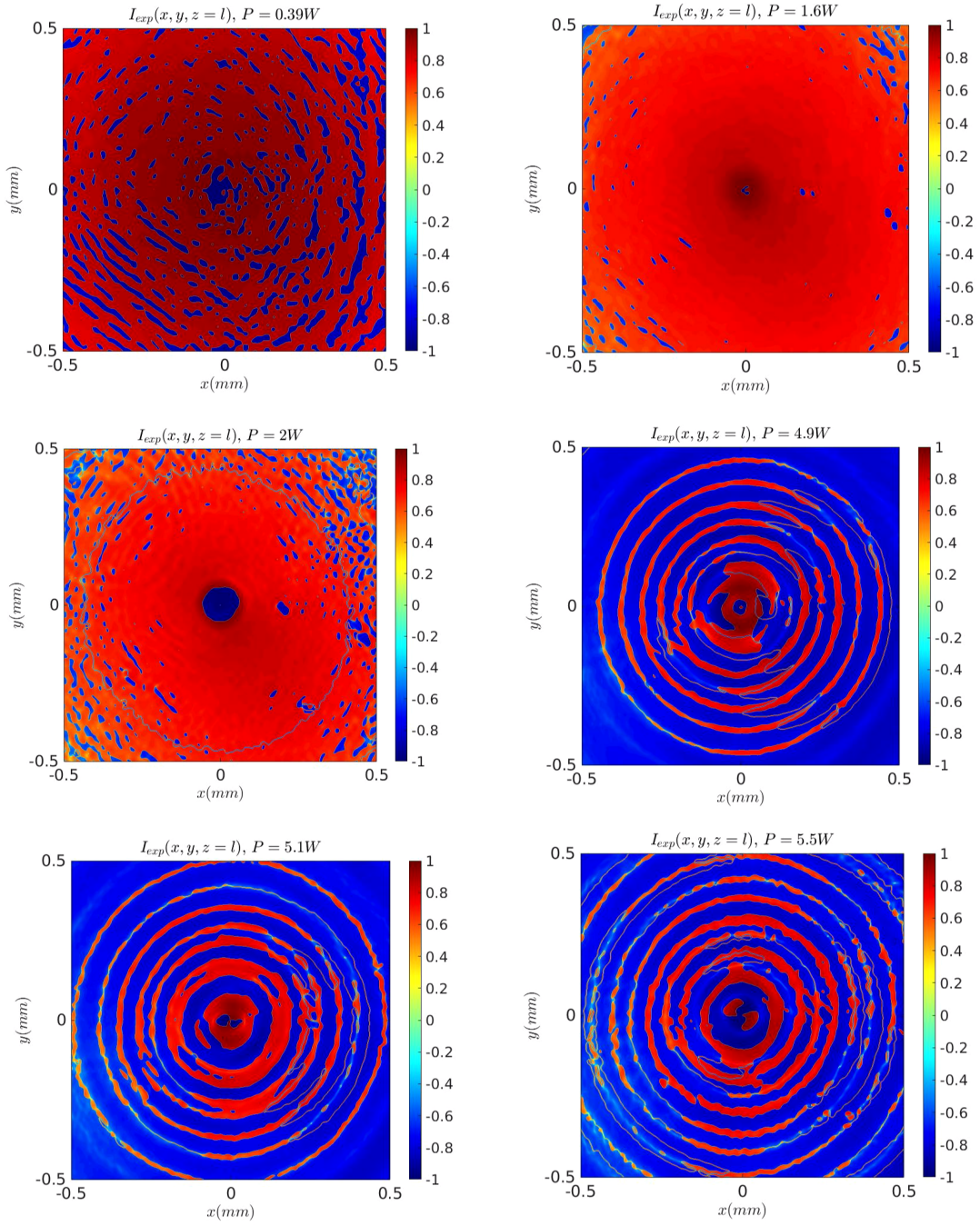

Figure 9.12 – Snapshots of the evolution of the for experimental the velocity field. The color indicates the magnitude (with the sign) of the radial velocity: red regions corresponds to the inward flux and blue regions to the outward flux.

9.5 ENERGY DISTRIBUTION COMPARISONS

To detect the actual signature of the violent relaxation process we look at the evolution of the energy distribution of the system. The local energy density can be defined as

$$E(\mathbf{r}, z) = \frac{|\nabla_\perp \mathcal{E}(\mathbf{r}, z)|^2}{2k\,|\mathcal{E}(\mathbf{r}, z)|^2} - k_0 \Delta n(\mathbf{r}, z), \tag{9.6}$$

the first term corresponding to the kinetic energy density and the second one to the potential one. Different definitions are possible for the kinetic term, all giving the same result for $\chi \to 0$ (see Appendix D). The energy distribution, is then defined as

$$\nu(E, z) = \frac{1}{P} \int d^2 r_\perp \, \delta\left[E - E(\mathbf{r}_\perp, z)\right] I(\mathbf{r}_\perp, z), \tag{9.7}$$

where δ is the Dirac Delta function and E is the energy density. For the optical Newton–Schrödinger equation,

As explained in Section 3.1.3, the energy distribution is expected to evolve in a system where an energy exchange takes place. In our optical setup, the violent relaxation is not the only possible source of energy exchange, because of the presence of reflections and absorption, as well as finite χ effects. For the latter, because of the considerations made in Section 4.2.2, we know that in our experimental regime they have a small impact on the dynamic of the system. This is explicitly shown in the next section. On the other hand, as long as dissipation effects are concerned, since all measurements are taken at the same value of z, the effect of reflections and absorption is the same for all powers. For these reasons, we can conclude that changes in the energy distribution are dominated by violent relaxation.

The evolution of the energy distribution is shown in Figure 9.13, for simulations (top) and experiment (bottom). Before the maximal self-focusing (around $P \approx 1.8W$), the energy distribution globally decreases because it is dominated by the potential energy and the system is collapsing. The energy is redistributed along the system essentially just before and just after the collapse, which is the moment where the violent relaxation is more efficient. After the collapse, the energy distribution presents two characteristic bumps: one at smallest energies, corresponding to the central region which has already completely relaxed (consisting of both the classical stationary state and the soliton), and the second bump at higher energies related to the more peripheral regions, which have not completely relaxed yet. We observe how, as power increases after the collapse, the energy distribution tends asymptotically to the quasi-stationary state, which has not been completely reached yet. At larger powers we observe also the formation of a soliton, associated with the minimal energy of the system. In Figure 9.14, we show the evolution of the energy distribution for each power. We observe a good quantitative agreement between experience (red curves) and simulation (blue curve). This confirms unambiguously the observation of the violent relaxation process.

9.5.1 *Evolution of the energy distribution: finite χ effects*

We determine the importance of finite χ effects in the evolution of the energy distribution, performing simulations with different values of χ, without dissipation

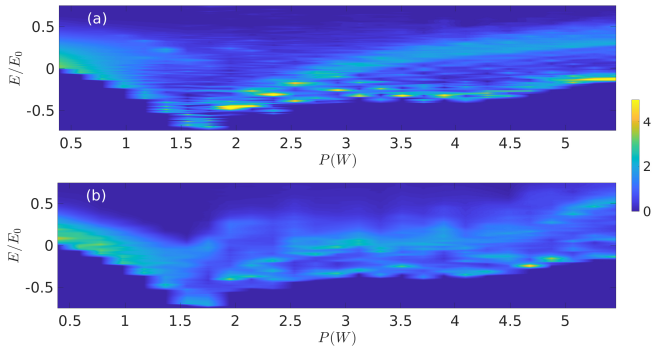

Figure 9.13 – Energy distribution map a for simulation (top) and the experiment (bottom). The energy axis is in units of $E_0 = (2\pi\kappa)/(\alpha\beta k_0 P)$.

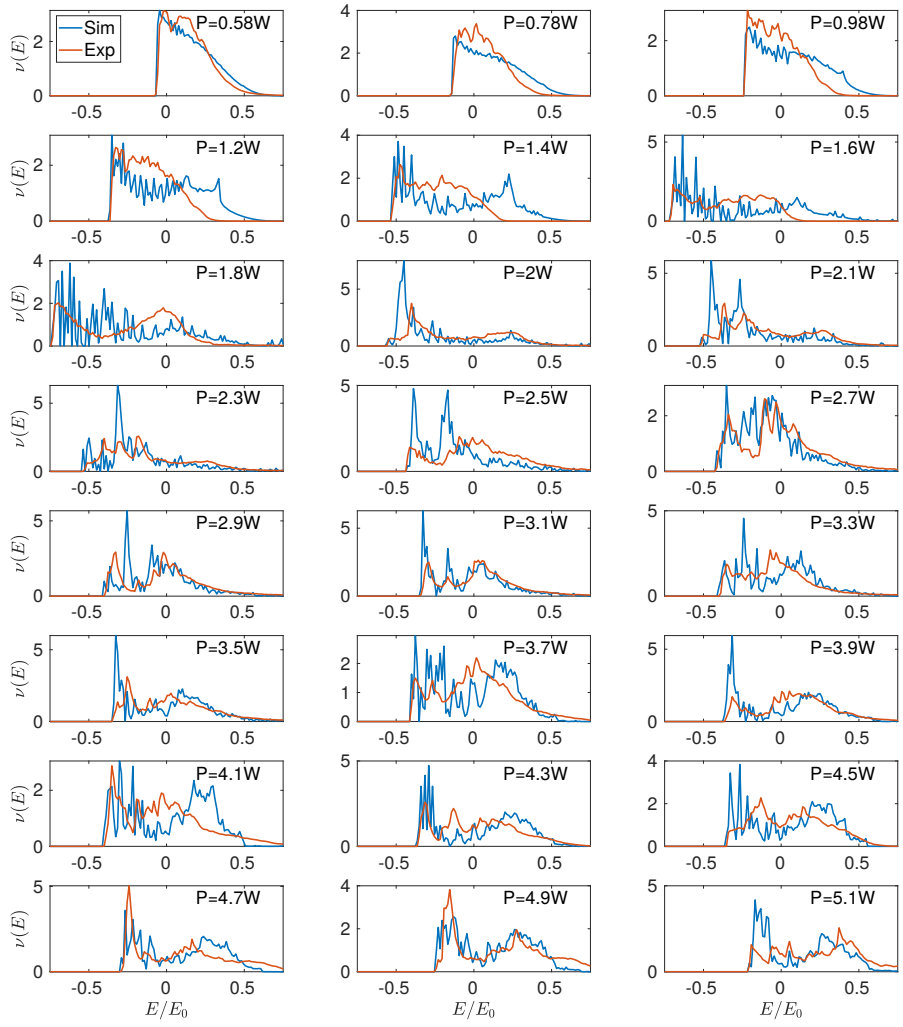

Figure 9.14 – Energy distribution at different values of power for simulation (blue curves) and experiment (red lcurves). The energy axis is in units of $E_0 = (2\pi\kappa)/(\alpha\beta k_0 P)$.

and reflections. We plot the evolution of the energy distribution in Figure 9.15, for different values of z, expressed in units of z_{dyn}. In the experiment, $z_{dyn} = 7.5\,cm$ (the end of the material) for $P \approx 1.77\,W$ (see Table 9.1). For values $z \lesssim 0.75 z_c$, we observe a weak finite χ effect, for all values simulated. For $z \gtrsim 3\, z_{dyn}$, we observe a convergence for the smallest values of χ, which coincides with the corresponding values of χ used in the experiment. We can conclude that the experiment χ is sufficiently small in order to have little incidence on the change of the energy distribution compared with violent relaxation.

$z(z_c)$	1.00	1.52	2.00	2.48	3.00	4.00	6.00	8.00
P(W)	0.11	0.26	0.44	0.70	1.00	1.77	3.98	7.08
χ	0.24	0.16	0.12	0.10	0.08	0.06	0.04	0.03

Table 9.1 – Some values of the power P with the associated value of χ and z in units of z_c. In the experiment the minimal value of the power is 0.39, the maximal one 5.46.

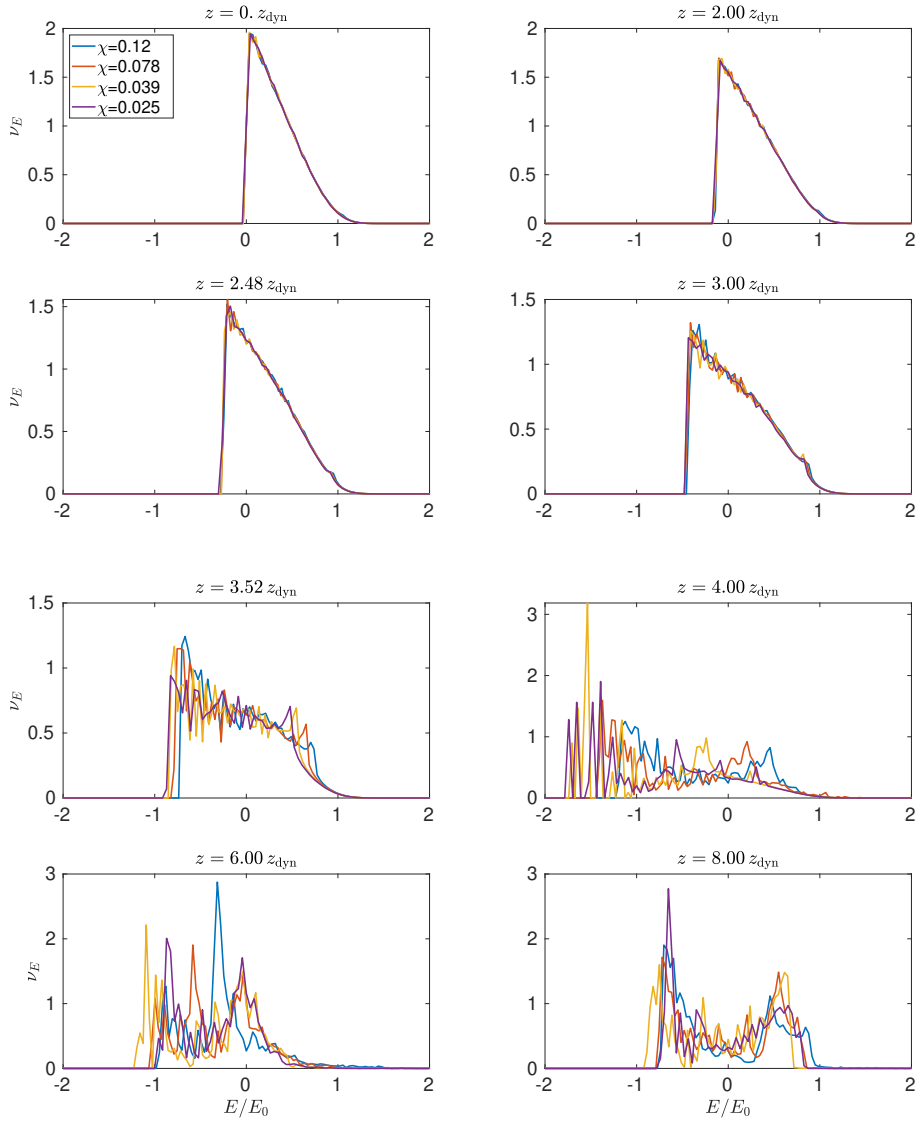

Figure 9.15 – Simulation of the evolution of the energy distribution for different values of the power χ. The energy axis is in units of $E_0 = (2\pi\kappa)/(\alpha\beta k_0 P)$

10 CONCLUSIONS

In this thesis, we focused on multiple aspects of the Newton–Schrödinger equation, investigating both theory and numerics and performing an experiment.

The experimental work, performed with a monochromatic laser beam propagating through a nonlinear non-local medium modeled by the Newton–Schröodinger equation, reported for the first time the violent relaxation mechanism, leading to the formation of a quasi-stationary state. This phenomenon, which is theoretically known for decades, but were not possible to observe in nature, is a crucial mechanism, responsible to the formation of galaxies and globular clusters. In addition, the experiment allows to control a range of parameters, including the nonlocal (gravitational) interaction strength and the strength of quantum gravity coupling $\hbar/m$, thus providing an effective test-bed for gravitational models that cannot otherwise be directly studied in experimental settings. The ability to tune the parameters of the interaction also provided a valid test-bed to compare theory and observations and a new approach to the study of the dynamics of long range interacting system.

The numerical work provided important results as well, both with the development of a new efficient method and the comparisons with the already existing ones.

Concerning the new method developed, exploiting a gauge condition on the potential, we optimized the integrating factor technique applied to Schrödinger-like equations. We called this method "IFC". Although the exact values of the piecewise constant c_n minimizing the error (5.44) (therefore maximizing the time-step) is in principle always possible to compute (e.g., with a computer algebra system), its expression depends on the particular numerical scheme chosen and it becomes complicated as the order of the method increases, resulting in a high computational cost. However, the near-optimal value obtained from the minimization of the L_2-norm of the nonlinear part of the equation, proved to be an accurate and efficient solution in the tested cases. Thus, being computationally extremely cheap and independent of the particular numerical scheme employed, this is the approach one should choose for most simulations, at least when the computation of the nonlinear term is not very expensive. For Schrödinger-like equations with hard to compute potentials, most of the computational time is spent in the calculation of the nonlinear term. For these very demanding equations, the extra cost needed to compute the optimum $\hat{c}_n$ (instead of the near optimum $\tilde{c}_n$) is negligible in comparison, so $\hat{c}_n$ could be preferable. For the cases tested here, we found a speed-up in the computation time up to a factor 5, the speed-up depending on the equation and on the physical regime. The numerical examples considered, show that this approach provides significant speed improvements, that with minor modifications of the original algorithm. Though we focused on the nonlinear Schrödinger and Schrödinger–Newton equations, the method principle is independent on the particular potential considered, so this approach can be extended to other Schrödinger-like equations. More generally, the idea behind the method presented can be, at least in principle, generalized and extended to other equations with similar gauge conditions.

Concerning the numerical comparisons between different methods, we studied the numerical integration of the Nonlinear Schrödinger and the Newton–Schrödinger equations using the integrating factor technique. This method was compared with another family of time-integrating solvers, the Split-Step integrators. For methods belonging to the integrating factor family, we tested fifth order time-adaptive algorithms while for the Split-Step family we focused on second, fourth and sixth order algorithm with fixed time-step and a fourth-order algorithm with adaptive time-step. We performed extensive tests with systems in one and two spatial dimensions, and with open or periodic boundary conditions. The comparisons between the results obtained in the tested cases, show that the IFC method can be more efficient than splitting algorithms, especially in the Nonlinear Schrödinger and periodical Newton–Schrödinger equations cases. For the Newton–Schrödinger equation in the non-periodical case on the other hand, splitting algorithms proved to be more efficient, even though the optimized integrating factor provided competitive results in terms of both speed and accuracy. Moreover, the results obtained for the Gross–Pitaevskii–Poisson equation pointed out how the presence of a short-range interaction term puts the integrating factor method in a clear more performing position. Finally, the achieved results show how, among the splitting algorithms at fixed step, working with higher order integrators is always more efficient. In particular, the Split-Step order 6 proved to be around 10 times faster compared with the lower order ones, while conserving the energy with the same error. The adaptive Split-Step produced good results as well, making the development of higher order version of this algorithm a very promising field of research.

Part IV

APPENDIX

A

ADIMENSIONALISATION

We discuss the adimensionalisation of the Newton–Schrödinger equation. Considering the most general case, one has

$$\begin{aligned} i a \frac{\partial \psi}{\partial t} + \frac{b}{2}\nabla^2\psi - cV\psi + i\frac{d}{2}\psi = 0 \\ \left(\nabla^2 - s\right) V = p\,|\psi|^2\,, \end{aligned} \tag{A.1}$$

where a, b, c, d, s, p are real constants (some of them possibly null), whose value and physical dimensions depend on the system considered. Adimensional variables, denoted with a "bar", are defined as

$$\psi = \alpha_\psi \overline{\psi} \qquad t = \alpha_t \bar{t} \qquad r = \alpha_r \bar{r} \qquad V = \alpha_V \overline{V}. \tag{A.2}$$

Choosing

$$\alpha_\psi = \sqrt{\frac{\mathcal{N}}{\alpha_r^d}} \qquad \alpha_t = \frac{a\alpha_r^2}{b} \qquad \alpha_V = \frac{b}{\alpha_r^2 c} \tag{A.3}$$

where $\mathcal{N} = \int d^d r\,|\psi|^2$ and α_r is arbitrary, the equations can be written as

$$\begin{aligned} i\frac{\partial \psi}{\partial t} + \frac{1}{2}\nabla^2\psi - V\psi + i\frac{f}{2}\psi = 0 \\ \left(\nabla^2 - h\right) V = g\,|\psi|^2 \end{aligned} \tag{A.4}$$

where the bar notation has been dropped for simplicity. In the latter equation, $f = \frac{d\alpha_r^2}{b}$, $g = \frac{c\mathcal{N}p\alpha_r^{4-d}}{b}$ and $h = \alpha_r^2 s$.

Notice that in this way one has

$$\int d^d r\,|\psi|^2 = e^{-ft}. \tag{A.5}$$

B

NUMERICAL ALGORITHMS

B.1 TSITOURAS SOLVER

In (B.1) we list the coefficients of Butcher tableau for the Tsitouras method.

$$
\begin{aligned}
a_{2,1} &= 0.161 \\
a_{3,1} &= -0.00848065549235699 \\
a_{3,2} &= 0.3354806554923570 \\
a_{4,1} &= 2.89715305710549 \\
a_{4,2} &= -6.359448489975075 \\
a_{4,3} &= 4.362295432869581 \\
a_{5,1} &= 5.32586482843926 \\
a_{5,2} &= -11.74888356406283 \\
a_{5,3} &= 7.495539342889836 \\
a_{5,4} &= -0.09249506636175525 \\
a_{6,1} &= 5.86145544294642 \\
a_{6,2} &= -12.92096931784711 \\
a_{6,3} &= 8.159367898576159 \\
a_{6,4} &= -0.07158497328140100 \\
a_{6,5} &= -0.02826905039406838,
\end{aligned}
\qquad
\begin{aligned}
b_1 &= 0.09646076681806523 \\
b_2 &= 0.01 \\
b_3 &= 0.4798896504144996 \\
b_4 &= 1.379008574103742 \\
b_5 &= -3.290069515436081 \\
b_6 &= 2.324710524099774 \\
b_7 &= 0,
\end{aligned}
$$

$$
\begin{aligned}
\widetilde{b}_1 &= 0.0946807557658394 \\
\widetilde{b}_2 &= 0.0091835655403432 \\
\widetilde{b}_3 &= 0.4877705284247615 \\
\widetilde{b}_4 &= 1.2342975669304789 \\
\widetilde{b}_5 &= -2.7077123499835254 \\
\widetilde{b}_6 &= 1.8666284181705870 \\
\widetilde{b}_7 &= \frac{1}{66},
\end{aligned}
$$

$$
\begin{aligned}
c_1 &= 0 \\
c_2 &= 0.161 \\
c_3 &= 0.327 \\
c_4 &= 0.9 \\
c_5 &= 0.9800255409045097 \\
c_6 &= 1 \\
c_7 &= 1.
\end{aligned}
\tag{B.1}
$$

B.2 FIXED TIME-STEP ALGORITHMS

We list below the pseudocodes for the Split-Step method at order 2 (SS2), 4 (SS4) and 6 (SS6) all at fixed time-step.

Algorithm 2 : SS2

$t \leftarrow t_{in}$
$\psi \leftarrow \psi(\vec{r}, t_{in})$
while $t < t_{fin}$ **do**
    $\psi \leftarrow \mathrm{FFT}^{-1}[e^{-i\hat{K}a_1 h}\mathrm{FFT}[\psi]]$
    $\psi \leftarrow e^{-iVb_1 h}\psi$
    $\psi \leftarrow \mathrm{FFT}^{-1}[e^{-i\hat{K}a_1 h}\mathrm{FFT}[\psi]]$
    $t \leftarrow t + h$
end while

Algorithm 3 : SS4

$t \leftarrow t_{in}$
$\psi \leftarrow \psi(\vec{r}, t_{in})$
while $t < t_{fin}$ **do**
    $\psi \leftarrow \mathrm{FFT}^{-1}[e^{-i\hat{K}a_1 h}\mathrm{FFT}[\psi]]$
    $\psi \leftarrow e^{-iV\omega b_1 h}\psi$
    $\psi \leftarrow \mathrm{FFT}^{-1}[e^{-i\hat{K}a_2 h}\mathrm{FFT}[\psi]]$
    $\psi \leftarrow e^{-iVb_2 h}\psi$
    $\psi \leftarrow \mathrm{FFT}^{-1}[e^{-i\hat{K}a_2 h}\mathrm{FFT}[\psi]]$
    $\psi \leftarrow e^{-iV\omega b_1 h}\psi$
    $\psi \leftarrow \mathrm{FFT}^{-1}[e^{-i\hat{K}a_1 h}\mathrm{FFT}[\psi]]$
    $t \leftarrow t + h$
end while

Algorithm 4 : SS6

$t \leftarrow t_{in}$
$\psi \leftarrow \psi(\vec{r}, t_{in})$
while $t < t_{fin}$ **do**
  $\psi \leftarrow \mathrm{FFT}^{-1}[e^{-i\hat{K}a_1 h}\mathrm{FFT}[\psi]]$
  $\psi \leftarrow e^{-iVb_1 h}\psi$
  $\psi \leftarrow \mathrm{FFT}^{-1}[e^{-i\hat{K}a_2 h}\mathrm{FFT}[\psi]]$
  $\psi \leftarrow e^{-iVb_2 h}\psi$
  $\psi \leftarrow \mathrm{FFT}^{-1}[e^{-i\hat{K}a_3 h}\mathrm{FFT}[\psi]]$
  $\psi \leftarrow e^{-iVb_3 h}\psi$
  $\psi \leftarrow \mathrm{FFT}^{-1}[e^{-i\hat{K}a_4 h}\mathrm{FFT}[\psi]]$
  $\psi \leftarrow e^{-iVb_4 h}\psi$
  $\psi \leftarrow \mathrm{FFT}^{-1}[e^{-i\hat{K}a_5 h}\mathrm{FFT}[\psi]]$
  $\psi \leftarrow e^{-iVb_5 h}\psi$
  $\psi \leftarrow \mathrm{FFT}^{-1}[e^{-i\hat{K}a_6 h}\mathrm{FFT}[\psi]]$
  $\psi \leftarrow e^{-iVb_5 h}\psi$
  $\psi \leftarrow \mathrm{FFT}^{-1}[e^{-i\hat{K}a_5 h}\mathrm{FFT}[\psi]]$
  $\psi \leftarrow e^{-iVb_4 h}\psi$
  $\psi \leftarrow \mathrm{FFT}^{-1}[e^{-i\hat{K}a_4 h}\mathrm{FFT}[\psi]]$
  $\psi \leftarrow e^{-iVb_3 h}\psi$
  $\psi \leftarrow \mathrm{FFT}^{-1}[e^{-i\hat{K}a_3 h}\mathrm{FFT}[\psi]]$
  $\psi \leftarrow e^{-iVb_2 h}\psi$
  $\psi \leftarrow \mathrm{FFT}^{-1}[e^{-i\hat{K}a_2 h}\mathrm{FFT}[\psi]]$
  $\psi \leftarrow e^{-iVb_1 h}\psi$
  $\psi \leftarrow \mathrm{FFT}^{-1}[e^{-i\hat{K}a_1 h}\mathrm{FFT}[\psi]]$
  $t \leftarrow t + h$
end while

where h is the time step, FFT and FFT^{-1} denote the fast Fourier transform and its inverse respectively, $\widehat{K}$ is the kinetic energy operator in Fourier space and V is the potential. The values of the coefficients a_i, b_i are listed in table Table B.1.

B.3 ADAPTIVE SPLIT-STEP

The pseudo-code for the adaptive Split-Step algorithm is described in ALG. (5), while the coefficients are listed in Table B.2.

SS2	SS4	SS6
$a_1 = \frac{1}{2}$	$a_1 = \frac{\omega}{2}$	$a_1 = 0.0502627644003922$
$b_1 = 1$	$b_1 = 1$	$b_1 = 0.148816447901042$
	$a_2 = \frac{1-\omega}{2}$	$a_2 = 0.413514300428344$
	$b_2 = 1 - 2\omega$	$b_2 = -0.132385865767784$
		$a_3 = 0.0450798897943977$
	$\omega = \frac{2+2^{1/3}+2^{-1/3}}{3}$	$b_3 = 0.067307604692185$
		$a_4 = -0.188054853819569$
		$b_4 = 0.432666402578175$
		$a_5 = 0.541960678450780$
		$b_5 = 0.5 - (b_1 + b_2 + b_3 + b_4)$
		$a_6 = 1 - 2(a_1 + a_2 + a_3 + a_4 + a_5)$

Table B.1 – Values of the a_i, b_i coefficients for the Split-Step algorithms.

Algorithm 5 : SSa

$t \leftarrow t_{in}$
$\psi \leftarrow \psi(\mathbf{r}, t_{in})$
while $t < t_f$ **do**
  $\Phi \leftarrow \psi$
  $\psi \leftarrow \mathrm{FFT}^{-1}[e^{-i\hat{K}a_1 h}\mathrm{FFT}[\psi]]$
  $\psi \leftarrow e^{-iVb_1 h}\psi$
  $\psi \leftarrow \mathrm{FFT}^{-1}[e^{-i\hat{K}a_2 h}\mathrm{FFT}[\psi]]$
  $\psi \leftarrow e^{-iVb_2 h}\psi$
  $\vdots$
  $\psi \leftarrow \mathrm{FFT}^{-1}[e^{-i\hat{K}a_7 h}\mathrm{FFT}[\psi]]$
  $\psi \leftarrow e^{-iVb_7 h}\psi$
  $\widetilde{\psi} \leftarrow \mathrm{FFT}^{-1}[e^{-i\hat{K}\tilde{a}_1 h}\mathrm{FFT}[\Phi]]$
  $\widetilde{\psi} \leftarrow e^{-iV\tilde{b}_1 h}\widetilde{\psi}$
  $\widetilde{\psi} \leftarrow \mathrm{FFT}^{-1}[e^{-i\hat{K}\tilde{a}_2 h}\mathrm{FFT}[\widetilde{\psi}]]$
  $\widetilde{\psi} \leftarrow e^{-iV\tilde{b}_2 h}\widetilde{\psi}$
  $\vdots$
  $\widetilde{\psi} \leftarrow \mathrm{FFT}^{-1}[e^{-i\hat{K}\tilde{a}_7 h}\mathrm{FFT}[\widetilde{\psi}]]$
  $\widetilde{\psi} \leftarrow e^{-iV\tilde{b}_7 h}\widetilde{\psi}$
  $err \leftarrow \sqrt{\frac{\sum_{i=1}^{N}|\psi(x_i,t_n)-\widetilde{\psi}(x_i,t_n)|^2}{\sum_{j=1}^{N}|\psi(x_j,t_n)|^2}}$
  if $err \leqslant tol$ **then**
    $t \leftarrow t + h$
  else
    $\psi \leftarrow \Phi$
  end if
  $h \leftarrow h \min\left\{\alpha\left(\frac{tol}{\Delta_n}\right)^{\frac{1}{4}}, \beta\right\}$
end while

SSa			
Order 4		Order 3	
a_1	0	$\tilde{a}_1$	0
b_1	0.0829844064174052	$\tilde{b}_1$	0.0829844064174052
a_2	0.245298957184271	$\tilde{a}_2$	0.245298957184271
b_2	0.3963098014983680	$\tilde{b}_2$	0.3963098014983680
a_3	0.604872665711080	$\tilde{a}_3$	0.604872665711080
b_3	-0.0390563049223486	$\tilde{b}_3$	-0.0390563049223486
a_4	0.5 - $(a_2 + a_3)$	$\tilde{a}_4$	0.5 - $(a_2 + a_3)$
b_4	1. - $2(b_1 + b_2 + b_3)$	$\tilde{b}_4$	1. - $2(b_1 + b_2 + b_3)$
a_5	0.5 - $(a_2 + a_3)$	$\tilde{a}_5$	0.3752162693236828
b_5	-0.0390563049223486	$\tilde{b}_5$	0.4463374354420499
a_6	0.604872665711080	$\tilde{a}_6$	1.4878666594737946
b_6	0.3963098014983680	$\tilde{b}_6$	-0.0060995324486253
a_7	0.245298957184271	$\tilde{a}_7$	-1.3630829287974774
b_7	0.0829844064174052	$\tilde{b}_7$	0

Table B.2 – Values of the parameters for the SSa.

C

LOSSES EFFECT

In absence of losses and in the limit $\chi \to 0$, the mapping between P and z described in Section 8.3.2 is exact. In this case the only mechanism responsible to the evolution of the energy distribution is the violent relaxation.

We first investigate the effect of losses in the mapping between P and z. In Figure C.1 (a-c) we show the difference between studying the dynamics in z (which corresponds to the original system) or in terms of the power (following the employed experiment procedure). Specifically, in Figure C.1 (a) we show the evolution of the beam intensity profile $I(x, y = 0, z; P = 5.46\,W)$ as a function of the propagation coordinate z/z_{dyn}, at fixed power, obtained from a simulation without losses. In Figure C.1 (c) on the other hand, we show the evolution of the intensity profile $I(x, y = 0, z = L = 30\,cm; P)$, obtained from a simulation with losses, varying the power, and expressing the propagation coordinated as L/z_{dyn}. The latter reproduces the experimental configuration. In both simulations we observe the same qualitative behavior. In Figure C.1 (b) we show the evolution of the transverse size of the system $R(z)$ for the same simulations presented in (a) and (c): without losses (blue curve) and with losses (black curve). The main difference is that the black curve collapses later compared with the blue one. This is due to the presence of losses, which slow-down the dynamics. For the same reason, the average beam size obtained varying the power at constant z, is shown to be slightly larger, compared to the blue curve. Despite these differences, the undergoing physics remains the same.

We now investigate the effect of losses in the evolution of the energy distribution after the collapse. In Figure C.1 (d) we show the evolution of the energy distribution, obtained from numerical simulations, from the lowest power to the largest one. The orange curve corresponds to the experimental configuration, with losses. The yellow curve correspond to a simulation without losses. In order to have both curves corresponding to the same output intensity, the yellow one is multiplied by a factor $T^4 e^{-\alpha L}$, which take into account losses. We observe that the difference form the initial energy distribution is much larger than the differences between these curves, which allows to conclude that the effect of violent relaxation dominates over losses in the evolution of the energy distribution.

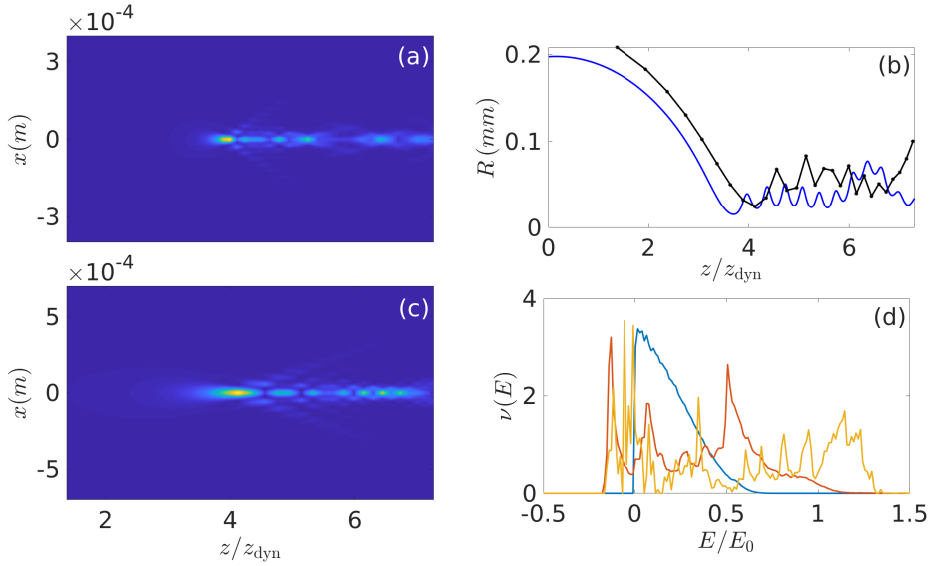

Figure C.1 – (a): evolution of the intensity profile $I(x, y = 0, z; P = 5.46\,W)$ for a simulation without losses. (b): evolution of the transverse size of the beam $R(z)$ without losses (blue curve) and with losses (black curve). (c): evolution of the intensity profile $I(x, y = 0, z = 30\,cm; P)$ for a simulation with losses, with P expressed in terms of z/z_{dyn} (see text). (d): evolution of the energy distribution from the initial condition (blue curve) to the largest power, with losses (orange curve) and without losses (yellow curve).

D

KINETIC ENERGY DENSITY IN THE CLASSICAL LIMIT

Here we show that computing the kinetic energy in the classical limit, using the operator Laplacian, gradient or Husimi distribution are equivalent. Let us define the Husimi representation of phase space [44]:

$$\Psi(\mathbf{x},\mathbf{p},t;\eta)=\frac{1}{2\pi\hbar}\left(\frac{1}{\pi\eta^2}\right)^{1/2}\int d^2r\,\mathcal{E}(\mathbf{r},t)\exp\left(-\frac{|\mathbf{x}-\mathbf{r}|^2}{2\eta^2}-i\frac{\mathbf{p}\cdot(\mathbf{r}-\mathbf{x}/2)}{\hbar}\right). \quad (D.1)$$

The distribution function is given by

$$\mathcal{F}(\mathbf{x},\mathbf{p},t;\eta)=|\Psi(\mathbf{x},\mathbf{p},t;\eta)|^2. \quad (D.2)$$

The classical limit is obtained by first taking the limit $\hbar\to 0$ and second $\eta\to 0$ [45]. In practice, in a simulation or in a experiment, the smallest value of η is chosen to be compatible with the condition $\eta\gg\xi$, where ξ is the healing length, the smallest structure in the system. The value of η gives the spatial resolution.

To compute the kinetic energy in a classical system one must evaluate the quantity $\langle|\mathbf{p}|^2\rangle$ which can be computed using (D.1):

$$\langle|\mathbf{p}|^2\rangle=\int d^2p\,\mathcal{F}(\mathbf{x},\mathbf{p},t;\eta)\,|\mathbf{p}|^2. \quad (D.3)$$

Using (D.2) one obtains

$$\langle|\mathbf{p}|^2\rangle=\left(\frac{1}{2\pi\hbar}\right)^2\frac{1}{\pi\eta^2}\times \quad (D.4)$$
$$\int d^2r\,d^2r'\,d^2p\,\mathcal{E}(\mathbf{r},t)\mathcal{E}^*(\mathbf{r}',t)e^{-|\mathbf{x}-\mathbf{r}|^2/2\eta^2}e^{-|\mathbf{x}-\mathbf{r}'|^2/2\eta^2}e^{-ip\cdot\mathbf{r}/\hbar}e^{ip\cdot\mathbf{r}'/\hbar}\,|\mathbf{p}|^2.$$

One can manipulate the above equation in two different ways, which will make appear the Laplacian or the squared gradient respectively. First, using that

$$|\mathbf{p}|^2e^{-ip\cdot\mathbf{r}/\hbar}=-\hbar^2\Delta_\mathbf{r}e^{-ip\cdot\mathbf{r}/\hbar}, \quad (D.5)$$

where $\Delta_\mathbf{r}$ is the Laplacian on the variable $\mathbf{r}$, and integrating (D.4) by parts twice about the variable $\mathbf{r}$ or $\mathbf{r}'$ one gets

$$\begin{aligned}\langle|\mathbf{p}|^2\rangle &= -\frac{1}{\pi\eta^2}\frac{1}{2}\left\{\int d^2r\mathcal{E}^*(\mathbf{r},t)e^{-|\mathbf{x}-\mathbf{r}|^2/2\eta^2}\Delta_\mathbf{r}\left[\mathcal{E}(\mathbf{r},t)e^{-|\mathbf{x}-\mathbf{r}|^2/2\eta^2}\right]+\right.\\ &\left.\int d^2r\mathcal{E}(\mathbf{r},t)e^{-|\mathbf{x}-\mathbf{r}|^2/2\eta^2}\Delta_\mathbf{r}\left[\mathcal{E}^*(\mathbf{r},t)e^{-|\mathbf{x}-\mathbf{r}|^2/2\eta^2}\right]\right\}. \quad (D.6)\end{aligned}$$

Second, using that

$$|\mathbf{p}|^2e^{-ip\cdot\mathbf{r}/\hbar}e^{ip\cdot\mathbf{r}'/\hbar}=\hbar^2\left[\nabla_\mathbf{r}e^{-ip\cdot\mathbf{r}/\hbar}\right]\left[\nabla_{\mathbf{r}'}e^{ip\cdot\mathbf{r}'/\hbar}\right], \quad (D.7)$$

where ∇_r is the gradient on the variable r, and integrating (D.4) by parts about the variables $\mathbf{r}$ and $\mathbf{r}'$ one has

$$\langle |\mathbf{p}|^2 \rangle = \frac{1}{\pi\eta^2} \int d^2r \left| \nabla_r \left[\mathcal{E}(\mathbf{r}, t) e^{-|\mathbf{x}-\mathbf{r}|^2/2\eta^2} \right] \right|^2 . \tag{D.8}$$

Equations (D.6) and (D.8) are exact. In the classical limit they can be simplified using that, in this limit,

$$\nabla_r \mathcal{E}(\mathbf{r}, t) \sim \mathcal{E}(\mathbf{r}, t)/\xi \gg \nabla_r e^{-|\mathbf{x}-\mathbf{r}|^2/2\eta^2} \sim e^{-|\mathbf{x}-\mathbf{r}|^2/2\eta^2}/\eta, \tag{D.9}$$

because $\eta \gg \xi$. One can then rewrite (D.6) as

$$\langle |\mathbf{p}|^2 \rangle \simeq -\frac{1}{\pi\eta^2} \frac{1}{2} \int d^2r \, e^{-|\mathbf{x}-\mathbf{r}|^2/\eta^2} \left[\mathcal{E}^*(\mathbf{r}, t) \Delta_r \mathcal{E}(\mathbf{r}, t) + \mathcal{E}(\mathbf{r}, t) \Delta_r \mathcal{E}^*(\mathbf{r}, t) \right] \tag{D.10}$$

and (D.8) as

$$\langle |\mathbf{p}|^2 \rangle \simeq \int d^2r \, e^{-|\mathbf{x}-\mathbf{r}|^2/\eta^2} \left| \nabla_r \mathcal{E}(\mathbf{r}, t) \right|^2 . \tag{D.11}$$

Taking first the limit $\eta \to 0$ of (D.10) and then the classical limit, one obtains

$$-\frac{1}{2} \left[\mathcal{E}^*(\mathbf{x}, t) \Delta_x \mathcal{E}(\mathbf{x}, t) + \mathcal{E}(\mathbf{x}, t) \Delta_x \mathcal{E}^*(\mathbf{x}, t) \right] \approx \left| \nabla_x \mathcal{E}(\mathbf{x}, t) \right|^2 . \tag{D.12}$$

BIBLIOGRAPHY

[1] Remo Ruffini and Silvano Bonazzola. « Systems of self-gravitating particles in general relativity and the concept of an equation of state. » In: *Physical Review* 187.5 (1969), p. 1767.

[2] Vanda Silveira and Claudio MG de Sousa. « Boson star rotation: A Newtonian approximation. » In: *Physical Review D* 52.10 (1995), p. 5724.

[3] Lajos Diosi. « Gravitation and quantummechanical localization of macroobjects. » In: *arXiv preprint arXiv:1412.0201* (2014).

[4] Roger Penrose. « On gravity's role in quantum state reduction. » In: *General relativity and gravitation* 28.5 (1996), pp. 581–600.

[5] Roger Penrose. « Quantum computation, entanglement and state reduction. » In: *Philosophical Transactions of the Royal Society of London. Series A: Mathematical, Physical and Engineering Sciences* 356.1743 (1998), pp. 1927–1939.

[6] Lawrence M Widrow and Nick Kaiser. « Using the Schrödinger equation to simulate collisionless matter. » In: *The Astrophysical Journal* 416 (1993), p. L71.

[7] Wayne Hu, Rennan Barkana, and Andrei Gruzinov. « Fuzzy cold dark matter: the wave properties of ultralight particles. » In: *Physical Review Letters* 85.6 (2000), p. 1158.

[8] Hsi-Yu Schive, Tzihong Chiueh, and Tom Broadhurst. « Cosmic structure as the quantum interference of a coherent dark wave. » In: *Nature Physics* 10.7 (2014), pp. 496–499.

[9] Angel Paredes and Humberto Michinel. « Interference of dark matter solitons and galactic offsets. » In: *Physics of the Dark Universe* 12 (2016), pp. 50–55.

[10] David JE Marsh and Jens C Niemeyer. « Strong constraints on fuzzy dark matter from ultrafaint dwarf galaxy Eridanus II. » In: *Physical review letters* 123.5 (2019), p. 051103.

[11] FW Dabby and JR Whinnery. « Thermal self-focusing of laser beams in lead glasses. » In: *Applied Physics Letters* 13.8 (1968), pp. 284–286.

[12] Carmel Rotschild, Oren Cohen, Ofer Manela, Mordechai Segev, and Tal Carmon. « Solitons in nonlinear media with an infinite range of nonlocality: first observation of coherent elliptic solitons and of vortex-ring solitons. » In: *Physical review letters* 95.21 (2005), p. 213904.

[13] Carmel Rotschild, Barak Alfassi, Oren Cohen, and Mordechai Segev. « Long-range interactions between optical solitons. » In: *Nature Physics* 2.11 (2006), pp. 769–774.

[14] J. Binney and S. Tremaine. *Galactic Dynamics*. Princeton University Press, 2008.

[15] J. Binney. « Discreteness effects in cosmological N-body simulations. » In: *Mon. Not. Roy. Astron. Soc.* 350 (2004), p. 939.

[16] James Binney. « Discreteness effects in cosmological N-body simulations. » In: *Monthly Notices of the Royal Astronomical Society* 350.3 (2004), pp. 939–948.

[17] Franco Dalfovo, Stefano Giorgini, Lev P Pitaevskii, and Sandro Stringari. « Theory of Bose–Einstein condensation in trapped gases. » In: *Reviews of Modern Physics* 71.3 (1999), p. 463.

[18] Akira Hasegawa. « Optical solitons in fibers. » In: *Optical Solitons in Fibers*. Springer, 1989, pp. 1–74.

[19] Christian Kharif, Efim Pelinovsky, and Alexey Slunyaev. *Rogue waves in the ocean*. Springer Science & Business Media, 2008.

[20] Claudio Conti, Marco Peccianti, and Gaetano Assanto. « Route to nonlocality and observation of accessible solitons. » In: *Physical review letters* 91.7 (2003), p. 073901.

[21] Yana Izdebskaya, Wieslaw Krolikowski, Noel F Smyth, and Gaetano Assanto. « Vortex stabilization by means of spatial solitons in nonlocal media. » In: *Journal of Optics* 18.5 (2016), p. 054006.

[22] D O'dell, S Giovanazzi, G Kurizki, and VM Akulin. « Bose–Einstein condensates with 1/r interatomic attraction: Electromagnetically induced "gravity". » In: *Physical Review Letters* 84.25 (2000), p. 5687.

[23] Abril Suárez and Pierre-Henri Chavanis. « Cosmological evolution of a complex scalar field with repulsive or attractive self-interaction. » In: *Physical Review D* 95.6 (2017), p. 063515.

[24] Pierre-Henri Chavanis. « Collapse of a self-gravitating Bose–Einstein condensate with attractive self-interaction. » In: *Physical Review D* 94.8 (2016), p. 083007.

[25] Argelia Bernal and F Siddhartha Guzman. « Scalar field dark matter: Head-on interaction between two structures. » In: *Physical Review D* 74.10 (2006), p. 103002.

[26] C. Canuto, M. Y. Hussaini, A. Quarteroni, and Th. A. Zang. *Spectral Methods. Fundamentals in Single Domains*. 2nd. Scientific Computation. Springer, 2008.

[27] J Douglas Lawson. « Generalized Runge–Kutta processes for stable systems with large Lipschitz constants. » In: *SIAM J. Numer. Anal.* 4.3 (1967), pp. 372–380.

[28] Sergio Blanes, Fernando Casas, and Ander Murua. « Splitting and composition methods in the numerical integration of differential equations. » In: *arXiv preprint arXiv:0812.0377* (2008).

[29] Philipp Bader, Sergio Blanes, Fernando Casas, and Mechthild Thalhammer. « Efficient time integration methods for Gross–Pitaevskii equations with rotation term. » In: *arXiv preprint arXiv:1910.12097* (2019).

[30] Christophe Besse, Geneviève Dujardin, and Ingrid Lacroix-Violet. « High order exponential integrators for nonlinear Schrödinger equations with application to rotating Bose–Einstein condensates. » In: *SIAM J. Numer. Anal.* 55.3 (2017), pp. 1387–1411.

[31] László Erdos and Horng-Tzer Yau. « Derivation of the nonlinear Schr\" odinger equation from a many body Coulomb system. » In: *arXiv preprint math-ph/0111042* (2001).

[32] Marcello Porta. « Mean-field evolution of fermionic systems. » In: *Séminaire Laurent Schwartz—EDP et applications* (2015), pp. 1–13.

[33] Claude Bardos, Laszlo Erdös, François Golse, Norbert Mauser, and Horng-Tzer Yau. « Derivation of the Schrödinger–Poisson equation from the quantum N-body problem. » In: *Comptes Rendus Mathematique* 334.6 (2002), pp. 515–520.

[34] Claude Bardos, François Golse, and Norbert J Mauser. « Weak coupling limit of the N-particle Schrödinger equation. » In: *Methods and Applications of Analysis* 7.2 (2000), pp. 275–294.

[35] Claude Bardos, François Golse, Alex Gottlieb, and Norbert J Mauser. « On the derivation of nonlinear Schrödinger and Vlasov equations. » In: *Dispersive Transport Equations and Multiscale Models*. Springer, 2004, pp. 1–23.

[36] Jean Ginibre and Giorgio Velo. « On a class of non linear Schrödinger equations with non local interaction. » In: *Mathematische Zeitschrift* 170.2 (1980), pp. 109–136.

[37] Michael Kopp, Kyriakos Vattis, and Constantinos Skordis. « Solving the Vlasov equation in two spatial dimensions with the Schrödinger method. » In: *Physical Review D* 96.12 (2017), p. 123532.

[38] Roger W Hockney and James W Eastwood. *Computer simulation using particles*. crc Press, 2021.

[39] Yu L Klimontovich. *The Statistical Theory of Non-Equilibrium Processes in a Plasma: International Series of Monographs in Natural Philosophy, Vol. 9*. Vol. 9. Elsevier, 2013.

[40] M. Joyce and B. Marcos. « Quantification of discreteness effects in cosmological N-bod y simulations: Initial conditions. » In: *Phys. Rev.* D75 (2007), p. 063516. eprint: astro-ph/0410451.

[41] Frederic A Rasio, Stuart L Shapiro, and Saul A Teukolsky. « Solving the Vlasov equation in general relativity. » In: *The Astrophysical Journal* 344 (1989), pp. 146–157.

[42] E Colomés, Z Zhan, and X Oriols. « Comparing Wigner, Husimi and Bohmian distributions: which one is a true probability distribution in phase space? » In: *Journal of Computational Electronics* 14.4 (2015), pp. 894–906.

[43] Eugene P Wigner. « On the quantum correction for thermodynamic equilibrium. » In: *Part I: Physical Chemistry. Part II: Solid State Physics*. Springer, 1997, pp. 110–120.

[44] Kôdi Husimi. « Some formal properties of the density matrix. » In: *Proceedings of the Physico-Mathematical Society of Japan. 3rd Series* 22.4 (1940), pp. 264–314.

[45] Philip Mocz, Lachlan Lancaster, Anastasia Fialkov, Fernando Becerra, and Pierre-Henri Chavanis. « Schrödinger-Poisson–Vlasov-Poisson correspondence. » In: *Physical Review D* 97.8 (2018), p. 083519.

[46] Rex T Skodje, Henry W Rohrs, and James VanBuskirk. « Flux analysis, the correspondence principle, and the structure of quantum phase space. » In: *Physical Review A* 40.6 (1989), p. 2894.

[47] Lawrence M Widrow and Nick Kaiser. « Using the Schrödinger equation to simulate collisionless matter. » In: *The Astrophysical Journal* 416 (1993), p. L71.

[48] David N Spergel and Paul J Steinhardt. « Observational evidence for self-interacting cold dark matter. » In: *Physical review letters* 84.17 (2000), p. 3760.

[49] Jesper Sommer-Larsen and Alexandre Dolgov. « Formation of disk galaxies: warm dark matter and the angular momentum problem. » In: *The Astrophysical Journal* 551.2 (2001), p. 608.

[50] Jeremy Goodman. « Repulsive dark matter. » In: *New Astronomy* 5.2 (2000), pp. 103–107.

[51] Marc Kamionkowski and Andrew R Liddle. « The dearth of halo dwarf galaxies: is there power on short scales? » In: *Physical Review Letters* 84.20 (2000), p. 4525.

[52] Giorgio Arcadi, Maíra Dutra, Pradipta Ghosh, Manfred Lindner, Yann Mambrini, Mathias Pierre, Stefano Profumo, and Farinaldo S Queiroz. « The waning of the WIMP? A review of models, searches, and constraints. » In: *The European Physical Journal C* 78.3 (2018), pp. 1–57.

[53] Gary Steigman and Michael S Turner. « Cosmological constraints on the properties of weakly interacting massive particles. » In: *Nuclear Physics B* 253 (1985), pp. 375–386.

[54] Timothy D Brandt. « Constraints on MACHO dark matter from compact stellar systems in ultra-faint dwarf galaxies. » In: *The Astrophysical Journal Letters* 824.2 (2016), p. L31.

[55] Angel Paredes and Humberto Michinel. « Interference of dark matter solitons and galactic offsets. » In: *Physics of the Dark Universe* 12 (June 2016), pp. 50–55. DOI: 10.1016/j.dark.2016.02.003. arXiv: 1512.05121 [astro-ph.CO].

[56] David J. E. Marsh and Jens C. Niemeyer. « Strong Constraints on Fuzzy Dark Matter from Ultrafaint Dwarf Galaxy Eridanus II. » In: *arXiv e-prints*, arXiv:1810.08543 (Oct. 2018), arXiv:1810.08543. arXiv: 1810.08543 [astro-ph.CO].

[57] Stephon Alexander, Jason J. Bramburger, and Evan McDonough. « Novel Substructure and Superfluid Dark Matter. » In: *arXiv e-prints*, arXiv:1901.03694 (Jan. 2019), arXiv:1901.03694. arXiv: 1901.03694 [astro-ph.CO].

[58] J. Diemand, B. Moore, and J. Stadel. « Earth-mass dark matter haloes as the first... » In: *Nature* 433 (2005), p. 389. eprint: astro-ph/0501589.

[59] WJG De Blok. « The core-cusp problem. » In: *Advances in Astronomy* 2010 (2010).

[60] Victor H. Robles, James S. Bullock, and Michael Boylan-Kolchin. « Scalar field dark matter: helping or hurting small-scale problems in cosmology? » In: 483 (Feb. 2019), pp. 289–298. DOI: 10.1093/mnras/sty3190. arXiv: 1807.06018 [astro-ph.CO].

[61] Ben Moore, Sebastiano Ghigna, Fabio Governato, George Lake, Thomas Quinn, Joachim Stadel, and Paolo Tozzi. « Dark matter substructure within galactic halos. » In: *The Astrophysical Journal Letters* 524.1 (1999), p. L19.

[62] Anatoly Klypin, Andrey V Kravtsov, Octavio Valenzuela, and Francisco Prada. « Where are the missing galactic satellites? » In: *The Astrophysical Journal* 522.1 (1999), p. 82.

[63] Lam Hui, Jeremiah P. Ostriker, Scott Tremaine, and Edward Witten. « Ultralight scalars as cosmological dark matter. » In: *Phys. Rev. D* 95 (4 2017), p. 043541. DOI: 10.1103/PhysRevD.95.043541. URL: https://link.aps.org/doi/10.1103/PhysRevD.95.043541.

[64] E Madelung. « Quantum theory in hydrodynamical form. » In: *Z. Phys* 40 ().

[65] Yuri S Kivshar and Govind P Agrawal. *Optical solitons: from fibers to photonic crystals*. Academic press, 2003.

[66] Yuen-Ron Shen. « The principles of nonlinear optics. » In: *New York* (1984).

[67] Govind P Agrawal. « Nonlinear fiber optics. » In: *Nonlinear Science at the Dawn of the 21st Century*. Springer, 2000, pp. 195–211.

[68] RW Boyd. *Nonlinear Optics (New York: Academic)*. 2003.

[69] Bahaa EA Saleh and Malvin Carl Teich. *Fundamentals of photonics*. john Wiley & sons, 2019.

[70] P. H. Chavanis. « Phase Transitions in Self-Gravitating Systems. » In: *Int. Jour. Mod. Phys. B* 20 (2006), pp. 3113–3198.

[71] Thierry Dauxois, Stefano Ruffo, Ennio Arimondo, and Martin Wilkens. « Dynamics and Thermodynamics of Systems with Long Range Interactions: an Introduction. » In: (2002). eprint: cond-mat/0208455.

[72] A. Campa, A. Giansanti, G. Morigi, and F. Sylos Labini. *Dynamics and Thermodynamics of Systems with Long Range Interactions: Theory and experiments*. AIP Conference Proceedings, 2008.

[73] A. Campa, T. Dauxois, and S. Ruffo. « Statistical mechanics and dynamics of solvable models with long-range interactions. » In: *Phys. Reports* 480 (Sept. 2009), pp. 57–159. arXiv: arXiv:0907.0323.

[74] Andrea Gabrielli, Michael Joyce, and Bruno Marcos. « Quasistationary states and the range of pair interactions. » In: *Physical review letters* 105.21 (2010), p. 210602.

[75] Andrea Gabrielli, Michael Joyce, Bruno Marcos, and Francois Sicard. « A dynamical classification of the range of pair interactions. » In: *Journal of Statistical Physics* 141.6 (2010), pp. 970–989.

[76] T. Padmanabhan. « Statistical mechanics of gravitating systems. » In: *Phys. Rept.* 188 (1990), p. 285.

[77] Peilong Chen and MC Cross. « Mixing and thermal equilibrium in the dynamical relaxation of a vortex ring. » In: *Physical review letters* 77.20 (1996), p. 4174.

[78] Renato Pakter and Yan Levin. « Nonequilibrium statistical mechanics of two-dimensional vortices. » In: *Physical review letters* 121.2 (2018), p. 020602.

[79] P.-H. Chavanis. « Kinetic theory of two-dimensional point vortices with collective effects. » In: *Journal of Statistical Mechanics: Theory and Experiment* 2 (Feb. 2012), p. 19. DOI: 10.1088/1742-5468/2012/02/P02019. arXiv: 1107.1447 [cond-mat.stat-mech].

[80] Michael Kastner. « Diverging equilibration times in long-range quantum spin models. » In: *Physical review letters* 106.13 (2011), p. 130601.

[81] OL Berman, R Ya Kezerashvili, GV Kolmakov, and Yu E Lozovik. « Turbulence in a Bose-Einstein condensate of dipolar excitons in coupled quantum wells. » In: *Physical Review B* 86.4 (2012), p. 045108.

[82] Sebastian Slama, Gordon Krenz, Simone Bux, Claus Zimmermann, and Philippe W Courteille. « Collective Atomic Recoil Lasing and Superradiant Rayleigh Scattering in a high-Q ring cavity. » In: *AIP Conference Proceedings*. Vol. 970. 1. American Institute of Physics. 2008, pp. 319–331.

[83] J Bleibel, A Domínguez, M Oettel, and S Dietrich. « Collective dynamics of colloids at fluid interfaces. » In: *The European Physical Journal E* 34.11 (2011), pp. 1–12.

[84] Y. Levin, R. Pakter, and F. Rizzato. « Collisionless relaxation in gravitational systems: from violent relaxation to gravothermal collapse. » In: *Phys. Rev.* E78 (2008), p. 021130.

[85] Y. Levin, R. Pakter, F. B. Rizzato, T. N. Teles, and F. P. d. C. Benetti. « Nonequilibrium Statistical Mechanics of Systems with Long-Range Interactions: Ubiquity of Core-Halo Distributions. » In: *Phys. Reports* 535 (Oct. 2014), p. 1.

[86] Donald Lynden-Bell. « Statistical mechanics of violent relaxation in stellar systems. » In: *Monthly Notices of the Royal Astronomical Society* 136 (1967), p. 101.

[87] Y. Y Yamaguchi, J. Barré, F. Bouchet, T. Dauxois, and S. Ruffo. « Stability criteria of the Vlasov equation and quasi-stationary states of the HMF model. » In: *Physica A* 337 (2004), pp. 36–66. eprint: cond-mat/0312480.

[88] Pierre-Henri Chavanis. « Hamiltonian and Brownian systems with long-range interactions: I Statistical equilibrium states and correlation functions. » In: *Physica A: Statistical Mechanics and its Applications* 361.1 (2006), pp. 55–80.

[89] P.-H. Chavanis. « Hamiltonian and Brownian systems with long-range interactions: II. Kinetic equations and stability analysis. » In: *Physica A Statistical Mechanics and its Applications* 361 (Feb. 2006), pp. 81–123. eprint: arXiv:cond-mat/0409641.

[90] Pierre-Henri Chavanis. « Hamiltonian and Brownian systems with long-range interactions: III. The BBGKY hierarchy for spatially inhomogeneous systems. » In: *Physica A: Statistical Mechanics and its Applications* 387.4 (2008), pp. 787–805.

[91] Pierre-Henri Chavanis. « Hamiltonian and Brownian systems with long-range interactions: IV. General kinetic equations from the quasilinear theory. » In: *Physica A: Statistical Mechanics and its Applications* 387.7 (2008), pp. 1504–1528.

[92] Peter Szekeres and Anthony Lun. « What is a shell-crossing singularity? » In: *The ANZIAM Journal* 41.2 (1999), pp. 167–179.

[93] S Sridhar. « Undamped oscillations of homogeneous collisionless stellar systems. » In: *Monthly Notices of the Royal Astronomical Society* 238.4 (1989), pp. 1159–1163.

[94] Qin Zhao, Mir Faizal, and Zaid Zaz. « Short distance modification of the quantum virial theorem. » In: *Physics Letters B* 770 (2017), pp. 564–568.

[95] Dean G Duffy. *Green's functions with applications*. Chapman and Hall/CRC, 2015.

[96] Alvaro Navarrete, Angel Paredes, José R Salgueiro, and Humberto Michinel. « Spatial solitons in thermo-optical media from the nonlinear Schrödinger-Poisson equation and dark-matter analogs. » In: *Physical Review A* 95.1 (2017), p. 013844.

[97] Irene M Moroz, Roger Penrose, and Paul Tod. « Spherically-symmetric solutions of the Schrödinger-Newton equations. » In: *Classical and Quantum Gravity* 15.9 (1998), p. 2733.

[98] Giovanni Manfredi, Paul-Antoine Hervieux, and Fernando Haas. « Variational approach to the time-dependent Schrödinger–Newton equations. » In: *Classical and Quantum Gravity* 30.7 (2013), p. 075006.

[99] Erwin Madelung. « Quantum theory in hydrodynamical form. » In: *Phys* 40 (1927), p. 322.

[100] Randall J LeVeque. *Finite difference methods for ordinary and partial differential equations: steady-state and time-dependent problems*. SIAM, 2007.

[101] Claudio Canuto, M Yousuff Hussaini, Alfio Quarteroni, and Thomas A Zang. *Spectral methods: fundamentals in single domains*. Springer Science & Business Media, 2007.

[102] John P Boyd. *Chebyshev and Fourier spectral methods*. Courier Corporation, 2001.

[103] Bengt Fornberg. *A practical guide to pseudospectral methods*. 1. Cambridge university press, 1998.

[104] Steven A Orszag. « Comparison of pseudospectral and spectral approximation. » In: *Studies in Applied Mathematics* 51.3 (1972), pp. 253–259.

[105] James W Cooley and John W Tukey. « An algorithm for the machine calculation of complex Fourier series. » In: *Mathematics of computation* 19.90 (1965), pp. 297–301.

[106] Matteo Frigo and Steven G Johnson. « FFTW user's manual. » In: *Massachusetts Institute of Technology* (1999).

[107] RA James. « The solution of Poisson's equation for isolated source distributions. » In: *Journal of Computational Physics* 25.2 (1977), pp. 71–93.

[108] John Magorrian. « grommet: an N-body code for high-resolution simulations of individual galaxies. » In: *Monthly Notices of the Royal Astronomical Society* 381.4 (2007), pp. 1663–1671.

[109] Reuben D. Budiardja and Christian Y. Cardall. « Parallel FFT-based Poisson solver for isolated three-dimensional systems. » In: *Comput. Phys. Commun.* 182.10 (2011), pp. 2265 –2275. ISSN: 0010-4655. DOI: https://doi.org/10.1016/j.cpc.2011.05.014. URL: http://www.sciencedirect.com/science/article/pii/S0010465511001809.

[110] Marlis Hochbruck and Alexander Ostermann. « Exponential integrators. » In: *Acta Numerica* 19 (2010), pp. 209–286.

[111] Roger Alexander. « Solving ordinary differential equations I: Nonstiff problems (E. Hairer, SP Norsett, and G. Wanner). » In: *Siam Review* 32.3 (1990), p. 485.

[112] John Charles Butcher. *Numerical methods for ordinary differential equations*. John Wiley & Sons, 2016.

[113] Brice Eichwald. « Intégrateurs exponentiels modifiés pour la simulation des vagues non linéaires. » PhD thesis. Université Nice Sophia Antipolis, 2013.

[114] John R Dormand and Peter J Prince. « A family of embedded Runge–Kutta formulae. » In: *J. Comp. Appl. Math.* 6.1 (1980), pp. 19–26.

[115] Ch Tsitouras. « Runge–Kutta pairs of order 5(4) satisfying only the first column simplifying assumption. » In: *Computers & Mathematics with Applications* 62.2 (2011), pp. 770–775.

[116] Gerhard Wanner and Ernst Hairer. *Solving ordinary differential equations II*. Springer Berlin Heidelberg, 1996.

[117] Kjell Gustafsson. « Control theoretic techniques for stepsize selection in explicit Runge–Kutta methods. » In: *ACM Transactions on Mathematical Software (TOMS)* 17.4 (1991), pp. 533–554.

[118] Herman JC Berendsen, JPM van Postma, Wilfred F van Gunsteren, ARHJ DiNola, and Jan R Haak. « Molecular dynamics with coupling to an external bath. » In: *The Journal of chemical physics* 81.8 (1984), pp. 3684–3690.

[119] Helge Holden, Kenneth H Karlsen, and Knut-Andreas Lie. *Splitting methods for partial differential equations with rough solutions: Analysis and MATLAB programs*. Vol. 11. European Mathematical Society, 2010.

[120] Masuo Suzuki. « General theory of fractal path integrals with applications to many-body theories and statistical physics. » In: *Journal of Mathematical Physics* 32.2 (1991), pp. 400–407.

[121] Mechthild Thalhammer and Jochen Abhau. « A numerical study of adaptive space and time discretisations for Gross–Pitaevskii equations. » In: *Journal of computational physics* 231.20 (2012), pp. 6665–6681.

[122] Sergio Blanes and Per Christian Moan. « Practical symplectic partitioned Runge–Kutta and Runge–Kutta–Nyström methods. » In: *Journal of Computational and Applied Mathematics* 142.2 (2002), pp. 313–330.

[123] Mechthild Thalhammer. « High-order exponential operator splitting methods for time-dependent Schrödinger equations. » In: *SIAM Journal on Numerical Analysis* 46.4 (2008), pp. 2022–2038.

[124] Endre Süli and David F Mayers. *An introduction to numerical analysis*. Cambridge university press, 2003.

[125] VE Zakharov and VS Synakh. « The nature of the self-focusing singularity. » In: *Zh. Eksp. Teor. Fiz* 68 (1975), pp. 940–947.

[126] Kimiaki Konno and Hiromitsu Suzuki. « Self-focussing of laser beam in nonlinear media. » In: *Physica Scripta* 20.3-4 (1979), p. 382.

[127] Catherine Sulem and Pierre-Louis Sulem. *The nonlinear Schrödinger equation: self-focusing and wave collapse*. Vol. 139. Springer Science & Business Media, 2007.

[128] Etienne Forest and Ronald D Ruth. « Fourth-order symplectic integration. » In: *Physica D: Nonlinear Phenomena* 43.1 (1990), pp. 105–117.

[129] Robert McLachlan. « Symplectic integration of Hamiltonian wave equations. » In: *Numerische Mathematik* 66.1 (1993), pp. 465–492.

[130] George Davies and Lawrence M. Widrow. « Test-Bed Simulations of Collisionless, Self-Gravitating Systems Using the Schrödinger Method. » In: *The Astrophysical Journal* 485.2 (1997), pp. 484–495. DOI: 10.1086/304440. URL: https://doi.org/10.1086/304440.

[131] P. J. E. Peebles. *The Large-Scale Structure of the Universe*. Princeton University Press, 1980.

[132] Thomas Roger, Calum Maitland, Kali Wilson, Niclas Westerberg, David Vocke, Ewan M Wright, and Daniele Faccio. « Optical analogues of the Newton–Schrödinger equation and boson star evolution. » In: *Nature communications* 7 (2016), p. 13492.

[133] Rivka Bekenstein, Ran Schley, Maor Mutzafi, Carmel Rotschild, and Mordechai Segev. « Optical simulations of gravitational effects in the Newton–Schrödinger system. » In: *Nature Physics* 11.10 (2015), pp. 872–878.

[134] M Chalony, J Barré, B Marcos, A Olivetti, and D Wilkowski. « Long-range 1D gravitational-like interaction in a neutral atomic cold gas. » In: ().

[135] Toshiya Kinoshita, Trevor Wenger, and David S Weiss. « A quantum Newton's cradle. » In: *Nature* 440.7086 (2006), pp. 900–903.

[136] S Hofferberth, Igor Lesanovsky, B Fischer, Thorsten Schumm, and Jörg Schmiedmayer. « Non-equilibrium coherence dynamics in one-dimensional Bose gases. » In: *Nature* 449.7160 (2007), pp. 324–327.

[137] Philip Makotyn, Catherine E Klauss, David L Goldberger, EA Cornell, and Deborah S Jin. « Universal dynamics of a degenerate unitary Bose gas. » In: *Nature Physics* 10.2 (2014), pp. 116–119.

[138] Ryo Kawahara and Hiizu Nakanishi. « Quasi-stationary states of two-dimensional electron plasma trapped in magnetic field. » In: *Journal of the Physical Society of Japan* 75.5 (2006), p. 054001.

[139] X-P Huang and CF Driscoll. « Relaxation of 2D turbulence to a metaequilibrium near the minimum enstrophy state. » In: *Physical review letters* 72.14 (1994), p. 2187.

[140] JR Danielson, F Anderegg, and CF Driscoll. « Measurement of Landau damping and the evolution to a BGK equilibrium. » In: *Physical review letters* 92.24 (2004), p. 245003.

[141] CC Damm, JH Foote, AH Futch Jr, AL Hunt, K Moses, RF Post, and JB Taylor. « Evidence for Collisionless Damping of Unstable Waves in a Mirror-Confined Plasma. » In: *Physical Review Letters* 24.10 (1970), p. 495.

[142] KW Gentle and A Malein. « Observations of nonlinear landau damping. » In: *Physical Review Letters* 26.11 (1971), p. 625.

[143] Masao Sugawa. « Observation of self-interaction of Bernstein waves by nonlinear Landau damping. » In: *Physical review letters* 61.5 (1988), p. 543.

[144] CHK Chen, KG Klein, and Gregory G Howes. « Evidence for electron Landau damping in space plasma turbulence. » In: *Nature communications* 10.1 (2019), pp. 1–8.

[145] Joseph E Borovsky and Michael H Denton. « A survey of the anisotropy of the outer electron radiation belt during high-speed-stream-driven storms. » In: *Journal of Geophysical Research: Space Physics* 116.A5 (2011).

[146] Tapio Simula, Matthew J Davis, and Kristian Helmerson. « Emergence of order from turbulence in an isolated planar superfluid. » In: *Physical review letters* 113.16 (2014), p. 165302.

[147] Johnathan Lau, Olga Goulko, Thomas Reimann, Daniel Suchet, Cédric Enesa, Frédéric Chevy, and Carlos Lobo. « Quasithermalization of collisionless particles in quadrupole potentials. » In: *Physical Review A* 101.3 (2020), p. 033605.

[148] L. D. Landau. « On the vibrations of the electronic plasma. » In: *J. Phys. (USSR)* 10 (1946), pp. 25–34.

[149] JH Malmberg and CB Wharton. « Collisionless damping of electrostatic plasma waves. » In: *Physical Review Letters* 13.6 (1964), p. 184.

[150] V Kelvin Neil and Andrew M Sessler. « Longitudinal resistive instabilities of intense coasting beams in particle accelerators. » In: *Review of Scientific Instruments* 36.4 (1965), pp. 429–436.

[151] L Jackson Laslett, V Kelvin Neil, and Andrew M Sessler. « Transverse resistive instabilities of intense coasting beams in particle accelerators. » In: *Review of Scientific Instruments* 36.4 (1965), pp. 436–448.

[152] R A KISHEK, PG O'SHEA, S Bernal, I Haber, J R HARRIS, Y Huo, H Li, and M Reiser. « The University of Maryland electron ring: A platform for study of galactic dynamics on a laboratory scale. » In: *Annals of the New York Academy of Sciences* 1045.1 (2005), pp. 45–54.

[153] D Comparat, T Vogt, N Zahzam, M Mudrich, and P Pillet. « Star cluster dynamics in a laboratory: electrons in an ultracold plasma. » In: *Monthly Notices of the Royal Astronomical Society* 361.4 (2005), pp. 1227–1242.

[154] Jacopo Bertolotti. *Off-Axis Digital Holography Tutorial*. https://jacopobertolotti.com/tutorials.html.

[155] Alessandro Alberucci and Gaetano Assanto. « Propagation of optical spatial solitons in finite-size media: interplay between nonlocality and boundary conditions. » In: *JOSA B* 24.9 (2007), pp. 2314–2320.

[156] SA Louis, Timothy R Marchant, and Noel F Smyth. « Optical solitary waves in thermal media with non-symmetric boundary conditions. » In: *Journal of Physics A: Mathematical and Theoretical* 46.5 (2013), p. 055201.

[157] Simon A Louis, Tim R Marchant, and Noel F Smyth. « 2-D solitary waves in thermal media with nonsymmetric boundary conditions. » In: *Studies in Applied Mathematics* 142.4 (2019), pp. 586–607.

[158] Thomas Roger, Calum Maitland, Kali Wilson, Niclas Westerberg, David Vocke, Ewan M Wright, and Daniele Faccio. « Optical analogues of the Newton–Schrödinger equation and boson star evolution. » In: *Nature communications* 7.1 (2016), pp. 1–8.

[159] Peter O. Vandervoort. « On chaos in the oscillations of galaxies. » In: *Monthly Notices of the Royal Astronomical Society* 411.1 (Jan. 2011), pp. 37–53. ISSN: 0035-8711. DOI: 10.1111/j.1365-2966.2010.17656.x. eprint: https://academic.oup.com/mnras/article-pdf/411/1/37/3485127/mnras0411-0037.pdf. URL: https://doi.org/10.1111/j.1365-2966.2010.17656.x.

[160] Allan W Snyder and D John Mitchell. « Accessible solitons. » In: *Science* 276.5318 (1997), pp. 1538–1541.

[161] M. Joyce, B. Marcos, and F. Sylos Labini. « Energy ejection in the collapse of a cold spherical self-gravitating cloud. » In: *Mon. Not. R. Astron. Soc.* 397 (2009), p. 775. eprint: arXiv:0811.2752.